Jets at High Q^2 at HERA and Test Beam Measurements with the EUDET Pixel Telescope

Dissertation

zur Erlangung des Doktorgrades

des Department Physik

der Universität Hamburg

vorgelegt von

Jörg Behr

aus Hamburg

Hamburg

2010

Gutachter der Dissertation:	Prof. Dr. Robert Klanner JProf. Dr. Johannes Haller
Gutachter der Disputation:	Prof. Dr. Robert Klanner Dr. Thomas Schörner-Sadenius
Datum der Disputation:	17.09.2010
Vorsitzender des Prüfungsausschusses:	Dr. Michael Martins
Vorsitzender des Promotionsausschusses:	Prof. Dr. Joachim Bartels
Dekan der MIN Fakultät:	Prof. Dr. Heinrich Graener
Leiter des Department Physik:	Prof. Dr. Daniela Pfannkuche

Abstract

In this thesis, the measurement of inclusive dijet and trijet cross sections in deep-inelastic ep scattering at HERA is presented. The kinematic phase space of the measurement was defined by $125 < Q^2 < 20000$ GeV^2 and $0.2 < y < 0.6$, where Q^2 and y are the virtuality and the inelasticity, respectively. The data sample was taken during the years 1998-2000 and 2004–2007 with the ZEUS detector and corresponded to an integrated luminosity of 374 pb^{-1}. The inclusive k_t jet algorithm was applied to the massless final-state objects in the Breit reference frame. The cross sections referred to jets with $E_{T,\mathrm{B}}^{\mathrm{jet}} > 8$ GeV and $-1 < \eta_{\mathrm{LAB}}^{\mathrm{jet}} < 2.5$, where the first quantity is the transverse jet energy in the Breit frame and the latter the jet pseudorapidity in the laboratory frame. For the selection of dijet (trijet) events it was required that at least the two (three) highest-transverse-energy jets have exceeded the transverse-energy threshold. Additionally, the invariant dijet mass of the two highest-transverse-energy jets in the event was required to be greater than 20 GeV. The measurements were compared to fixed-order NLO QCD calculations as implemented in the NLOJET++ program. The agreement in shape and normalisation between theory and the measurement was good. The ratio, $R_{3/2}$, between the cross sections for trijet and dijet production was determined as a function of the average transverse jet energy in the Breit frame, $\overline{E_{T,\mathrm{B}}^{\mathrm{jet}}}$, in intervals of Q^2. The quantity $R_{3/2}$ was utilised for an extraction of the strong coupling, α_s, with partially reduced systematic uncertainties. The extracted value was in agreement with the world average value of α_s.

In a second part, test-beam measurements were performed with the EUDET pixel telescope. During the work for this thesis, the online-monitoring software was improved, the MIMOSA 26 sensors were integrated into the offline analysis software and the first data taken with these sensors were analysed. The first data were taken with the demonstrator telescope together with three MIMOSA 26 sensors that were operated as devices-under-test. The second data sample was taken with a telescope that consisted of six MIMOSA 26 sensors, of which five could be used. The single-point resolution and the detection efficiency were determined and found to be consistent with the expectation.

Kurzfassung

In dieser Arbeit wird die Messung von inklusiven Dijet- und Trijetwirkungsquerschnitten in tief-unelastischer ep-Streuung präsentiert. Der kinematische Phasenraum der Messung war durch $125 < Q^2 < 20000$ GeV^2 und $0.2 < y < 0.6$ gegeben, wobei Q^2 bzw. y die Virtualität bzw. die Inelastizität ist. Der inklusive k_t-Jet-Algorithmus wurde im Breit-Bezugssystem auf masselose Objekte des Endzustandes angewendet. Die Wirkungsquerschnitte entsprechen Jets mit $E_{T,\mathrm{B}}^{\mathrm{jet}} > 8$ GeV und $-1 < \eta_{\mathrm{LAB}}^{\mathrm{jet}} < 2.5$, wobei die erste Größe der transversalen Jet-Energie im Breit-Bezugssystem und die letztere Größe der Pseudorapidität im Laborsystem entspricht. Dijetereignisse (Trijetereignisse) wurden mit der Bedingung selektiert, dass mindestens die zwei (drei) Jets mit der höchsten transversalen Energie den transversalen Energieschnitt passieren. Zusätzlich wurde verlangt, dass die invariante Dijetmasse der beiden Jets mit den höchsten transversalen Energien größer als 20 GeV ist. Die Messungen wurden mit QCD-Vorhersagen in nächst-führender Ordnung verglichen, wie sie in dem NLOJET++-Programm implementiert sind. Die Übereinstimmung zwischen der Theorie und der Messung war sowohl in Form als auch in Normierung gut. Das Verhältnis $R_{3/2}$ zwischen Dijet- und Trijetwirkungsquerschnitten wurde als Funktion von der mittleren transversalen Jet-Energie im Breit-Bezugssystem $\overline{E_{T,\mathrm{B}}^{\mathrm{jet}}}$ in Intervallen von Q^2 bestimmt. Die Größe $R_{3/2}$ wurde in einer Bestimmung der starken Kopplung α_s verwendet, wobei eine teilweise Reduzierung der systematischen Unsicherheiten erreicht wurde. Der extrahierte Wert stimmte mit dem Weltmittelwert von α_s überein.

Im zweiten Abschnitt wurden Teststrahlmessungen mit dem EUDET-Pixelteleskop durchgeführt. Im Rahmen der Arbeit für diese Dissertation wurde die Onlinemonitoring-Software verbessert, die MIMOSA-26-Sensoren wurden in die Analysesoftware integriert und die ersten Daten, die mit diesen Sensoren gemessen wurden, wurden analysiert. Der erste Datensatz wurde mit dem Demonstratorteleskop zusammen mit drei MIMOSA-26-Sensoren, die als Untersuchungsobjekte fungierten, aufgenommen. Der zweite Datensatz wurde mit dem Teleskop bestehend aus sechs MIMOSA-26-Sensoren aufgenommen, wobei fünf dieser Sensoren verwendet wurden. Die Auflösung und die Detektionseffizienz wurde bestimmt und entsprachen der Erwartung.

Contents

1. Introduction

In elementary particle physics the basic subatomic structure of matter in our universe is explored in order to strengthen our understanding of the universe, its history and the knowledge of the fundamental forces acting between the matter constituents which are at the moment believed to be elementary particles. Over the years, a theory called the "Standard Model" that has the ability to describe the interactions between the elementary particles was developed and tested experimentally in highly convincing and great detail. In this theory, the electro-weak interaction, which is an extension of "Quantum Electrodynamics" (QED), and the strong force between particles is described with the aid of a renormalisable quantum field theory. At the present time, a generally accepted theory that unifies the electro-weak and the strong interaction with gravitation is lacking.

In the standard model, it is assumed that the elementary particles of the matter are formed by spin-1/2 fermions – the leptons and quarks. The interaction between these particles is mediated by the exchange of gauge bosons. Six known different leptons (electron, muon, tau and the associated neutrinos) and their anti-matter correspondents exist in nature. These leptons are organised in three families, and they interact both electromagnetically and weakly, and, if neutral, only weakly. The six strongly-interacting and electro-weakly-interacting quarks are not observed as free and well-isolated particles. These particles compose the hadronic matter in the universe. The theory that describes the phenomena of the strong interaction is "Quantum Chromodynamics" (QCD).

Scattering experiments always played an important role in the investigation of the structure of the matter. At the beginning of the 20th century, Rutherford and his collaborators have performed scattering experiments with α particles that were shot into thin gold foils [1, 2]. Owing to the unexpected large angles of the scattered α particles, they concluded that the atoms must have relatively small hard cores – the atomic nuclei. In the 1950s, scattering experiments of electrons and atomic nuclei were performed at Stanford (USA), and a kinematic region was found in which the data could be described by the scattering of the electrons with the constituents of the nuclei. In later experiments, also evidence for the substructure of the proton was experimentally found. This substructure was identified with pointlike quarks and gluons.

The experiment HERA was a unique high-energy lepton-proton collider operated from the beginning of the 1990s until summer 2007 in Hamburg, Germany. One of the main and important achievements at HERA was the investigation of the substructure of the proton with a very high accuracy at larger centre-of-mass energies (≈ 320 GeV) than available before in fixed-target experiments.

In this thesis, an analysis of processes initiated by the strong interaction as measured in the ZEUS detector at HERA is presented. The analysis has focused on the investigation of collimated bunches of particles in the detector – the so-called "jets".

Measurements of jet cross sections are a well established tool for studying the details of the partonic interaction and have been performed for many different observables at HERA [3–21]. In particular, perturbative QCD, the factorisation ansatz, the parton distribution functions and the strength of the strong coupling, α_s, can be studied. In a previous QCD analysis [22] at ZEUS, it has been demonstrated that the measured jet quantities are sensitive to the distribution of gluons inside the proton and that the uncertainty on the gluon density can be significantly reduced compared to extractions in which jets were not considered. At large boson virtualities, Q^2, the experimental and theoretical systematic uncertainties become relatively small. Therefore, the usage of the large available HERA data sample can provide powerful physical constraints.

The measurements of dijet and trijet production at high Q^2 in neutral-current deep-inelastic scattering at HERA have so far been performed with either smaller data sets [10, 11, 16–18] or normalised to the cross section of inclusive neutral-current deep-inelastic scattering [5]. In this thesis, the measurement of inclusive dijet and trijet cross sections at high Q^2 is presented using an integrated luminosity of 374 pb^{-1}. Theoretical predictions were compared to the data and tested. The experimental and theoretical systematic uncertainties were studied. The ratio between the cross sections for trijet and dijet production was utilised for an extraction of the strong coupling, α_s, with partially reduced systematic uncertainties. The results for the inclusive dijet cross-section measurement are currently in the ZEUS-internal publishing procedure[1] and expected to be submitted to the journal soon [23].

The analysis of jet production presented in this thesis is based on standard model physics. However, it should be mentioned that at the time being, the standard model in its current form has several shortcomings [24]. Some of the main difficulties in this theory are referred to in the following: The origin of the particle masses is not understood, since the Higgs boson resists to be discovered. As already mentioned, the standard model does not incorporate gravitation. Moreover, the standard model depends on a large number of parameters whose values are not predicted by the theory itself, it does not provide a natural dark matter candidate which is consistent with the cosmological observations and it can not explain the huge difference between the electro-weak and the Planck scale.

It is generally believed that at least some of these obstacles can possibly be resolved with discoveries at the "Large Hadron Collider" (LHC) [25] or at planned future electron-positron linear collider experiments [26, 27]. For the latter future experiments and for an upgrade of the LHC, an enormous effort in detector research and development is ongoing at the moment. Since the track reconstruction of particles in these detectors will be a crucial part in many measurements, adequate technologies for tracking detectors are currently being investigated and new technologies are developed. In order to provide an infrastructure for this purpose, the EUDET project was launched several years ago. One part of this project is dedicated to the construction and the support of a test-beam telescope equipped with silicon pixels sensors. During the work for this thesis, new sensors with a larger number of pixel and faster readout were integrated into the analysis software and the first data taken with these sen-

[1] At the time of writing this thesis, the publication draft was in the "post-reading phase".

sors were analysed in order to study the performance and the characteristics of the test-beam telescope.

The thesis is subdivided into two parts:

1. **Jets at High Q^2:** In chapter 2, the main and for this analysis important theoretical concepts like deep-inelastic scattering, the theory of QCD and jet physics are introduced briefly. After discussing the experimental setup in chapter 3, chapter 4 is devoted to the Monte Carlo simulations used for the correction of the data and the fixed-order calculations to which the data were compared. The details on the event reconstruction and the applied event selection criteria are given in chapter 5. In order to perform a precise jet measurement, several corrections like the calibration of the hadronic energy scale and a correction of the trigger efficiency have been applied. These necessary corrections are discussed in chapter 6. The application of the data unfolding procedure and the obtained final data sample are presented in chapter 7 followed by a detailed discussion of the involved theoretical and experimental systematic uncertainties in chapter 8. The results of the jet measurements are shown and discussed in 9. Finally, a summary and conclusion is given in chapter 10.

2. **Test Beam Measurements with the EUDET Pixel Telescope:** After giving a more general introduction in chapter 11, the experimental setup is discussed in chapter 12. Afterwards, the main components of the data-acquisition software and the offline analysis software are presented (chapters 13 and 14). The results of the measurement with the EUDET pixel telescope are presented in chapter 15 and, finally, summarised in chapter 16.

Part I.

Jets at High Q^2 at HERA

2. Theory of HERA Physics

In this chapter, an overview of basic theoretical concepts important for the presented jet analysis is given. The chapter starts with a brief introduction to "deep-inelastic scattering" and the event kinematics at HERA in section 2.1. In this section, also the inclusive deep-inelastic-scattering cross section is described. The phenomena investigated in this analysis can be understood with the help of the theory of quantum chromodynamics (section 2.2) whose main characteristics like the renormalisation and factorisation theorem are introduced in section 2.2.1. Starting with section 2.2.2, the main physical properties of jets and their influence on the presented analysis are discussed.

2.1. Deep Inelastic Scattering

In the 1950s, R. Hofstadter investigated the scattering of electrons of a few hundred MeV with atomic nuclei. Besides the elastic scattering and the inelastic excitation of resonances, a region at large momentum transfers was observed that could be explained by quasi-elastic scattering of electrons with the constituents (the nucleons) of the atomic nuclei [28, 29]. In the 1960s, scattering experiments with electrons (e) and protons (p) were performed with a greater centre-of-mass energy and, therefore, greater momentum transfers. The resonances of the proton were investigated [30] in analogy to the observed resonances of the atomic nuclei.

In the year 1967, Bjorken established the hypothesis that, in the limit of infinite momentum transfer and large inelasticity, the structure of the proton can be described by a dimensionless variable – the Bjorken scaling variable, x_{Bj}. This behaviour was called "scaling invariance" [31].

In the 1960s, in ep scattering experiments at SLAC the "scaling invariance" was observed experimentally [32–34]. Feynman proposed [35] to explain this behaviour in analogy to Hofstadter's experiments with the scattering of electrons with pointlike constituents of the proton – the "partons". This kinematic regime of large momentum transfer was called "deep-inelastic scattering" (DIS).

At that time, several new particles (hadrons) were observed in scattering experiments. In 1964, Zweig [36] and Gell-Mann [37] tried to explain independently of each other these observed hadrons by introducing fundamental particles called "quarks". In analogy to the nuclei, these quarks should be the constituents of the hadrons. These hadrons should consist of three spin-$\frac{1}{2}$ quarks in the case of nucleon-like particles, while the mesons should consist of a quark-antiquark bound state. The quarks were later identified [38] with the "partons" introduced by Feynman. However, unlike the constituents of atoms and nuclei, quarks have not been observed as free and isolated particles.

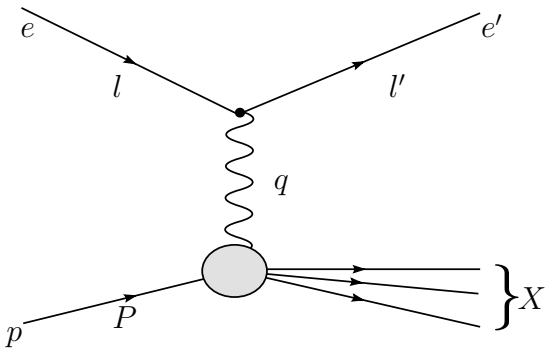

Figure 2.1: Kinematic quantities in deep-inelastic ep scattering at HERA.

2.1.1. Kinematic at HERA

In deep-inelastic scattering an electron or positron[1] couples to a parton from the proton via the exchange of a gauge boson. The boson can be, within the standard model, either a photon or a Z^0 in neutral-current (NC) or a $W^{\pm}$ in charged-current (CC) events. In the analysis presented here, NC DIS events were investigated.

The kinematics of deep-inelastic scattering are illustrated in figure 2.1, where $l = (E_{el}, \vec{p}_{el})$ and $l' = (E'_{el}, \vec{p}'_{el})$ indicate the four-momenta of the initial- and final-state electrons. The proton's four-momentum is denoted as $P = (E_p, \vec{p_p})$. It should be remarked that the process illustrated is an electro-weak process in lowest order.

At HERA electrons with energies of 27.5 GeV were collided with 920 GeV protons. The centre-of-mass energy, $\sqrt{s}$, can be determined according to

$$\sqrt{s} = \sqrt{(l+p)^2} = \sqrt{4 \cdot E_{el}E_p + m_p^2 + m_{el}^2} \approx \sqrt{4 \cdot E_{el}E_p} \approx 318 \text{ GeV}, \tag{2.1}$$

where m_{el} (m_p) is the mass of the electron (proton).

The kinematics of the process at a fixed $\sqrt{s}$ can be described by the following variables:

- The virtuality, Q^2, of the exchanged boson is given by

$$Q^2 = -q^2 = -(l - l')^2 . \tag{2.2}$$

  Here, q is the four-momentum transfer. Two kinematic regimes can be distinguished: in photoproduction events the exchanged photon is quasi-real and $Q^2 \approx 0$ GeV^2. In contrast, for DIS the exchanged boson is virtual and Q^2 is significantly larger than $Q^2 \gg \Lambda^2_{\text{QCD}} > (0.2 \text{ GeV})^2$.

- The inelasticity, y, of the scattering process can be determined according to

$$y = \frac{Pq}{Pl}. \tag{2.3}$$

  In the proton rest frame, y is given by $y = 1 - \frac{E'_{el}}{E_{el}}$.

[1] In the following, the term "electron" denotes generically both the positron and the electron unless otherwise stated.

- The Bjorken scaling variable, x_{Bj} (or sometimes just x), is defined as

$$x_{\mathrm{Bj}} = \frac{Q^2}{2Pq}. \tag{2.4}$$

  In the quark-parton model (section 2.1.2), it can be interpreted as the longitudinal momentum fraction carried by the incoming parton.

Neglecting the masses of the electron and the proton, these variables are related by $Q^2 = x_{\mathrm{Bj}} \cdot y \cdot s$. Therefore, two variables are sufficient to describe the event kinematics.

In DIS events, the wavelength of the boson is related to the boson virtuality and can be calculated according to

$$\lambda \approx \frac{\hbar c}{\sqrt{Q^2}}. \tag{2.5}$$

Hence, DIS events at HERA with $Q^2 > 1$ GeV^2 provide a powerful tool to investigate the substructure (< 1 fm [39, 40]) of the proton.

2.1.2. The Inclusive DIS Cross Section

The cross section for inclusive DIS events can be derived from the leptonic, $L_{\mu\nu}$, and hadronic tensor, $H^{\mu\nu}$, according to $d\sigma \sim L_{\mu\nu}H^{\mu\nu}$ [41]. The leptonic tensor describes the coupling of the electron and the boson, while the hadronic tensor parametrises the unknown structure of the current at the hadronic part of the process.

In leading-order (LO) electro-weak theory the NC DIS cross section for left- (l) and right-handed (r) electron beams for point-like spin-$\frac{1}{2}$ partons is given by

$$\frac{d^2\sigma_{\mathrm{NC}}\left(e^-_{l,r}p\right)}{dxdQ^2} = \frac{2\pi\alpha^2}{xQ^4}\left[Y_+F_2^{l,r}\left(x,Q^2\right) + Y_-xF_3^{l,r}\left(x,Q^2\right) - y^2F_L^{l,r}\left(x,Q^2\right)\right], \tag{2.6}$$

where α is the fine-structure constant and $Y_\pm = 1 \pm (1-y)^2$. Masses are neglected. The structure functions F_2 and xF_3 can be interpreted in the quark-parton model. In this model it is assumed that the partons in the proton are point-like spin-1/2 particles. These partons carry the longitudinal momentum-fraction x of the proton momentum and are assumed to be approximately free in the "infinite momentum frame", in which the proton has an infinite momentum and in which the transverse momenta of the partons are negligible. Therefore, for large energy transfers at small distances the scattering of the electron occurs incoherently on single partons. The structure functions F_2 and xF_3 are given by

$$F_2^{l,r}\left(x,Q^2\right) = \sum_f \left[xq_f\left(x,Q^2\right) + x\overline{q}_f\left(x,Q^2\right)\right] \cdot A_f^{l,r}\left(Q^2\right), \tag{2.7}$$

$$xF_3^{l,r}\left(x,Q^2\right) = \sum_f \left[xq_f\left(x,Q^2\right) - x\overline{q}_f\left(x,Q^2\right)\right] \cdot B_f^{l,r}\left(Q^2\right). \tag{2.8}$$

In these equations the sums run over all flavours, f, and q_f ($\overline{q}_f$) represents the quark (antiquark) densities in the proton. The quantities $A_f^{l,r}(Q^2)$ and $B_f^{l,r}(Q^2)$ are expressed according to

$$A_f^{l,r}\left(Q^2\right) = e_f^2 - 2e_f\left(v_e \pm a_e\right) v_f P_Z + \left(v_e \pm a_e\right)^2 \left(v_f^2 + a_f^2\right) P_Z^2, \tag{2.9}$$

$$B_f^{l,r}\left(Q^2\right) = \mp 2e_f\left(v_e \pm a_e\right) a_f P_Z \pm 2\left(v_e \pm a_e\right)^2 v_f a_f P_Z^2, \tag{2.10}$$

where $a_f = T_{3f}/\sin 2\theta_W$ and $v_f = \left(T_{3f} - 2e_f \sin^2\theta_W\right)/\sin 2\theta_W$ are the neutral-current axial-vector and vector-vector couplings. These quantities are given in terms of the third component of the weak isospin, T_{3f}, and the Weinberg angle, θ_W. The electric charge in units of the elementary charge is indicated as e_f. The variable $P_Z = Q^2/\left(Q^2 + M_Z^2\right)$ is the ratio of the Z^0- and photon-propagator terms.

The longitudinal structure function, F_L, is related to the part of the cross section that describes the absorption of longitudinally polarised virtual photons. In the quark-parton model, F_L vanishes and the Callan-Gross [42] relation, $2xF_1 = F_2$, holds. This relation is a consequence of the pointlike quarks having spin $\frac{1}{2}$ and zero transverse momentum. However, in QCD the magnitude of F_L is closely correlated with the gluon density inside the proton [43]. Recently the H1 and ZEUS collaborations have measured F_L directly [44, 45]. The data provide strong evidence for a non-vanishing F_L. The data are directly sensitive to the gluon density in the proton.

With the aid of the replacements $F_2^{l,r} \to F_2^{r,l}$ and $xF_3^{l,r} \to -xF_3^{r,l}$ the corresponding cross section for positron beams is achieved. Arbitrarily polarised cross sections are given by a linear combination of the corresponding fully polarised cross sections.

The terms in the equations 2.9 and 2.10 proportional to P_Z are arising from the γ/Z^0 interference, whereas the terms proportional to P_Z^2 are coming from the pure weak interaction. They become important in the region with $Q^2 \gtrsim M_{Z^0}^2$.

While F_2 is proportional to the sum of the quark and antiquark densities, the structure function xF_3 is proportional to the difference of these densities. Therefore, xF_3 is more strongly dependent on the valence-quark densities, whereas F_2 is sensitive to both the valence- and the sea-quark densities. The latter dominate the cross section in the lower Q^2 region over a wide range of the accessible kinematic phase space at HERA.

The inclusive DIS cross sections, $d\sigma/dQ^2$, for neutral- and charged-current events have been measured at HERA as depicted in figure 2.2. In the lower Q^2 region, the charged-current cross section is suppressed due to the large mass of the $W^\pm$ boson. In this region, the neutral-current cross sections for electrons and positrons are very similar, whereas with increasing Q^2 the contribution from the weak interaction becomes more significant. Hence, also the neutral-current cross sections for electrons and positrons start to differ significantly in that region. The charged- and neutral-current cross sections become comparable in the high Q^2 region which can be interpreted as electroweak unification. The remaining differences between the cross sections for electrons and positrons in the high Q^2 regime are related to the different sensitivity of the weak force to the individual quark flavours in the proton. Hence, the contributions from the proton structure to the cross sections for e^-p and e^+p scattering differ in that region.

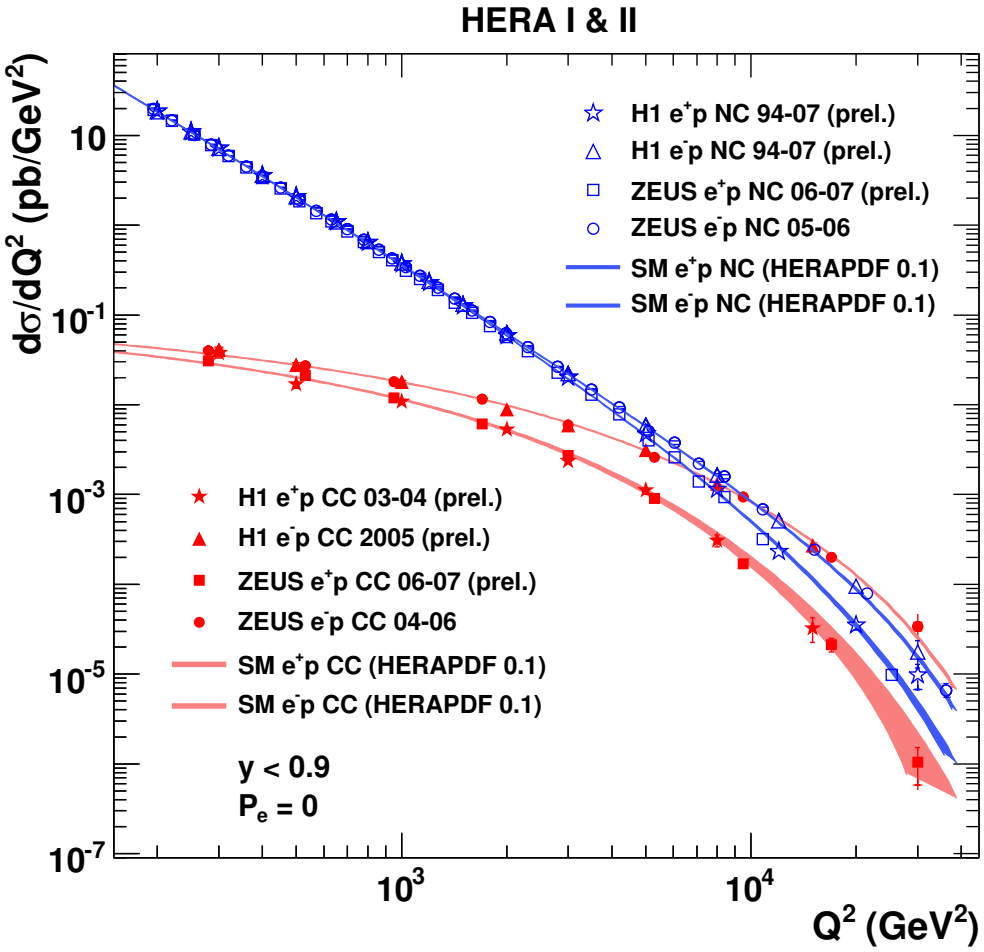

Figure 2.2: The differential inclusive neutral- and charged-current cross sections as a function of the virtuality, Q^2, for electron and positron beams in comparison with the standard model prediction. Shown are measurements from ZEUS and H1 (figure taken from [46]).

2.2. Quantum Chromodynamics

The strong interactions between quarks are described by the theory of quantum chromodynamics (QCD). This theory is a non-Abelian quantum field theory[2] with the gauge-group $\mathrm{SU}(3)_c$ acting on a degree of freedom called "colour".

The colour spinor of a quark can be written as $\psi = (q_R, q_G, q_B)$, where the quantities $q_{R,G,B}$ represent the colour components. A local $\mathrm{SU}(3)_c$ transformation can be expressed according to

$$\psi' = \exp\left(i\frac{g_s}{2}\lambda_j\beta_j(x)\right)\psi. \tag{2.11}$$

[2] An introduction in quantum field theory can be found in [47, 48] and more QCD specific discussions in [49, 50].

The quantity g_s is the coupling of the strong interaction and the expression $\lambda_j \beta_j(x)$ is a combination of eight independent real transformations, β_j, with the Gell-Mann matrices, λ_j, that can be regarded as a 3D generalisation of the Pauli matrices. The λ_j are generators of SU (3) in the three-dimensional fundamental representation, and their commutation relations define the algebra of SU (3). The $\mathrm{SU}(3)_\mathrm{c}$ covariant derivative is given by the following replacement:

$$\partial^\mu \Rightarrow D^\mu = \partial^\mu + i\frac{g_s}{2}\left(\lambda_1 b_1^\mu + \ldots + \lambda_8 b_8^\mu\right). \tag{2.12}$$

The consequence of the local $\mathrm{SU}(3)_\mathrm{c}$ invariance is the appearance of eight gauge fields, $b_1^\mu, b_2^\mu, \ldots b_8^\mu$, the quanta of which are called *gluons*. The first direct evidence for the existence of gluons was found in 1979 at PETRA [51] in three-jet events.

With the introduction of the field-strength tensor,

$$G_j^{\mu\nu} = \partial^\nu b_j^\mu - \partial^\mu b_j^\nu + g_s f_{jkl} b_k^\mu b_j^\nu, \tag{2.13}$$

where f_{jkl} represents the $\mathrm{SU}(3)_\mathrm{c}$ structure constants, the Lagrangian can be derived according to [52]

$$\mathcal{L}_\mathrm{inv} = \sum_{\text{flavour f}} \overline{\psi}_{f,\alpha}\left(i\gamma_\mu D^\mu - m_f\right)_{\alpha\beta}\psi_{f,\beta} - \frac{1}{4} tr\left(G_{\mu\nu}G^{\mu\nu}\right). \tag{2.14}$$

In this equation the quark mass for the flavour f is denoted by m_f, while α and β are $\mathrm{SU}(3)_\mathrm{c}$-triplet indices running from 1 to 3. The quantisation of $\mathcal{L}_\mathrm{inv}$ can be achieved by introducing a "ghost" and a "gauge-fixing" density [49]. Thus, the total QCD Lagrange density is $\mathcal{L}_\mathrm{QCD} = \mathcal{L}_\mathrm{inv} + \mathcal{L}_\mathrm{gauge} + \mathcal{L}_\mathrm{ghost}$.

The main difference between QED and QCD is the appearance of a non-Abelian term in the field-strength tensor (equation 2.13) resulting, as a consequence, in gluons carrying colour charge. Hence, the gluons are interacting with themselves via three-gluon and four-gluon vertices. The strength of the coupling[3], α_s, strongly depends on the involved energy scale of the process. As a further consequence, at very short distances the coupling becomes small ("asymptotic freedom"), whereas at large distances the coupling strength grows. As a result, particles carrying colour charge are not observed as free and well-isolated particles ("confinement"), because at a certain distance between two quarks, it becomes energetically favourable to produce new quarks and antiquarks from the vacuum.

2.2.1. Perturbative Quantum Chromodynamics

The knowledge of the QCD Lagrangian allows to derive prescriptions (Feynman rules) for the perturbative calculation of amplitudes for any order in the strong coupling, α_s. The prediction for the cross-section σ up-to the order n for an investigated process can be expressed according to

$$\sigma = k_0 \cdot \alpha_s^0 + k_1 \cdot \alpha_s^1 + k_2 \cdot \alpha_s^2 \ldots = \sum_{i=0}^{n} k_i \cdot \alpha_s^i. \tag{2.15}$$

[3]More details can be found in chapter 2.2.1.1.

The coefficients k_i have to be determined by evaluating the Feynman diagrams related to the corresponding order in α_s. The naive application of these rules to the calculation of amplitudes with virtual and real corrections typically results in mathematical difficulties. In particular, virtual corrections have to be determined by calculating the value of integrals over the momenta of closed quark and gluon loops. Since these momenta are physically not constrained, the corresponding integrals diverge leading to the so-called "ultraviolet divergences".

The technique for the treatment of these divergences is the "renormalisation theory" by making the divergent integrals temporarily finite with some "regularisation" procedures – for instance by dimensional regularisation or by introducing an ultraviolet cut-off parameter. These regularised divergences can for instance be absorbed in the definition of the strong coupling.

Additionally, the hard scattering processes have to be separated from the soft in perturbation theory not calculable interactions inside the hadrons with the application of a "factorisation" procedure.

Both the renormalisation and the factorisation are described in this section.

2.2.1.1. Renormalisation and the Strong Coupling

Theories are renormalisable if the introduction of a finite number of renormalisable parameters ensures that the perturbative calculation in all orders gives finite results. The procedure to treat the regularised divergences is defined by a "renormalisation scheme" and a corresponding dimensional renormalisation scale, μ_R. In general, a renormalised observable Γ_R in quantum field theory is not allowed to depend on an arbitrary chosen value of μ_R, which means that Γ_R has to fulfil the renormalisation group equation [53],

$$\mu_R \cdot \frac{d\Gamma_R}{d\mu_R} \stackrel{!}{=} 0. \tag{2.16}$$

In order to solve this equation, the free parameters of the theory like the coupling have to be functions of the renormalisation scale. In case of QCD: $\alpha_s := \alpha_s(\mu_R)$.

The characteristic quantity of the renormalisation group is the β function that describes the change of the coupling at the scale μ_R to the arbitrary scale μ:

$$\beta(\alpha) = \frac{\partial \alpha}{\partial t}, \qquad t = \ln\left(\frac{\mu^2}{\mu_R^2}\right) \tag{2.17}$$

Hence, in leading-order perturbation theory the strong coupling can be determined according to

$$\alpha_s\left(\mu^2\right) = \frac{\alpha_s(\mu_R^2)}{1 + \frac{\alpha_s\left(\mu_R^2\right)}{12\pi}\left(33 - 2n_f\right)\ln\left(\frac{\mu^2}{\mu_R^2}\right)}, \tag{2.18}$$

where n_f is the number of contributing quark flavours. With the aid of the introduction of the parameter $\Lambda^{(n_f)}$, the following formula for the scale behaviour of the coupling $\alpha_s(\mu^2)$ can be derived:

$$\Lambda^{(n_f)^2} := \mu_R^2 \exp\left(\frac{-12\pi}{(33-2n_f)\,\alpha_s(\mu_R^2)}\right), \;\Rightarrow\; \alpha_s\left(\mu^2\right) = \frac{12\pi}{(33-2n_f)\ln\left(\frac{\mu^2}{\Lambda^{(n_f)^2}}\right)}. \tag{2.19}$$

The parameter $\Lambda^{(n_f)}$ is not predicted by the theory of QCD; its value has to be determined experimentally and depends on the number of active quark flavours, n_f. In higher-order perturbative QCD calculations, the structure of equation 2.19 and, therefore, the value of $\Lambda^{(n_f)}$ depends on the applied "renormalisation scheme". The widely utilised "modified minimal subtraction scheme" [54] ($\overline{\text{MS}}$) was employed for all calculations used in the presented analysis. Only the coefficients β_0 and β_1 in equation 2.17 are universal [55–57] and do not depend on the applied calculation scheme.

In contrast to QED, the coupling of QCD rises with increasing scale, μ_R, if $11 - \frac{2}{3} \cdot n_f > 0$, which is the case in the standard model with six quarks. This behaviour is related to the non-Abelian structure of QCD. For $\mu_R^2 \gg \Lambda^{(n_f)^2}$ the coupling becomes sufficiently small in order to express the cross section as a series expansion in powers of α_s. The property of "asymptotic freedom" of QCD emerges in the limit of $\mu_R \to \infty$ in which the strong coupling vanishes ($\alpha_s \to 0$). On the other hand, in the region with $\mu_R^2 \to \Lambda^{(n_f)^2}$ the value of α_s grows and non-perturbative methods have to be exploited – e.g. all-order resummation methods or lattice calculations.

The renormalisation group equation 2.16 can only be fulfilled if the observable is calculated to all orders in α_s. Any truncation in the series expansion results in a dependence of the observable on μ_R. Since the choice of μ_R is arbitrary, several proposals [58–60] for reasonable scale choices were made. It was suggested that the actual choice of μ_R should be related to the scale of processes under study. This variable could for instance be set to Q^2 for inclusive DIS events or to the average transverse energy of the partons, $\overline{E}_T$, for jet production [61]. In this analysis, however, the default renormalisation scale was set to $\mu_R^2 = Q^2 + \overline{E}_T^2$. A more detailed discussion of the scale dependence can be found in the chapters 8.2 and 9.

It is convenient to quote values of α_s in the $\overline{\text{MS}}$ scheme at the mass of the Z^0 boson, $M_Z = 91.1876 \pm 0.0021$ GeV [66]. At HERA the value of $\alpha_s(M_Z)$ was extracted – as depicted in figure 2.3 – using for instance cross-section measurements of inclusive jets in photoproduction [6, 62], of inclusive jets at low Q^2 [21], of inclusive jets at high Q^2 [63] and of normalised multi-jets at high Q^2 [5]. All these extracted values have a precision comparable with LEP results [64] and are compatible with the world average value [65] of α_s from the year 2006, which is $\alpha_s(M_Z) = 0.1189 \pm 0.0010$.

2.2.1.2. Factorisation

At small distances, corresponding to large momentum transfers and small values of $\alpha_s \ll 1$, the interactions between the partons can be calculated with the application of perturbative methods. On the other hand at larger distances, partons are bound into colourless objects – the hadrons – and are interacting with small momentum

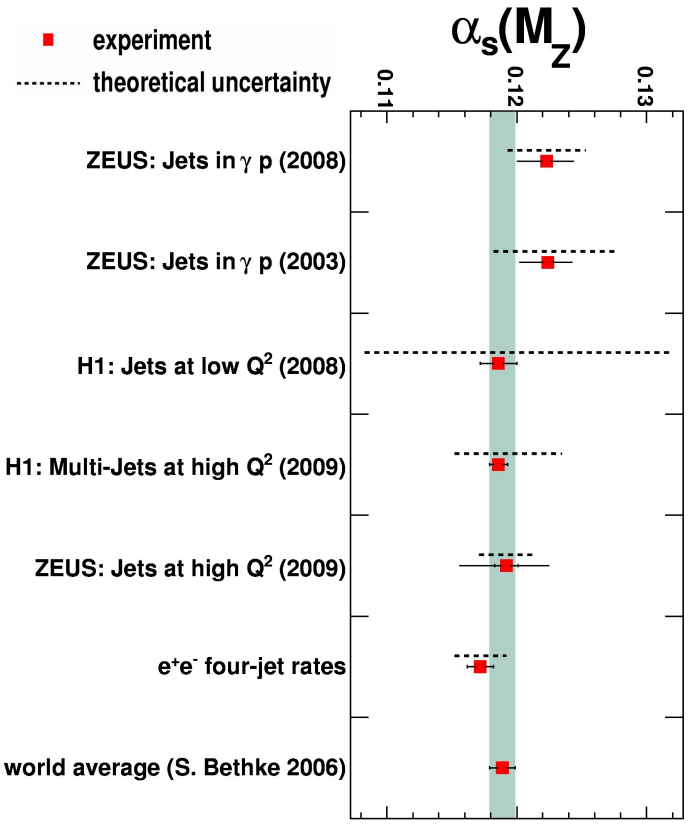

Figure 2.3: Extracted $\alpha_s(M_Z)$ values at HERA from inclusive jets in photoproduction [6, 62], from inclusive jets at low Q^2 [21], from inclusive jets at high Q^2 [63] and from normalised multi-jets at high Q^2 [5] in comparison with a LEP result [64] and the world average from 2006 [65].

transfers. Hence, perturbative QCD (pQCD) is not applicable anymore for the prediction of these processes. Today, the distributions of partons inside the proton (structure functions) can typically not be determined theoretically from first principles. Perhaps with future developments in lattice QCD [67] the structure functions can be extracted from the theory only.

Owing to the factorisation theorem [68] of QCD, the theoretical cross-section prediction can be subdivided into two parts: the cross section for *ep* scattering can be calculated by convoluting the amplitudes for the electron-parton interaction and the parton distribution functions (PDFs). These parton distribution functions have to be measured in scattering experiments. The PDFs are assumed to be universal in the sense that, once extracted, they are applicable for the prediction of any scattering process in which the proton is involved.

In the theoretical calculations, divergences are arising for instance from the emission of collinear gluons with respect to the emitting parton. These divergences can be absorbed in the definition of the PDFs by introducing similarly to the renormalisation procedure a new scale μ_F – the factorisation scale. This scale corresponds to the transverse energy limit under which the emission of partons is factorised into the PDFs. Contributions with larger scales than μ_F are treated perturbatively.

In practice, however, the PDFs are not extracted experimentally for all possible combinations of the longitudinal momentum fraction, x, and μ_F. In analogy to the renormalisation group equation 2.16, the dependences of the quark and gluon densities are induced by evolution equations that describe, for a fixed value of x, the change with respect to μ_F. Common "factorisation schemes" are the $\overline{\text{MS}}$ [54] and the "DIS

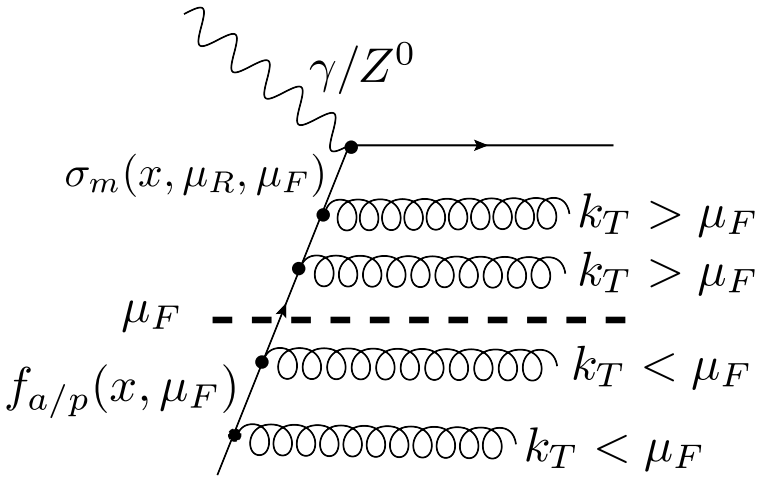

Figure 2.4: Feynman diagram for a process in higher orders of α_s. Gluon emissions with transverse momenta $k_T < \mu_F$ are absorbed in the parton distribution functions. The hard matrix element for order m is given by $\sigma_m(x, \mu_R, \mu_F)$ and the probability to find a parton a inside the proton by $f_{a/p}(x, \mu_F)$.

scheme" [69].

Since theoretical predictions can not be calculated to all orders, approximations have to be used. In the derivation of the evolution equations, the emitted initial-state partons are ordered in so-called "parton ladders" e.g. with respect to their transverse momentum, k_t, or x.

In the case of the "**D**okshitzer, **G**ribov, **L**ipatov, **A**ltarelli and **P**arisi" [70–73] (DGLAP) evolution equations all emitted partons are ordered in k_T according to $\mu^2_{F,0} \ll \ldots \ll k^2_{T,i} \ll k^2_{T,i+i} \ll \ldots \ll \mu^2_F$ as illustrated in figure 2.4. This relation is often called "strong ordering". Moreover, the x parameter has to be sufficiently small and, on the other hand, μ^2_F has to be reasonably large. If these conditions are fulfilled, then each parton from the ladder effectively contributes a term $\alpha_s \cdot \ln \mu^2_F/\mu^2_{F,0}$ to the cross section. Since each order in α_s is accompanied by a term $\ln \mu^2_F/\mu^2_{F,0}$, this is called the "leading log approximation". Terms with $\alpha_s \cdot \ln 1/x$ are neglected due to the requirement of sufficient large x.

The DGLAP equations are given by

$$\frac{\partial q_i(x,\mu^2_F)}{\partial \ln \mu^2_F} = \frac{\alpha_s}{2\pi} \cdot \sum_{q_j \overline{q_j}} \int_x^1 \frac{dz}{z} \left[q_i\left(z,\mu^2_F\right) \cdot P_{q_i q_j}\left(\frac{x}{z}\right) + g\left(z,\mu^2_F\right) \cdot P_{q_i g}\left(\frac{x}{z}\right) \right], \quad (2.20)$$

$$\frac{\partial g(x,\mu^2_F)}{\partial \ln \mu^2_F} = \frac{\alpha_s}{2\pi} \cdot \sum_{q_j \overline{q_j}} \int_x^1 \frac{dz}{z} \left[q_i\left(z,\mu^2_F\right) \cdot P_{g q_j}\left(\frac{x}{z}\right) + g\left(z,\mu^2_F\right) \cdot P_{gg}\left(\frac{x}{z}\right) \right]. \quad (2.21)$$

These correlated equations connect the quark and the gluon densities in the proton via the Altarelli-Parisi splitting functions P_{ab}. The quantities P_{ab} are describing the probability that a parton a with momentum fraction y splits into a new parton b with momentum fraction $x < y$.

Besides the DGLAP approach also other evolution equations as for instance the BFKL [74, 75] scheme in the low-x region are available. In this scheme, the partons are not ordered in k_T but in x. The CCFM approach [76–79] tries to combine DGLAP and BFKL.

The reduced cross section, which is defined as the inclusive cross section multiplied with $xQ^4/\left(2\pi\alpha^2 Y_+\right)$, is depicted in figure 2.5 as a function of Q^2 in different regions of

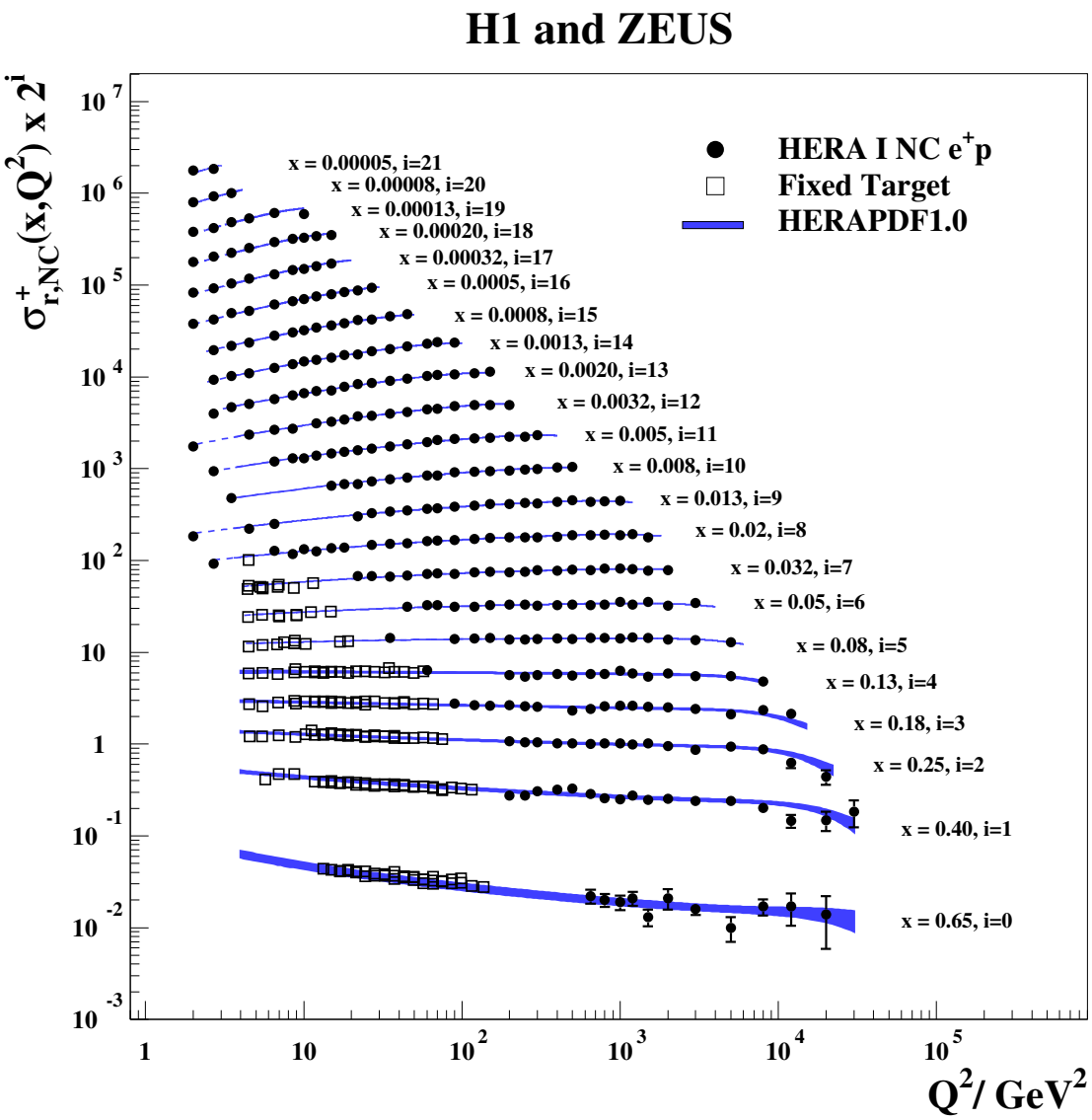

Figure 2.5: The reduced cross section as a function of the virtuality, Q^2, and the momentum fraction, x (figure taken from [80]).

x. In the medium x region ($0.05 \lesssim x \lesssim 0.18$), the cross section depends only weakly on Q^2 which can be interpreted as "scaling". However, this behaviour only occurs in that specific kinematic region, whereas in the other regions, the reduced cross section strongly depends on Q^2 ("scaling violations"). This scaling violation is caused by the non-Abelian structure of QCD.

The PDFs are typically extracted within a global QCD fit of several observables (e.g. DIS cross sections, heavy flavour production, Drell-Yan production, W production) with possibly different sensitivity to the various quark flavours or to the gluon. Since the inclusive DIS cross section measurement is only sensitive to

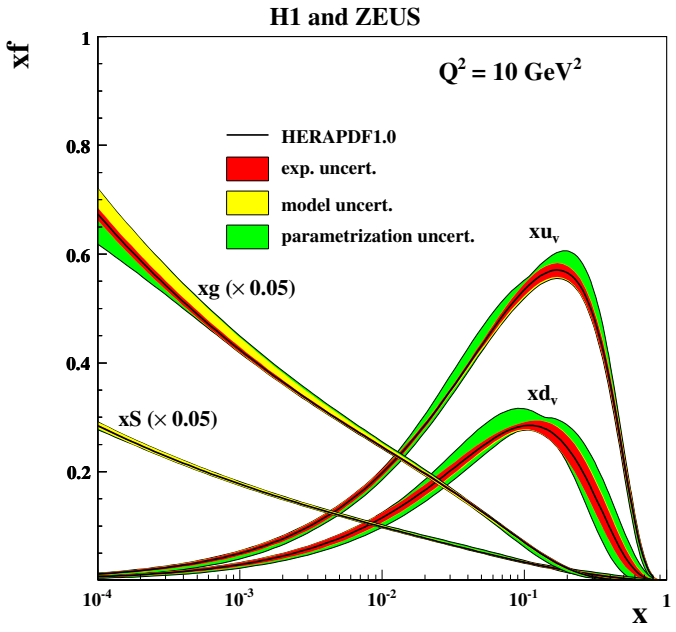

Figure 2.6: The parton distribution functions and the corresponding experimental, model and parametrisation uncertainties as extracted by the HERAPDF [80] analysis. Shown are the valence- and sea-quark densities as well as the gluon density at the scale $Q^2 = 10$ GeV^2. The gluon and sea-quark densities were multiplied with a factor of 0.05.

the gluons via scaling violations ($\partial F_2/\partial \ln Q^2 \sim \alpha_s \cdot x \cdot g$), also other measurements like jets in DIS or $p\overline{p}$ collisions are usually included in the fits in order to enhance the sensitivity to the gluons and to α_s. Typically, in these fits the x dependences of the PDFs are parametrised at a starting scale $\mu^2_{F,0}$. Afterwards, they are evolved to the interesting scale μ^2_F and convoluted with the corresponding matrix element in order to obtain the cross-section prediction for the process under study at the relevant scale.

Recent extractions of the proton PDFs were performed by several groups such as the CTEQ [81], MSTW[82], H1[83] and ZEUS [22, 84] collaborations, while the latter two also have extracted the PDFs from a combined fit. Typically, these PDF sets are made available via common interfaces (e.g. [85]) in order to be easily applicable and exchangeable.

Figure 2.6 depicts the PDFs and their estimated experimental, model and parametrisation uncertainties as extracted by the HERAPDF [80] analysis. Shown are the valence- and sea-quark densities as well as the gluon density at $\mu^2_F = Q^2 = 10$ GeV^2. The gluon- and sea-quark densities were scaled with a factor of 0.05 to enhance visibility. One of the important discoveries at HERA was the observation that the gluon density rises dramatically towards low x. The rise is more pronounced with increasing Q^2. This behaviour can also be seen in figure 2.5, where the slope of the reduced cross section[4] at low x is related to the gluon density.

2.2.2. Jet Physics

Jets are defined by jet algorithms. These algorithms identify collimated bunches of final-state hadrons produced approximately in the same direction. These hadrons have been

[4] In this specific region, the main contribution to the reduced cross section is coming from F_2.

formed in the process of hadronisation (section 4.1.2) of partons into colourless hadrons. Up to now, this process of hadronisation can only be understood phenomenologically and not perturbatively. The jets are related to the underlying QCD dynamics of quarks and gluons. Hence, jets allow a detailed and stringent study of the properties and production characteristics of the QCD interaction such as the hard matrix element, the parton cascade, the hadronisation, the strength of the coupling and the gluon density inside the proton.

Experimentally the energy and momentum of the jet has to be measured precisely. On the other hand, in order to allow a comparison with theoretical predictions, the jet observables have to fulfil certain criteria such as infrared and collinear safety. Whereas the latter requires an observable to be insensitive to collinear splittings of partons, the first is related to the insensitivity to emissions of low-energetic particles. The infrared sensitivity is further discussed in chapter 4.2.2.

2.2.2.1. The Breit Reference Frame

The presented jet analysis was performed in the so-called "Breit reference frame" [86, 87] which is particularly appropriate for the study of jets in DIS. In this specific reference frame (among others), the factorisation of the jet cross section into the PDFs and the hard matrix element is guaranteed [88]. The Breit frame is defined as the reference frame in which the parton from the proton and the virtual exchanged boson collide head-on without transferring energy from the electron to the parton. Thus, the Breit frame can be defined according to $2x_{\mathrm{Bj}}\vec{P} + \vec{q} = 0$, where x_{Bj} represents the Bjorken scaling variable and $\vec{P}$ and $\vec{q}$ the momenta of the incoming proton and the exchanged virtual boson, respectively.

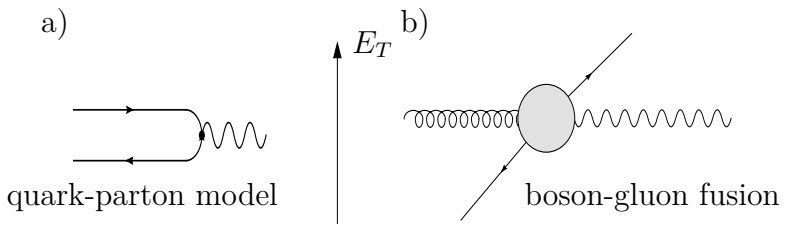

Figure 2.7: The a) quark-parton model and b) boson-gluon fusion process in the Breit reference frame.

In the Breit frame, the exchanged boson is space-like and collides head-on with the parton from the proton. Hence, for the quark-parton-model process in the Breit frame the transverse momentum of the produced quark is zero as indicated in figure 2.7a. In contrast, transverse energies of the hadronic final state in this frame are closely related to the occurrence of hard QCD interactions as depicted in figure 2.7b, where a gluon has fluctuated into a $q\overline{q}$ pair. Therefore, the presence of transverse momenta in the Breit frame can be used for both the identification of hard QCD processes and the suppression of purely electro-weak processes and the proton remnant.

2.2.2.2. Boson Gluon Fusion and QCD Compton Events

In the plain quark-parton model no QCD interactions are involved. Two processes in which the strong interaction is contributing in lowest order are depicted in figure 2.8. These processes are usually called a) QCD-Compton and b) boson-gluon-fusion process.

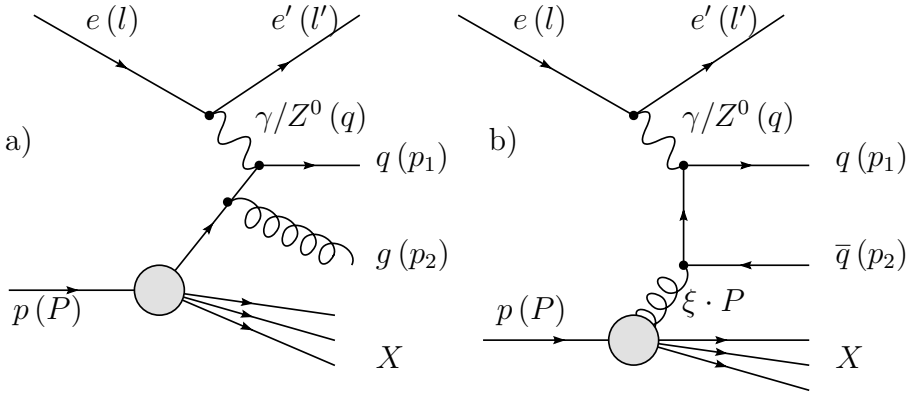

Figure 2.8: Illustration of a) the QCD-Compton and b) the boson-gluon fusion process.

In the case of a QCD-Compton (QCDC) process, the quark emits a gluon before or after the coupling to the exchanged boson. In contrast, in the boson-gluon fusion (BGF) process, a gluon from the proton fluctuates into a quark-antiquark pair that couples to the exchanged boson. This process is already in leading-order sensitive to the gluon density in the proton. In both processes, in the final state two partons, the electron and the proton remnant are produced. Higher-order processes are created by the emission of further gluons. Due to the introduction of cuts in the Breit frame, the obtained event sample is enriched with QCDC and BGF events.

The discussed processes can be characterised using the following quantities:

$$M = \sqrt{\left(\sum_{i=1}^{n} p_{i,\mathrm{B}}\right)^2}, \quad \overline{E_{T,\mathrm{B}}} = \frac{1}{n}\cdot\sum_{i=1}^{n} E_{i,T,\mathrm{B}}, \quad \eta^* = \frac{1}{2}\cdot\left|\eta_{1,\mathrm{B}} - \eta_{2,\mathrm{B}}\right|, \quad \xi = x_{\mathrm{Bj}}\cdot\left(1 + \frac{M^2}{Q^2}\right),$$

where M is the invariant mass of the n-jet system and $\overline{E_{T,\mathrm{B}}}$ the average transverse energy in the Breit frame. The variable η^* describes the difference of pseudorapidities, $\eta_{i,\mathrm{B}}$, of the final-state partons in the Breit frame. This difference is invariant under longitudinal Lorentz transformations. The pseudorapidity is defined as $\eta = -\ln\tan\frac{\theta}{2}$, where θ is defined as the polar angle of the parton. The variable η^* is closely related to the angular dependent parts of the QCD matrix element. The variable ξ represents the momentum fraction of the parton entering the hard process. For instance, for a dijet system, the squared dijet centre-of-mass energy is given by

$$M_{jj}^2 = (q + \xi P)^2 = (p_1 + p_2)^2 = q^2 + 2q\xi P + (\xi P)^2\,. \tag{2.22}$$

If the $(\xi P)^2 \ll Q^2$ term is neglected, then the variable ξ can be derived according to

$$M_{jj}^2 \approx -Q^2 + 2q\xi P, \qquad \Rightarrow \qquad \xi = \frac{Q^2}{2qP} + \frac{M_{jj}^2}{2qP} = x_{\mathrm{Bj}} \left(1 + \frac{M_{jj}^2}{Q^2}\right). \tag{2.23}$$

Therefore, the M_{jj}^2/Q^2 term is related to the additional energy needed to produce two final-state partons

2.2.2.3. Jet Algorithms

The combination of particles from the hadronic final state into jets can be performed in various different ways. Since a jet is actually not an uniquely defined object, several requirements for jet definitions were proposed [89]: The algorithm has to be applicable easily in the theoretical calculations as well as in experimental environments. The jet definition has to be defined at any order in perturbation theory and it has to be infrared and collinear safe. Furthermore, the jet cross section should be relatively insensitive to hadronisation effects in order to preserve the close correspondence between the final-state partons and the jet.

A jet definition usually consists of an algorithm that maps the momenta of the final state particles into the momenta of a certain number of jets, of some parameters like typically at least the resolution scale and of a "recombination scheme" which specifies how the four-momenta of the objects have to be combined.

Nowadays, basically two main classes of jet algorithms are available. Sequential recombination algorithms such as the "k_t" [90, 91], "Cambridge/Aachen" [92, 93] or the "anti-k_t" [94] algorithm utilise a distance measure and a successive recombination procedure for the combination of close-by particles. In contrast, cone algorithms perform a search for coarse regions of energy flow. Since the search for all possible stable cones is too slow, approximate methods have to be applied. In the past, seed particles were used as starting points for the cone construction which induced infrared unsafe algorithms. However, this was solved by inventing a "seedless cone algorithm" (SISCone) [95]. Typically, the shape of jets – the "catchment area" [96] – reconstructed with the cone and the "anti-k_t" algorithms is more regular[5] in contrast to the shape of jets reconstructed with the "k_t" algorithm.

In this analysis, the longitudinal invariant inclusive k_t algorithm [90, 91] was utilised for the reconstruction of jets. This algorithm uses the variables η and the azimuthal angle, ϕ, of the detector objects, hadrons or partons. In addition, the transverse energy, E_T, is exploited. The jet reconstruction was performed in the Breit reference frame assuming that the measured objects are massless. The latter leads to invariant quantities under longitudinal Lorentz transformations.

The algorithm consists of the following steps:

1. Two catalogues are used: a list of all measured objects, and a list of reconstructed jets which is empty at the beginning.

2. For all objects i the distance to the beam axis, $d_i = E_{T,i}^2 \cdot R_0^2$, and the distance d_{ij} to the other objects j is calculated according to $d_{ij} = \min\left(\mathrm{E}_{\mathrm{T,i}}^2, \mathrm{E}_{\mathrm{T,j}}^2\right)\mathrm{R}_{\mathrm{ij}}^2$, where

[5] In fact, the "anti-k_t" algorithms produces jets with a perfectly conical shape.

R_{ij} is the distance in the $\eta - \phi$ plane given by $R_{ij} = \sqrt{(\eta_i - \eta_j)^2 + (\phi_i - \phi_j)^2}$. The variable R_0 was set to unity in the presented jet analysis.

3. Afterwards, the smallest distance $d_{\min}$ is determined from all d_i and d_{ij}.

4. If $d_{\min}$ belongs to the list $\{d_i\}$, then a jet has been reconstructed and put into the list of jets. The $d_{\min}$ is removed from the list of objects.

5. In contrast, if $d_{\min}$ belongs to the list $\{d_{ij}\}$, then the particles i and j are combined into a new particle. The particles i and j are removed from the list $\{d_{ij}\}$.

6. The procedure is repeated until all objects are clustered into jets.

The resulting jets are defined by the particles i clustered to the jet. In this analysis, the "E_T scheme" [89] was employed. This means that the transverse energy, the pseudorapidity and the azimuthal angle of a jet are given by

$$E_{T,\text{jet}} = \sum_i E_{T,i}, \qquad \eta_{\text{jet}} = \frac{\sum_i E_{T,i}\eta_i}{E_{T,\text{jet}}}, \qquad \phi_{\text{jet}} = \frac{\sum_i E_{T,i}\phi_i}{E_{T,\text{jet}}}. \tag{2.24}$$

The reconstructed jets are massless ($E_i = |\vec{p}_i|$). Due to the definition, the reconstructed jets always have a distance greater than R_0 to each other.

3. Experimental Setup

In this chapter, the experimental setup is briefly described.

3.1. DESY

In 1959, the "Deutsche Elektronen-Synchrotron" (DESY) was founded as a national research centre for the development and operation of particle accelerators in Hamburg, Germany. At the present time, DESY is an international research institute devoted to elementary particle physics, photon science and accelerator science. For the field of photon physics, DESY provides the electron ring accelerator DORIS III and the "Free Electron Laser" (FLASH). PETRA III, which is one of the most brilliant storage-ring-based x-ray source worldwide, started operation in 2009. The commissioning of the "European X-ray Free Electron Laser" (XFEL) is planned for 2013.

3.2. HERA

The "Hadron Elektron Ring Anlage" (HERA) collider was, up to now, the only electron-proton collider in the world, offering unique opportunities to explore the structure of the proton and to study various processes involving strong, electromagnetic and weak interactions. HERA was constructed with the goal to provide greater centre-of-mass energies than available before in fixed-target experiments.

HERA was running from 1992-2007. It was located underground inside a tunnel and consisted of one storage ring for protons and one for electrons. The circumference was 6.3 km. Until 1998, HERA reached a centre-of-mass energy of about ≈ 300 GeV. Starting from 1998 the energy of the protons was increased to 920 GeV in order to reach a centre-of-mass energy of ≈ 320 GeV.

Four experiments were situated on the HERA ring; two multi-purpose experiments (H1 and ZEUS) and two fixed-target experiments (HERMES and HERA-B). At H1 and ZEUS, electrons and protons collided head-on, whereas at HERMES only the electron beam and at HERA-B only the proton beam was used. HERMES investigated the spin structure of the nucleon and HERA-B aimed to study CP violation in the B system.

In 2001, HERA and the H1 and ZEUS experiments were upgraded to achieve higher luminosities [97] and spin rotators [98] were installed for the H1 and ZEUS experiments. Up to 2001, the lepton beam was longitudinally unpolarised. The period up to the year 2000 is called "HERA I" and the period starting with 2003 is called "HERA II".

Before being injected into the HERA accelerator, electrons/positrons and protons were accelerated by a system of several preaccelerators as shown in figure 3.1. Protons were produced by shooting H^- ions, which were accelerated in the LINAC III, through a stripper foil in which the electrons were removed. The resulting protons were injected

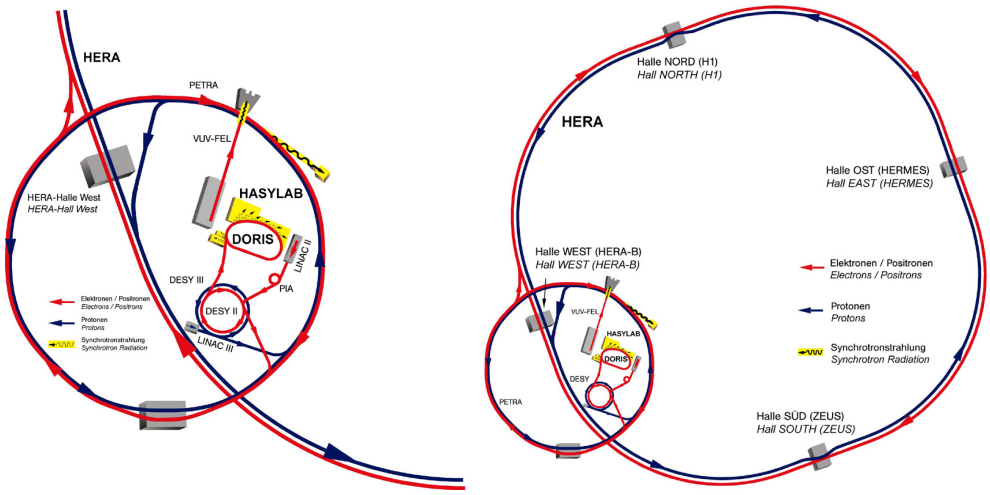

Figure 3.1: A schematic view of the HERA collider and the preaccelerators.

into DESY III where their energy was increased to 7.5 GeV. Before the protons were injected into HERA, they were accelerated in PETRA II up to 40 GeV. In contrast, electrons/positrons were preaccelerated in LINAC II to an energy of 450 MeV. After this stage, the electrons/positrons were accelerated to energies of about 7 GeV in DESY II. Just like the protons, the electrons/positrons were injected into PETRA II and, finally, transferred to HERA.

Electrons and protons are grouped in so-called bunches and are collided with each other. The time difference between two bunches was about 96 ns; therefore, the distance between two bunches was equal to 28.8 m. The maximum number of stored bunches was 210. In order to investigate background events initiated by beam-gas events, unpaired as well as empty bunches were used.

At HERA, transverse polarisation of the electron beam built up naturally due to the Sokolov-Ternov effect [99, 100] with a build-up time of approximately 40 minutes. Starting from the year 2003, spin rotators [98] on either side of the H1 and ZEUS detectors changed the transverse polarisation of the beam into longitudinal and back again to ensure the preservation of the polarisation around the ring. The electron beam polarisation was measured using two independent polarimeters, the transverse polarimeter (TPOL) [101] and the longitudinal polarimeter (LPOL) [102]. Both devices exploited the spin-dependent cross sections for Compton scattering of circularly polarised photons off electrons to measure the beam polarisation.

3.3. The ZEUS Detector

The ZEUS detector was one of the two multi-purpose detectors at the HERA ring accelerator designed to study various aspects of *ep* scattering. The detector had a dimension of about $12 \times 11 \times 20$ m^3 and a weight of 3600 tons. A detailed description can be found in [103].

The geometry is described using a right-handed coordinate system with its origin at the nominal interaction point. The z-axis points along the proton direction and

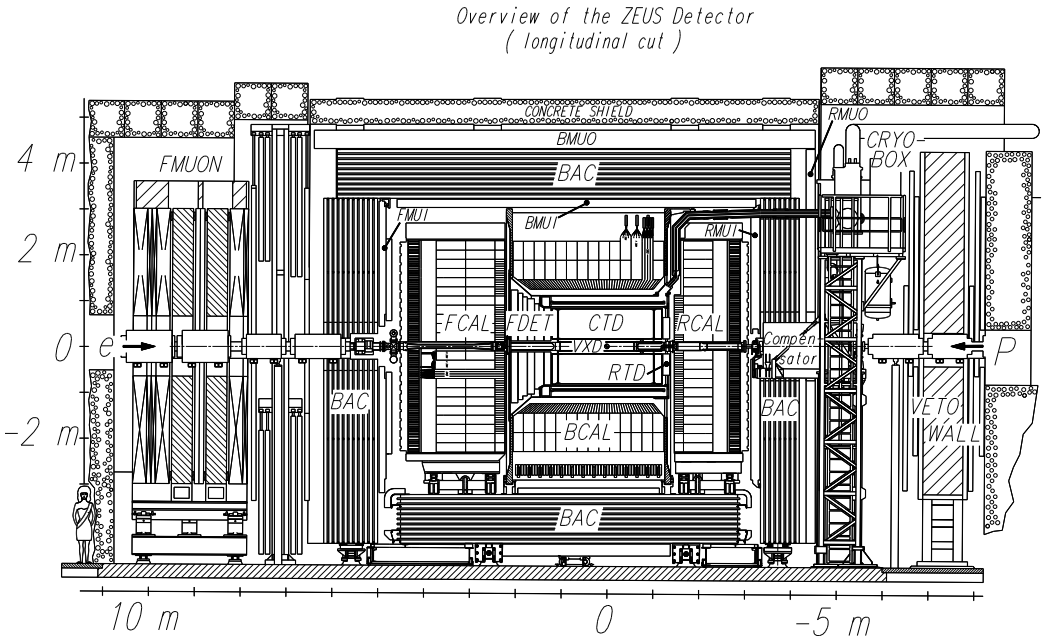

Figure 3.2: View of the ZEUS detector along the beam direction.

the y-axis points upwards. A schematic view of the detector is shown in figures 3.2 and 3.3 where a longitudinal and transverse cross section of the ZEUS detector is illustrated. Since the difference in energy of the two colliding particles is large, the centre-of-mass frame is boosted in the direction of the proton beam. Therefore, the ZEUS detector was designed to be asymmetric, because of the large forward-backward asymmetry of the particle production.

The innermost part of the main detector consisted of the tracking system enclosed by a thin superconducting solenoid producing an axial magnetic field of 1.43 T. The "Central Tracking Detector" (CTD) and the "Microvertex Detector" (MVD) were arranged cylindrically around the beam pipe; the MVD was the inner component providing also a forward section (FMVD). In the backward and forward regions, the CTD was supplemented with planar drift chambers – the forward and rear tracking detectors (FTD and RTD). During the upgrade of ZEUS, the forward tracker was supplemented with a straw tube tracker (STT). The STT has been designed to improve the track finding and reconstruction capabilities in the forward region. The Uranium Calorimeter (CAL), which was the main device for energy measurement of particles, was located outside the solenoid. The CAL was enclosed by a low-resolution backing calorimeter (BAC) that also served as a iron yoke providing a return path for the magnetic field flux of the solenoid. The BAC was equipped with proportional chambers making it possible to measure energy leakage out of the CAL and to reconstruct high-energetic muons. Muon chambers were mounted outside the BAC (RMUI, BMUI, FMUI and RMUO, BMUO, FMUO). An iron-scintillator wall (VETOWALL) was installed in the rear direction to reject background related to the proton beam.

The detectors used for the luminosity measurement were located outside the central ZEUS detector. In the following, some of the main components important for the

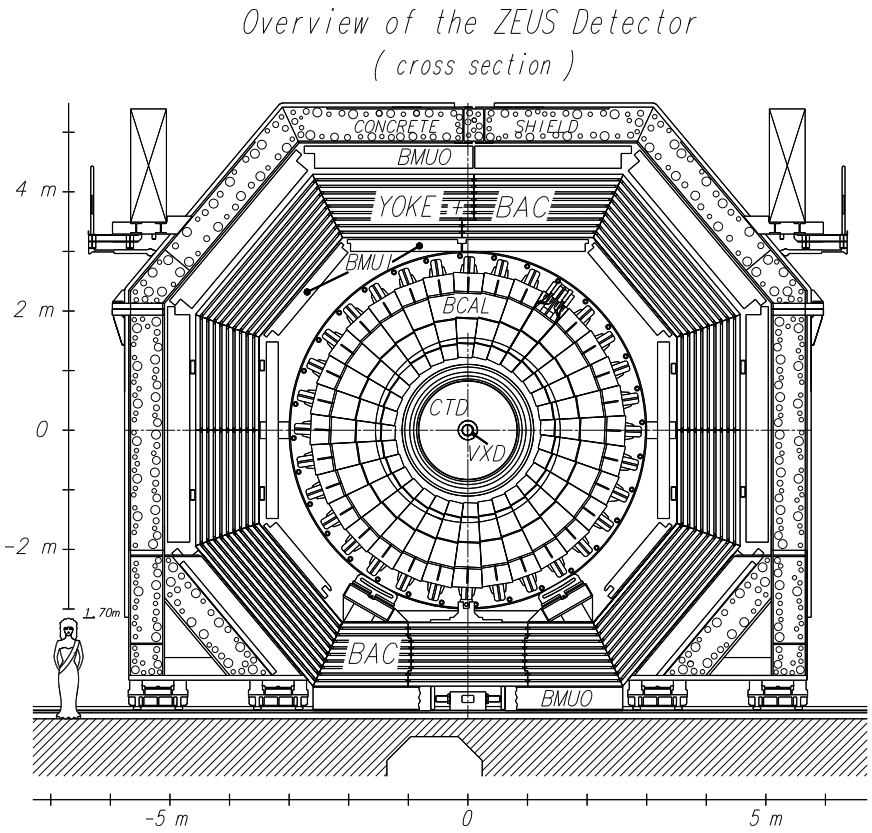

Figure 3.3: Cross section of the ZEUS detector perpendicular to the beam direction.

presented analysis are discussed.

3.3.1. The Central Tracking Detector and the Microvertex Detector

Charged particles were tracked in the CTD [104–107], which was a wire chamber oriented parallel to the beam axis. The CTD provided high precision measurements of the positions, directions and momenta of charged particles. The CTD allowed to measure the z position of the event vertex with a resolution of about 4 mm. Additionally, the measurement of the mean energy loss, dE/dx, of particles along their tracks helped to distinguish different particle types.

The chamber was filled with a mixture of argon, CO_2 and ethane. It covered the polar angle of $15° < \theta < 164°$. The active volume had a length of 205 cm; the inner radius of the CTD was 16.2 cm, the outer radius was 85 cm. The CTD was subdivided into multi-layers consisting of 72 cylindrical drift-chamber layers. It was organised into nine "superlayers" of eight sense wire layers each as shown in figure 3.4. Five of the superlayers had wires parallel to the chamber axis and were called "axial superlayers". The remaining four layers were so-called "stereo superlayers". The wires of the stereo superlayers were mounted with angles of about $\pm 5°$ with respect to the beam axis in order to allow track reconstruction of the z coordinate with an achieved resolution of about 2 mm, whereas in the $r - \phi$ plane a resolution of ≈ 200 μm was achieved. Charged particles traversing the CTD have ionised the

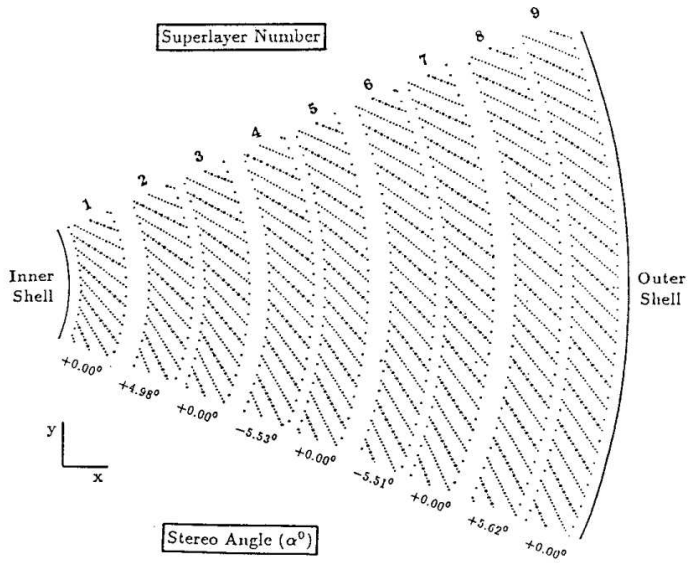

Figure 3.4: Overview of one CTD octant. Each octant had nine superlayers.

gas mixture and produced electron-ion pairs along their trajectory. Owing to the applied electric field, the electrons drifted to the sense wires. The magnetic field caused the path of the drift electron to be tilted by a Lorentz angle of 45° with respect to the radial direction. This effect was accounted for by mounting the wire planes at the same angle. For particles traversing through all 9 superlayers, the resulting transverse momentum, p_T, resolution during the years 1992–2000 was given by [108] $\sigma_{p_T}/p_T = 0.0058 \cdot p_T \otimes 0.0065 \otimes 0.0014/p_T$, where $\otimes$ denotes the quadratic sum. The first term corresponds to the resolution of the hit position measurements, while the second and the term arise from multiple scattering within and before the CTD, respectively.

Starting from the year 2004, a silicon microvertex detector (MVD) [109], installed between the beam-pipe and the inner radius of the CTD, was used in addition. It consisted of a barrel section with three cylindrical layers and a forward section with four planar layers perpendicular to the HERA beam direction. In total 200000 channels were read. The total area of silicon was 2.9 m^2. The MVD provided an intrinsic hit position resolution of ≈ 20 μm for normal incident tracks. The MVD improved the vertex reconstruction and extended the tracking acceptance.

3.3.2. The Uranium Calorimeter (CAL)

The CAL [110–114] was a high-resolution uranium sampling calorimeter which consisted of alternating layers of absorber (depleted uranium) and active material (plastic scintillator) material. The thickness of the uranium (scintillator) was 3.3 mm (2.5 mm). The material thickness had been chosen to provide linear and equal response to electrons and hadrons over a wide range of energies. The CAL was almost hermetic with a solid-angle coverage of 99.7%.

The CAL was divided into three sections, the forward (FCAL), the barrel (BCAL) and the rear (RCAL) calorimeter as shown in figure 3.5. The depth of the material was chosen such that a maximum of energy was absorbed. The maximum energy was

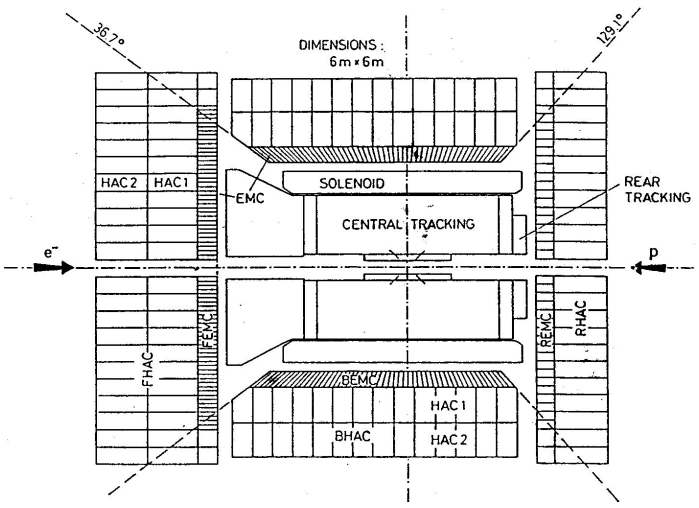

Figure 3.5: Cross section of the ZEUS detector. Shown are the three sections of the CAL.

about 30 GeV in the RCAL and increased to about 800 GeV in the FCAL.

The FCAL and RCAL were subdivided vertically into modules, whereas the BCAL modules were wedge-shaped. Each module was further segmented into towers with a front surface dimension of about 20×20 cm^2. The towers were segmented into an electromagnetic (EMC) and two (one), in case of the FCAL (RCAL), hadronic sections (HAC). Each hadronic section of a tower was identified as one calorimeter cell. The EMC sections of the FCAL (RCAL) were divided vertically into four (two) cells. The BCAL was divided into one EMC and two HAC sections. The modules were segmented into 14 towers along the beam direction. Since the outer regions of the FCAL and RCAL were shielded by the BCAL, these regions were not equipped with EMC sections. The front surface dimension of the EMC cells in the RCAL (FCAL) was 20×10 cm^2 (20×5 cm^2).

The scintillator plates were readout on either side of the cell with photomultipliers. These photomultipliers were connected to the cell via wavelength shifters. The impact position of particles could be estimated by utilising the pulse-high difference of the signals provided by the two photomultiplier. The CAL was calibrated to a precision of $\approx \pm 1\%$ on a channel-by-channel basis using the natural radioactivity of uranium providing a stable and time independent reference signal. The electronic readout was calibrated using test pulses simulating the photomultiplier signals. The timing resolution of the CAL was < 1 ns for energy deposits greater than 4.5 GeV. Hence, it was used in the trigger system.

The energy resolution of the CAL was determined under test beam conditions without inactive material in front of the CAL as $\sigma/E = 18\%/\sqrt{E} \otimes 1\%$ for electrons and $\sigma/E = 35\%/\sqrt{E} \otimes 1\%$ for hadrons, were E denote the energy in GeV and $\otimes$ represents the quadratic sum.

3.3.3. Luminosity System

The luminosity of the storage ring, $\mathcal{L}$, is given by

$$\mathcal{L} = f \frac{N_p N_e}{4\pi\sigma_x\sigma_y}, \tag{3.1}$$

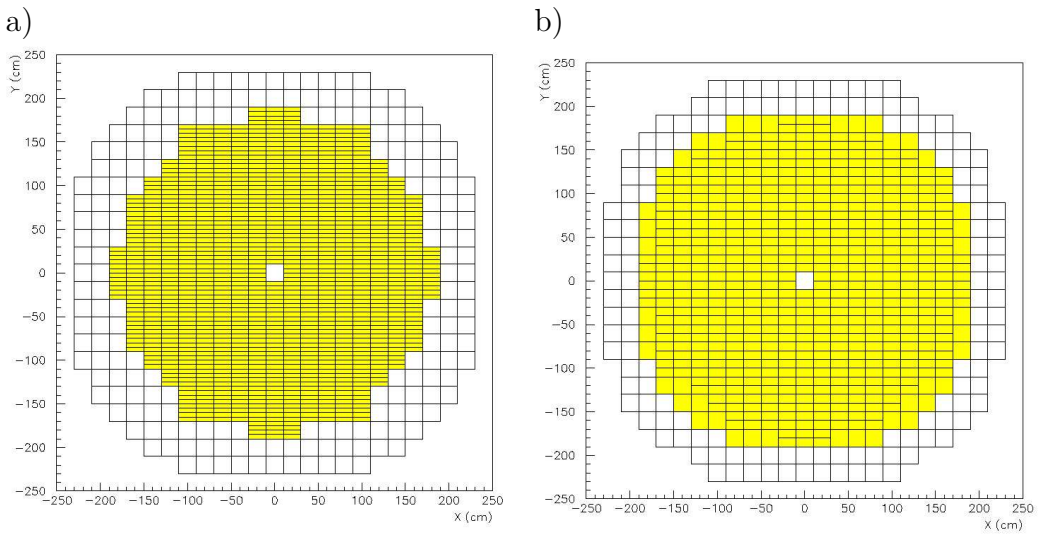

Figure 3.6: The cell structure of the a) FCAL and the b) RCAL. The outer parts are covered by HAC sections, whereas the inner parts contains also EMC cells.

where N_p (N_e) denotes the number of protons (electrons) per bunch, the quantity $\sigma_x\sigma_y$ the spatial extension of the bunches and f the bunch crossing frequency. Any cross section measurement relies on the accurate knowledge of the luminosity. Figure 3.7 shows the delivered luminosity of the HERA storage ring as a function of time for the various data-taking periods.

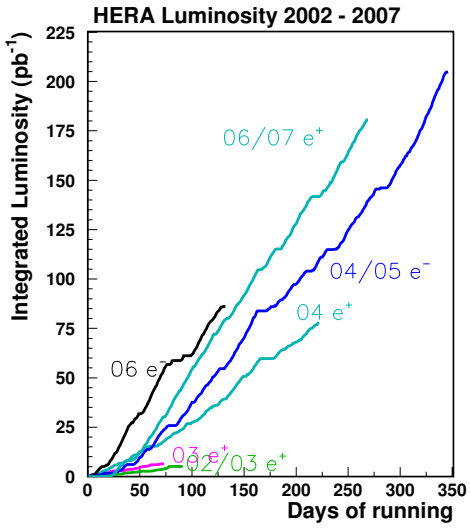

Figure 3.7: The delivered luminosity of the HERA ring as a function of time for the various data-taking periods.

The luminosity can be determined by measuring the event rate of a well known process. At ZEUS the luminosity measurement is based on the Bethe-Heitler process $ep \to ep\gamma$ [115], because the theoretical cross section for this process is high ($\sim$ 300 mb [116]) and known with an accuracy of about 0.5%.

At ZEUS the luminosity was measured with detectors which consisted of a lead–scintillator calorimeter [116–118] and, in the 2004–2007 running period, an independent magnetic spectrometer (SPEC) [119]. Due to the increased luminosity in HERA II,

the rate of synchrotron radiation increased by a factor of almost 7 compared to HERA I and of Bethe-Heitler events by a factor of $4-5$. In order to cope with these new conditions, the luminosity system was upgraded in HERA II.

The photon detector was a lead–scintillator calorimeter positioned at $z=-107$ m from the nominal interaction point. With the aid of carbon filters the calorimeter was shielded against synchrotron radiation. Since these filters worsen the energy resolution, in HERA II two Cherenkov detectors [120] measured a signal related to the energy deposits in the filters. The energy resolution of the photon calorimeter was $\approx 18\%/\sqrt{E}$ ($\approx 25\%/\sqrt{E}$) in the HERA I (HERA II) period. To determine the luminosity with the photon calorimeter, the rate of Bethe-Heitler events was measured by counting the hits in the detector with an energy deposit above a certain threshold.

The SPEC [119] detected Bethe-Heitler photons through their pair conversion, $\gamma \to e^+e^-$, in the thin beam pipe window. The SPEC used a dipole magnet with a typical field of 0.5 T in order to separate the e^+e^- pairs. Two tungsten/scintillator sandwich calorimeters have measured the energies and positions of the separated leptons with an resolution of about $17\%/\sqrt{E}$ and < 1 mm, respectively. The luminosity was determined by measuring coincident energy deposits in the two calorimeters.

3.3.4. Trigger and Data Acquisition System

The time difference between two bunch crossings was 96 ns – equivalent to a rate of about 10 MHz. The total interaction rate, which was dominated by background due to beam-gas interactions, was in the order of $10-100$ kHz while the rate of DIS ep events in the detector was in the order of a few Hz.

The purpose of the trigger system [121–123] at ZEUS was to select interesting events, in particular because the event rate needed to be reduced to a few Hz to make the events recordable. Therefore, a sophisticated three-level trigger system was connected to the ZEUS detector. A schematic overview is shown in figure 3.8.

At the "First Level Trigger" (FLT) [124, 125] only coarse information was available. The FLT was designed to reduce the rate to below 1 kHz. Every detector component had its own FLT, which stored the data in a pipeline and prepared the information for the trigger decision within 2 μs after the bunch crossing. The information from the local FLTs were passed to the "Global First Level Trigger" (GFLT) which decided whether to accept or reject the event. Within a time interval of 4.6 μs, the decision was returned to the readout systems of the different components.

If an event was accepted by the GFLT, the data were transferred from the pipeline to a data buffer and to the local "Second Level Trigger" (SLT) [126]. The SLT was software based and ran on a network of transputers. Just as for the FLT, every component of the detector had its own SLT. A "Global Second Level Trigger" (GSLT) [127] decided after receiving the local information from every component whether an events has to be accepted. The GSLT was designed to reduce the event rate to below 100 Hz and to produce a decision within $1-3$ ms after the corresponding bunch crossing. If the event had been accepted by the GSLT, then the data were transferred to the "Event Builder"[128] that collected the information to store it in an ADAMO [129] database record.

The "Third Level Trigger" (TLT) [130, 131] made use of a computer farm. The

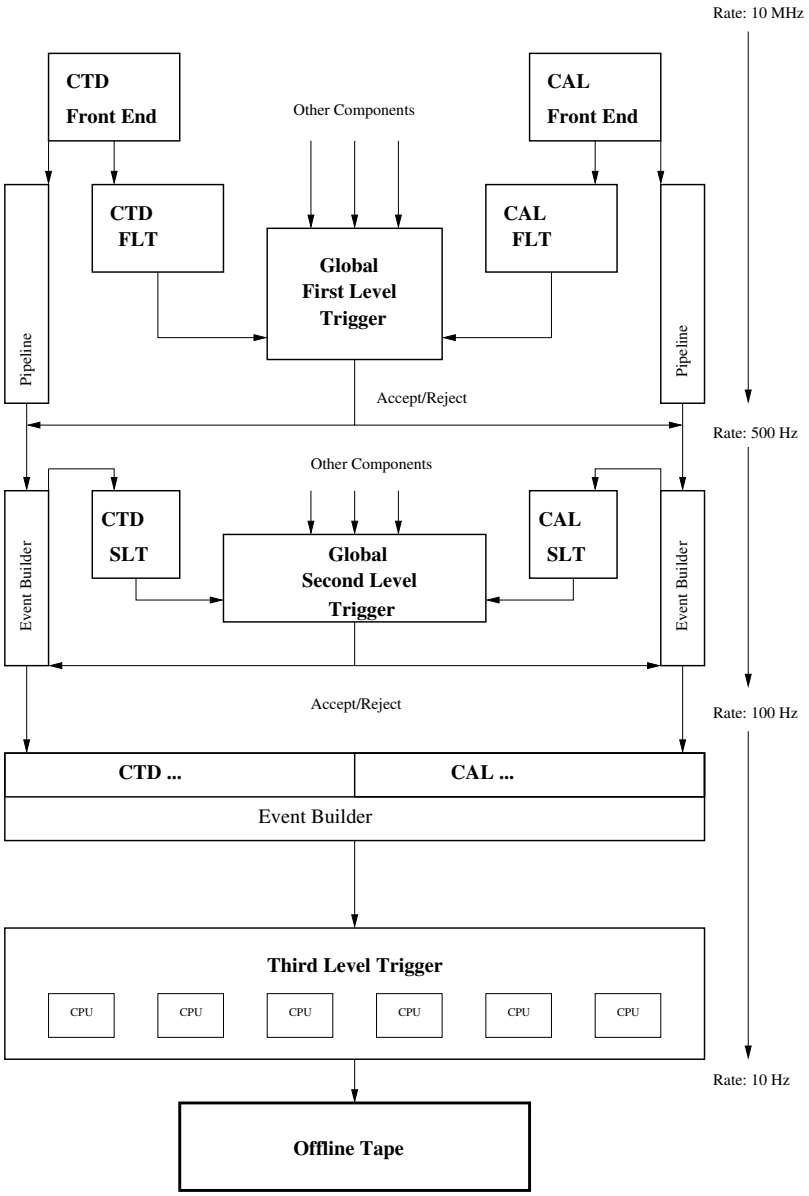

Figure 3.8: An overview of the ZEUS trigger system.

events were fully reconstructed by using the information stored in the ADAMO tables. The TLT was designed to reduce the event rate to few Hz. If the event was accepted by the TLT, the data were stored on tape for the full offline reconstruction and data analysis.

4. Fixed-Order Calculations and Monte Carlo Simulations

In order to be able to compare the data with fixed-order perturbative QCD calculations, Monte Carlo (MC) simulations that provide detailed information of the final state as measured in the detector were utilised, e.g. for the determination of the detector response. Typically, these Monte Carlo simulations perform the generation of the hadronic finale state by using approximate methods, while the matrix element is calculated only in leading order.

In this chapter, the main components of the Monte Carlo simulations are briefly described and also the programs providing the fixed-order perturbative QCD calculations and the used settings are discussed.

Finally, the jet observables investigated in the presented thesis are introduced.

4.1. Monte Carlo Simulations

In order to compare the data with simulations, Monte Carlo programs have to provide a detailed and comprehensive simulation of the final state in the detector. These programs use approximations and phenomenological models for the estimation of the properties of the final state.

In this analysis, neutral-current DIS events were generated using the Heracles program [132] with the Djangoh interface [133] to the hadronisation programs Lepto or Ariadne. More details on the latter two programs are given below in section 4.1.1. The Heracles program includes radiative QED corrections such as initial- and final-state radiation, vertex and propagator terms and two-boson exchange. Since the probability for real QED radiation is related to the mass of the radiating particle, the main contributions are arising from the leptonic part of the process. These QED corrections may influence the reconstruction of the event kinematics and, thus, have to be taken into account in order to describe the data.

The Monte Carlo simulations utilised in this analysis have used the CTEQ5D [134] proton PDFs as provided by the PDFLIB library [135].

After the event generation, the leading-order hard matrix element has to be calculated and initial- and final-state parton cascades have to be simulated in order to approximate the contributions from higher-order processes. Afterwards, the fragmentation of final-state partons into colourless hadrons is performed with phenomenological hadronisation models. These individual stages are illustrated schematically in figure 4.1. Furthermore, the final-state particles are passed through a simulation of the full detector. In the following, the main components of the Monte Carlo simulations are briefly discussed.

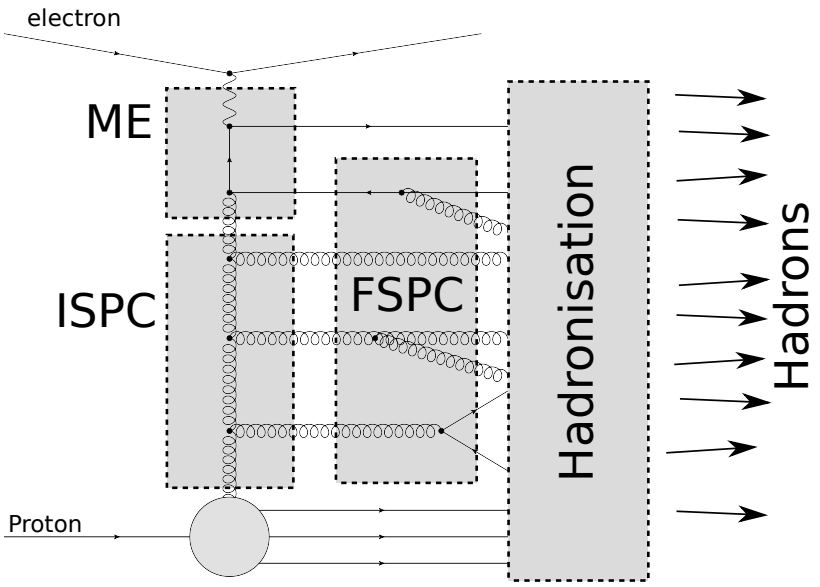

Figure 4.1: Schematic sketch of the individual parts of the Monte Carlo event generation: the hard matrix element (ME), initial- and final-state parton cascades (ISPC, FSPC) and the hadronisation of partons into colourless hadrons.

4.1.1. LEPTO and ARIADNE

The Monte Carlo program LEPTO [136] generates the quark-parton model, the boson-gluon fusion and QCD-Compton processes. The region with infrared divergences is suppressed with cuts for instance on the minimal invariant mass of the final-state partons. Higher-order contributions are approximated by the emission of partons. This approximation is based on the parton-shower approach [137] which utilises the Altarelli-Parisi evolution equations in the "leading log approximation". These emitted partons can be either generated in the initial or in the final state of the event. While the final-state shower is coming from the outgoing partons generated by the hard matrix element, the initial-state partons are produced by the initial state parton shower [138] with decreasing scale towards the initial-state proton.

In contrast to the parton-shower approach as implemented in LEPTO, the Monte Carlo program ARIADNE [139, 140] is based on the so-called "colour-dipole model" [141–146] which was originally developed and optimised for the description of the hadronic final state in e^+e^- annihilation experiments. According to the "colour-dipole model", higher-order processes are approximated by the emission of gluons from colour-dipole fields between the final-state objects carrying colour charge. Moreover, the emitted gluons form new colour dipoles which can possibly radiate further gluons. Since ARIADNE only calculates the matrix element for the QCD-Compton process, an additional event generator has to be used. Therefore, in the analysis presented here, LEPTO was used for the generation of gluon-induced processes.

4.1.2. Hadronisation

Perturbative QCD predictions are insufficient for the description of processes in which the strong coupling becomes large. The observed behaviour of the strong interaction is the so-called "confinement": the partons (quarks and gluons) can't be observed as free and isolated particles. With increasing distance and, thus, with decreasing energy scale, the force between partons becomes so large that the energy stored in the field is large enough for the production of further particles. At present, the transition of partons created in the hard scattering or the parton cascade to the colourless hadrons – the "hadronisation" – can only be described with phenomenological models and can't be derived from first principles.

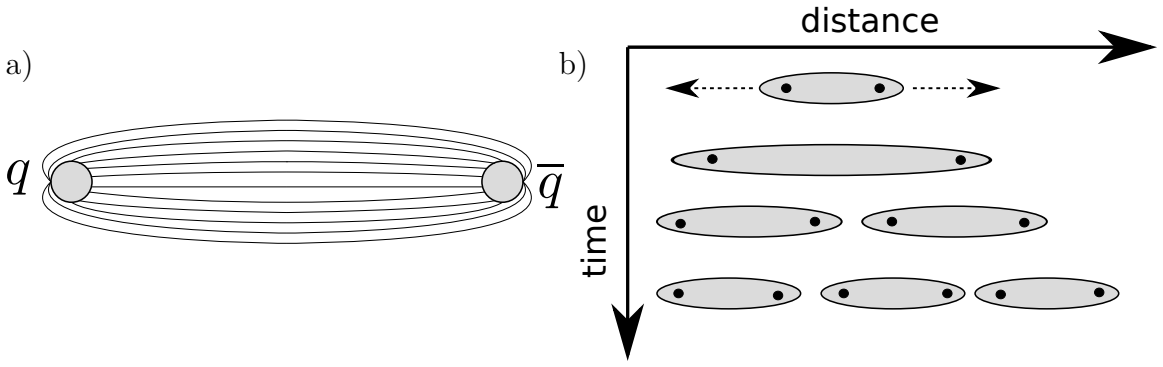

Figure 4.2: a) A colour-flux string between a quark-antiquark pair. b) The fragmentation of a quark-antiquark pair into colourless hadrons.

In this analysis, the JETSET program [147–149] which implements the "Lund String Model" [150] for the hadronisation process was utilised. In this model, two colour-charged quarks are connected via a colour field with each other as depicted in figure 4.2a. This field can be illustrated as a thin string with an energy density in the order of $O\,(1\ \mathrm{GeV/fm})$. For larger distances, the related potential is assumed to increase linearly with the distance between the two quarks. If the energy exceeds a certain threshold, the string can split with a certain probability into a new $q\overline{q}$ pair. As a consequence, two strings instead of just one are remaining. The procedure repeats, as shown in figure 4.2b, until the available energy is too small for further $q\overline{q}$ pair production. The resulting colourless strings form the final-state hadrons of the event. In this thesis, the hadron level is defined in terms of hadrons with lifetimes $\tau \geq 10$ ps.

Besides the "Lund String Model" also other hadronisation models such as the cluster fragmentation [151, 152] are available.

4.1.3. Detector Simulation

The stable hadrons obtained from the hadronisation procedure described in the previous section and other final-state particles were passed through the GEANT-based [153] ZEUS detector- and trigger-simulation programs [103]. The interaction of particles in detector material and the response and readout of active material were simulated.

The format of the Monte Carlo output was equivalent to the format of the data. Therefore, the Monte Carlo simulations could be analysed with the same analysis programs as the "real" data.

In the following, the reconstructed events are said to be at "detector level", the available information after the hadronisation procedure is called "hadron level", whereas the information directly after the parton cascade and before the hadronisation is called "parton level". Since the fixed-order calculations (see next section 4.2) only provide predictions for the partonic cross sections, these predictions are also referred to as "parton level" predictions.

4.2. Fixed-Order Calculations

Technically, the theoretical cross section in next-to-leading order (NLO) pQCD consists of virtual and real contributions. Since in these contributions divergent terms are present, several mechanisms have been developed in order to perform the numerical integration over the phase space by integrating parts of the matrix element analytically. In the subtraction method [154, 155], the divergent terms are subtracted, later added and integrated analytically. In the phase space slicing method [156], the phase space is divided into a region in which the integration can be performed without difficulties and a divergent region by introduction a cut-off parameter. In the latter phase-space region, approximations are applied and integrated analytically, whereas in the region without divergences the integration can be performed using standard numerical methods.

In this section, the two programs DISENT and NLOJET++ used for the determination of NLO QCD predictions and the employed settings are presented. In this section also the infrared sensitivity of dijet cross-section predictions is discussed.

4.2.1. The Programs DISENT and NLOJet++

The program DISENT [157] calculates collinear and infrared safe quantities up-to the order $O(\alpha_s^2)$. The program makes use of an extended version of the "subtraction method" [154] – the "dipole formalism" [158] – in order to cope with the appearance of divergences.

Similar to DISENT, dijet cross sections up-to the order $O(\alpha_s^2)$ can also be calculated with the NLOJET++ program [159]. Unless otherwise stated, the program NLOJET++ was the default program for the NLO calculations. In addition to the NLO predictions of dijet cross sections ($O(\alpha_s^2)$), NLOJET++ is also able to perform NLO calculations for the production of trijet ($O(\alpha_s^3)$) events. The results for the production of dijets from both programs NLOJET++ and DISENT were cross-checked and found to agree to better than $\pm 1\%$.

In this analysis, the calculations were performed in the $\overline{\text{MS}}$ renormalisation and factorisation schemes, while the number of flavours was set to five. The default factorisation scale was $\mu_F = Q$, whereas the renormalisation scale was set to $\mu_R^2 = Q^2 + \overline{E}_{T,\text{B}}^2$, where $\overline{E}_{T,\text{B}}$ represents the average transverse energy in the Breit frame of the final-state partons forming the dijet or trijet system, respectively. The theoretical calculations were performed using the CTEQ6.6 parametrisation [81] of the proton PDFs. The

strong coupling was calculated at two loops corresponding to $\alpha_s(M_Z) = 0.118$. On the generated partons in the event, the k_t cluster algorithm was applied in order to obtain jet cross-section predictions. In the calculations, *inclusive* dijet (trijet) cross sections were determined, which means that the reconstruction of at least two (three) jets in the final state was required.

4.2.2. Infrared Sensitivity

In some regions of the dijet phase space, the cancellation between soft and collinear singularities in NLO theoretical predictions is incomplete [160–163]. Real emissions of gluons are suppressed in regions in which the the azimuthal difference, $\Delta\phi_{jj}$, of the two jets is close to π, in which the transverse momentum difference, ΔE_T^{jj}, is close to 0 or in which the invariant dijet mass, M_{jj}, is close to the threshold. In these regions, the transverse momenta of the two jets balance each other. However, if the two jets are slightly decorrelated, soft gluon emission is allowed but kinematically constrained. As a consequence, some of the virtual divergences are left uncancelled which results in theoretical fixed-order calculations that become sensitive to soft gluon emission. Nevertheless, the theory can be made infrared insensitive by introducing e.g. asymmetric transverse energy cuts or an invariant mass cut.

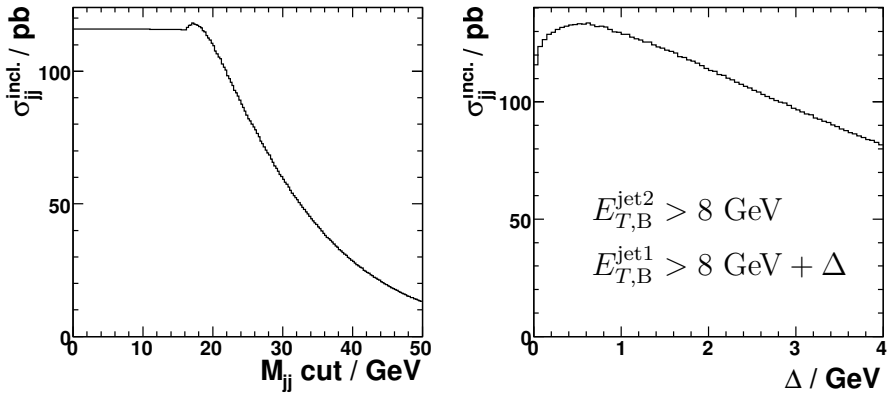

Figure 4.3: The total inclusive dijet cross section determined with DISENT as a function of a) an applied invariant-mass cut and b) of Δ. The variable Δ corresponds to the difference of the two imposed transverse-energy cuts.

Figure 4.3 illustrates, as an example, the total inclusive dijet cross section determined with DISENT as a function of the applied cut either on M_{jj} or on Δ, which is defined as the difference between the cuts on the transverse energies of the hardest- and second-hardest jets in the event. The illustrated functions are not monotonically decreasing with increasing cut values, which means that the fixed-order calculations are not reliable in regions in which the two jets have balanced transverse momenta. This behaviour appears in any fixed-order calculation and can only be avoided by using all-order resummed calculations or by utilising non-perturbative methods. However, by introducing the described cuts, the influence of infrared sensitive regions can be significantly reduced.

In chapter 8.2, a more detailed discussion of the infrared sensitivity for the investigated dijet phase space is presented.

4.3. Jet Observables

In this section, the phase space and the observables in which the jet measurement was performed are summarised.

In perturbative QCD, the jet cross section, σ_{jet}, in ep collisions can be described theoretically as a series expansion in powers, m, of α_s,

$$\sigma_{\text{jet}} = \sum_m \alpha_s^m \left(\mu_R\right) \sum_{a=q,\bar{q},g} f_{a/p}\left(x, \mu_F\right) \otimes \hat{\sigma}_{a,m}\left(x, \mu_R, \mu_F\right) \left(1 + \delta_{\text{had}}\right)_{\ldots}, \tag{4.1}$$

with coefficients which are convolutions of the PDFs, $f_{a/p}$, for a parton a inside the proton and the hard-scattering matrix element, $\hat{\sigma}$. Therefore, with the aid of jet measurements detailed and stringent tests of perturbative QCD can be performed. In particular, the dijet cross sections are more sensitive to the limitations of fixed-order predictions (section 4.2.2) than inclusive jet cross sections. Furthermore, the dijet cross sections are sensitive to the gluons inside the proton even in leading order. Therefore, this data allow an extraction of the gluon PDF with presumably improved precision. Moreover, the jet cross section is sensitive to α_s and can be exploited for an extraction of this coupling.

In this thesis, differential inclusive dijet and trijet cross sections were measured with beam energies of 27.5 GeV for the electrons and 920 GeV for the protons in the kinematic region of the virtuality, $125 < Q^2 < 20000$ GeV^2, and the inelasticity, $0.2 < y < 0.6$. In this high-Q^2 region, the theoretical uncertainties of the NLO QCD calculations become relatively small.

The k_t jet algorithm in the longitudinally invariant inclusive mode was applied to the massless final-state objects in the boson-quark collinear frame, the Breit reference frame. The cross sections refer to jets with $E_{T,\text{B}}^{\text{jet}} > 8$ GeV and $-1 < \eta_{\text{LAB}}^{\text{jet}} < 2.5$, where the first variable is the transverse jet energy in the Breit frame and the latter the jet pseudorapidity in the laboratory frame. For the selection of dijet (trijet) events it was required that at least the two (three) highest-transverse-energy jets exceed the transverse-energy threshold. Additionally, the invariant dijet mass of the two highest-transverse-energy jets in the event was required to be greater than 20 GeV. The latter cut was also imposed for the selection of trijet events.

The jet measurement corresponded to unpolarised lepton beams, whereas the data were neither corrected for Z^0 exchange nor for γ/Z^0 interference. Therefore, the theoretical predictions have to account for the different electron and positron cross sections especially in the higher Q^2 regime[1]. The data sample corresponded to an integrated luminosity of 203 pb^{-1} for the electron data and 171 pb^{-1} for the positron data.

In order to perform a comprehensive study of the pQCD predictions, differential dijet cross sections were measured as functions of several kinematic and jet quantities,

[1] All corrections are described in following chapters. Only for completeness these details are given here, because these details are part of the definition of the presented jet measurement.

$$Q^2, \qquad x_{\mathrm{Bj}}, \qquad \eta^*, \qquad M_{jj}, \qquad \overline{E^{\mathrm{jet}}_{T,\mathrm{B}}}, \qquad \log_{10}(\xi).$$

These quantities are defined in the sections 2.1.1 and 2.2.2.2. The quantity η^* is sensitive to the angular dependent part of the hard matrix element; its measurement allows therefore a detailed test of this part of the matrix element. The centre-of-mass energy of the dijet system can be studied by measuring M_{jj}. The variables Q^2 and $\overline{E^{\mathrm{jet}}_{T,\mathrm{B}}}$ can be utilised to investigate the scale dependence of the cross sections. It was studied whether the quality of the data description by the NLO calculations changes with decreasing scale. Therefore, the dijet cross sections as a function of $\overline{E^{\mathrm{jet}}_{T,\mathrm{B}}}$ were also measured in different regions of Q^2. Since in leading order the variable ξ is related to the momentum fraction carried by the struck quark, its sensitivity to the PDFs can be used to investigate the contributions from gluon-induced events. Due to this sensitivity, the differential dijet cross section as function of $\log_{10}(\xi)$ was also measured in different regions of Q^2 in order to test the scale dependence of the PDFs.

The inclusive trijet cross sections were measured differentially in the variables

$$Q^2, \qquad x_{\mathrm{Bj}}, \qquad \overline{E^{\mathrm{jet}}_{T,\mathrm{B}}}.$$

The trijet cross sections as a function of $\overline{E^{\mathrm{jet}}_{T,\mathrm{B}}}$ were also studied in various regions of Q^2 in order to investigate the scale dependence of trijet production.

The cross section ratio, $R_{3/2}$, between the cross sections for trijet and dijet production was determined double-differentially as a function of $\overline{E^{\mathrm{jet}}_{T,\mathrm{B}}}$ in regions of Q^2. In previous analyses at ZEUS [11], the quantity $R_{3/2}$ was measured in a much wider Q^2 range including the region with low Q^2. In contrast, in this analysis the measurement was restricted to the high Q^2 region. In the cross-section ratio, the luminosity uncertainty of the measurement cancels and other correlated systematic uncertainties like the jet energy scale uncertainty are reduced. Furthermore, by measuring $R_{3/2}$, the experimental systematic uncertainties can be reduced, while preserving at least partially the stronger dependence of the trijet production on α_s. Even in the theoretical predictions uncertainties e.g. related to the PDFs can be slightly reduced. The double-differential cross-section ratio, $R_{3/2}$, was therefore used for an extraction of the strong coupling, α_s.

5. Event Reconstruction and Selection

In this chapter, the investigated data sample is specified and the electron identification and the reconstruction of the hadronic final state is described. Since a precise reconstruction of the kinematic variables was crucial for this analysis, various different reconstruction methods that make use of different measured quantities were considered, their resolution was investigated and the outcome is discussed in section 5.4.4. In this chapter also the employed cuts for the selection of the inclusive DIS event sample and for the inclusive dijet and trijet samples are introduced[1].

5.1. The Data Sample

The data for this analysis were taken with the ZEUS detector at HERA during the years 1998–2000 and 2004–2007. The data sample corresponded to an integrated luminosity of 374 pb^{-1}. During the data taking electrons/positrons with energies of 27.5 GeV were collided with protons, which had energies of 920 GeV. Thus, a centre-of-mass energy of $\sqrt{s} \approx 318$ GeV was achieved. Starting from the year 2004, HERA provided longitudinally polarised lepton beams.

The data were divided into parts ("runs") with stable data-taking conditions.

Period	Luminosity	Polarisation
1998–2000 e^-	16.7 pb^{-1}	0
1998–2000 e^+	65.1 pb^{-1}	0
2004–2005 e^-	134.2 pb^{-1}	-0.07
2006 e^-	52.1 pb^{-1}	$+0.09$
2006–2007 e^+	105.5 pb^{-1}	-0.07

Table 5.1: The data samples used in this analysis and the corresponding luminosities and average polarisations.

In table 5.1 for each data-taking period the corresponding luminosity and the average polarisation are given. The total net polarisation of the data used in this analysis was -0.03. The differential integrated luminosity, dL/dP, as a function of the polarisation, P, for the data taken during the years 2004–2007 is shown in figure 5.1.

5.2. Reconstruction of the Hadronic Final State

The measured hadronic final state contained charged and neutral particles. The energies of both types of particles were measured in the calorimeter, whereas for the charge particles in addition tracks in the tracking detectors could be reconstructed. In general, the momentum resolution for a charged particle with a relatively low transverse momentum determined with the tracking detectors was typically better than the momentum

[1] In the previous chapter 4.3, the investigated jet observables were defined.

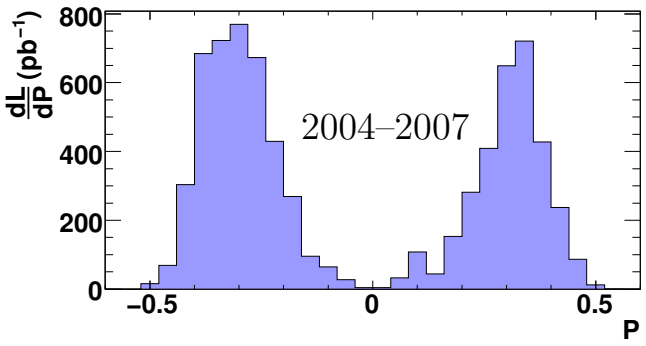

Figure 5.1: The differential integrated luminosity, dL/dP, as a function of the polarisation, P, for the data taken during the years 2004–2007.

determined from the calorimeter. Therefore, at ZEUS a dedicated algorithm was developed that combines all the available information such that the optimal resolution is obtained. These so-called "energy-flow objects" (EFOs) [164, 165] were used in previous jet analyses based e.g. on data from the years 1998–2000 [16]. However, it turned out that starting from the year 2004 this algorithm has introduced a systematic effect in jet analyses [166] coming from a mismatch of calorimeter energy deposits and tracks in the intersection regions between the BCAL and FCAL or RCAL; the "super-crack" regions. Therefore, these "energy-flow objects" were not used in the jet analysis presented here.

In this analysis, the objects of the hadronic final state were reconstructed by using two different methods:

- **Calorimeter Cells:** The smallest calorimeter units are the so-called "cells" (see chapter 3). After removing those cells associated with the scattered electron candidate[2], minimum cell energy thresholds of $E_{\mathrm{EMC-cell}} > 0.05$ GeV and $E_{\mathrm{HAC-cell}} > 0.1$ GeV were required depending on whether the cell was part of the electro-magnetic (EMC) or the hadronic (HAC) section of the calorimeter. These requirements were introduced in order to suppress calorimeter noise. Each cell was read-out by two photo-multiplier tubes, one on either side of the cell. Cells with energies greater than 1.5 GeV were removed from the analysis if the energy difference between the two photo-multiplier tubes exceeded more than 90% of the total cell energy. This cut suppressed signals due to high-voltage discharges.

- **Calorimeter Energy Deposits:** Energy deposits [167] ("islands") in the calorimeter were merged together from nearest neighbouring cells after imposing the cuts on the cells described above. These islands were corrected for energy loss in inactive material in front of the calorimeter, for back-splash effects in the calorimeter and for energy loss in the super-crack regions. The positions of the islands were determined by calculating the energy-weighted sum of the individual cell positions. Those islands identified as the scattered electron (see next section 5.3 for more details) were excluded from the reconstruction of the hadronic final state.

[2]The electron identification is described in the following section 5.3.

While for the reconstruction of jets the cell information was adopted for the input to the jet cluster algorithm, the kinematic quantities (see next section 5.4) were in general reconstructed from the variables provided by the island algorithm described above, which gave typically a much better correlation between the reconstructed and the "true" variables for inclusive event variables.

5.3. Electron Identification

The identification of a scattered electron in the measured final state of the detector is a crucial part in many *ep* scattering analyses. In neutral-current deep-inelastic scattering processes the presence of a scattered electron distinguishes the event from charged-current or photoproduction events.

The electron-identification algorithm primary utilised in this analysis was the SINISTRA algorithm[168]. In the SINISTRA algorithm, a neural network approach is implemented which is based on the different properties of hadronic and electromagnetic showers in the calorimeter. The algorithm discriminates between electrons and strongly interacting particles by analysing the lateral and longitudinal energy distribution of energy deposits in the calorimeter. The determined energy of the scattered electron is obtained by adding up all the energies of the associated calorimeter cells. Afterwards, this energy is corrected for energy loss in inactive material between the nominal interaction region and the calorimeter and for non-uniformities in the calorimeter response. A probability p, which is equal to 0 for hadronic and equal to 1 for electromagnetic showers, is assigned to each cluster.

In order to estimate the systematic effect (see chapter 8) introduced by the electron-identification algorithm, a second algorithm was used – the EM algorithm [169, 170]. This algorithm is combining the information from the calorimeter energy deposits with tracking information statistically in order to determine a total probability for each electron candidate.

In this analysis, always the electron candidate with the highest probability was used and assumed to be the scattered DIS electron.

5.4. Kinematic Reconstruction

The kinematics of events in *ep* scattering can be completely reconstructed by measuring the characteristics of the final state in the detector. In deep-inelastic scattering several measured event quantities like the azimuthal, ϕ_{el}, and polar angle, θ_{el}, or the energy, E'_{el} of the scattered electron or the transverse or longitudinal momentum of the hadronic finale state are available and can be exploited. Owing to this over-determination, the event reconstruction can be optimised by considering only those quantities that lead to estimators of the kinematic variables with the best achievable experimental precision. Since the reconstruction methods make use of different properties of the measurement, the resolution and the bias of kinematic quantities strongly depends on the investigated phase-space region. The sensitivity to initial or final-state QED radiation differs for the various reconstruction methods.

The relation between the kinematic variables is given by

$$Q^2 = x_{\mathrm{Bj}} \cdot y \cdot s, \tag{5.1}$$

where Q^2 represents the virtuality of the exchanged boson, x_{Bj} the Bjorken scaling variable, y the inelasticity of the scattering processes and $\sqrt{s}$ the electron-proton centre-of-mass energy. If initial state QED radiation is neglected, then the variable s is fixed and related to the well-known beam energies. Thus, the number of free parameters reduces to two.

In the following, three different reconstruction methods used in this analysis for the determination of the event kinematics are described.

5.4.1. Electron Method

The electron method ("el") [171] makes use of the measured polar angle and the measured calorimeter energy of the scattered electron. The kinematic variables are given according to

$$Q^2_{\mathrm{el}} = 2 \cdot E_{el} \cdot E'_{el} \left(1 + \cos\theta_{\mathrm{el}}\right), \quad \text{and} \quad \mathrm{y_{el}} = 1 - \frac{\mathrm{E'_{el}}}{2\mathrm{E_{el}}} \left(1 - \cos\theta_{\mathrm{el}}\right), \tag{5.2}$$

where E_{el} (E'_{el}) corresponds to the initial-state (final-state) energy of the electron and θ_{el} to the polar angle of the scattered electron. The quantity $x^{\mathrm{el}}_{\mathrm{Bj}}$ can be reconstructed by the application of equation 5.1.

The electron method is less affected by final-state QED radiation of the scattered electron, because usually these photons are emitted approximately parallel or with a small angle with respect to the electron and are clustered to the same electromagnetic island. However, initial state radiation changes the effective energy E_{el} in the interaction with the proton and, thus, leads to a systematic shift of the reconstructed quantities.

The relative resolutions can be obtained from

$$\frac{dx^{\mathrm{el}}_{\mathrm{Bj}}}{x^{\mathrm{el}}_{\mathrm{Bj}}} = \frac{1}{y_{\mathrm{el}}} \frac{dE'_{\mathrm{el}}}{E'_{\mathrm{el}}} + \tan\left(\frac{\theta_{\mathrm{el}}}{2}\left[x^{\mathrm{el}}_{\mathrm{Bj}} \frac{E_p}{E_{el}} - 1\right]\right) d\theta_{\mathrm{el}}, \tag{5.3}$$

$$\frac{dQ^2_{\mathrm{el}}}{Q^2_{\mathrm{el}}} = \frac{dE'_{\mathrm{el}}}{E'_{\mathrm{el}}} - \tan\left(\frac{\theta_{\mathrm{el}}}{2}\right) d\theta_{\mathrm{el}}, \tag{5.4}$$

according to [172], where E_p is the proton beam energy. The resolution diverges like $1/y_{\mathrm{el}}$ for $y_{\mathrm{el}} \to 0$.

5.4.2. Jacquet-Blondel Method

The kinematic variables can be reconstructed independently of the scattered electron by exclusively making use of the measured quantities of the hadronic final state. This so-called Jacquet-Blondel method [173] ("jb") was developed for the kinematic reconstruction of charged-current events in which a scattered electron in the final

state cannot be detected[3]. The Jacquet-Blondel method is the only viable method for the reconstruction of the kinematics in these events.

The particles of the hadronic final state that are scattered close to the beam pipe, that are fragments of the proton remnant or that have only a limited transverse energy are measured less reliably or are even undetectable. Therefore, the Jacquet-Blondel method utilises only the transverse momentum, p_T^{had}, and the longitudinal momentum balance , $(E - p_z)_{\text{had}}$, of the hadronic final state. In contrast to the electron method, the Jacquet-Blondel method is, therefore, insensitive to initial-state QED radiation from the electron.

The kinematic variables are obtained with the momenta in x and y direction, p_x and p_y, according to

$$y_{\text{jb}} = \frac{\sum_i (E_i - p_{z,i})}{2E_{el}}, \tag{5.5}$$

$$Q^2_{\text{jb}} = \frac{\left(\sum_i p_{x,i}\right)^2 + \left(\sum_i p_{y,i}\right)^2}{1 - y_{\text{jb}}}, \tag{5.6}$$

with the hadronic transverse momentum

$$p_T^{\text{had}} = \sqrt{\left(\sum_i p_{x,i}\right)^2 + \left(\sum_i p_{y,i}\right)^2}. \tag{5.7}$$

The sums in these equations run over all measured final-state objects excluding the electron. The inefficient reconstructions of particles scattered into the proton direction typically have only a small influence on the reconstruction obtained with this method because of the low transverse momenta.

5.4.3. Double-Angle Method

The double-angle method [171] ("DA") exploits the fact that angles are measured typically with a very high precision. The angles are in first order independent from the absolute energy calibration of the calorimeter. The angle measurements are in general much more precise than absolute energy measurements.

The DA method utilises the polar angle of the scattered electron and the angle γ_{had}, which corresponds in the leading-order quark-parton model to the scattering angle of the parton. This leads to the equation

$$\cos\gamma_{had} = \frac{p^2_{T,\text{had}} - \left(\sum_i (E_i - p_{z,i})\right)^2}{p^2_{T,\text{had}} + \left(\sum_i (E_i - p_{z,i})\right)^2}. \tag{5.8}$$

The kinematic variables are estimated according to

$$Q^2_{\text{DA}} = 4E^2_{el} \cdot \frac{\sin\gamma_{\text{had}}(1 + \cos\theta_{\text{el}})}{\sin\gamma_{\text{had}} + \sin\theta_{\text{el}} - \sin(\theta_{\text{el}} + \gamma_{\text{had}})}, \tag{5.9}$$

$$x_{\text{DA}} = \frac{E_{el}}{E_p} \cdot \frac{\sin\gamma_{\text{had}} + \sin\theta_{\text{el}} + \sin(\theta_{\text{el}} + \gamma_{\text{had}})}{\sin\gamma_{\text{had}} + \sin\theta_{\text{el}} - \sin(\theta_{\text{el}} + \gamma_{\text{had}})}. \tag{5.10}$$

[3]The neutrino escapes the detector undetected.

With the aid of these equations the energy, E'_{DA}, of the scattered electron can be reconstructed as

$$E'_{\mathrm{DA}} = \frac{2 \cdot E_{el} \sin \gamma_{\mathrm{had}}}{\sin \gamma + \sin \theta_{\mathrm{el}} - \sin(\gamma_{\mathrm{had}} + \theta_{\mathrm{el}})}. \tag{5.11}$$

5.4.4. Resolutions of the Reconstruction Methods

The reconstruction methods for the kinematic variables exhibit different resolutions, because the various measured quantities used in the reconstruction have different experimental properties. The resolution was investigated with the help of LEPTO, which allowed to directly compare reconstructed quantities with the generated ("true") variables. The inclusive DIS event selection cuts described in the following section 5.5.1 were applied to the data and to the MC sample.

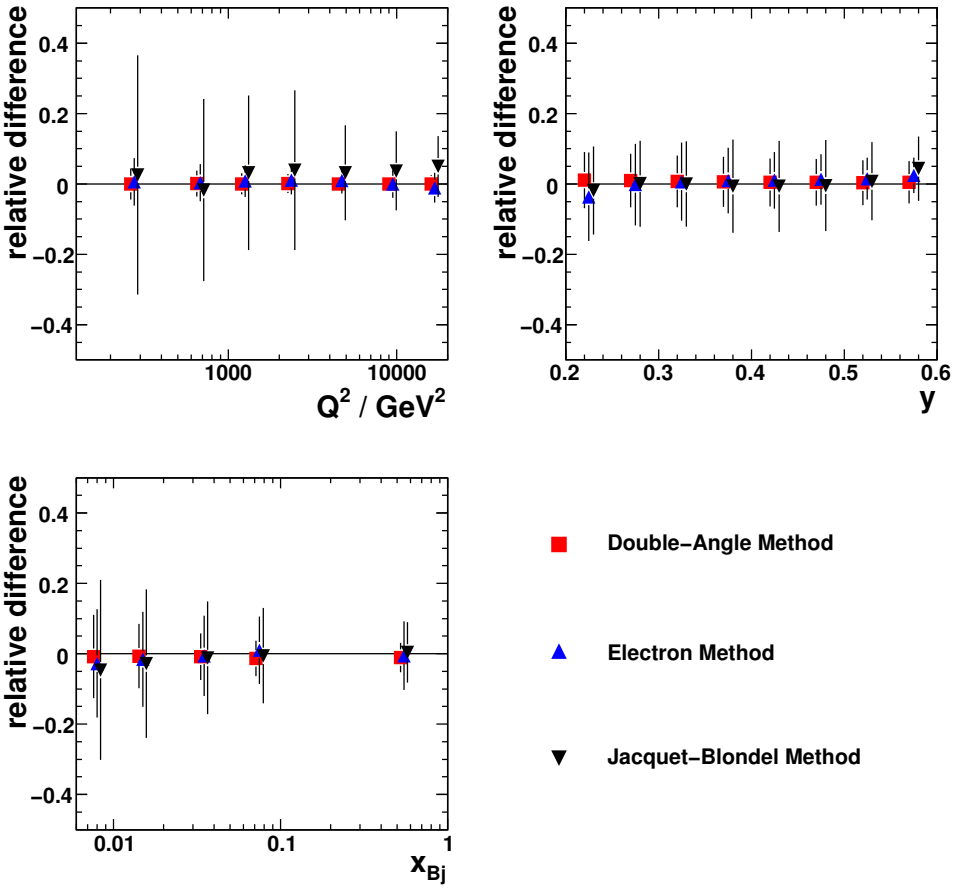

Figure 5.2: The estimated relative resolution for the reconstruction methods for the variables Q^2, y and x_{Bj}. The bars indicate one standard deviation of a fitted Gaussian function to the distributions in each Q^2, y and x_{Bj} interval. For a better visibility the shown points are displaced in x direction.

The outcome of this study is depicted in figure 5.2, where for the variables Q^2, y and x_{Bj} the relative difference between reconstructed and generated values is shown

as a function of the corresponding generated quantity. The ordinates of the displayed points represent the positions of the maxima of the distributions, which were fitted with Gaussian functions. The bars show the standard deviation extracted from the fitting procedure.

The double-angle method has provided the best resolution and the smallest bias over the full investigated phase-space region for the variables Q^2, y and x_{Bj}. Therefore, the double-angle method was used for the phase-space cuts and for the Lorentz transformation from the laboratory to the Breit frame (see chapters 2.2.2.1 and 4.3).

5.5. Event Selection

In this analysis, dijet and trijet production in neutral-current deep-inelastic scattering in the region of large virtualities, Q^2, was investigated. These events are characterised by the exchange of a photon or Z^0 boson and identified by a scattered electron in the final state.

In the lower Q^2 region, the electron was scattered into the RCAL . With virtualities of $Q^2 > 500$ GeV^2 the scattered electron was mostly reconstructed in the BCAL, while electrons were scattered into the FCAL typically only for highest Q^2 values. Since the electron as well as the hadronic final state in NC DIS processes can be measured, the total measured transverse momentum should vanish due to momentum conservation. Hence, this quantity was used among others for the selection of NC DIS events and it was used to discriminate neutral- from charged-current events in which the scattered neutrino in the final state has escaped the detector undetected.

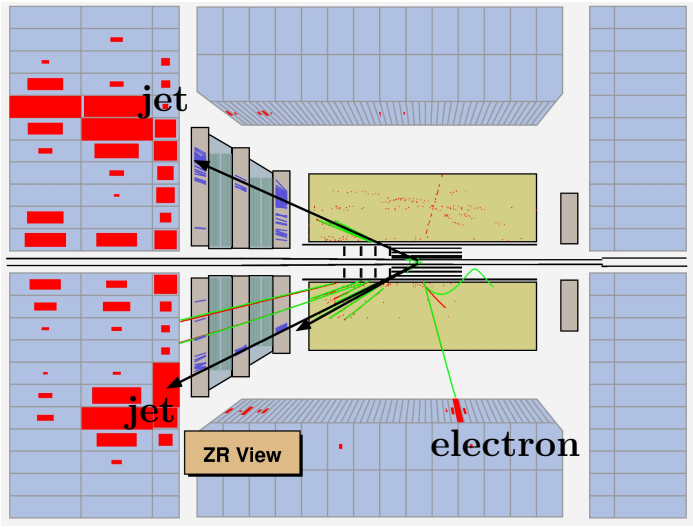

Figure 5.3: Neutral-current deep-inelastic scattering event display shown in the ZR-view.

Figure 5.3 shows the ZEUS event display [174] of a NC DIS process in the ZEUS detector. The displayed lines indicate reconstructed tracks and the clusters depict energy deposits in the calorimeter. Additionally, the jets are indicated as arrows. In the forward region of the detector, the proton remnant can be seen around the beam pipe. The scattered electron can be found in the BCAL with an associated track pointing to the energy deposit in the calorimeter.

The selection strategy applied in this analysis was based on an inclusive NC DIS event selection. Afterwards, out of these selected events those events with at least two or three hard jets were selected. All the described selection criteria were applied to the data as well as to the MC simulations LEPTO and ARIADNE on detector level[4]. Only those cuts related to the definition of the phase space of the measurement were applied to the MC hadron and parton levels.

5.5.1. Inclusive DIS Event Selection

The following cuts have defined the kinematic phase space of the measurement:

- In this analysis events with large Q^2 values were selected and analysed. Therefore, a cut[5] on the virtuality as reconstructed with the double-angle method was applied:
$$125 < Q^2_{\mathrm{DA}} < 20000 \text{ GeV}^2. \tag{5.12}$$
- In addition a cut on the inelasticity, y, of the scattering processes was applied:
$$0.2 < y_{\mathrm{DA}} < 0.6. \tag{5.13}$$
The upper cut was introduced to restrict the measurement to a region with a good detector acceptance, as shown in figure 5.4c after an inclusive dijet selection, and the lower cut was implemented in order to exclude a region of the jet phase space with large hadronisation corrections (figure 5.4d).

In order to increase the purity of the selected data sample, a couple of additional requirements were imposed in addition to the two phase-space cuts described above:

- **Data Quality:** The status of all detector components was recorded for every run separately. The so-called "EVTAKE" algorithm has decided offline whether a run could be used for physics analyses. In this analysis, only runs with "EVTAKE" equal to 1 were considered.

  Starting from the year 2004, HERA provided longitudinally polarised lepton beams. Since two different detectors have measured the polarisation, it was decided on a run-by-run basis which of these detectors was used depending on which one was active longest. The status flags "LPOLTAKE" and "TPOLTAKE" describe the availability of the corresponding polarisation detectors. On a run-by-run basis one of them was required to be in a good condition depending on the choice for that particular run.

- **Trigger:** The trigger system at ZEUS was structured into three different levels (chapter 3) in order to achieve an efficient data taking with only a small amount of background events. At each of these levels a chain of trigger bits was used for the event selection. It was required at each level that at least one of the bits from the employed chain was set[6]. Additionally, the DST bit 12 was required,

[4]More details on the MC simulations are given in chapter 4.
[5]The motivation for the measurement in these phase-space regions is given in chapter 4.3.
[6]This corresponds to a logical OR.

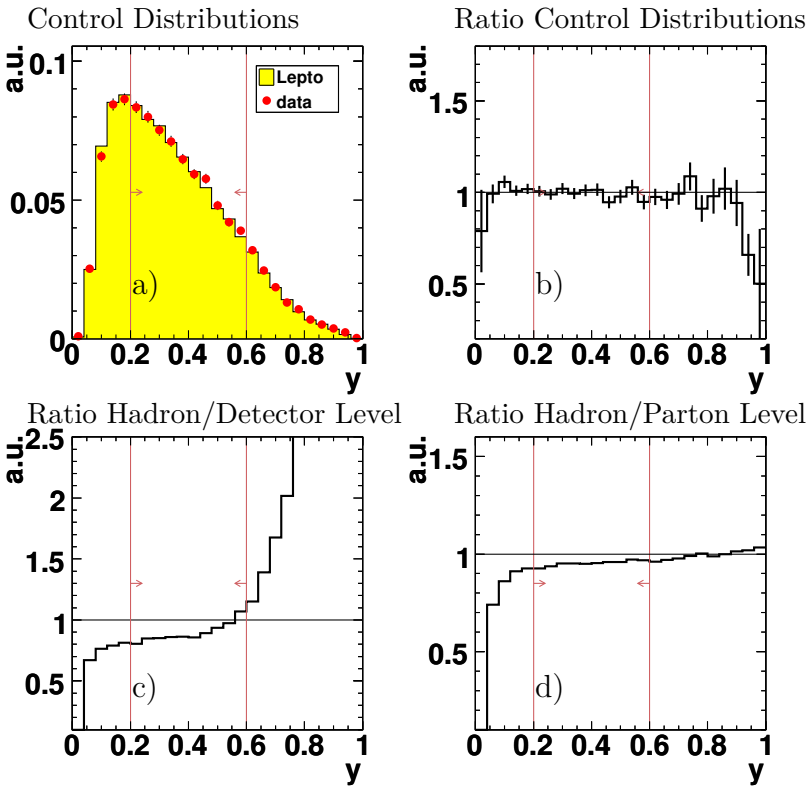

Figure 5.4: Several plots determined after an inclusive dijet selection: a) Normalised control distributions as a function of y for data and LEPTO. b) The ratio of these normalised control distributions. c) The ratio between hadron- and detector-level distributions (in arbitrary units). d) The ratio between hadron- and parton-level distributions.

which was suited for high-Q^2 NC DIS analyses. This bit required that the inelasticity was $y_{\mathrm{el}} > 0.95$, that the virtuality was $Q^2_{\mathrm{DA}} > 80$ GeV^2 and that an electron candidate in the final state with an energy $E'_{\mathrm{el}} > 5$ GeV was found.

FLT Bit Number	1998–2000
43	$E_T^{\mathrm{CAL}} > 11.5$ GeV and good track
44	($E_{\mathrm{EMC}}^{\mathrm{BCAL}} > 5$ GeV and good track) or $E_{\mathrm{EMC}}^{\mathrm{RCAL}} > 3.5$ GeV
FLT Bit Number	**2004–2007**
40	$E_{\mathrm{EMC}}^{\mathrm{CAL}} > 20$ GeV
43	$E_T^{\mathrm{CAL}} > 20$ GeV and good track
50	($E_{\mathrm{CAL}} > 15$ GeV or $E_{\mathrm{EMC}}^{\mathrm{CAL}} > 10$ GeV or $E_{\mathrm{EMC}}^{\mathrm{BCAL}} > 3.5$ GeV or $E_{\mathrm{EMC}}^{\mathrm{RCAL}} > 2$ GeV) and $E_T^{\mathrm{CAL}} > 1$ GeV and good track

Table 5.2: Some of the requirements of the adopted first-level trigger bits.

At the FLT only coarse tracking and calorimeter information were available. Therefore, events were selected based on the energy and transverse energy as measured with the calorimeter. Starting from the year 2004, additional tracking information for the trigger veto were used in order to adapt the trigger rate to the higher instantaneous luminosity. A more detailed discussion of the tracking-veto

requirements can be found in chapter 6.4. In table 5.2 a short summary of the main requirements of the FLT bits used in this analysis is presented.

At the SLT the background was further reduced by the application of cuts on the calorimeter-based timing and on energy measurements. Compared to the arrival time of particles coming from the interaction region of the *ep* scattering, background events typically had a different time signature. The timing measurements of the RCAL and BCAL could be used to suppress beam-related background events. Cosmic-ray events, for instance, were rejected by applying cuts on the time difference between the upper and bottom part of the BCAL. Moreover, the ZEUS GLOBAL TRACKING TRIGGER [126] reconstructed tracks online by combining information extracted from the CTD and from the MVD in order to reconstruct the vertex position and to reject background events.

At the TLT the trigger bit DIS03 was required, which is together with DST bit 12 a high-Q^2 trigger based on the identification of the scattered electron candidate using localised energy deposits in the calorimeter. Compared to the SLT, the TLT made use of more sophisticated electron-identification algorithms which are more closely related to those used in offline analyses. Additionally, loose cuts on the energy of the scattered electron, $E'_{el} > 4$ GeV, the longitudinal momentum balance, $30 < E - p_z < 100$ GeV, and on the transverse distance between the electron cluster and the centre of the beam pipe, $R_{\mathrm{el}}^{\mathrm{RCAL}} > 35$ cm, were applied.

- **Vertex Position:** The interaction region between the electrons and protons in the detector had a finite length due to the length of the electron and proton bunches. Interactions that were initiated, for instance, by collision of particles from the beams with beam gas were typically distributed evenly in z. Hence, a cut on the vertex position could be used to increase the amount of events consistent with the hypothesis of being *ep* interactions. The events were selected if the vertex position, z_{vtx}, along the beam axis was in the range of plus and minus three times half of the width of the z_{vtx} distribution with respect to the nominal vertex position and if $\chi^2 < 10$ was fulfilled. In order to determine this range, the distribution was approximated with a Gaussian. Since the nominal vertex position and the width of the distributions have varied between the different data-taking periods, the cut values were adapted to account for this effect. The imposed cut values are given in table 5.3.

Table 5.3: The applied cuts on the z_{vtx} position.

Period	
1998–2000 $e^{\pm}$	$-34 < z_{\mathrm{vtx}} < 34$ cm
2004–2005 e^{-}	$-32 < z_{\mathrm{vtx}} < 30$ cm
2006–2007 e^{+}	$-29 < z_{\mathrm{vtx}} < 27$ cm

- **Electron Reconstruction:** Several cuts were applied in order to select a well-reconstructed electron. These cuts helped to increase the purity of the data sample and to reduce the amount of background events. The SINISTRA algorithm was used for the electron identification.

- **Probability:** It was required that the probability for the electron candidate determined by the SINISTRA algorithm was greater than 90%. Out of the list of electron candidates the candidate with the highest probability was considered.
- **Electron Energy:** The energy of the scattered electron was required to be greater than 10 GeV. This cut helped to suppress events originating from photoproduction in which a wrongly identified electron mainly due to the decay of neutral pions into photons was reconstructed. In addition, the cut restricted the measurement to a region in which the electron-finding efficiency was high and reasonably well understood.
- **Isolation:** The total energy not associated with the electron candidate within a cone of radius 0.7 units in the pseudorapidity-azimuth plane around the electron direction was determined. It was required that the fraction of this energy with respect to the total energy in that particular cone was smaller than 10%. Events in which jets were falsely identified as final-state electrons were suppressed with this requirement.
- **Matching Track:** For events in which the electron candidate was reconstructed within the acceptance[7] of the tracking detectors, a matching track was required by determining the distance of closest approach between the track extrapolated to the CAL surface and the energy-cluster position. This distance was required to be smaller than 10 cm. Additionally, the track momentum had to exceed 3 GeV. Since the angular resolution of the tracking detectors was in general better than the angular resolution of the calorimeter, for events in which the electron was found inside the CTD acceptance the angles θ_{el} and ϕ_{el} and the coordinates were reconstructed from the associated track.

- **Geometry Cuts:** Several geometrical cuts on the reconstructed position of the electron in the calorimeter were imposed. Owing to these cuts, regions were removed in which the MC simulations do not describe the data sufficiently well.
  - **RCAL Chimney:** A cryogenic support pipe was located behind the upper half of the RCAL. Thus, in this region of the calorimeter detector material had to be removed. In order to avoid problems with the simulation of this region, events were removed in which the electron position in x and y direction in the RCAL was $|x_{\mathrm{electron}}| < 10$ cm and $y_{\mathrm{electron}} > 80$ cm.
  - **Super Crack:** Events in which the electrons were scattered close to the intersection region between the BCAL and RCAL or FCAL were rejected. In this region it could happen that the electron entered the BCAL without being fully absorbed; it could have leaked into the outer parts of the RCAL or FCAL. In general, the MC simulations had problems to simulate this leakage adequately. Thus, events with

[7] The acceptance of the tracking detectors was given by $0.3 < \theta_{\mathrm{el}} < 2.85$, where θ_{el} is the polar angle of the scattered electron candidate.

$$-104 \text{ cm} < z_{\text{electron}} < -98.5 \text{ cm} \quad \text{and} \quad 164 \text{ cm} < z_{\text{electron}} < 174 \text{ cm}$$

were removed from the data sample, where z_{electron} denotes the longitudinal position of the scattered electron.

– **RCAL Radius:** Events in which the electron was scattered very close to the rear beam pipe were rejected by requiring that the transverse distance between the centre of the beam pipe and the scattered electron was larger than $R_{\text{el}}^{\text{RCAL}} > 36$ cm. This condition suppressed events with a large fraction of undetected electron energy.

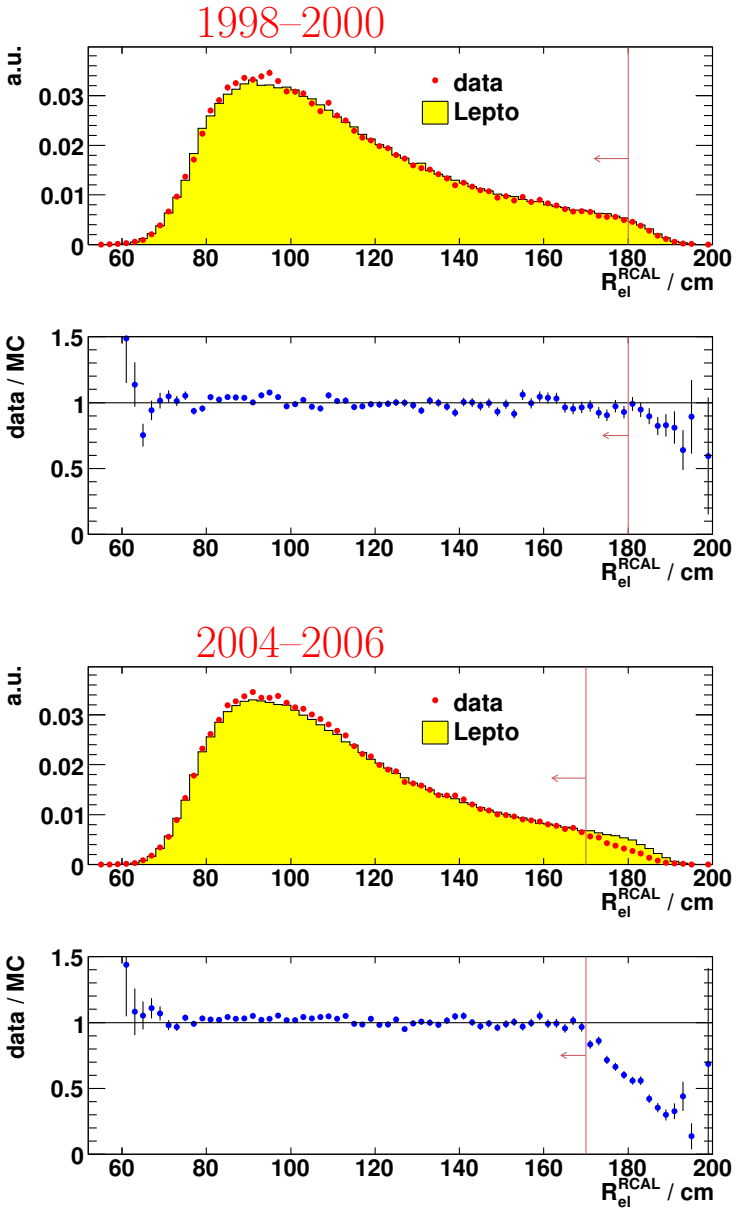

Figure 5.5: The distribution of the transverse distance, $R_{\text{el}}^{\text{RCAL}}$, between the electron candidate in the RCAL and the centre of the beam pipe and the ratio of the normalised distributions for data from the years 1998–2000.

Figure 5.6: The distribution of the transverse distance, $R_{\text{el}}^{\text{RCAL}}$, between the electron candidate in the RCAL and the centre of the beam pipe and the ratio of the normalised distributions for data from the years 2004–2006.

Additionally, the distribution of the quantity $R_{\text{el}}^{\text{RCAL}}$ was studied for all data-taking periods separately. The results of this investigation are depicted in figures 5.5 and 5.6, which show the distributions of $R_{\text{el}}^{\text{RCAL}}$ for data

and LEPTO as well as ratio histograms between the normalised distributions. In the outer region of the RCAL, the MCs tend to not simulate the behaviour of the data anymore. Starting from the year 2004, this observed discrepancy was found to be more pronounced. Therefore, for the data from the years 1998–2000 $R_{\mathrm{el}}^{\mathrm{RCAL}} < 180$ cm and for data from the years 2004–2007 $R_{\mathrm{el}}^{\mathrm{RCAL}} < 170$ cm was required.

- **Longitudinal Momentum Conservation:** A large fraction of the potential background events were induced by photoproduction events in which the electron escaped through the beam pipe undetected. These photoproduction events were suppressed by applying cuts on the longitudinal momentum balance,

$$E - p_z = (E_{\mathrm{el}} - p_{z,\mathrm{el}}) + (E_{\mathrm{had}} - p_{z,\mathrm{had}})\,, \tag{5.14}$$

of the electron ("el") and the hadronic system ("had") with the total energy E and the momentum p_z in z direction. With $E_{\mathrm{el}} = 27.5$ GeV and $p_{z,\mathrm{el}} = -27.5$ GeV for electrons and $E_{\mathrm{had}} = 920$ GeV and $p_{z,\mathrm{had}} = 920$ GeV for the protons in the initial state, the quantity $E - p_z$ has a nominal value of ≈ 55 GeV. Owing to momentum conservation, this quantity should be the same for the final state. Radiative effects and the finite resolution of the detector can change the value of this quantity, though. In contrast, however, the quantity $E - p_z$ is typically small for photoproduction events. Therefore it was required that

$$38 < \sum_i (E - p_z)_i < 65 \text{ GeV} \tag{5.15}$$

was fulfilled. The sum in this formula runs over all energy deposits in the detector. Additionally, this condition has suppressed events related to beam-gas interaction.

- **Transverse Momentum Balance:** In order to suppress events with energy deposits arising from cosmic-ray events and beam-related background, it was required that

$$\frac{p_T}{\sqrt{E_T}} < 2.5\ \sqrt{\mathrm{GeV}}, \tag{5.16}$$

where p_T represents the transverse momentum[8] and E_T is the total transverse energy in the calorimeter. This quantity is related to the resolution of the variable p_T, which is proportional to $1/\sqrt{E_T}$.

- **Inelasticity:** In photoproduction events, the decay of neutral pions into photons can result in a wrongly identified electron candidate. A cut on the inelasticity $y_{\mathrm{el}} < 0.95$ as reconstructed with the electron method helped to suppress these background events. The inelasticity was reconstructed with the electron method, because in the high-y region this method provides the best resolution (see section 5.4.1). The influence of this cut was marginal due to the definition of

[8] The quantity p_T is a measure of the missing transverse momentum if the detector covers the full solid angle.

the investigated phase-space region. However, it was applied to be consistent with the requirements of DST bit 12.

- **Elastic QED-Compton Scattering:** In elastic Compton scattering ($ep \to e\gamma p$) the proton does not dissociate in the interaction. These events are characterised by two electromagnetic clusters in the detector with balancing transverse momenta and a back-to-back configuration in the azimuthal plane. In contrast to inelastic QED Compton scattering which is reasonably well described by the MC simulations [175], the elastic scattering is not. Therefore, these events were rejected if besides the electron a second electron candidate with an azimuthal separation $\Delta\phi > 3$ from the first electron candidate was found, a ratio of transverse momenta of the two candidates between 0.8 and 1.2 was measured, and in addition the rest of the calorimeter energy, besides the two electromagnetic energy clusters, was below 3 GeV.

- **Validity of QED Corrections:** In the phase-space region at low x_{Bj} and very low y, the QED predictions from the MC simulations are not reliable due to a lack of higher orders in the calculation [133]. Therefore, this region was removed from the data sample by requiring $y_{\mathrm{jb}} \cdot \left(1 - x_{\mathrm{Bj}}^{\mathrm{DA}}\right)^2 > 0.004$.

- **FCAL Projection of the Hadronic Scattering Angle:** In previous analyses [176] it was found that the hadronic activity in the very forward direction of the detector is simulated poorly. Therefore, a cut on the polar angle, γ_{had}, of the hadronic system was made. It was required that the radius of the projection of γ_{had} in the FCAL was $R_{\gamma_{\mathrm{had}}}^{\mathrm{FCAL}} > 18$ cm for events with $\cos\gamma_{\mathrm{had}} > 0$. This cut had only a very weak influence due to the phase-space cut on the inelasticity, y, that suppressed events with large hadronic activity in the forward direction. However, this phase-space cut was omitted in the study of the jet energy scale discussed in chapter 6.3.1 and, thus, the cut on the FCAL projection of γ_{had} has improved the agreement between the data and the MC simulations.

- **Number of Tracks:** In order to improve the description of the data by the MC simulations a loose cut on the number of tracks was applied. Only those tracks were considered that had a transverse momentum of $p_T > 0.2$ GeV and that have passed at least three CTD superlayers. The appearance of at least one of these selected tracks was required.

5.5.2. Inclusive Jet Selection

After the application of the cuts described in the previous chapter the jet selection was performed. The jets were clustered using the k_T cluster algorithm in the longitudinally invariant inclusive mode based on calorimeter cells (see section 5.2) after excluding those associated with the scattered electron candidate. The jet reconstruction was performed in the Breit reference frame, and, afterwards, the four momenta of the jets were propagated back to the laboratory frame.

The following cuts were imposed in order to select a clean sample of jet events:

- **Distance between the Electron and the Jet:** The distance, ΔR, in the pseudorapidity-azimuth plane of the laboratory frame between every jet with $E_{T,\mathrm{B}}^{\mathrm{jet}} > 5$ GeV and the electron was determined according to

$$\Delta R^2 = \left(\eta_{\mathrm{LAB}}^{\mathrm{jet}} - \eta_{\mathrm{LAB}}^{\mathrm{el}}\right)^2 + \left(\phi_{\mathrm{LAB}}^{\mathrm{jet}} - \phi_{\mathrm{LAB}}^{\mathrm{el}}\right)^2 . \tag{5.17}$$

  The variables $\eta_{\mathrm{LAB}}^{\mathrm{jet}}$, $\phi_{\mathrm{LAB}}^{\mathrm{jet}}$ and $\eta_{\mathrm{LAB}}^{\mathrm{el}}$, $\phi_{\mathrm{LAB}}^{\mathrm{el}}$ represent the pseudorapidities and the azimuthal angles of the jet and the electron, respectively. Events were rejected if the quantity ΔR was smaller than 1 for any pair of jet and electron candidate in order to suppress events in which the electron was not well isolated. This condition helped to improve the purity of the sample and further reduced the amount of photoproduction background.

- **Backward Jets:** Radiative photons coming from the initial-state electron could wrongly be identified as jets. Therefore, events with jets in the backward region of the detector were rejected by requiring the absence of jets with $E_{T,\mathrm{B}}^{\mathrm{jet}} > 5$ GeV and $\eta_{\mathrm{LAB}}^{\mathrm{jet}} < -1$.

- **Low Transverse Energy:** Jets with $E_{T,\mathrm{lab}}^{\mathrm{jet}} < 3$ GeV were removed from the event because of their large jet energy scale uncertainty (see chapter 6.3.1 for further details).

The dijet and trijet samples were selected by imposing the following cuts that also defined the phase space of the jet measurement:

- **Pseudorapidity:** It was required that at least two (three) jets in the pseudorapidity region $-1 < \eta_{\mathrm{LAB}}^{\mathrm{jet}} < 2.5$ were found for the selection of the inclusive dijet (trijet) sample.

- **Transverse Energy:** Out of these jets the two (three) were selected with the highest transverse energies in the Breit frame. These jets were required to fulfil $E_{T,\mathrm{B}}^{\mathrm{jet}} > 8$ GeV.

- **Invariant Dijet Mass:** Additionally to the previous two phase-space cuts, it was required that the invariant dijet mass, M_{jj}, of the two jets with the highest transverse energies in the Breit frame had to be greater than 20 GeV. It should be noted that also for the selection of the trijet sample only the two jets with the highest transverse energies were used for the application of the invariant mass cut. Due to this condition it was ensured that the trijet sample was a subset of the dijet sample.

  This cut was introduced to make the NLO QCD predictions for dijet production insensitive to infrared cut-offs (see chapter 4.2.2). Even though this requirement was introduced, the NLO QCD calculations in the region $0.65 < \eta^* < 2$ showed a sensitivity to these cut-offs. Thus, a more detailed study of this behaviour is presented in chapter 8.2.

After the application of all the cuts described in this chapter[9], the final dijet (trijet) sample consisted of 31440 (2856) events.

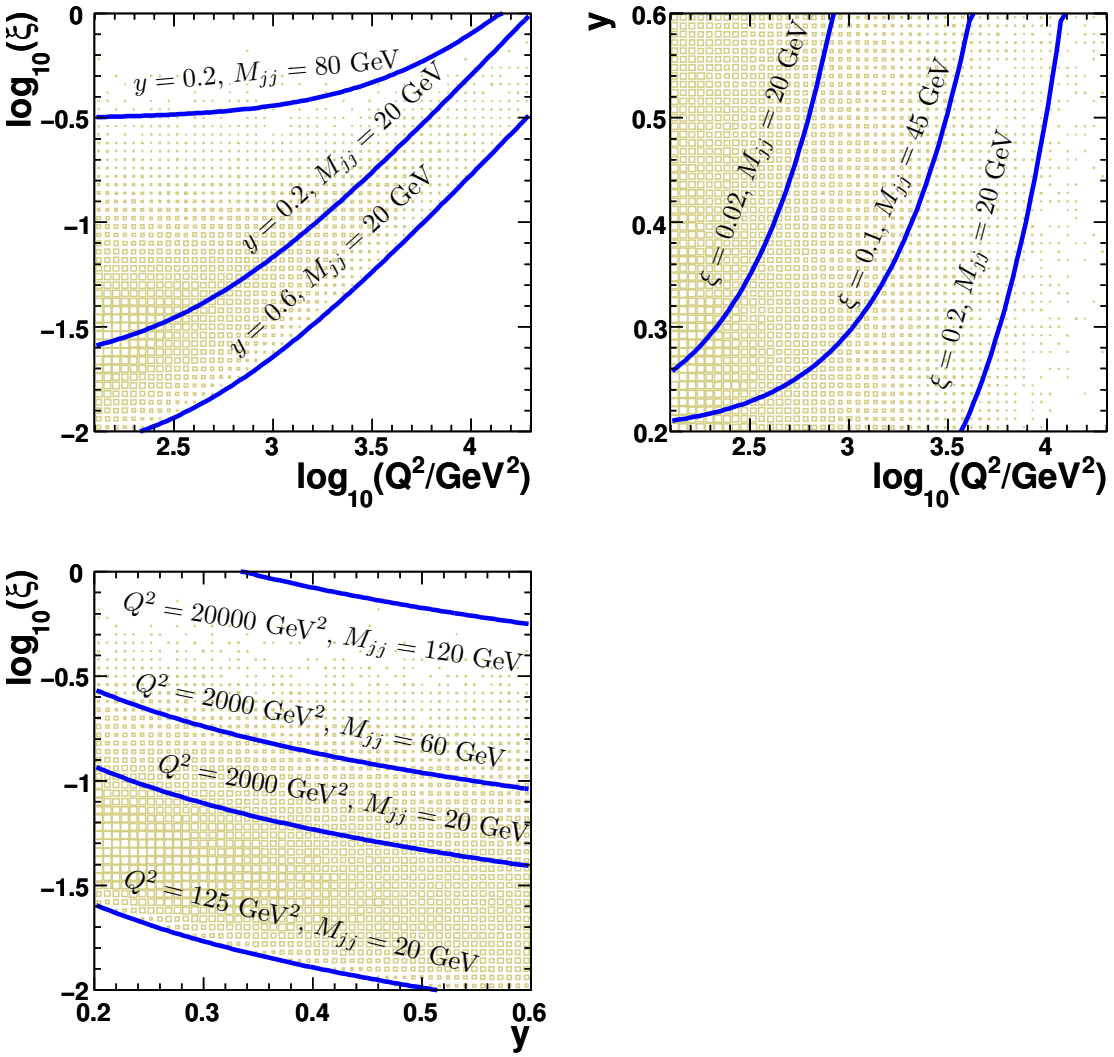

Figure 5.7: Correlation plots between the virtuality, Q^2, the inelasticity, y, and the momentum fraction carried by the struck parton, ξ, for inclusive dijet production as predicted by the LEPTO hadron level. The solid lines depict several kinematic configurations.

Figure 5.7 shows correlation plots between the virtuality, Q^2, the inelasticity, y, and the momentum fraction carried by the struck parton, ξ, for inclusive dijet production as predicted by the LEPTO hadron level. The indicated lines depict as examples several kinematic configurations for different values of the invariant dijet mass, M_{jj}.

The phase-space region with large values of ξ is mainly explored by dijet events with low y and large M_{jj}, while in the very low-ξ region the events typically have lower Q^2 and higher y values. Moreover, the invariant dijet mass and the transverse energy cuts in the Breit frame suppress events with low ξ with increasing values of Q^2.

[9]The agreement between the MC simulations and the data is demonstrated in chapter 7.1.

6. Data Corrections and Reweighting

In order to measure jet cross sections precisely several corrections had to be imposed: The average lepton polarisation differed from zero and, hence, the influence of the polarisation on the data had to be removed in order to be able to compare the NLO QCD calculations with the data. The programs utilised for these calculations usually provide only predictions for unpolarised lepton beams. The z_{vtx} distribution is an important quantity for the reconstruction of the kinematic variables as well as for the cross sections in terms of normalisation. Therefore, the z_{vtx} distribution in the MC was reweighted in order to improve the data description. These corrections are discussed in this chapter followed by a detailed discussion of the hadronic energy scale and of the correction that has accounted for inactive material in the detector. Finally, a study of the trigger efficiency and a Q^2 reweighting procedure is presented.

6.1. Polarisation Correction

The lepton beam in HERA was naturally transversely polarised. Starting from the year 2004, spin rotators on either side of the ZEUS detector changed the transverse polarisation of the beam into longitudinal polarisation. Since the inclusive neutral current DIS cross section depends on the lepton polarisation, P, and due to the fact that neither of the two NLO QCD calculations used in this thesis take this effect into account, the data were corrected for the polarisation effect. Since the employed MC simulations have assumed unpolarised lepton beams, a dedicated correction had to be derived from a different program. After this correction procedure, the data corresponded to unpolarised lepton beams.

The corrections were obtained by calculating the inclusive DIS cross section ratio, $\frac{\sigma_{\text{nopol}}}{\sigma_{\text{pol}}}$, as a function of Q^2 with the HECTOR program [177], where σ_{nopol} is the prediction for the unpolarised and σ_{pol} the prediction of the polarised cross section.

Figure 6.1 shows the quantity $\frac{\sigma_{\text{nopol}}}{\sigma_{\text{pol}}}$ as a function of Q^2 for the longitudinally polarised data samples (2004/2005 e^-, 2006 e^-, 2006/2007 e^+). The average polarisations are also given in the figure. The cross-section ratio increases with increasing Q^2 and amounts to approximately $\pm 2\%$ in the highest Q^2 region analysed. The average correction factors in the highest Q^2 region for the full combined data sample typically differ from unity by less than $+0.36\%$. In order to minimise binning effects, a cubic-spline interpolation was performed. The data-event weights were determined using this interpolation function.

The systematic uncertainty arising from the polarisation correction was estimated and is discussed in chapter 8.1. The systematic effect on the cross sections was found to be negligible.

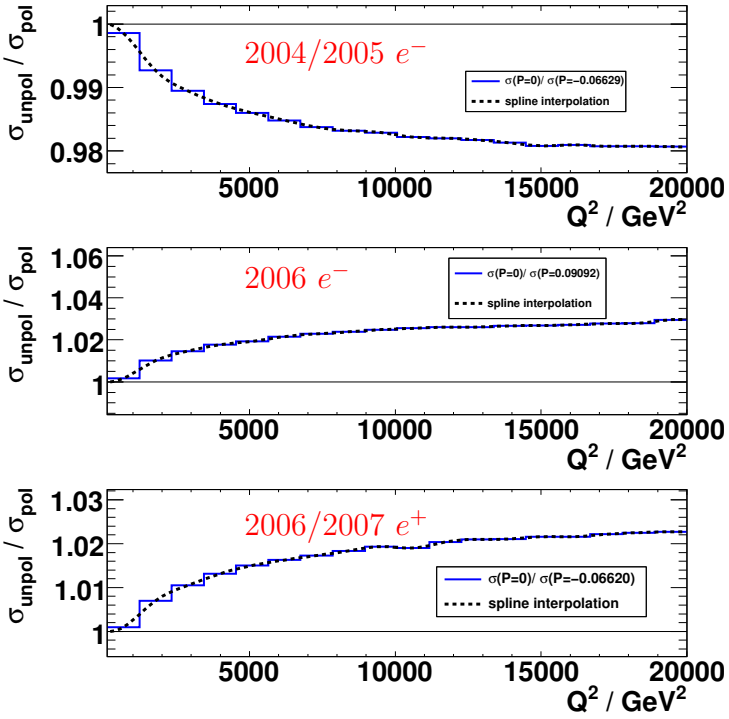

Figure 6.1: The inclusive DIS cross-section ratio, $\frac{\sigma_{\text{nopol}}}{\sigma_{\text{pol}}}$, for the unpolarised, σ_{pol}, and polarised (with average polarisation P), σ_{pol}, inclusive DIS cross-section predictions as a function of Q^2 determined with HECTOR.

6.2. Reweighting of the Longitudinal Vertex Distribution

Precise knowledge of the longitudinal vertex distribution, z_{vtx}, of the ep interaction is important because the z_{vtx} position affects the measurement of kinematic variables, the acceptance and the normalisation of the cross-section measurement. The latter effect is caused by the application of tight vertex cuts: these cuts lead to a reduced amount of considered data, while the luminosity system provides a luminosity measure for all ep interactions along the whole z axis range. Therefore, the MC simulations must describe the relative amount of events reconstructed outside the accepted z_{vtx} region in order to get an accurate cross-section normalisation.

The true z_{vtx} distribution is influenced by the beam optics, the HERA collider timing and the length of the proton and electron bunches, which is 8.5 cm for the proton and 0.83 cm for the electron bunches, respectively. The central part of the distribution is in a good approximation Gaussian and is mainly formed by the overlap of both bunches. Owing to the collision between neighbouring and nominal bunches, so-called *satellite peaks* are reconstructed near the central peak.

Only the z_{vtx} distributions of the 1998–2000 $e^{\pm}$ and 2004–2006 e^- data were found to be well described by the MC simulations including the satellite regions. Hence, a reweighting procedure was imposed for the 2006/2007 e^+ data sample:

- The inclusive DIS event selection presented in chapter 5 – omitting all jet and z_{vtx} cuts – was used. Instead of using the bits FLT 40, 43 or 50, however, the trigger selection was changed to the bit FLT 30, which required an isolated energy deposit in the RCAL. This adjustment was performed in order to obtain a data sample triggered independently from any tracking information.

- The z_{vtx} distribution in the range from -100 cm to $+100$ cm was determined for the data, which were corrected for acceptance effects (see section 7.2), and for the MC hadron level. The data and the MC distributions were normalised such that the integral was equal to unity.

- The sum of four Gauss functions,

$$g = \sum_{i=0}^{3} a_i \cdot e^{-\frac{1}{2} \cdot \frac{(z_{\text{vtx}} - b_i)^2}{\sigma_i^2}}, \tag{6.1}$$

was fitted to each distribution in order to obtain the parameters a_i, b_i and σ_i for the data and the MC simulation separately. The minimisation procedures converged with $\chi^2/\text{ndf} = 1.15$ for LEPTO and $\chi^2/\text{ndf} = 1.14$ for the data, which indicate that the fits were reasonably successful.

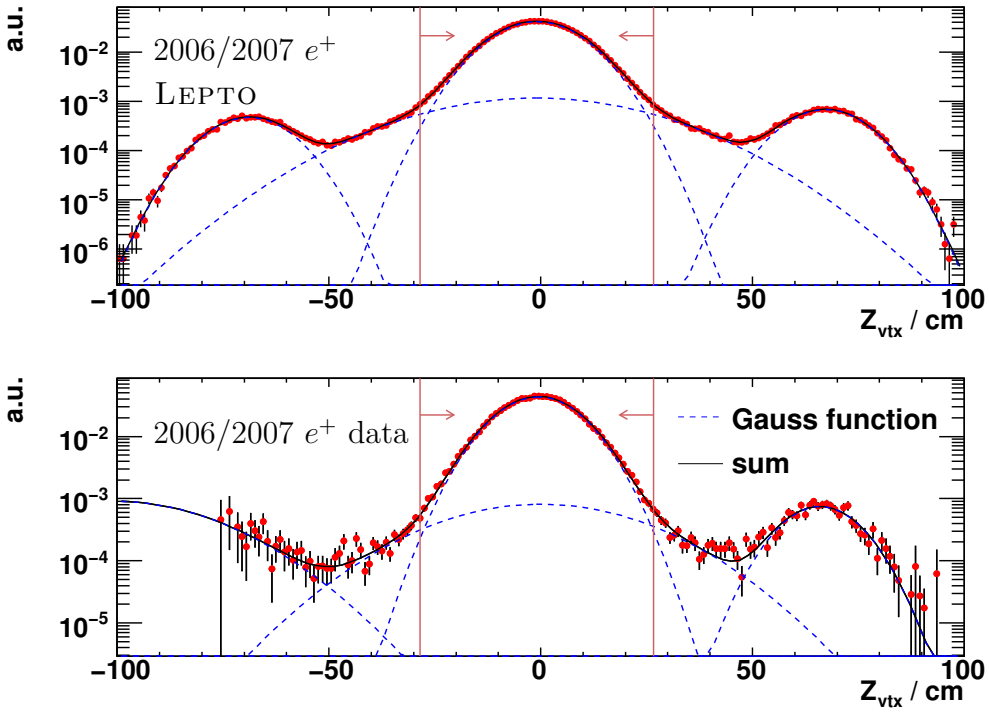

Figure 6.2: The z_{vtx} distribution for the 2006/2007 e^+ data and LEPTO MC simulation and the fit result of the sum of four Gauss functions.

Figure 6.2 shows the results of the fits to the individual data and MC distributions. The bulk of the distributions is quite well reproduced by the fit results. Only in the transition region between the central and the *satellites peaks* smaller deviations are visible.

- In order to enhance the sensitivity to shape differences between the data and the MC simulation, the bin-by-bin ratio data over MC was determined and fitted with $g_{\text{data}}/g_{\text{MC}}$. The fit was performed in several individual steps:

1. The results from the fits to the individual distributions were used as starting parameters, the corresponding fit uncertainties defined the starting step sizes of the minimisation procedure.
2. The mean values, b_i, of all Gauss functions were fixed and all other parameters were determined.
3. The obtained results from the previous step were used as starting parameters and all parameters were released and fitted simultaneously.

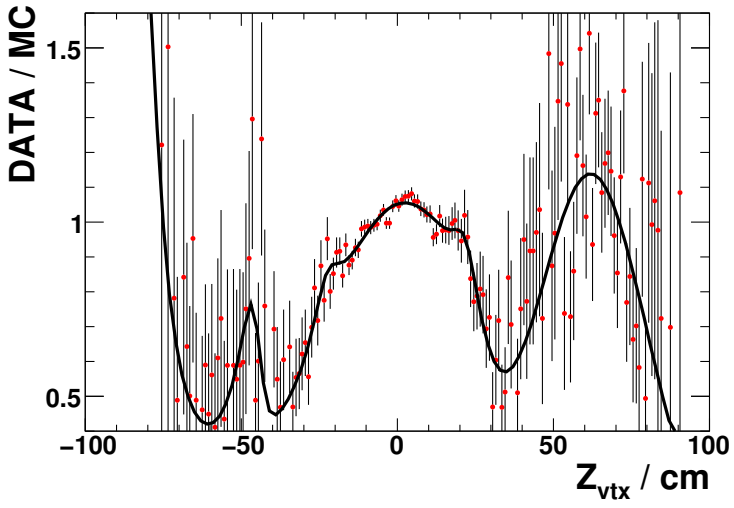

Figure 6.3: The bin-by-bin ratio data over MC as a function of z_{vtx} for the 2006/2007 e^+ period.

Figure 6.3 presents the result of the fit to the bin-by-bin ratio data over MC. The minimisation procedure has converged with $\chi^2/\text{ndf} = 0.91$, which indicates that the fit was reasonably successful. The result of this fit was used as a reweighting function in order to adjust the weight of each MC event depending on its "true" z_{vtx} value.

The extracted reweighting function was obtained from a data sample triggered by the FLT bit 30, whereas the reweighting was performed on the inclusive DIS sample triggered by the bits FLT 40,43 or 50 (see chapter 5.5).

The plots presented in figure 6.4 show the z_{vtx} distribution on detector level before and after applying the reweighting. It can be noted that the reweighting significantly improves the agreement between the data and the MC simulation over the full investigated z_{vtx} range. In the regions of the satellite peaks, the data tend to be slightly above the MC, but the deviation is still within the statistical uncertainties. The systematic effect of this correction is discussed in chapter 8.1.

6.3. Jet Corrections

In chapter 5.2 the reconstruction of the hadronic final state was discussed. In this analysis the jets were clustered by making use of the information extracted from calorimeter cells.

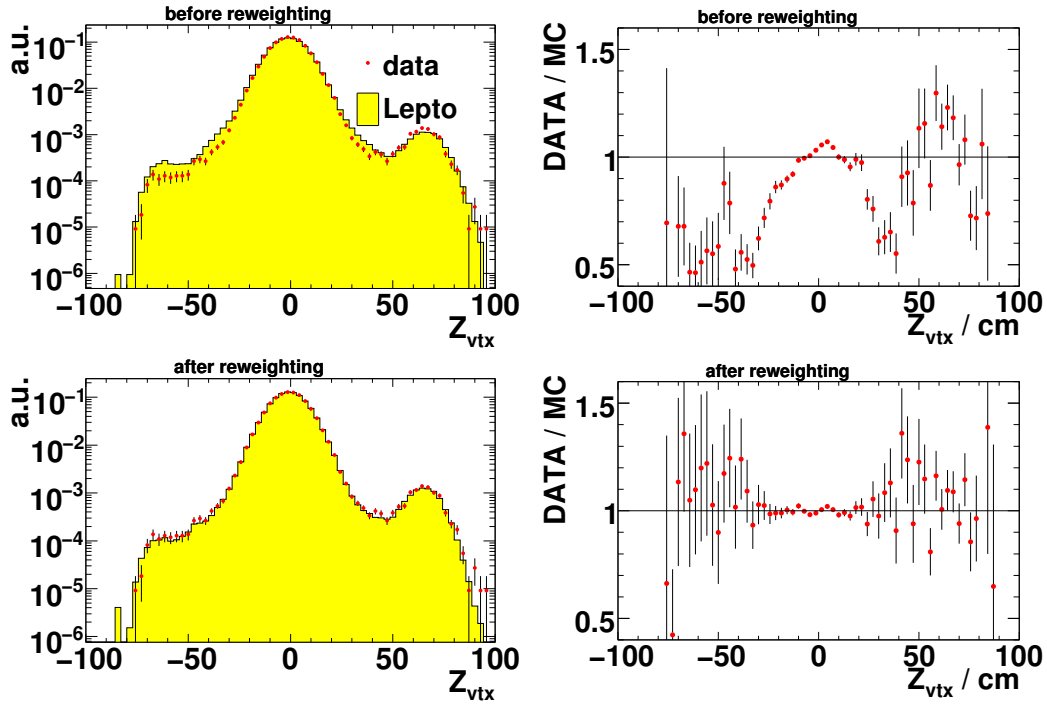

Figure 6.4: The z_{vtx} distributions on detector level for data and LEPTO before and after applying the z_{vtx} reweighting as well as ratio plots between the data and LEPTO.

The uncertainty of the hadronic energy scale is typically one of the largest contribution to the systematic uncertainties in jet measurements from the ZEUS collaboration. Therefore, a detailed understanding of the energy scale and its calibration was essential for the measurement presented here. In this section several studies of the jet energy scale are described.

Furthermore, the jet energy correction that accounts for inactive material in front of the calorimeter is discussed as well. This correction helped to reduce the influence of detector effects and to improve the correlation between detector and hadron level.

Finally, the comparison of the calibrated jet sample with tracking information is shown and the momentum balance of the dijet system is discussed.

6.3.1. The Hadronic Energy Scale

In previous ZEUS publications [15, 178, 179], the hadronic energy-scale uncertainty of jets with $E_T^{\text{lab}} < 10$ GeV was estimated to be $\pm 3\%$, and $\pm 1\%$ for jets with $E_T^{\text{lab}} > 10$ GeV. This systematic uncertainty was found to be the dominant systematic uncertainty in large regions of the jet phase space. Therefore, in this analysis a detailed study of the hadronic energy scale was performed with the aim of improving the calibration of the measurement.

In order to derive a correction for the jet energy scale, an independent reference scale was required. In this analysis, the transverse energy, E_T^{DA}, of the scattered electron as reconstructed with the double-angle method was used because of its approximate independence of the absolute energy scale of the calorimeter. The conservation of

energy and momentum was exploited to determine the energy corrections by balancing the kinematic quantities of the electron with those of the hadronic final state.

In theory the total hadronic transverse energy, E_T^{had}, is balanced by E_T^{DA}:

$$\frac{E_T^{had}}{E_T^{\mathrm{DA}}} = 1. \tag{6.2}$$

Under the assumption that the MC simulations describe all involved energy scales *and* inactive detector material correctly, the double ratio of quantity 6.2 between data and MC should be equal to unity.

In fact in practice, the MC simulations do not describe the hadronic energy scale observed in the data. However, if the double-angle variables are sufficiently well described by the MC simulations[1], then with the aid of a hadronic final state approximation with jets ($E_T^{\mathrm{had}} \approx E_T^{\mathrm{jet}}$) correction factors, $c_{\mathrm{jet-scale}}$, can be derived according to

$$\frac{\left(\frac{E_T^{\mathrm{jet}}}{E_T^{DA}}\right)_{\mathrm{data}}}{\left(\frac{E_T^{\mathrm{jet}} \cdot c_{\mathrm{jet-scale}}}{E_T^{DA}}\right)_{\mathrm{MC}}} \stackrel{!}{=} 1. \tag{6.3}$$

It should be noted that this correction is a relative correction between the data and the MC simulations under the assumption of a linear jet energy scale. Thus, the correction factors have to be independent of the energy. This linearity was checked and is discussed in the following section 6.3.1.1.

The study of the jet energy scale was subdivided into two parts: First, the energy scale of jets with $E_T^{\mathrm{lab}} > 10$ GeV was investigated. Afterwards, in a second step the jet energy scales were corrected and the energy scale of jets with $3 < E_T^{\mathrm{lab}} < 10$ GeV was studied.

6.3.1.1. Jets with $\mathbf{E_{T,lab}^{jet} > 10}$ GeV

In order to obtain adequate correction factors for the jet energy scale, the analysis cuts as discussed in chapter 5.5 were slightly adjusted. The correction procedure based on the transverse momentum balance between the jet and the electron by selecting single-jet events. The vectorial sum of these momenta in the laboratory frame only vanishes for events with exactly one jet and no further hadronic activity. In practice, however, this stringent constraint had to be relaxed. Therefore, events with a significant amount of transverse energy were suppressed with the requirement that no further jets with $E_{T,\mathrm{lab}}^{\mathrm{jet}} > 5$ GeV were reconstructed. The systematic influence of this cut is discussed later.

Additionally, the following adjustments were implemented:

- The phase-space cuts on the inelasticity y were removed in order to increase the amount of events in the sample with hadronic activity in the forward direction of the detector.

[1] The figures in chapter 7.1 demonstrate the agreement between the data and the MC for the double-angle variables.

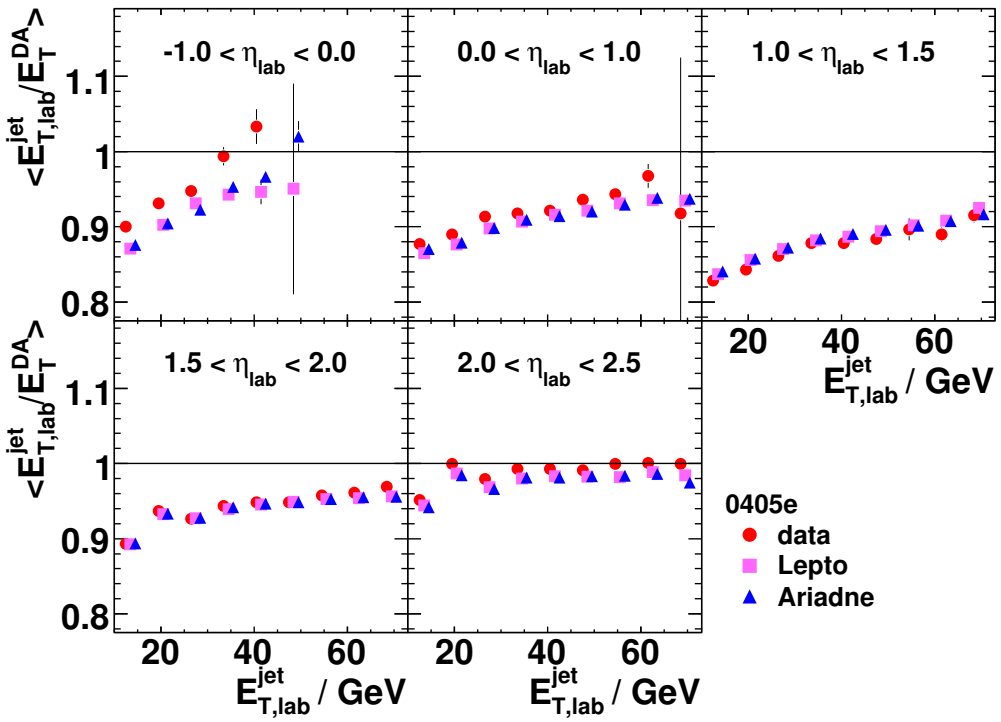

Figure 6.5: The average ratio, $\left\langle E^{\text{jet}}_{T,\text{lab}}/E^{DA}_{T,\text{lab}}\right\rangle$, in the 2004–2005 e^- data and in the MC as a function of the jet transverse energy, $E^{\text{jet}}_{T,\text{lab}}$, in five regions of the pseudorapidity, $\eta^{\text{jet}}_{\text{lab}}$, ***before*** the jet energy scale correction.

- The jet clustering was performed in the laboratory frame in order to be able to omit the Lorentz transformation to the Breit frame, because the presented study is related to the detector geometry.
- As previously mentioned, the Breit reference frame was not used at all. Thus, the cuts on the pseudorapidity, $\eta^{\text{jet}}_{\text{Breit}}$, and on the transverse energies in the Breit frame were omitted.
- The cut $E^{\text{jet}}_{T,\text{lab}} > 3$ GeV and the distance cut between the electron and the jets was omitted.

Figure 6.5 shows the average ratio, $\left\langle \frac{E^{\text{jet}}_{T,\text{lab}}}{E^{DA}_{T,\text{lab}}}\right\rangle$, as functions of $E^{\text{jet}}_{T,\text{lab}}$ and $\eta^{\text{jet}}_{\text{lab}}$ for the 2004–2005 e^- data[2], ARIADNE and LEPTO. Obviously, the data are not described by the MC simulations.

The double ratio,

$$\frac{\left\langle \frac{E^{\text{jet}}_{T}}{E^{DA}_{T}}\right\rangle_{\text{data}}}{\left\langle \frac{E^{\text{jet}}_{T}}{E^{DA}_{T}}\right\rangle_{\text{MC}}}, \tag{6.4}$$

[2]Figures for the other data-taking periods can be found in appendix A.1.

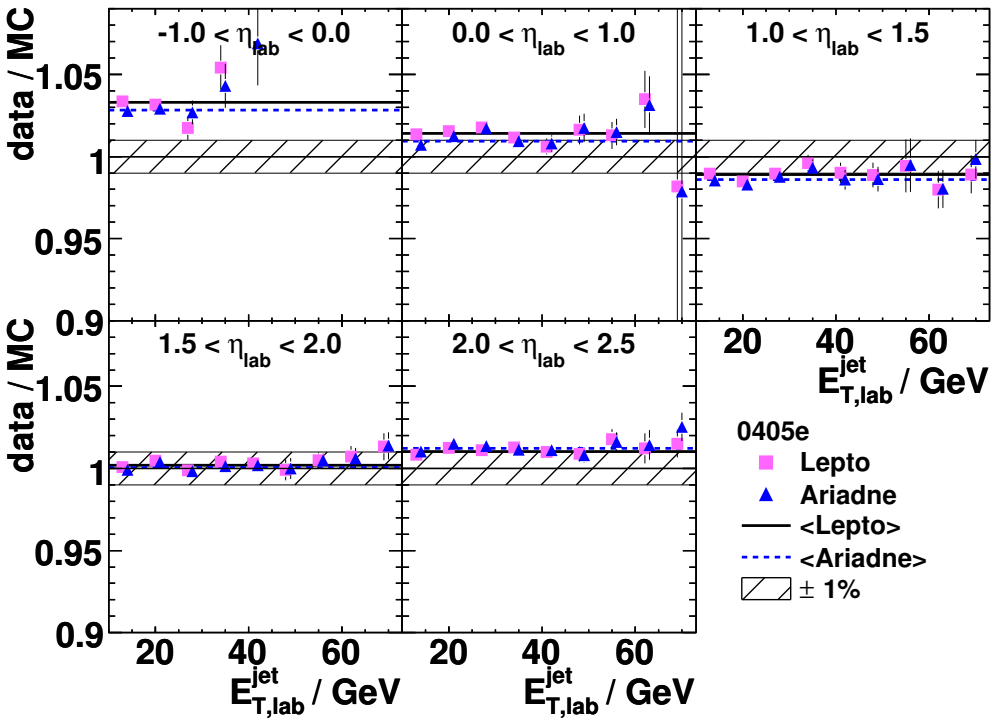

Figure 6.6: The double ratio between the 2004–2005 e^- data and the MCs as a function of the jet transverse energy, $E^{\text{jet}}_{T,\text{lab}}$, in five regions of the pseudorapidity, $\eta^{\text{jet}}_{\text{lab}}$, ***before*** the jet energy scale correction. The hatched area indicates the 1% uncertainty region on the jet energy scale. The horizontal lines depict the average double ratio for ARIADNE and LEPTO in each $\eta^{\text{jet}}_{\text{lab}}$ interval separately.

between data and ARIADNE or LEPTO as a function of $E^{\text{jet}}_{T,\text{lab}}$ is presented in figure 6.6. The 1% uncertainty region is indicated as a hatched area and the results of a weighted averaging for the two MC samples in each $\eta^{\text{jet}}_{\text{lab}}$ interval are also shown as solid and dashed lines. A distinct systematic energy scale difference between the data and the MC simulations can be noted. Since the difference is, within the uncertainties, independent of the jet transverse energy, the jet energy scale in the MC was corrected by applying, depending on the $\eta^{\text{jet}}_{\text{lab}}$ interval, multiplicative correction factors (equation 6.3) to the jet energy.

The outcome of this energy-scale adjustment can be seen in the figures 6.7 and 6.8. The agreement between data and MC energy scales is reasonable and within the indicated 1% uncertainty region.

The average ratios, as illustrated in figure 6.7, are not equal to unity after the correction, because only the relative difference between data and the MCs was reduced with the correction. In principle, this kind of distributions can be exploited in order to derive corrections that account for inactive material in front of the calorimeter. However, for this purpose a dedicated purely MC-based correction method was employed (see chapter 6.3.2 for further details).

The described correction procedure is based on single-jet events. Since, however, this strict requirement had to be relaxed for practical reasons, a systematic bias

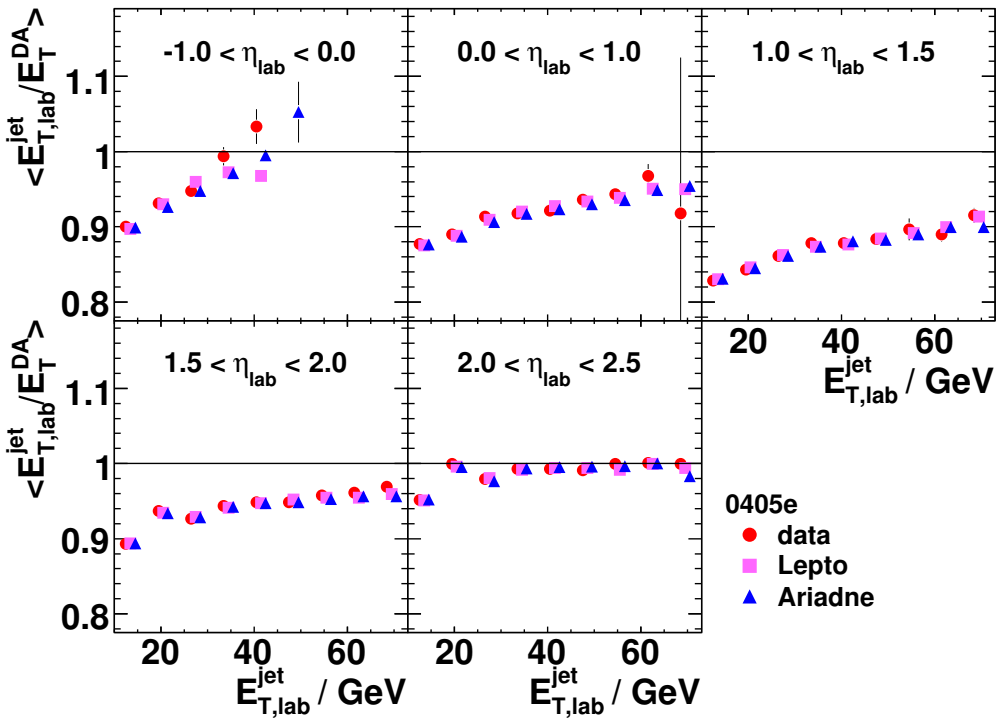

Figure 6.7: The average ratio ***after*** the jet energy scale correction. Other details as in the caption to figure 6.5.

coming from the cut $E^{\text{jet}}_{T,\text{lab}} > 5$ GeV that suppresses events with further jets was introduced. Owing to the difficult simulation of low-E_T hadronic activity such as the proton remnant, the obtained correction factors depend on the actual chosen cut value. Figure 6.9 shows the relative change of the correction factors with respect to the choice of the cut value for all data-taking periods in the region $1.5 < \eta^{\text{jet}}_{\text{lab}} < 2.0$ of the detector. The default cut value is indicated as a vertical line. Similar figures for the other $\eta^{\text{jet}}_{\text{lab}}$ intervals can be found in appendix A.1. The observed dependence is weak and covered by the assumed 1% energy-scale uncertainty.

6.3.1.2. Jets with $3 < E^{\text{jet}}_{T,\text{lab}} < 10$ GeV

In the previous section, the energy scale of jets with $E^{\text{jet}}_{T,\text{lab}} > 10$ GeV was discussed and corrected in the MC simulations. For low-energetic jets a similar study is more challenging because the amount of single-jet events is significantly smaller and, therefore, one can not make use anymore of the transverse momentum balance of the electron with a single, well-isolated jet. Nevertheless, a method for the study of the energy scale of jets with $3 < E^{\text{jet}}_{T,\text{lab}} < 10$ GeV was designed. However, an additional correction was not derived.

The study consisted of the following steps:

- The energy scale of all jets was corrected as described in section 6.3.1.1.
- The full DIS event and jet selection as described in chapter 5.5 – omitting the dijet/trijet selection – was applied, and it was required that $E^{\text{jet}}_{T,\text{Breit}} > 5$ GeV.

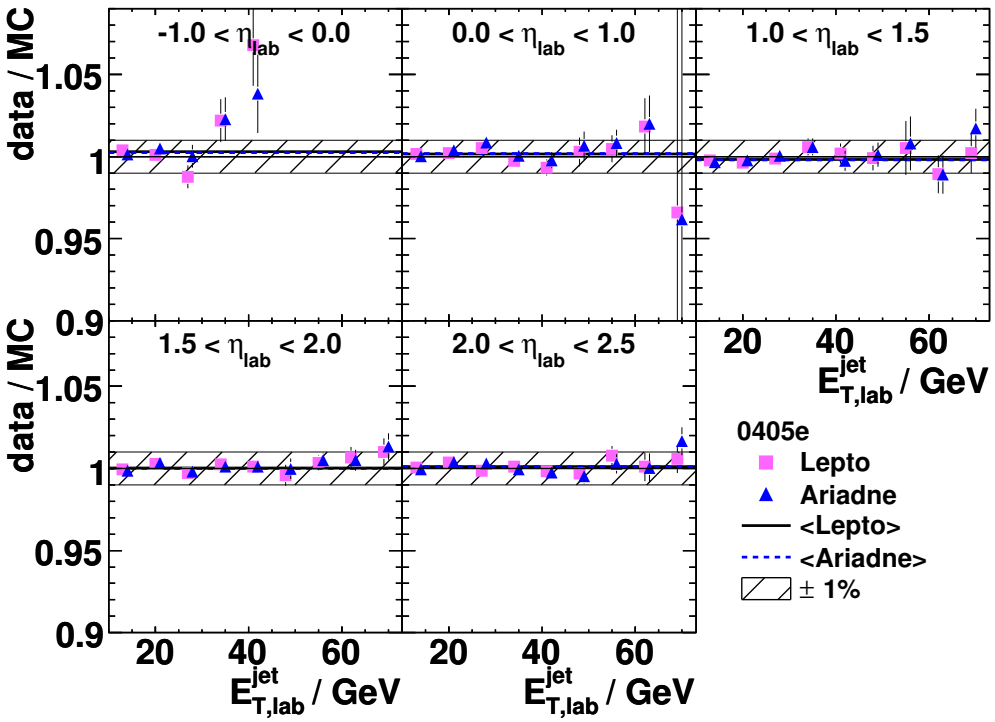

Figure 6.8: The double ratio ***after*** the jet energy scale correction. Other details as in the caption to figure 6.6.

- A sample of events with two jets was selected using the following requirements:
  1. The first jet had to have $E^{\text{jet}}_{T,\text{lab}} > 10$ GeV.
  2. The second jet had to be reconstructed with $3 < E^{\text{jet}}_{T,\text{lab}} < 10$ GeV.
  3. It was required that no further jets in the event with $E^{\text{jet}}_{T,\text{lab}} > 3$ GeV were found.

- A "reference vector",
$$p^{\text{reference}}_{\text{lab}} = p^{\text{DA}}_{\text{lab}} + p^{\text{jet}>10\text{GeV}}_{\text{lab}}, \tag{6.5}$$
was constructed, where $p^{\text{DA}}_{\text{lab}}$ is the double-angle four-momentum and $p^{\text{jet}>10\text{GeV}}_{\text{lab}}$ the four-momentum of the jet with $E^{\text{jet}}_{T,\text{lab}} > 10$ GeV. The transverse momentum ratio, R, of the investigated jet and the "reference vector" was determined in data and in the MC simulations,
$$R = \frac{p^{3<\text{jet}<10\text{GeV}}_{T,\text{lab}}}{p^{\text{reference}}_{T,\text{lab}}}, \tag{6.6}$$
where $p^{3<\text{jet}<10\text{GeV}}_{T,\text{lab}}$ is the transverse momentum of the jet under study with $3 < E^{\text{jet}}_{T,\text{lab}} < 10$ GeV and $p^{\text{reference}}_{T,\text{lab}}$ is the transverse momentum of the "reference vector" (equation 6.5).

In figure 6.10 the ratio R is shown in comparison with LEPTO for the 1998–2000 $e^{\pm}$, for the 2004-2005 e^{-} and for the 2006-2007 e^{+} data. The quantity R differs

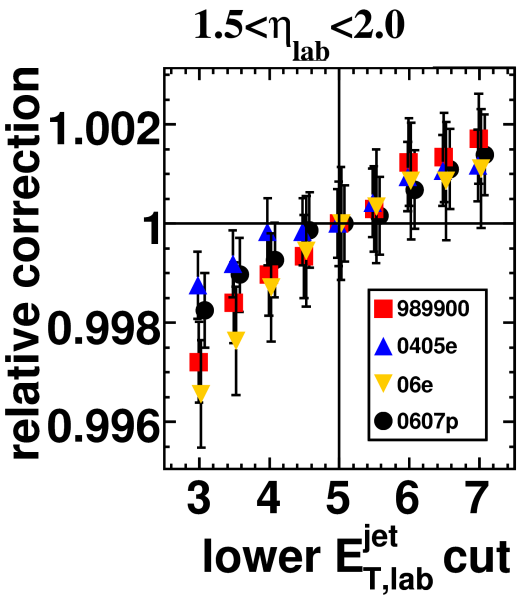

Figure 6.9: The relative change of the hadronic energy scale correction factors as a function of the lower $E^{\text{jet}}_{T,\text{lab}}$ cut for all data-taking periods in the region $1.5 < \eta^{\text{jet}}_{\text{lab}} < 2.0$.

from unity due to missing corrections that account for inactive material between the interaction region and the calorimeter. In addition, the double-ratios $\frac{\langle R_{\text{data}} \rangle}{\langle R_{\text{Lepto}} \rangle}$ between the average values and the corresponding uncertainties are summarised in figure 6.11. The agreement is on average within 3%, which is indicated as a filled band, for all data-taking periods. The energy-scale difference between data and LEPTO was found to be stable in time.

6.3.2. Jet Energy Correction

Particles are created in the *ep* scattering process and typically pass through detector material and lose energy before their energy is measured in the calorimeter. Therefore, the measurement of the energy typically underestimates the "true" particle energy.

The employed MC simulations provided full access to the generated hadronic final state. Due to the full detector simulation, this information can be compared with the reconstructed final state. Therefore, it was possible to approximately reduce the influence of inactive material on the measurement of the jet energies by imposing a dedicated correction method.

The derived correction procedure was applied to jets whose energies had been calibrated as described in section 6.3.1.1. Contrary to the correction described in section 6.3.1, where only the MC jets were adjusted, the correction described in this section was applied to the data jets as well as to MC jets assuming a correct description of inactive material in the detector. Since the double ratios between the data and the MCs as shown e.g. in figure 6.7 are approximately independent of the transverse momentum, this behaviour can be interpreted as a hint for a reasonably good description of inactive material by the MC because the energy loss of particles in material is in general not a linear function of the energy. In addition, a reasonably good description of observables like the jet transverse energy or pseudorapidity[3] by

[3]Distributions that demonstrate the agreement between the data and the MC can be found in

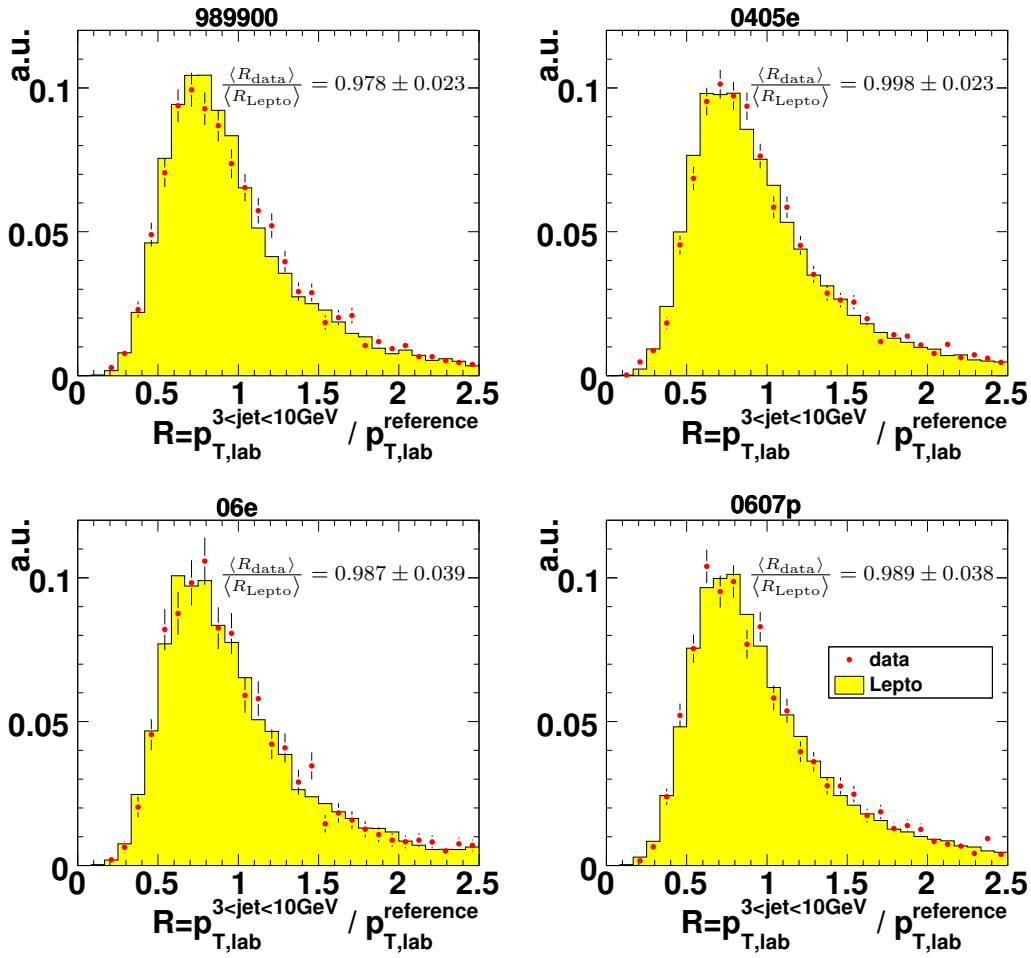

Figure 6.10: Distributions of the quantity R. In addition, the double-ratios $\frac{\langle R_{\rm data}\rangle}{\langle R_{\rm Lepto}\rangle}$ between the average ratios $\langle R\rangle$ in data and LEPTO for jets with $3 < E_{T,\rm lab}^{\rm jet} < 10$ GeV are indicated.

the MC simulation was essential.

Even though this correction procedure was supposed to eliminate only detector effects, a dependence on the details of the generated hadronic final state was introduced. The correction functions were therefore determined for ARIADNE and LEPTO separately, and, depending on which MC was used for the data unfolding, the corresponding correction factors were applied.

The correction procedure consisted of the following steps:

- The event had to be selected on hadron level and on detector level. The selection that was described in chapter 5 was used – omitting the dijet/trijet selection in order to increase the statistics. Instead a cut on $E_{T,\rm Breit}^{\rm jet} > 5$ GeV was introduced.

- The distance r in the $\eta - \phi$ plane between all pairs of detector and hadron level

chapter 7.1.

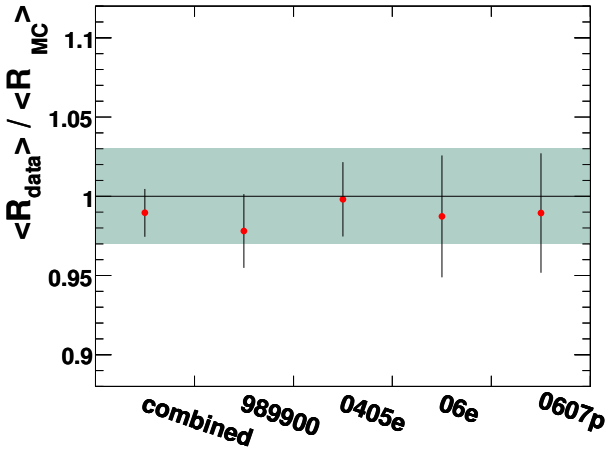

Figure 6.11: The double-ratio $\frac{\langle R_{\text{data}} \rangle}{\langle R_{\text{Lepto}} \rangle}$ between the average ratios, $\langle R \rangle$, in data and in LEPTO for jets with $3 < E^{\text{jet}}_{T,\text{lab}} < 10$ GeV.

jets was determined according to $r = \left[\left(\eta^{\text{Breit}}_{\text{had}} - \eta^{\text{Breit}}_{\text{det}} \right)^2 + \left(\phi^{\text{Breit}}_{\text{had}} - \phi^{\text{Breit}}_{\text{det}} \right)^2 \right]^{\frac{1}{2}}$. After the calculation of r for all pairs, the resulting list was sorted with increasing r and processed starting with the smallest r. If $r < 0.7$, then the hadron level jet was "matched" to the detector level jet and both jets were marked and removed from the list.

- From these pairs of matched jets, the average reconstructed $\left\langle E^{\text{jet,det}}_{T,\text{Breit}} \right\rangle$ as a function of $\left\langle E^{\text{jet,had}}_{T,\text{Breit}} \right\rangle$ was determined in 14 regions of $\eta^{\text{jet}}_{\text{lab}}$ in order to account for the detector geometry.

- With a straight-line fit the dependence of $\left\langle E^{\text{jet,det}}_{T,\text{Breit}} \right\rangle$ on $\left\langle E^{\text{jet,had}}_{T,\text{Breit}} \right\rangle$ was parametrised according to $\left\langle E^{\text{jet,det}}_{T,\text{Breit}} \right\rangle = a_0 + a_1 \cdot \left\langle E^{\text{jet,had}}_{T,\text{Breit}} \right\rangle$. It should be noted that the correction was performed in the Breit frame. If the derivation of the correction functions would be performed in the laboratory frame, then the correction could presumably be improved.

- From this fit result, a correction factor,

$$C = \frac{1}{a_1} - \frac{a_0}{\left\langle E^{\text{jet,det}}_{T,\text{Breit}} \right\rangle \cdot a_1}, \tag{6.7}$$

for the four-momentum of the jet in question was derived.

The correction was performed for data jets and for MC jets and the correction factors were determined for all data-taking periods separately.

The average detector level $\left\langle E^{\text{jet,det}}_{T,\text{Breit}} \right\rangle$ as a function of $\left\langle E^{\text{jet,had}}_{T,\text{Breit}} \right\rangle$ for LEPTO[4] in the range $-1 < \eta^{\text{jet}}_{\text{lab}} < 2.5$ before and after applying the correction for the 1998–2000 data is shown in figure 6.12. On average, the correction method improves the energy correlation between detector level jets and hadron level jets.

[4]For the other data-taking periods the jet energy corrections are illustrated in the figures A.1 and A.1 in appendix A.1.

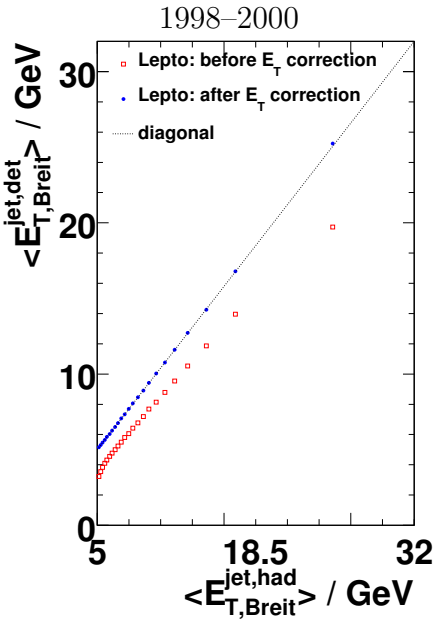

Figure 6.12: The average detector level $\left\langle E_{T,\mathrm{Breit}}^{\mathrm{jet,det}} \right\rangle$ as a function of $\left\langle E_{T,\mathrm{Breit}}^{\mathrm{jet,had}} \right\rangle$ in the range $-1 < \eta_{\mathrm{lab}}^{\mathrm{jet}} < 2.5$ for LEPTO before and after applying a correction for inactive material in front of the calorimeter for the 1998–2000 period.

6.3.3. The Calibrated Jet Sample

After applying the corrections to the jets described and derived in the previous sections, a rather independent investigation of the jet-energy-scale uncertainty was performed. The jets used in this analysis were clustered from calorimeter cells only. Hence, a procedure based on reconstructed tracks was used as an independent validation of the calibration of the jet sample. The procedure relies on an accurate simulation of charged tracks and it is less reliant on the simulation of energy loss and hadronic showers in detector material. The latter are typically less well simulated.

The following analysis modifications were imposed:

- The single-jet selection discussed in section 6.3.1.1 was used for the event selection, and each jet was forced to be inside the acceptance of the CTD by requiring $\left|\eta_{\mathrm{lab}}^{\mathrm{jet}}\right| < 1$.
- In order to guarantee adequately reconstructed tracks it was required, for all tracks, that $n_i \leqslant 1$, $n_o \geqslant 3$ and $p_T^{\mathrm{track}} > 0.3$ GeV, where n_i is the number of inner superlayer hits, n_o the number of outer superlayer hits and p_T^{track} the transverse momentum of the track. The track associated to the scattered electron was rejected.
- Jets were reconstructed from the selected tracks with the k_T jet cluster algorithm (section 2.2.2.3). In addition, a matching between the calorimeter jets and the jets consisting of tracks was performed. It was required that the distance r in the $\eta - \phi$ plane had to be $r < 0.6$, and that no further jet with $E_{T,\mathrm{lab}}^{\mathrm{track-jet}} > 3.5$ GeV was allowed to be inside a radius of 1.3 around the calorimeter jet.

Figure 6.13 shows the double ratio of the average transverse-energy ratios, $\bar{t} = \left\langle \frac{E_{T,\mathrm{lab}}^{\mathrm{CAL-jet}}}{E_{T,\mathrm{lab}}^{\mathrm{track-jet}}} \right\rangle$, between data and the MC simulations for the various data-taking periods. The observed calorimeter energy scale difference between data and the MC simulations

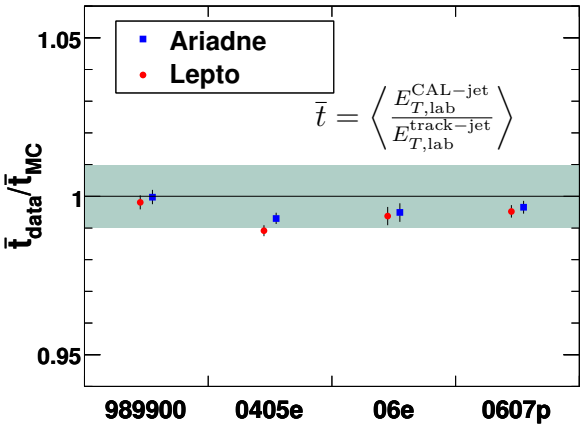

Figure 6.13: The double ratio of the average transverse-energy ratios, $\bar{t} = \left\langle \frac{E_{T,\mathrm{lab}}^{\mathrm{CAL-jet}}}{E_{T,\mathrm{lab}}^{\mathrm{track-jet}}} \right\rangle$, between data and LEPTO and ARIADNE.

is consistent with ±1% assuming that the track jets are the same in data and in the MC. Only a small difference between the two MC simulations that might come from the different treatment of the parton cascade is observed.

As an additional check, the four-momenta $p_{\mathrm{lab}}^{\mathrm{jet1}}$ and $p_{\mathrm{lab}}^{\mathrm{jet2}}$ of the two selected jets after applying the full dijet selection as described in chapter 5 were employed in a comparison with the electron momentum, $p_{\mathrm{lab}}^{\mathrm{electron}}$. The two jet momenta were corrected – as described in section 6.3.2 – for inactive material and vectorially added to $p_{\mathrm{lab}}^{\mathrm{jet1+jet2}}$. The transverse momentum balance, $d = \frac{p_{T\mathrm{lab}}^{\mathrm{jet1+jet2}}}{p_{T\mathrm{lab}}^{\mathrm{electron}}}$, was determined.

The obtained distributions of d for the combined data sample are depicted in figure 6.14. Presented are distributions for all selected dijet events and for dijet events with $E_{T,\mathrm{lab}}^{\mathrm{jet1}} > 10$ GeV and $3 < E_{T,\mathrm{lab}}^{\mathrm{jet2}} < 10$ GeV in order to be more sensitive to the energy scale of jets with low transverse energies. The electron momentum was reconstructed with the electron method and with the double-angle method. The peak positions of the distributions are close to unity which is caused by the correction that accounts for inactive material (see section 6.3.2). For the remaining deviation from unity is accounted for in the cross-section determination with the application of the acceptance correction as described in chapter 7.2, because the agreement between the data and the MC is reasonably well.

Since the relative shifts of these distributions between data and MC are a measure of the relative jet-energy-scale difference assuming that the electron energy scale is the same between data and MC, the average of the variable d was calculated and the double ratio, $\overline{d_{\mathrm{data}}}/\overline{d_{\mathrm{MC}}}$, between data and MC was determined. The observed jet-energy-scale uncertainty, which is shown in figure 6.15, was found to be smaller than ±1% for all dijet events, below 3% if the second jet had $E_{T,\mathrm{lab}}^{\mathrm{jet2}} < 10$ GeV and consistently for the full data-taking period.

With the aid of transverse energy ratios, $E_{T,\mathrm{B}}^{\mathrm{jet2}}/E_{T,\mathrm{B}}^{\mathrm{jet1}}$, between the first and the second jet in selected dijet events, the change of the jet energy scales between low- and high-transverse-energy jets can be investigated. In order to enrich the sample with low-energetic jets, only those dijet events were considered in which one jet with $E_{T,\mathrm{lab}}^{\mathrm{jet1}} > 10$ GeV and another with $E_{T,\mathrm{lab}}^{\mathrm{jet2}} < 10$ GeV was reconstructed.

Figure 6.16 depicts, separately for the four different data-taking periods, distributions

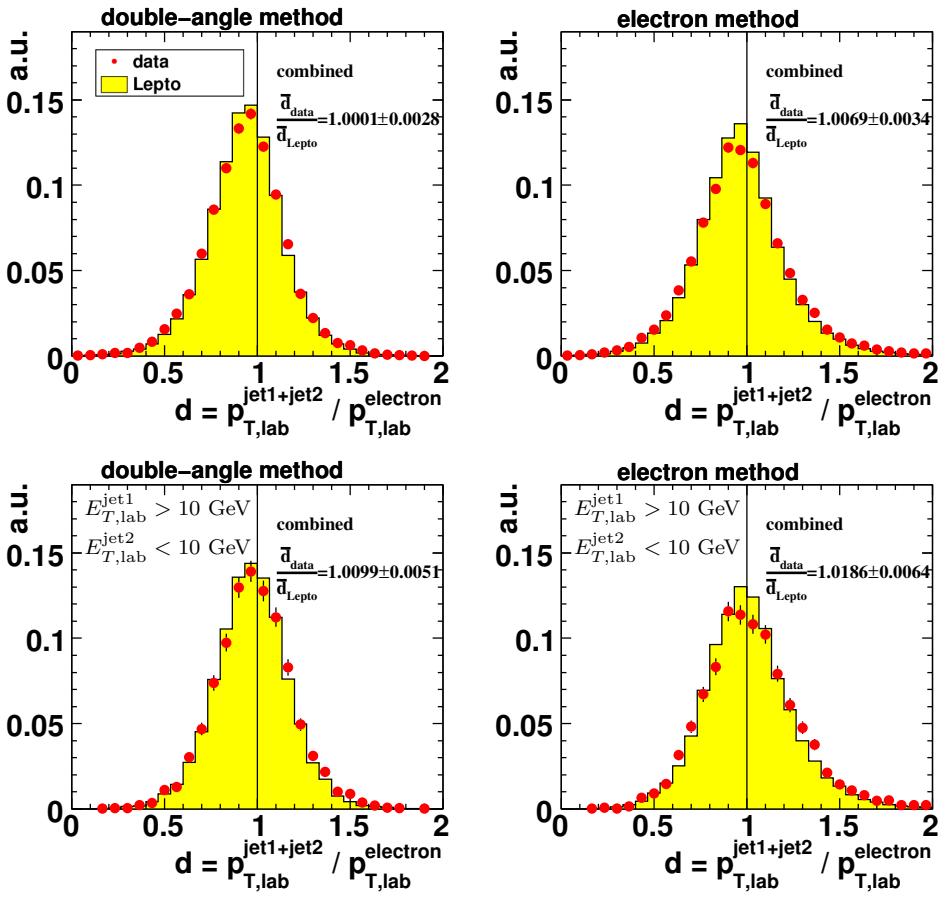

Figure 6.14: The transverse momentum balance of the dijet system with respect to the electron for all selected dijet events and for dijet events with $E^{\text{jet1}}_{T,\text{lab}} > 10$ GeV and $3 < E^{\text{jet2}}_{T,\text{lab}} < 10$ GeV for the combined data sample. The electron momentum was reconstructed with the electron method and with the double-angle method.

of the quantity $E^{\text{jet2}}_{T,\text{B}}/E^{\text{jet1}}_{T,\text{B}}$ for data and LEPTO. Even though the MC simulation is not describing the shape perfectly, significant differences between the periods can not be observed, indicating that the relative difference between jet energy scales of low- and high-energetic jets was constant as a function of time.

It should be noted that the data sample used for the derivation of the jet energy scale correction was enriched with jets arising from quarks (quark-parton-model process) instead of gluons, whereas in the studies using the dijet system, the sample was enriched with jets coming from the fragmentation of gluons. However, any significant differences between the jet energy scale of these two types of jets was not be observed.

6.3.4. Conclusion

The correction methods presented in this section for correcting the jet energies for energy loss in inactive material (section 6.3.2) and the hadronic energy-scale difference (section 6.3.1) between data and MC simulations have improved the reconstruction of the hadronic final state and the description of the involved jet energy scales.

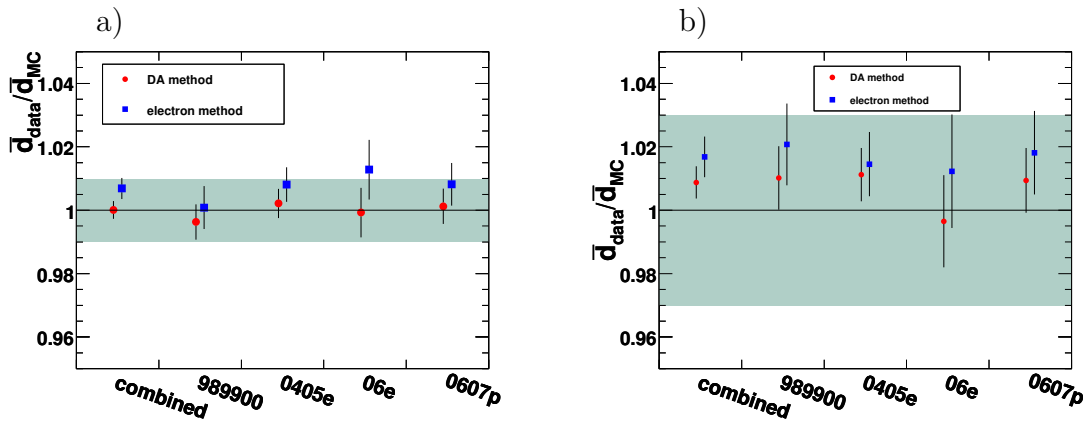

Figure 6.15: The ratio data over MC of the transverse momentum balance of the dijet system split into the several data-taking periods for a) all selected dijet events and b) for dijet events with $E_{T,\mathrm{lab}}^{\mathrm{jet1}} > 10$ GeV and $E_{T,\mathrm{lab}}^{\mathrm{jet2}} < 10$ GeV. The electron momentum was reconstructed with the electron method and with the double-angle method.

The correction of the hadronic energy scale was based on the transverse momentum balance of the electron with the hadronic final state. In practice, however, single-jet events with $E_{T,\mathrm{lab}}^{\mathrm{jet}} > 10$ GeV were selected and the transverse energy of these jets was compared to the transverse energy of the event as reconstructed with the double-angle method.

After correcting the MC jet energy scale, its uncertainty for jets with $3 < E_{T,\mathrm{lab}}^{\mathrm{jet}} < 10$ GeV was investigated and found to be consistent with $\pm 3\%$. The calibrated jet sample was validated by comparing the calorimeter jets with jets clustered from tracks. In addition, the transverse momentum balance of the dijet system with respect to the electron was investigated and also the ratio of the jet transverse energies of the dijet system.

All these studies have demonstrated that the jet-energy-scale uncertainty was consistent in the analysed data-taking periods and that an uncertainty of $\pm 1\%$ for jets with $E_{T,\mathrm{lab}}^{\mathrm{jet}} > 10$ GeV and $\pm 3\%$ for jets with $3 < E_{T,\mathrm{lab}}^{\mathrm{jet}} < 10$ GeV was a reasonable estimation.

The jet-energy-scale uncertainty was treated as a systematic uncertainty, and its effect on the cross sections is discussed later in chapter 8.1.

6.4. The Trigger Efficiency

A detailed understanding of the performance of the trigger system is one of the most crucial elements in jet analyses at ZEUS.

At the first-level trigger, the CTD was used for beam-gas rejection and for the improvement of the acceptance for certain physics processes which, for example, have a distinctive track topology but may have deposited only small amounts of energy in the calorimeter. Each beam crossing was analysed for the presence of tracks and for tracks coming from a vertex consistent with originating from the *ep* interaction region. At the FLT the accurate stereo information provided by the CTD could not

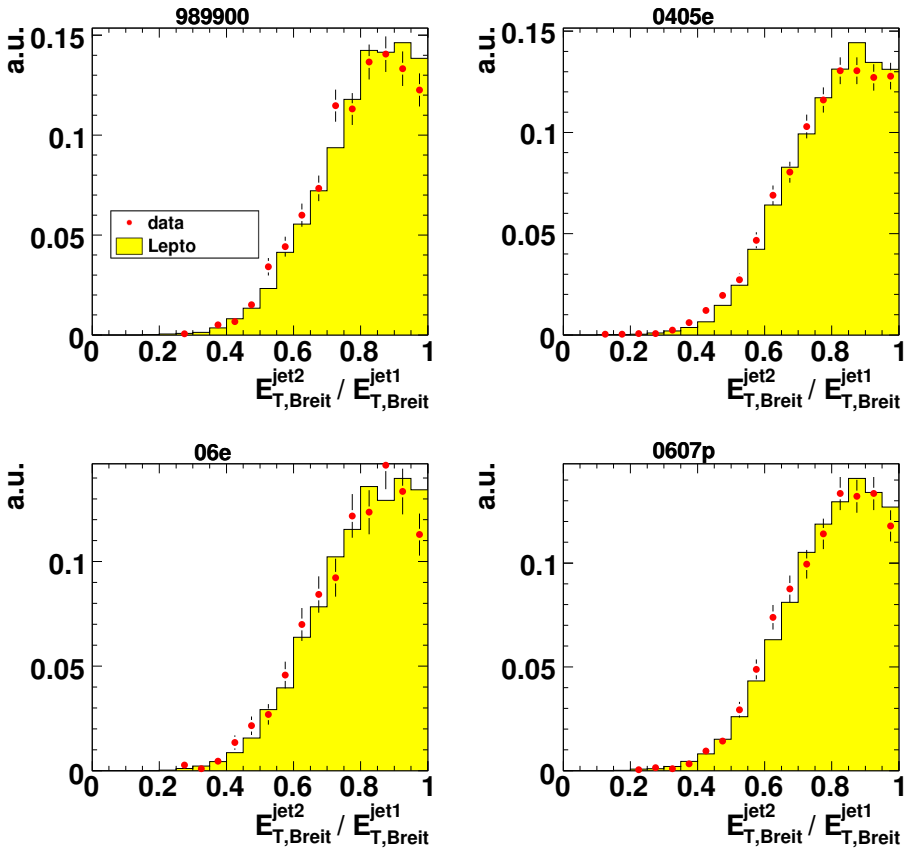

Figure 6.16: The ratio of transverse energies, $E^{\mathrm{jet2}}_{T,\mathrm{B}}/E^{\mathrm{jet1}}_{T,\mathrm{B}}$, for the four data-taking periods. Dijet events with $E^{\mathrm{jet1}}_{T,\mathrm{lab}} > 10$ GeV and $E^{\mathrm{jet2}}_{T,\mathrm{lab}} < 10$ GeV were selected.

be used due to the insufficient processing time. Therefore, three dimensional space point information was obtained by using the technique of z-by-timing [180] which utilised a time difference measurement at each CTD wire in order to reconstruct the z coordinate with an average resolution of 4.4 cm.

Depending on the multiplicity of all tracks and of the multiplicity of vertex-fitted tracks the CTD FLT has assigned a track class to each event as indicated in figure 6.17.

	track-veto condition: reject event if ...
"type a"	track class ≤ 2 or (track class $= 8$ and track multiplicity ≥ 26)
"type b"	track class ≤ 2

Table 6.1: The track-veto conditions for the applied trigger chain in the years 2004–2007.

Starting from the year 2004, the employed trigger chain has used the CTD FLT tracking information as a trigger veto[5]. The track-veto conditions for the FLT bits

[5]The trigger chain for the years 1998 to 2000 was only very weakly reliant on tracking information.

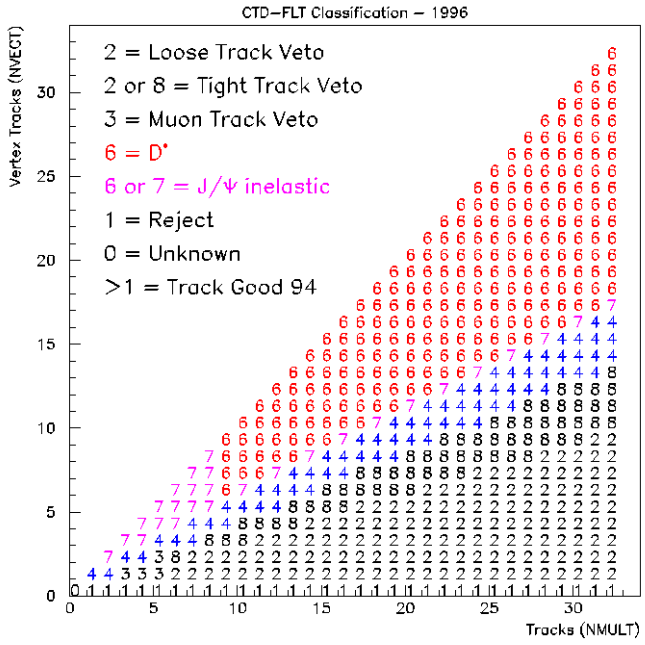

Figure 6.17: The CTD FLT event classification (figure taken from [181]).

40,43 and 50 are summarised in table 6.1. In the following these two conditions are called "type a" and "type b".

The track-veto efficiency,

$$\epsilon^{\text{trk}} = \frac{\text{noveto \&\& FLT}\,(30)}{FLT\,(30)}, \tag{6.8}$$

was investigated with an unbiased data sample triggered by FLT bit 30, which only required an isolated energy deposit in the RCAL and was therefore independent of the CTD. The quantity noveto && FLT (30) represents the number of events which were accepted by the track-veto condition and which had a set FLT bit 30. The quantity FLT (30) represents the total number of events triggered by FLT bit 30.

Figures 6.18 and 6.19 show control distributions, ratio histograms between the data and LEPTO control distributions, the track-veto efficiency "type a" and the track-veto efficiency ratio between the data and the MC as functions of y_{DA} and z_{vtx}, respectively, for the 2006/2007 e^+ period[6]. The track-veto efficiency of a MC simulation where the CTD gas gain[7] was not tuned [182, 183] to match the data gain is also presented. The tuning of the CTD gas gain has improved the description of the data by about +2%. Nevertheless, a discrepancy between the data and the MC simulation remains. This discrepancy is a strong function of the kinematic variable y_{DA} and only weakly dependent on z_{vtx}.

In order to improve the agreement between the data and the MC simulations, a correction procedure was imposed which consisted of the following steps:

1. The track-veto efficiency ratio, $\epsilon^{\text{trk}}_{\text{data}}/\epsilon^{\text{trk}}_{\text{MC}}$, was determined as a function of y_{DA} and fitted with $p = a_0 + a_1 \cdot y_{\text{DA}}$.

[6]Figures for the other periods can be found in the appendix A.2.

[7]The CTD gas gain depends on the quantity of Argon in the gas mixture, the high voltage settings and the pressure.

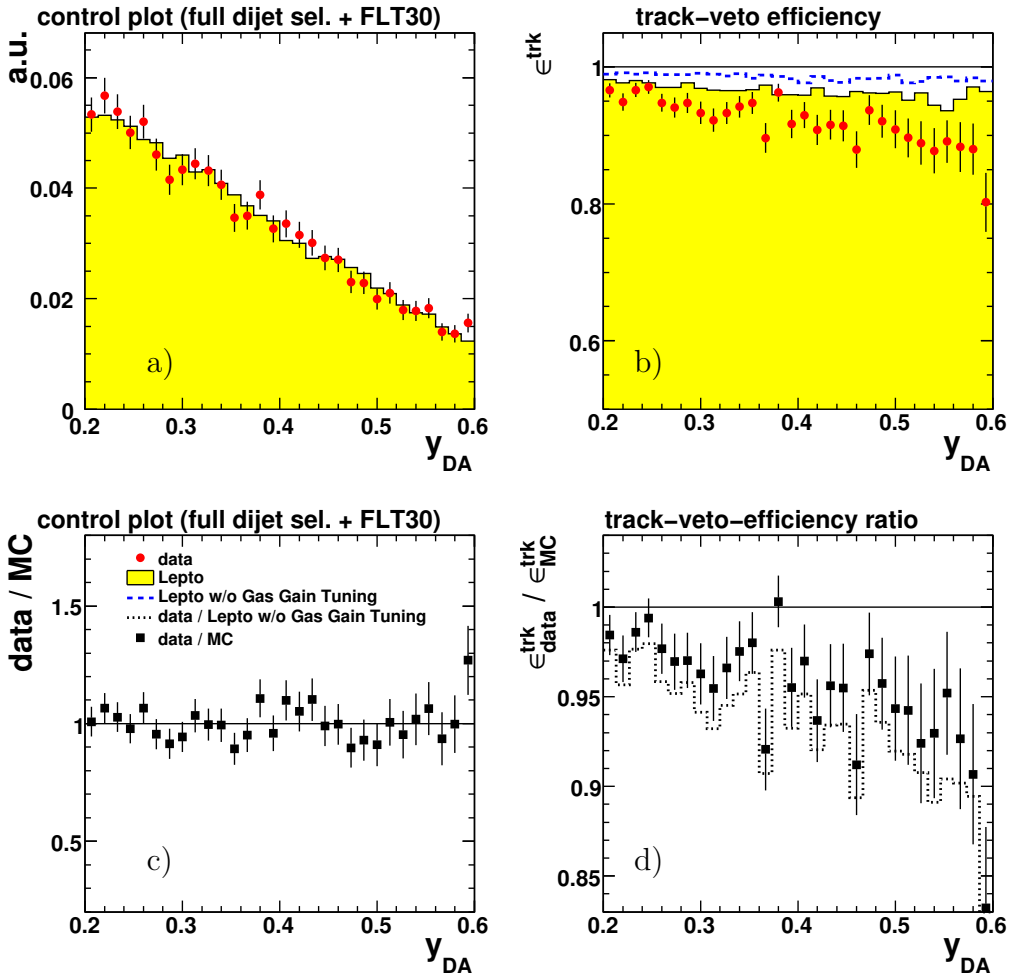

Figure 6.18: Study of the 2006/2007 e^+ track-veto efficiency as a function of y_{DA} for data and LEPTO: a) Control distributions. b) The track-veto efficiency ϵ^{trk}. c) Ratio of the individual control distributions. d) Ratio of the track-veto efficiencies $\epsilon^{\mathrm{trk}}_{\mathrm{data}}/\epsilon^{\mathrm{trk}}_{\mathrm{MC}}$.

2. For each MC event a random number, r, was created uniformly distributed between 0 and 1. The event was rejected on detector level if $r > p\,(y_{\mathrm{DA}})$.

3. The correction was performed separately for LEPTO and ARIADNE and separately for the different data-taking periods.

Since the correction function was obtained from a data sample triggered by FLT bit 30, which is a low-Q^2 trigger, the Q^2 dependence of $\epsilon^{\mathrm{trk}}_{\mathrm{data}}/\epsilon^{\mathrm{trk}}_{\mathrm{MC}}$ was investigated and found to be constant within the statistical uncertainties as indicated in figure 6.20. Hence, it was a reasonable approach to apply the correction to all events independent of their actual Q^2 values.

The track-veto condition "type b" has differed slightly from the condition "type a", as documented in table 6.1. However, the dependence on y_{DA}, as indicated in figure 6.21, was found to be very similar. Therefore, the determined correction for "type a" was also applied to "type b".

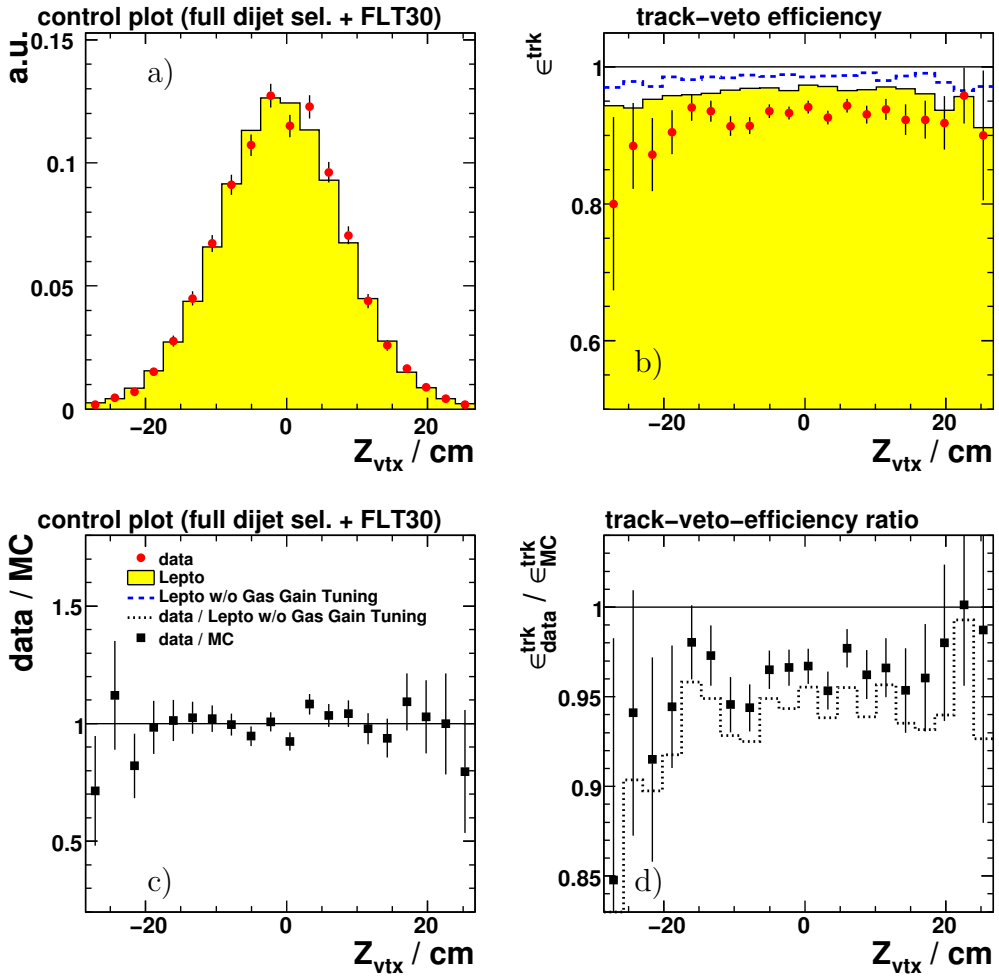

Figure 6.19: Study of the 2006/2007 e^+ track-veto efficiency as a function of z_{vtx} for the data and LEPTO: a) Control distributions. b) The track-veto efficiency ϵ^{trk}. c) Ratio of the individual control distributions. d) Ratio of the track-veto efficiencies $\epsilon^{\mathrm{trk}}_{\mathrm{data}}/\epsilon^{\mathrm{trk}}_{\mathrm{MC}}$.

Figure 6.22 presents control distributions and the track-veto efficiency for data and MC as a function of y_{DA} after applying the previously described correction procedure. It can be noted that the correction has significantly improved the description of the data. The average size of the correction for the 2006/2007 e^+ data was approximately 4%, for the 2004/2005 e^- data about 2%; for the 2006 e^- sample the size of the correction was slightly smaller ($\approx 1\%$).

The systematic influence of the trigger correction on the cross sections was investigated and the effect is discussed in chapter 8.1.

The trigger efficiency before and after correcting for the inadequate track-veto simulation was investigated by using again an unbiased data sample triggered by FLT bit 30. The efficiency, ϵ, was defined as

$$\epsilon = \frac{\mathrm{FLT}\,(40, 43, 50)\ \&\&\ \mathrm{FLT}\,(30)}{\mathrm{FLT}\,(30)}, \tag{6.9}$$

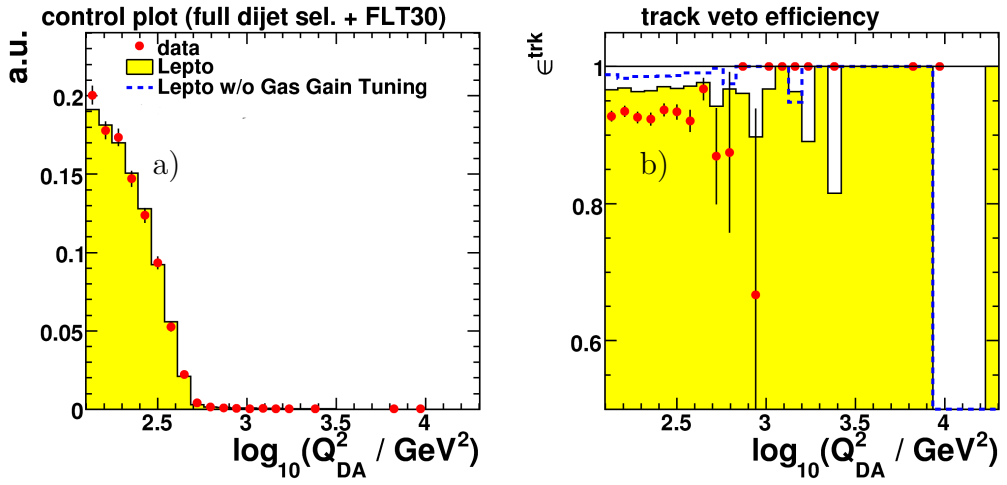

Figure 6.20: Study of the 2006/2007 e^+ track-veto efficiency as a function of Q^2 for the data and LEPTO: a) Control distributions. b) The track-veto efficiency ϵ^{trk}.

where FLT $(40, 43, 50)$ && FLT (30) represents the number of selected events with FLT bit 30 and at least one of the bits 40,43 or 50 set. The quantity FLT (30) represents the total number of events triggered by FLT bit 30.

Figure 6.23 shows the trigger efficiency, ϵ, and the ratio $\epsilon_{\mathrm{data}}/\epsilon_{\mathrm{MC}}$ before and after applying the track-veto correction in intervals of the average transverse energy in the Breit frame, $\overline{E^{\mathrm{jet}}_{T,\mathrm{B}}}$, of the dijet system. After applying the correction for the track-veto-efficiency difference between data and MC simulations, the data efficiency is described reasonably well by the MC. Figures for the 2006–2007 periods can be found in appendix A.2.

The efficiencies of the SLT and TLT trigger used in this analysis have been investigated in previous analyses at ZEUS (e.g. in [184]) and were found to be well described.

6.5. Dijet Reweighting

A good description of the data by the MC simulations is necessary in order to be able to use the simulations for determining the acceptance corrections[8]. Any observed discrepancy can be either due to an inadequate simulation of the detector or due to an inadequate modeling of the underlying processes. While the first issue can be solved by improving the detector simulation, the latter can be partially cured by improving the employed physical models. In practice, however, it is often more convenient to adjust the MC event weights.

In this analysis a reweighting was imposed to improve the description of the Q^2 dependence of the data after requiring the full dijet selection. In order to determine these reweighting functions, the data Q^2 distribution was corrected for acceptance effects (see chapter 7.2) and then compared to ARIADNE and to LEPTO. Afterwards,

[8]See chapter 7 for more details.

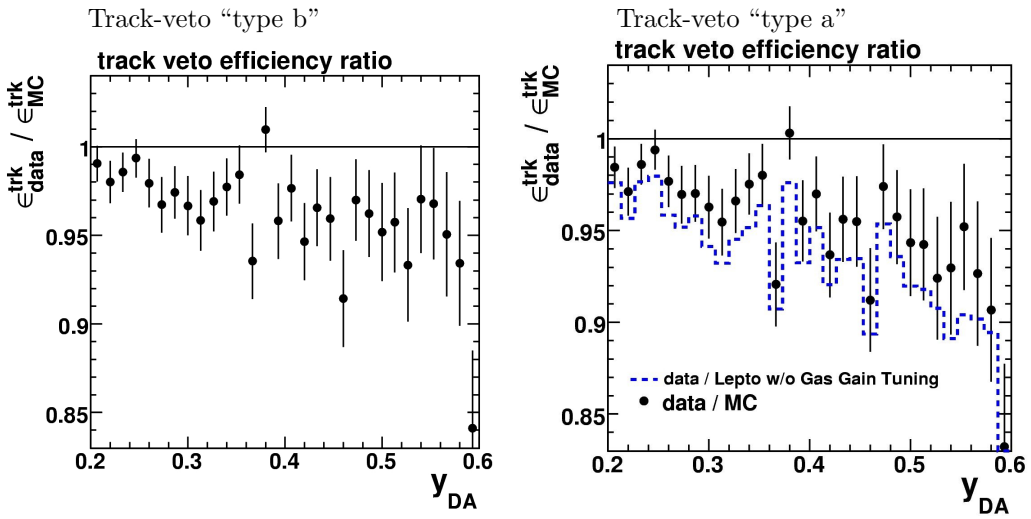

Figure 6.21: Study of the 2006/2007 e^+ track-veto efficiency ratio $\epsilon^{\mathrm{trk}}_{\mathrm{data}}/\epsilon^{\mathrm{trk}}_{\mathrm{MC}}$ between data and LEPTO as a function of y_{DA} for the data and LEPTO.

the ratio of the normalised[9] data and MC distributions was fitted with

$$f_{\mathrm{Ariadne}} = a_0 + a_1 \cdot \frac{Q^2}{\mathrm{GeV}^2} \qquad \text{or} \qquad \mathrm{f_{Lepto}} = \mathrm{b_0} + \mathrm{b_1} \cdot \log_{10}\left(\frac{\mathrm{Q}^2}{\mathrm{GeV}^2}\right). \tag{6.10}$$

Histograms showing the Q^2 and the x_{Bj} distributions for both MC simulations before and after reweighting the MC events[10] with f_{Lepto} or f_{Ariadne} are presented in figure 6.24. The reweighting procedure improves the accuracy of the description in the high-Q^2 region and at higher x_{Bj} values as demonstrated with the ratio histograms. The effect on the cross sections, however, was very small, because the bin widths were chosen such that migration effects were sufficient small.

[9] The distributions were normalised such that the integral was equal to unity.
[10] All events were reweighted; not only selected events.

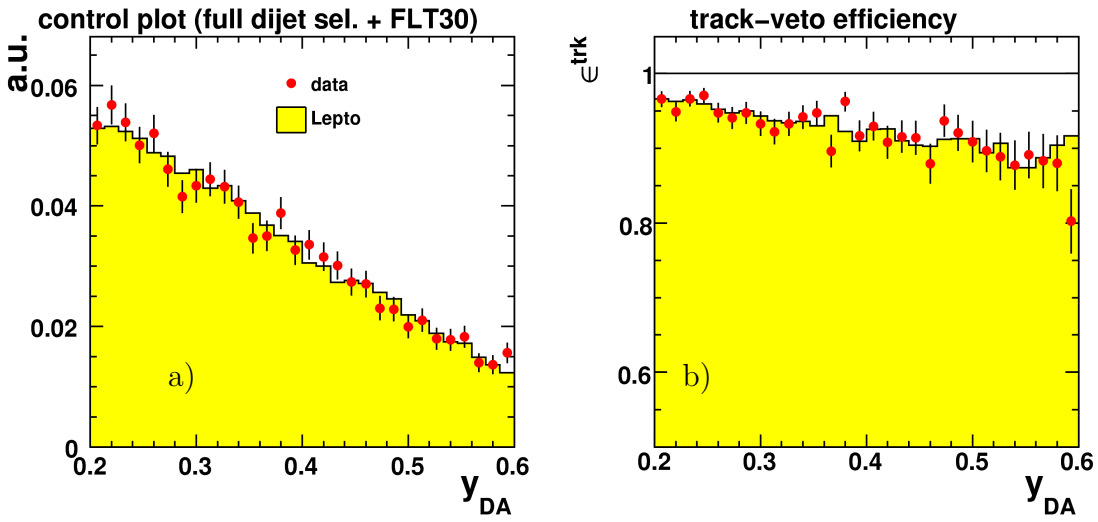

Figure 6.22: Study of the 2006/2007 e^+ track-veto efficiency as a function of y_{DA} for data and LEPTO **after** applying the correction: a) Control distributions. b) The track-veto efficiency ϵ^{trk}.

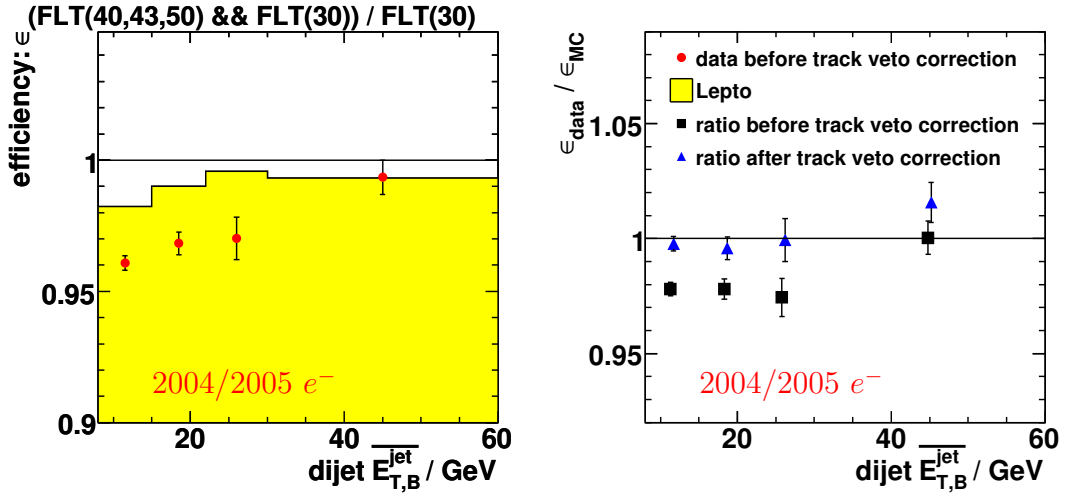

Figure 6.23: The 2004/2005 e^- trigger efficiency, ϵ, and the ratio $\epsilon_{\mathrm{data}}/\epsilon_{\mathrm{MC}}$ before and after applying the track-veto correction in regions of the average transverse energy in the Breit frame, $\overline{E_{T,\mathrm{B}}^{\mathrm{jet}}}$, of the dijet system.

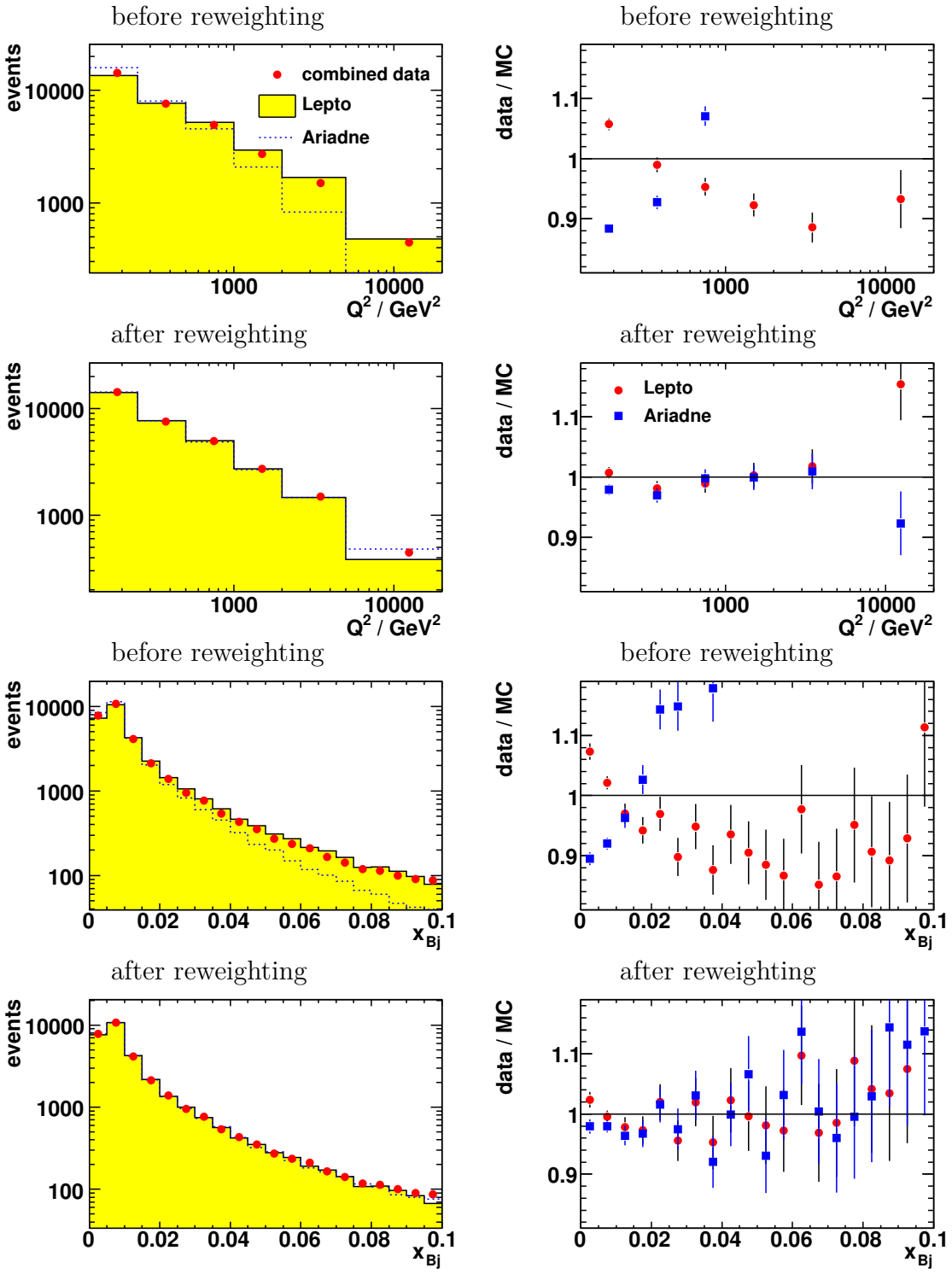

Figure 6.24: The Q^2 and the x_{Bj} distributions after selecting dijet events for LEPTO and ARIADNE before and after reweighting the MC events.

7. Unfolding the Data

A reasonably well understood detector is crucial for a precise cross-section measurement. Hence, the MC simulations must describe the shape of all relevant data distributions with an adequate and sufficient precision. Due to these requirements, control distributions for the final data sample are presented in this chapter after employing the corrections that were introduced and described in the previous chapter 6. It will be demonstrated that the MC simulations describe the data reasonably well.

Each detector has its own unique acceptance and response function. Therefore, the analysis was tuned and optimised under the consideration of the ZEUS detector performance in order to measure jets precisely. For this reason, detector related cuts that remove inefficient or not well understood detector regions were imposed in section 5. These detector properties lead to deviations of the measured quantities from the "true" physical observables, and it is not possible anymore to compare the results from different experiments. Therefore, it is mandatory to correct for these detector effects. In addition, the data are influenced by higher-order QED and electroweak contributions to physical processes. Furthermore, hadronisation corrections are necessary if the measurement is compared to next-to-leading order QCD predictions. These processes and effects were accounted for by unfolding the data distributions or correcting the theoretical predictions, respectively, with the application of bin-by-bin correction procedures determined from MC simulations. These corrections are described in this chapter as well.

7.1. The Final Data Sample

The MC simulations must describe the relevant data distributions with a sufficient precision to be suitable for unfolding the data. The inclusive DIS data sample and the inclusive jet samples were studied separately. In the following "uncorrected" distributions correspond to distributions corrected for all effects described in chapter 6. The correction that accounts for inactive material in front of the calorimeter is slightly different for Ariadne and Lepto. The data shown in the figures in this chapter were corrected with factors extracted from Lepto. The MC distributions were normalised to the data. In this section, histograms in linear and logarithmic scaling of the vertical axis are presented and discussed.

7.1.1. The Inclusive DIS Sample

The inclusive DIS data sample was obtained by applying all cuts described in chapter 5 omitting the cuts on jet quantities.

The plots in figure 7.1 show the uncorrected data, Lepto and Ariadne distributions of the z_{vtx} quantity, the energy of the scattered electron (E_{el}, E_{DA}) reconstructed with the electron and double-angle method respectively, the polar angle, θ_{el}, and

the azimuthal angle, ϕ_{el}, of the scattered electron and the scattering angle, γ_{had}, of the hadronic final state. The values of the imposed cuts are drawn as vertical lines indicating with small arrows the selected part of the data. The two MC simulations describe the data distributions reasonably well. The quantity E_{el} shows small deviations between the data and the MC simulations which is mainly caused by an inadequate calibration of the electron energy for the 2006–2007 data. The distinct drop in the ϕ_{el} distribution is caused by the geometry cuts that remove events in which the electron was scattered close to a RCAL solenoid support pipe.

Figure 7.2 shows uncorrected data and MC model distributions of the kinematic variables, Q^2, x_{Bj} and y, reconstructed with the double-angle method, of the total $E - p_z$ and of the individual electron and hadronic $E - p_z$. In general, these variables are well described by both MC simulations. The shape of the Q^2 distribution at larger values is also well described, which proves that the polarisation was sufficiently accounted for. In the high-$E - p_z$ region the data tend to be above the MC models. However, this region was excluded by a cut in order to restrict the measurement to a region where the data are well described. Furthermore, a small shift in the $E - p_z$ can be noted.

The distributions of the transverse momentum of the electron reconstructed with the double-angle method, $p_{T,DA}$, as well as with the electron method, $p_{T,el}$, of the transverse momentum, p_T^{had}, and the transverse energy, E_T^{had}, of the hadronic system, of the total transverse momentum, p_T, and of the variable $p_T/\sqrt{E_T}$, where E_T is the total transverse energy, are shown in figure 7.3. The observed E_T^{had} spectrum of Ariadne is harder than in the data, whereas Lepto describes the data distribution well. Furthermore, smaller deviations were found in the high-p_T region. In this region, Ariadne describes the data slightly better. The observed differences were covered by the systematic uncertainties.

The quality of the inclusive DIS data description by the two MC simulations is reasonably good.

7.1.2. The Inclusive Jet Sample

After selecting the inclusive DIS sample, the jets were reconstructed and events were selected by imposing the cuts described in chapter 5.5. In the following control histograms for the inclusive dijet and trijet samples are shown and discussed.

7.1.2.1. The Inclusive Dijet Sample

The plots in figure 7.4 show the uncorrected data in comparison with predictions from Lepto and Ariadne for the inclusive dijet variables in which the cross sections were measured. Presented are distributions of the kinematic variables Q^2 and x_{Bj}, of the average transverse energy in the Breit frame of the two jets, $\overline{E_{T,\text{B}}^{\text{jet}}}$, of the invariant dijet mass, M_{jj}, of $\log_{10}(\xi)$ and of η^*. In the higher Q^2 regime, the two MC simulations differ from each other with Lepto providing a slightly better data description. All the other variables shown in this figure are reasonably well described by the two MC simulations.

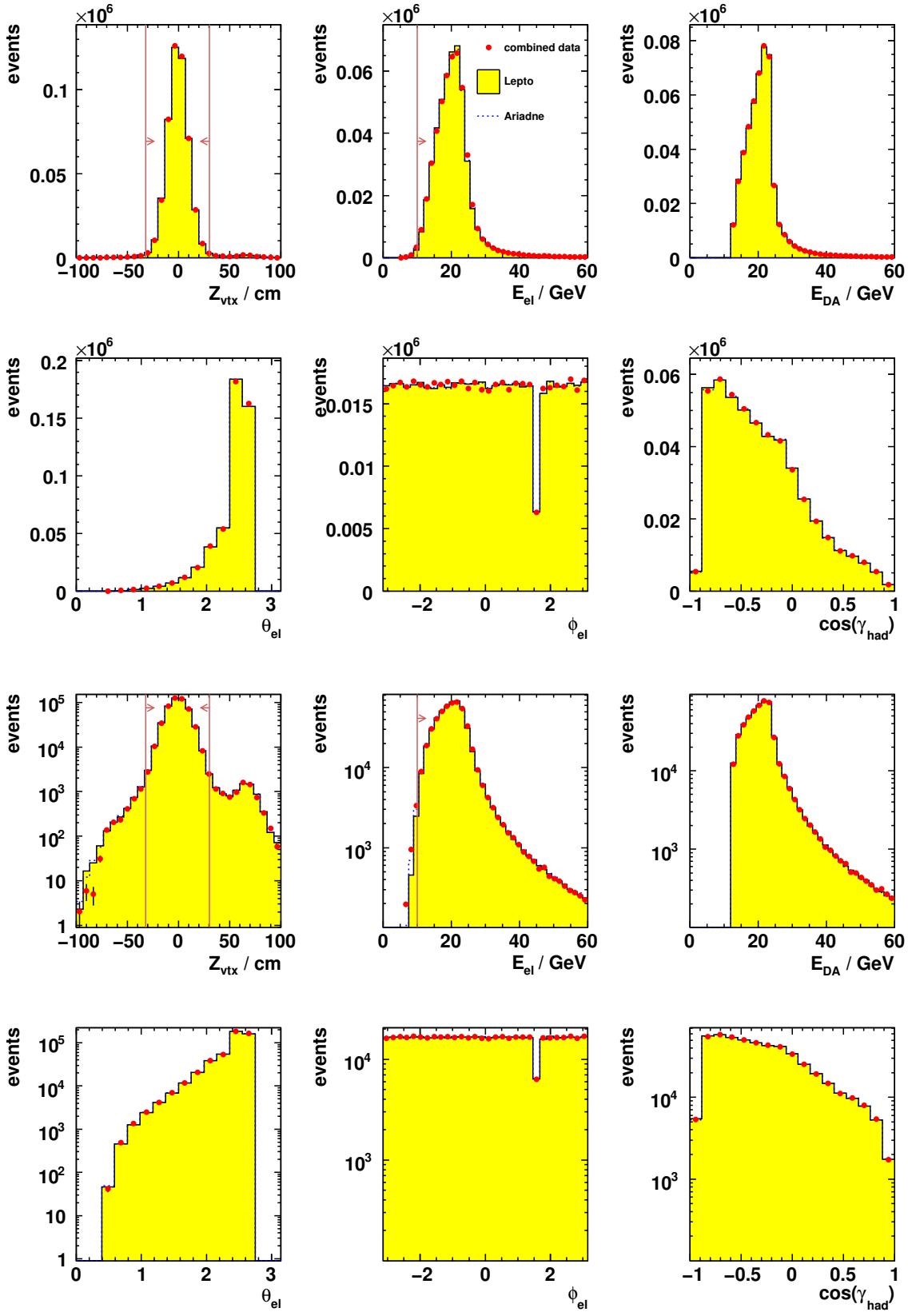

Figure 7.1: Comparison of uncorrected data and MC model predictions for inclusive DIS variables in linear and logarithmic vertical axis.

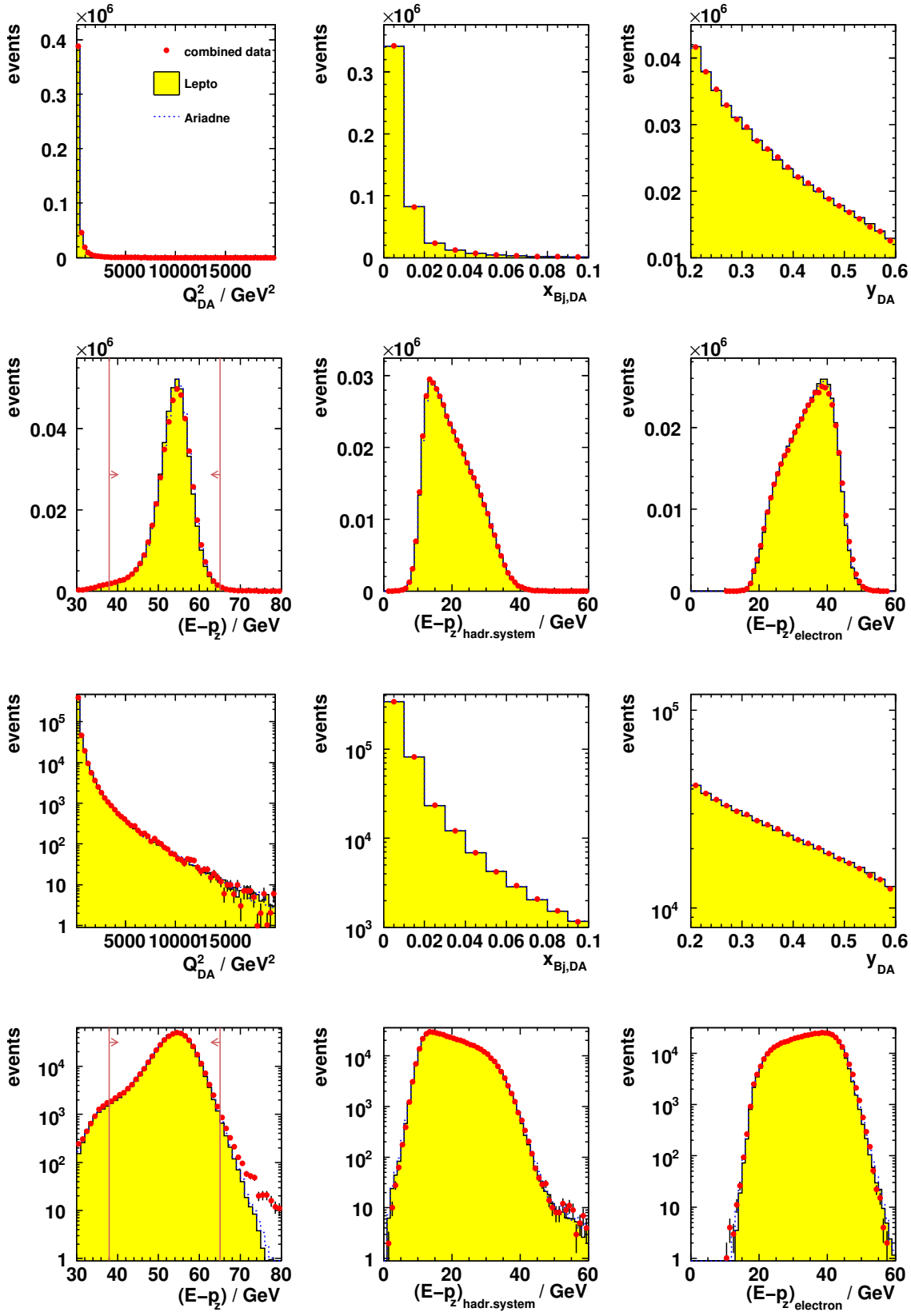

Figure 7.2: Comparison of uncorrected data and MC model predictions for inclusive DIS variables in linear and logarithmic vertical axis.

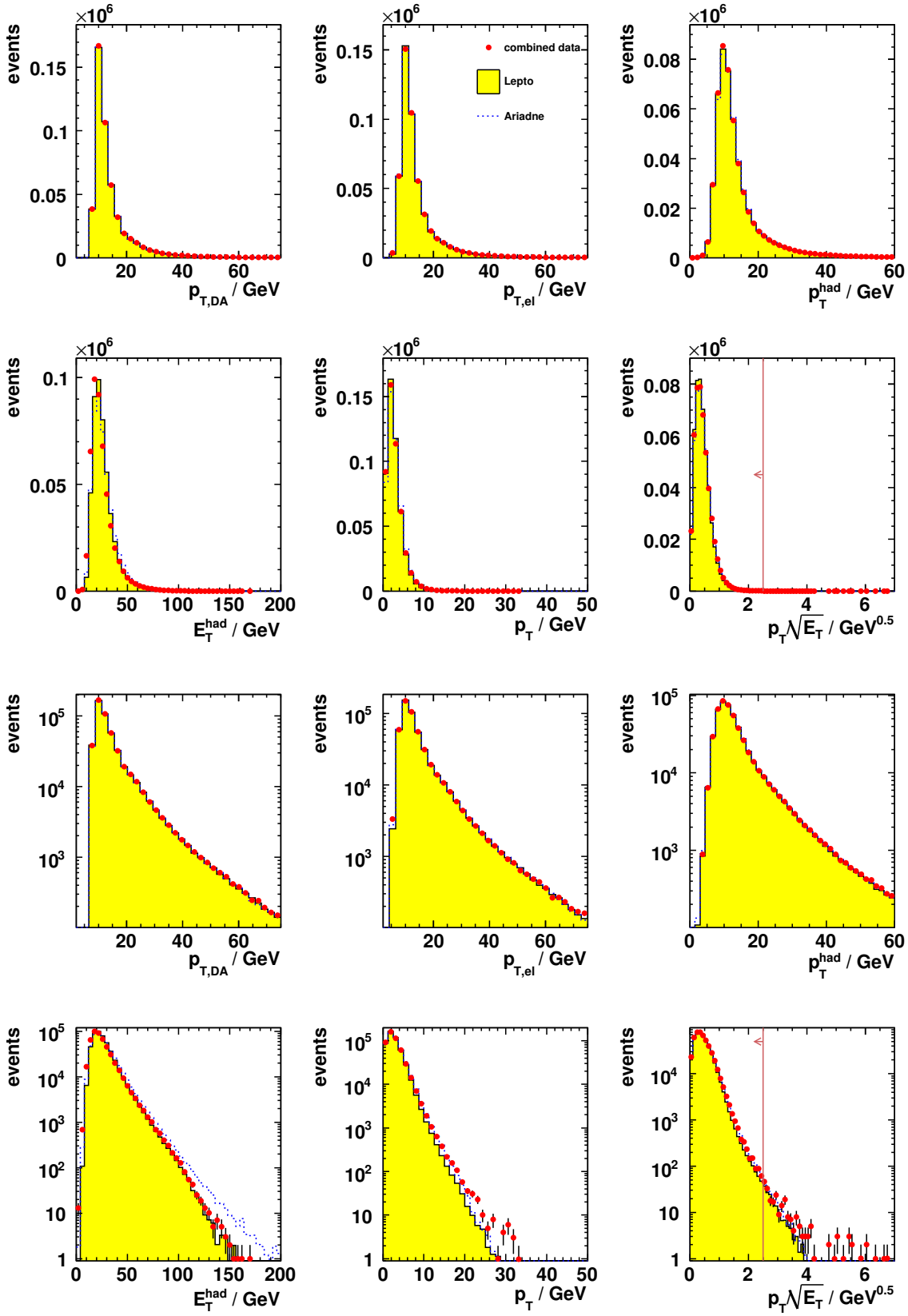

Figure 7.3: Comparison of uncorrected data and MC model predictions for inclusive DIS variables in linear and logarithmic vertical axis.

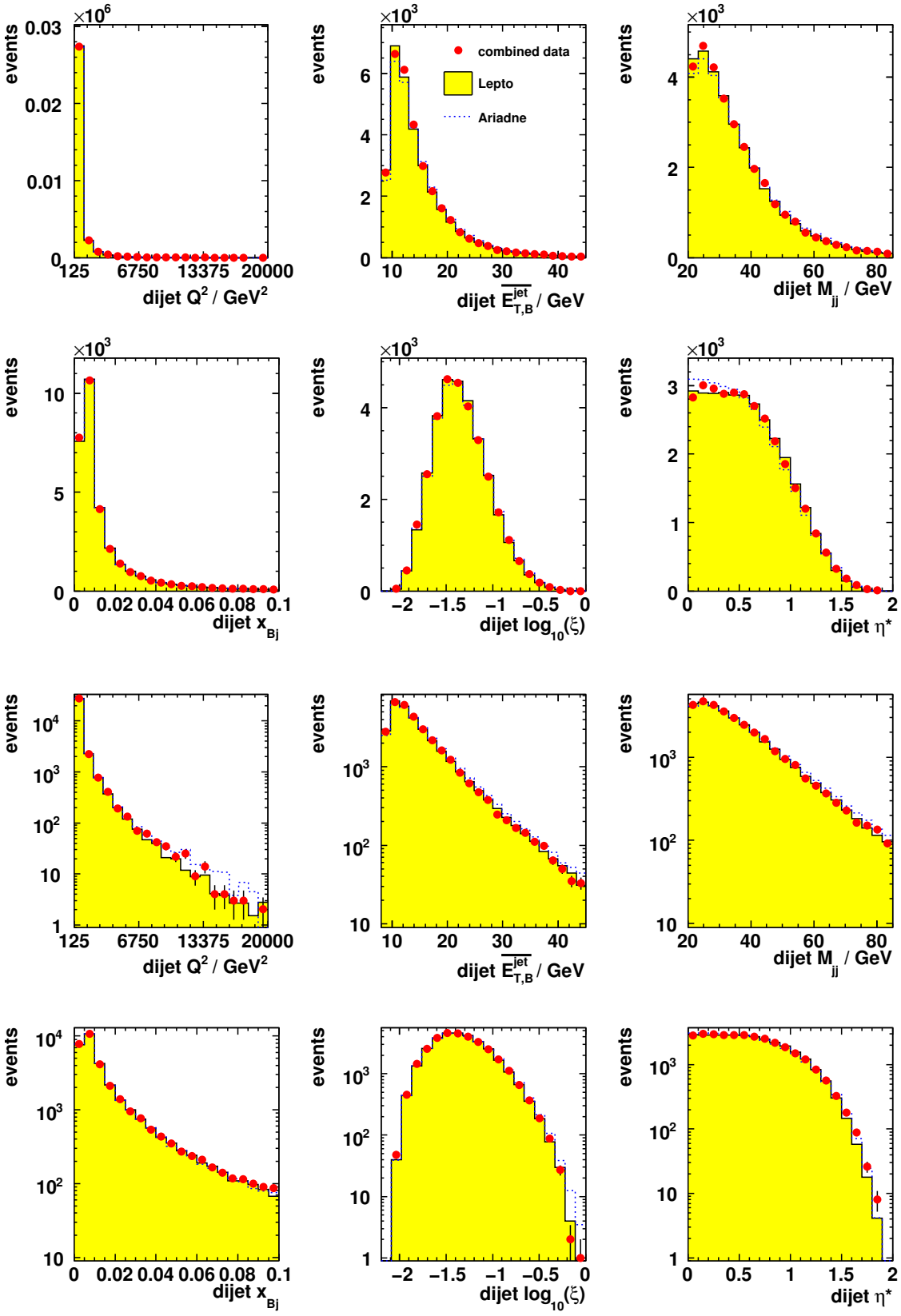

Figure 7.4: Comparison of uncorrected data and MC model predictions for inclusive dijet variables in linear and logarithmic vertical axis.

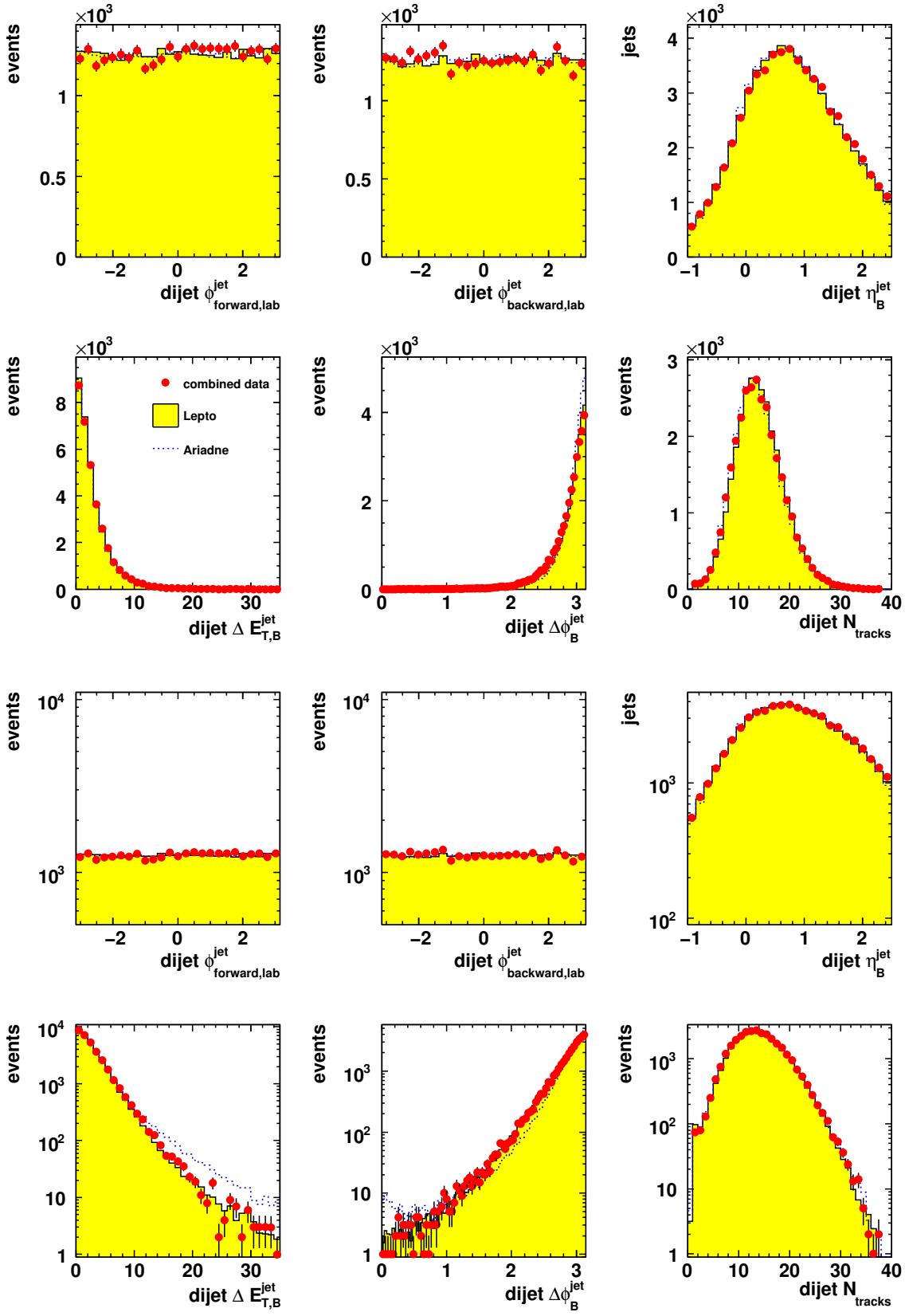

Figure 7.5: Comparison of uncorrected data and MC model predictions for inclusive dijet variables in linear and logarithmic vertical axis.

Figure 7.5 shows comparison plots of the azimuthal angle, $\phi^{\text{jet}}_{\text{lab}}$, of the most forward and of the most backward jet in the laboratory frame. In addition, distributions of the pseudorapidity, $\eta^{\text{jet}}_{\text{B}}$, of the two jets in the Breit frame, of the transverse energy and azimuthal difference, $\Delta E^{\text{jet}}_{T,\text{B}}$ and $\Delta\phi^{\text{jet}}_{\text{B}}$, of the two selected jets and of the total number of reconstructed tracks are shown. The quantities $\Delta E^{\text{jet}}_{T,\text{B}}$ and $\Delta\phi^{\text{jet}}_{\text{B}}$ are sensitive to higher-order QCD dynamics due to exact transverse momentum balance in the Breit frame between the two selected jets in LO. Since the MC simulations only provide a LO matrix element calculation for dijet production, the higher-order processes must be simulated by the modeling of the parton cascade. However, the data and MC agreement is reasonable, again, with LEPTO providing a slightly better description of the data.

Figures 7.6 and 7.7 present control distributions of the variables $\log_{10}(\xi)$ and $\overline{E^{\text{jet}}_{T,\text{B}}}$ in different regions of Q^2. The agreement between the data and the two MC simulations is good.

7.1.2.2. The Inclusive Trijet Sample

The plots in figure 7.8 show the uncorrected data distributions compared to the predictions from LEPTO and ARIADNE for inclusive trijet variables. Presented are distributions of the kinematic variables Q^2 and x_{Bj}, of the average transverse energy in the Breit frame of the three selected jets, $\overline{E^{\text{jet}}_{T,\text{B}}}$, of the invariant trijet mass, M_{jjj}, and of the transverse energy of the third jet, $E^{\text{jet3}}_{T,\text{B}}$. It can be noted that LEPTO and ARIADNE significantly differ from each other. Since the two MC simulations make use of different approaches for the modelling of the parton cascade, the measurement of trijet quantities has an enhanced sensitivity to details in the modelling of the parton cascade, because the third jet is generated solely in this cascade. In general, LEPTO provides a slightly better description of the investigated trijet variables. In some regions of the trijet phase space the agreement between the data and LEPTO is not satisfactory, e.g. for higher values of x_{Bj} and $\overline{E^{\text{jet}}_{T,\text{B}}}$. However, the observed deviations are covered by the systematic uncertainty (chapter 8), because in these regions ARIADNE provides a slightly better description.

Control distributions of the variable $\overline{E^{\text{jet}}_{T,\text{B}}}$ for the three selected jets in different regions of Q^2 are shown in figure 7.9. Within statistical uncertainties the two MC simulations describe the data in all investigated Q^2 regions.

7.1.3. Jet Profiles

In the last two sections, the quality of the inclusive DIS data sample and the inclusive dijet and trijet data samples were investigated by comparing uncorrected data distributions with MC predictions. In addition, in this section the jet profiles are investigated and discussed. A precise description of the energy flow inside a jet is mandatory in order to simulate the detector response to jets correctly. Therefore, jet profiles were investigated, because these quantities are sensitive to details of the simulation of the hadronic final state. For this study the dijet selection was omitted and all jets with $E^{\text{jet}}_{T,\text{B}} > 8$ GeV were selected.

Figures 7.10 and 7.11 show the average differential transverse energy in the laboratory frame per jet as a function of the azimuthal difference, $\phi^{\text{jet}}_{lab} - \phi^{\text{cell}}_{\text{lab}}$, between the CAL cell and the jet axis in different regions of η^{jet}_{lab} and $E^{\text{jet}}_{T,lab}$. Only those CAL cells that were assigned to the jet were considered. Both ARIADNE and LEPTO describe the shape of the jet profile distributions. Only in the central part close to the jet axis the description is slightly worse, but covered by the systematic uncertainty. With increasing $E^{\text{jet}}_{T,lab}$ the azimuthal expansion of the jets produced by ARIADNE starts to deviate from the data, whereas LEPTO is closer to the data.

After applying the full dijet selection, the average differential transverse energy in the Breit frame as a function of the azimuthal difference between the jet with the greatest $E^{\text{jet}}_{T,\text{B}}$ and all cells was investigated. Figure 7.12 shows these energy flow distributions for data and the two MC simulations separately for the four data-taking periods. The distributions were normalised to the number of selected dijet events. In contrast to the plots shown in figure 7.10 and 7.11, in this study all CAL cells were considered. First, it should be noted that no distinct and significant differences between the periods were found. The two pronounced maxima at 0 and π were caused by the two selected jets, because the transverse momentum in the Breit frame is conserved. Since the azimuthal difference was determined with respect to the jet with the greatest $E^{\text{jet}}_{T,\text{B}}$, the obtained distributions are asymmetric. A small disagreement between the data and the MCs can be seen in the pedestal region. However, the distribution in the range of the two selected jets is reasonably well described; again LEPTO provides a better description of the data.

7.1.4. Jet Energy Resolution

The measured values of jet quantities differ from the "true" values. The spread of the difference ("meas. - true") – the resolution – is one important quantity that determines the quality of the measurement. The precision of this analysis is limited by the measurement resolution of the jet energies. Therefore, a dedicated study of the jet energy resolution was performed.

The study was divided into two parts:

1. In order to determine the jet energy resolution only from the data, a sample of jets was selected that allowed to compare the jet transverse energy, $E^{\text{jet}}_{T,\text{lab}}$, in the laboratory frame with a reference scale. For this purpose, the single jet selection, which was used for the investigation of the jet energy scale (chapter 6.3.1.1), was applied to the data. The double-angle method provides for each event an independent measurement of the transverse energy ($E_{T,\text{DA}}$) in the event. Thus, by determining the distribution of

$$\frac{E^{\text{jet}}_{T,\text{lab}} - E_{T,\text{DA}}}{E_{T,\text{DA}}} \tag{7.1}$$

   in regions of $E_{T,\text{DA}}$, the resolution was approximated by fitting a Gaussian function to these distributions. One standard deviation was taken as relative jet energy resolution, σ_{rel}.

2. In a rather independent study, the jet energy resolution was determined purely from the MC by making use of the available hadron-level information. The momenta of the measured jets on detector level were compared to those on hadron level after the application of the jet matching procedure described in section 6.3.2. For matched pairs of jets, distributions of

$$\frac{E_{T,\mathrm{lab}}^{\mathrm{det,jet}} - E_{T,\mathrm{lab}}^{\mathrm{had,jet}}}{E_{T,\mathrm{lab}}^{\mathrm{had,jet}}} \tag{7.2}$$

in regions of $E_{T,\mathrm{lab}}^{\mathrm{had,jet}}$ were obtained, fitted with Gaussian functions and σ_{rel} was extracted. The quantity $E_{T,\mathrm{lab}}^{\mathrm{det,jet}}$ ($E_{T,\mathrm{lab}}^{\mathrm{had,jet}}$) is the jet transverse energy on detector level (hadron level) in the laboratory frame.

In figure 7.13 the results of this study are depicted. Shown is the relative jet energy resolution, σ_{rel}, as a function of the reference transverse energy, $E_{T,\mathrm{DA}}$ or $E_{T,\mathrm{lab}}^{\mathrm{had,jet}}$ respectively, for data and for LEPTO. The prediction for the jet energy resolution obtained by using purely MC information was found to be slightly smaller than the extracted resolution from the data. An explanation could be that the resolution of $E_{T,\mathrm{DA}}$ was neglected. Hence, the data points indicate the convolution of the jet energy resolution and the resolution of the quantity $E_{T,\mathrm{DA}}$.

For a sampling calorimeter the resolution scales approximately with $\Delta E/E \propto 1/\sqrt{E}$. Therefore, the data points were fitted with

$$\sigma_{\mathrm{rel}} = \frac{a}{\sqrt{E_T}}, \tag{7.3}$$

which gives $a = 0.5616 \pm 0.0031$. The fit result is indicated as a dashed line in figure 7.13. For a precise measurement of the resolution the goodness of the fit is not satisfactory, but for a rough estimate of the jet energy resolution the result is reasonable. The determined value for jets is significantly larger than the resolution of $0.35/\sqrt{E}$ [103] for single hadrons without absorber material in front of the calorimeter.

7.2. Acceptance Correction

Owing to the limited detector acceptance, the detector resolution and the (possibly non-linear) response of the individual detector components, an unfolding method has to be applied to the measured data. Several different methods are available – for instance iterative procedures based on Bayesian statistics [185] or methods that extract multiplicative estimators for the acceptance correction from MC simulations[1]. The latter procedure was employed in this analysis and is described in the following.

The acceptance correction, C_i^A, can be determined from MC simulations by calculating the ratio of the number of selected events on hadron level, N_i^{had}, and the corresponding number on detector level,N_i^{det}, in bin i:

$$C_i^A = \frac{N_i^{\mathrm{had}}}{N_i^{\mathrm{det}}} \tag{7.4}$$

[1] An overview over several unfolding methods can be found in [186].

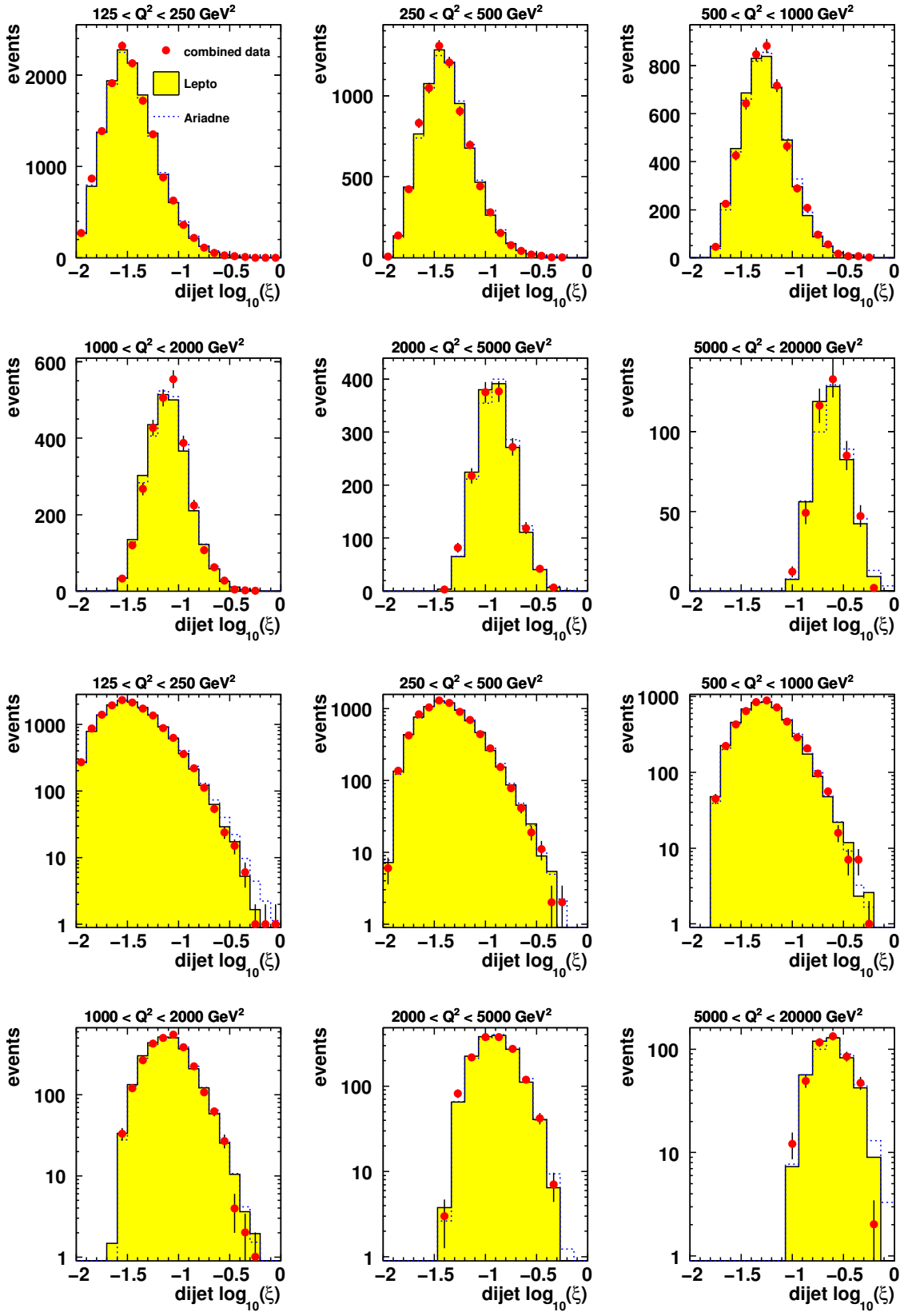

Figure 7.6: Comparison of uncorrected data and MC model predictions after the inclusive dijet selection for the variable $\log_{10}(\xi)$ in different regions of Q^2.

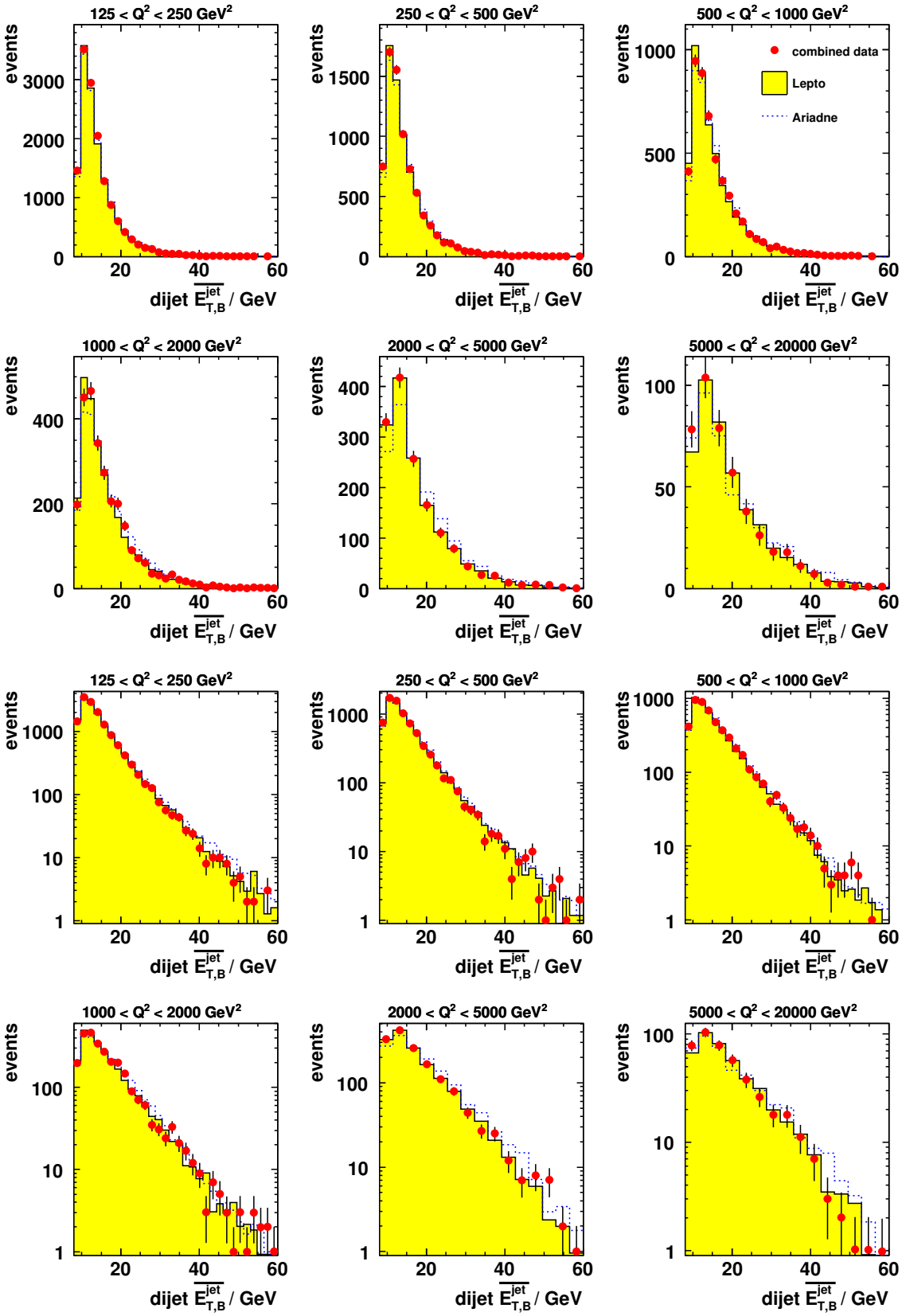

Figure 7.7: Comparison of uncorrected data and MC model predictions after the inclusive dijet selection for the variable $\overline{E^{\mathrm{jet}}_{T,\mathrm{B}}}$ in different regions of Q^2.

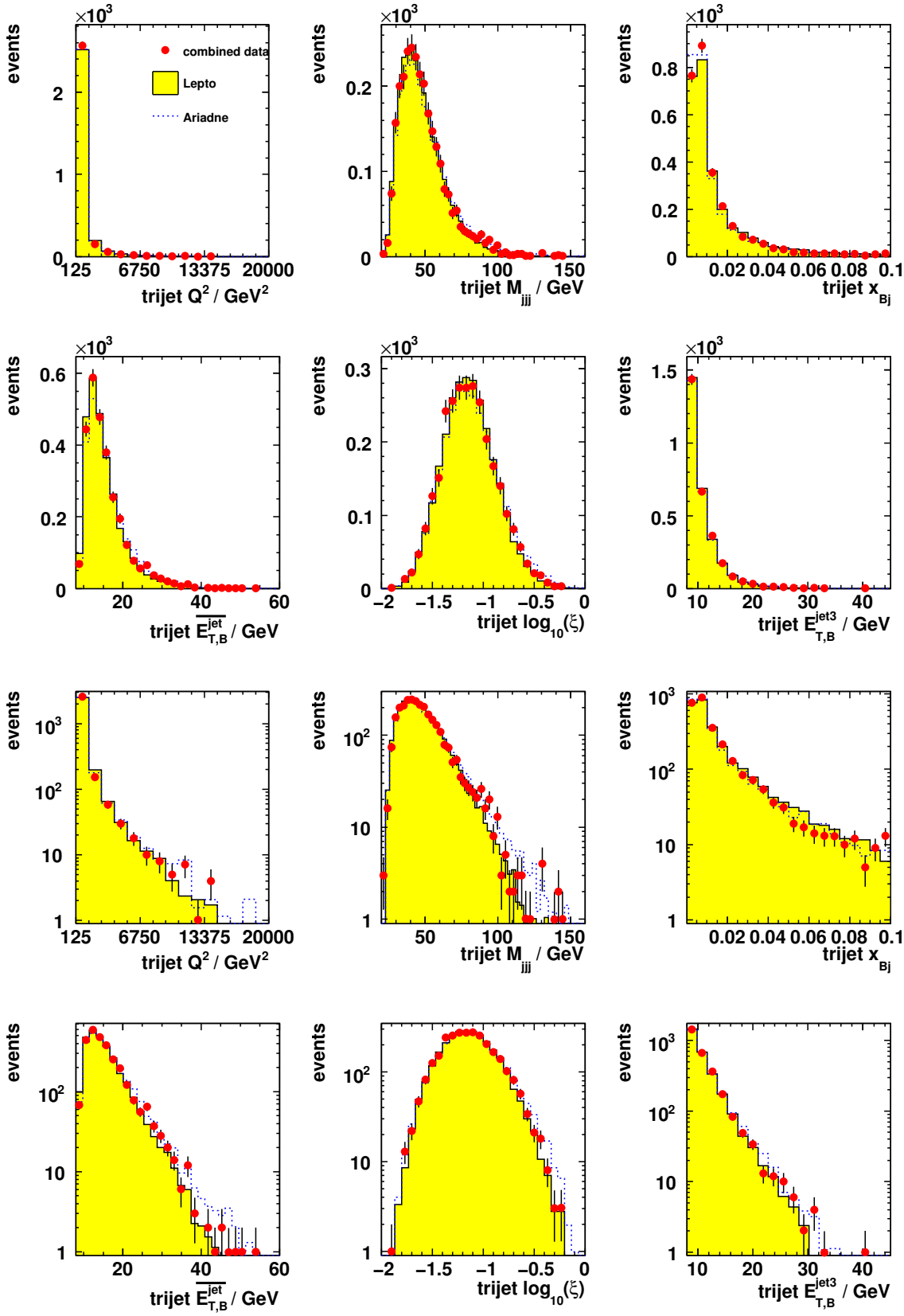

Figure 7.8: Comparison of uncorrected data and MC model predictions after the inclusive trijet selection.

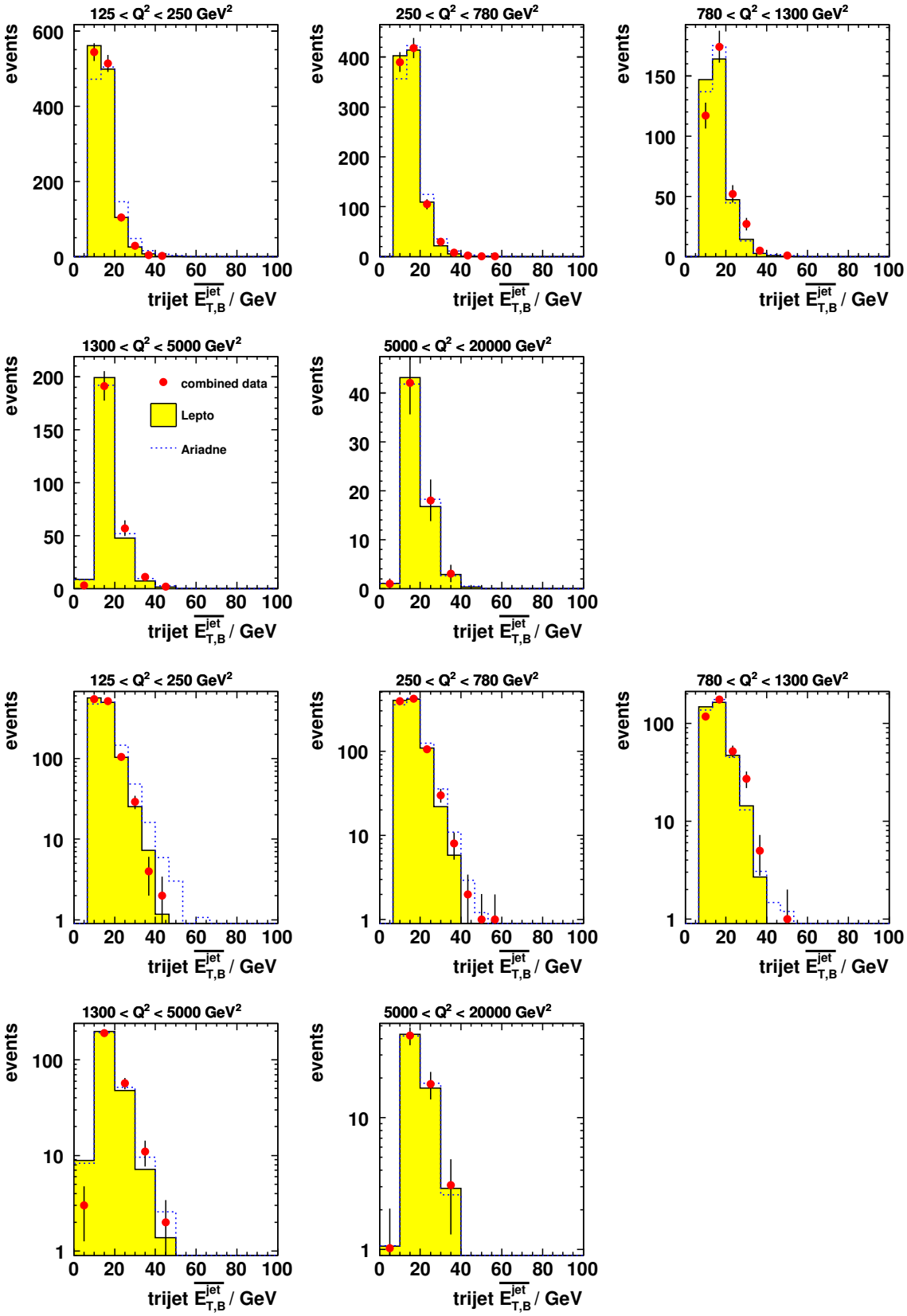

Figure 7.9: Comparison of uncorrected data and MC model predictions after the inclusive trijet selection for the variable $\overline{E^{\mathrm{jet}}_{T,\mathrm{B}}}$ in different regions of Q^2.

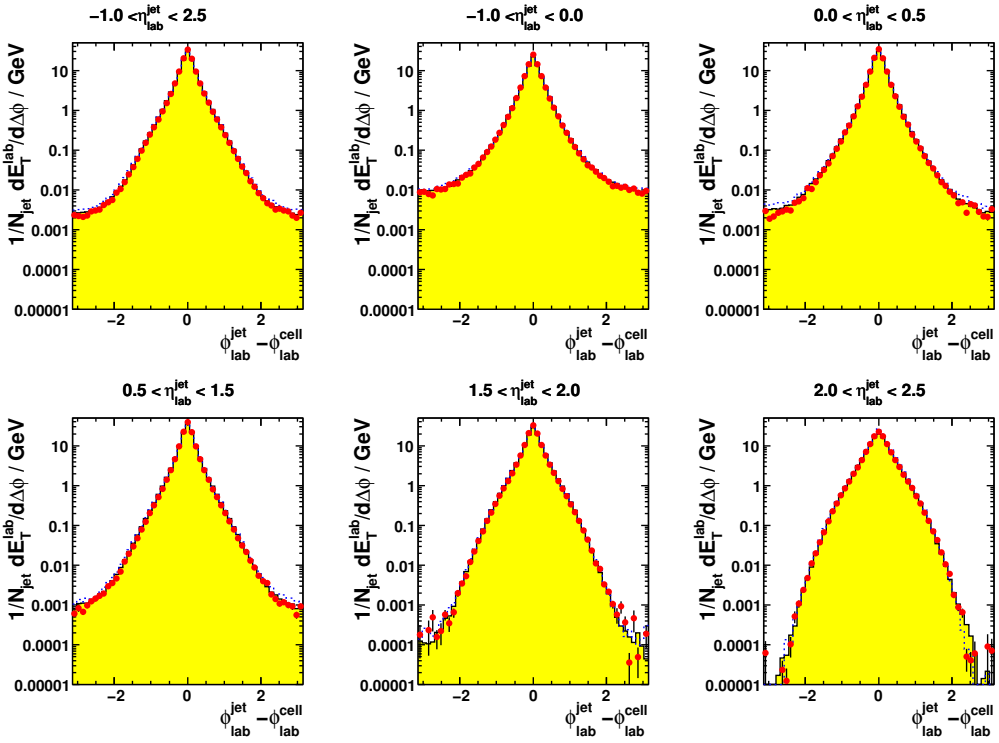

Figure 7.10: Jet profiles as a function of $\Delta\phi = \phi^{\text{jet}}_{\text{lab}} - \phi^{\text{cell}}_{\text{lab}}$ in different regions of $\eta^{\text{jet}}_{\text{lab}}$ with logarithmic y-axis scaling.

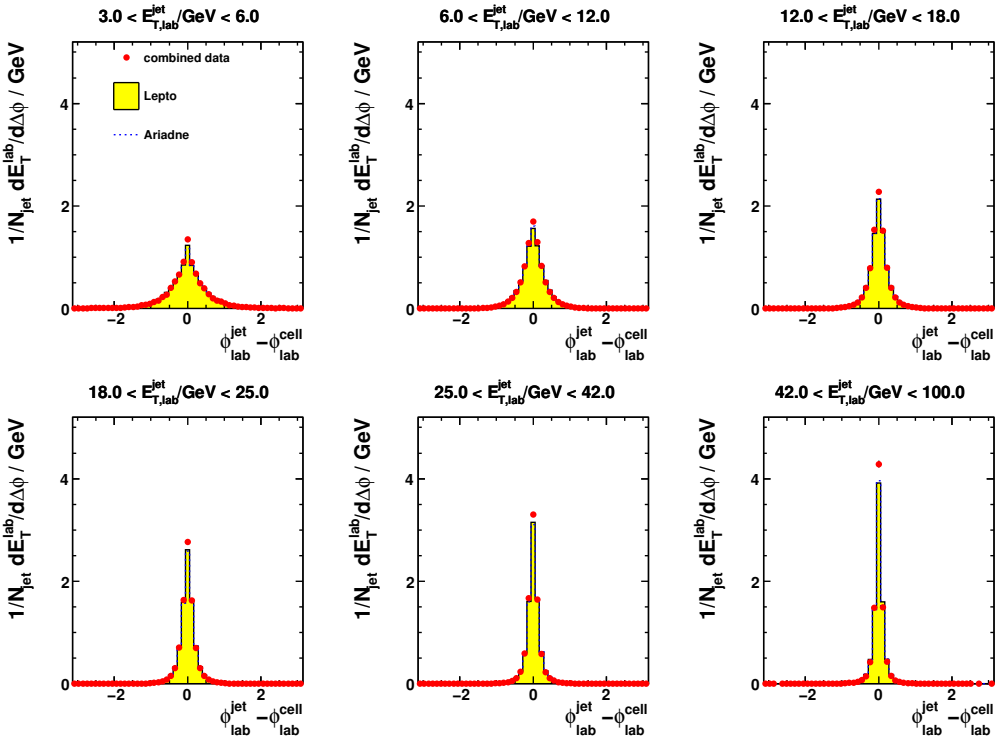

Figure 7.11: Jet profiles as a function of $\Delta\phi = \phi^{\text{jet}}_{\text{lab}} - \phi^{\text{cell}}_{\text{lab}}$ in different regions of $E^{\text{jet}}_{T,\text{lab}}$ with linear y-axis scaling.

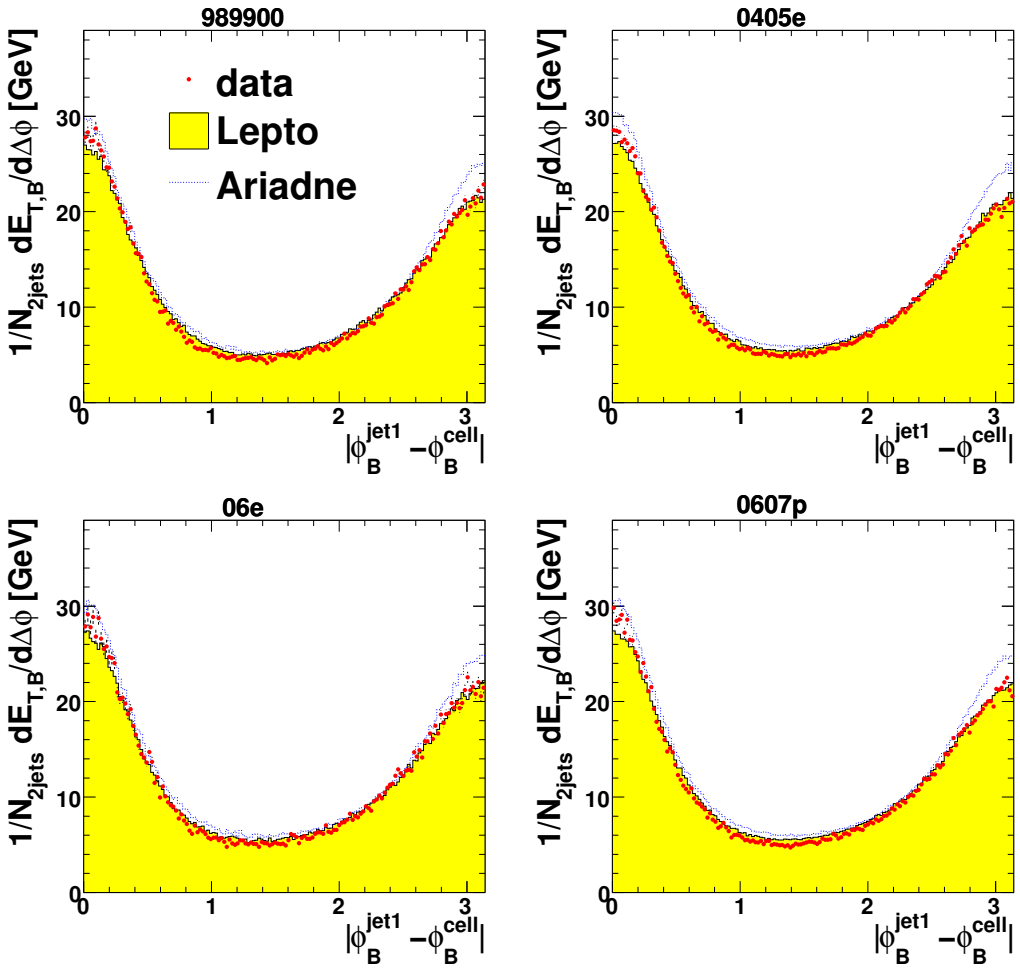

Figure 7.12: The average differential transverse energy in the Breit frame per dijet event as a function of the azimuthal difference between the jet with the highest $E_{T,\mathrm{B}}^{\mathrm{jet}}$ and the CAL cells.

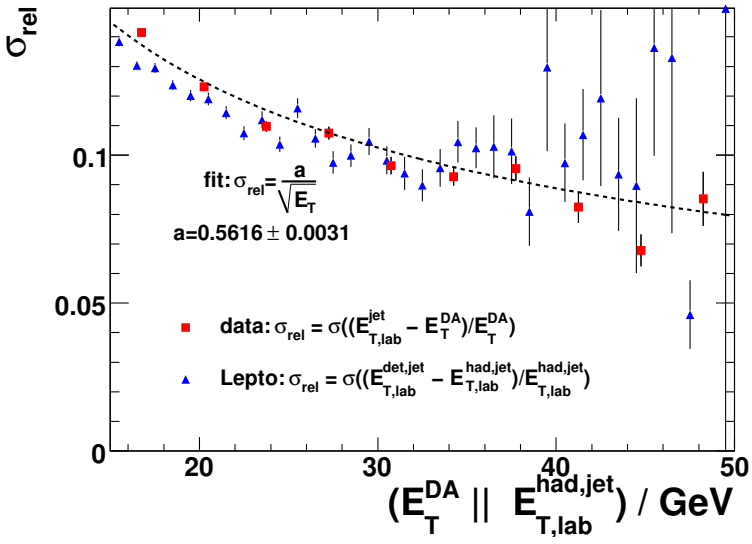

Figure 7.13: The relative jet energy resolution, σ_{rel}, as a function of the reference transverse energy, $E_{T,\mathrm{DA}}$ or $E_{T,\mathrm{lab}}^{\mathrm{had,jet}}$, and the result of a fit to the data.

The acceptance correction is a multiplicative quantity that corrects the data for detector effects. In order to be able to use C_i^A for the data correction, two criteria have to be fulfilled:

1. The detector simulation has to provide a good description of the shape of all relevant data distributions. This was demonstrated in the section 7.1.

2. The migration between neighbouring bins must be sufficiently small.

7.2.1. Migration, Efficiency and Purity

If the resolution of the detector in a certain bin of an observable is worse than the chosen bin width or of comparable size, then the migration of events between bins is large. The MC simulations must describe these bin-to-bin migrations as well as the migrations in and out of the jet sample. The migrations were investigated by using LEPTO.

The efficiency ϵ in bin i is defined as

$$\epsilon_i = \frac{N_i^{\text{det\&had}}}{N_i^{\text{had}}}, \tag{7.5}$$

where N_i^{had} is the number of events on hadron level and $N_i^{\text{det\&had}}$ the number of events that were generated and reconstructed in the same bin i.

The purity p is defined as

$$p_i = \frac{N_i^{\text{det\&had}}}{N_i^{\text{det}}}. \tag{7.6}$$

It was required that ϵ_i and p_i were typically greater than 40%. The ratio between efficiency ϵ_i and purity p_i is equal to the acceptance correction

$$C_i^A = \frac{p_i}{\epsilon_i} = \frac{N_i^{\text{had}}}{N_i^{\text{det}}} \tag{7.7}$$

in bin i.

The variables that are used in the calculation of efficiency, purity and acceptance correction are statistically correlated. Thus, the statistical uncertainties cannot be calculated by just adopting a simple error propagation method. Hence, the definitions 7.5, 7.6 and 7.7 were transformed into uncorrelated quantities. If a is the number of events reconstructed and generated in the same bin, b the number of events generated but not reconstructed in the same bin and c the number of events reconstructed but not generated in the same bin, then the variables p_i, ε_i and C_i^A are given by

$$p_i = \frac{a_i}{a_i + c_i}, \qquad \varepsilon_i = \frac{a_i}{a_i + b_i}, \qquad C_i^A = \frac{a_i + b_i}{a_i + c_i}. \tag{7.8}$$

The statistical uncertainties can now be determined from the uncorrelated variables a_i,b_i and c_i with error propagation.

Figures 7.14 shows as one example the two-dimensional migration matrices for inclusive dijet and trijet cross sections as a function of Q^2. The area of each box is

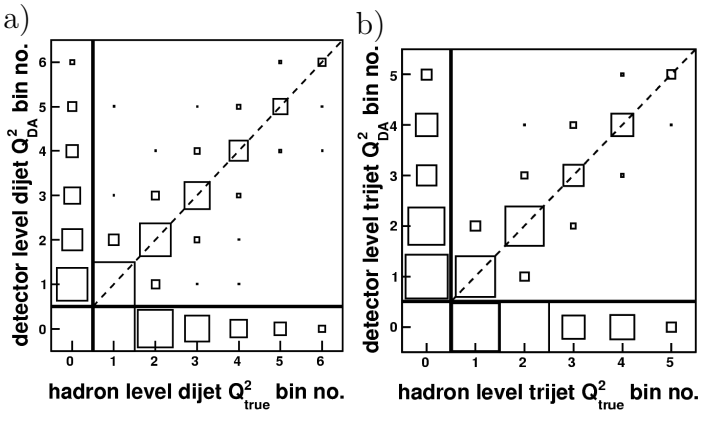

Figure 7.14: Migration matrices for the inclusive a) dijet and b) trijet cross-sections $\frac{d\sigma}{dQ^2}$.

proportional to the number of entries. Events in the bins of column (row) number 0 were not selected on hadron (detector) level. The smaller the effect of the migration is, the larger is the number of entries of the diagonal elements, which are marked by a hatched line.

The migration matrices can be used to determine the efficiency, the purity and the acceptance correction for each cross-section bin. Figure 7.16 shows these quantities for the single-differential[2] inclusive dijet cross sections. For the single-differential inclusive trijet cross sections these quantities are indicated in figure 7.15. It should be mentioned that the bin widths were adjusted such that a reasonable compromise between the number of bins and the amount of migration was obtained. The efficiency in the second Q^2 bin is lower compared to the other bins due to events in which the electron was scattered into the crack region between the RCAL and the BCAL. Except for this region, the acceptance correction has a size of about 30%. In most of the bins the efficiency and the purity are greater than or close to 40%.

7.3. QED and Electro-Weak Contributions

Higher-order QED processes like initial- and final-state radiation, internal loops, the running of α_{em} have influenced the measurement presented here. In addition, at higher values of Q^2, electro-weak effects such as the Z^0-boson exchange and the γ/Z^0 interference become important.

The data were corrected for QED effects. In contrast, the electro-weak correction factors were applied to the pQCD calculations.

The MC simulations used in this analysis have included QED effects (see chapter 4 for details). Hence, correction factors were derived by using a second MC sample generated with the same settings but without the simulation of higher-order QED processes. The QED correction factors,

$$C_i^{\mathrm{QED}} = \frac{\sigma_i^{\mathrm{BORN}}}{\sigma_i^{\mathrm{QED}}}, \tag{7.9}$$

consist of the cross-sections predictions for bin i with higher-order QED effects, σ_i^{QED}, and the Born cross section, σ_i^{BORN}.

[2]The efficiencies, the purities and the acceptance corrections for the double-differential cross sections are shown in appendix A.3.

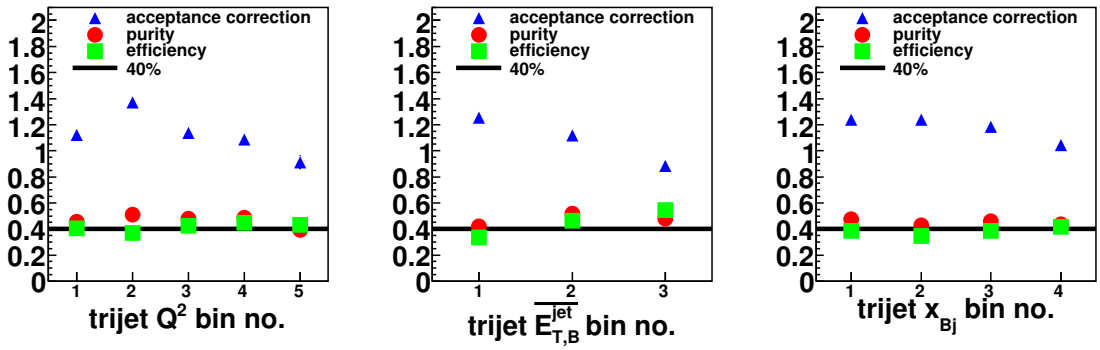

Figure 7.15: Efficiencies, purities and acceptance corrections for the single-inclusive trijet cross sections.

The jet data were compared with fixed-order pQCD predictions from DISENT or NLOJET++. These calculations do not include the contributions from Z^0 and γ/Z^0-interference processes. Thus, electro-weak correction factors for the theoretical calculations were determined with two MC samples; one sample was generated with electro-weak effects, and the other sample without these effects, which gives

$$C_i^{\mathrm{EW}} = \frac{\sigma_i^{\mathrm{Z0}}}{\sigma_i^{\mathrm{NOZ0}}}, \tag{7.10}$$

where σ_i^{Z0} is the cross section including electro-weak effects and σ_i^{NOZ0} is without these contributions. A LEPTO stand-alone executable [187] was used for the determination of these correction factors. Since the inclusive DIS cross section for electrons and positrons is different (see chapter 2.1.2), the quantity C_i^{EW} was determined for electrons and positrons separately. The applied electro-weak correction was a luminosity weighted average of these individual corrections. Owing to the large luminosity of these MC samples, the statistical uncertainties are in general much smaller than the data statistical uncertainties and were set to 0.

Figure 7.17 shows the obtained QED and electro-weak correction factors in bins of the dijet cross-section measurements. Figures that present these corrections for the double-differential measurement and for the trijet cross sections are shown in appendix A.3. The electro-weak contributions to the cross section increase with increasing virtuality Q^2. The QED correction factors are in general flat and have a typical size of 5%.

7.4. Hadronisation Corrections

The corrected data distributions can not be compared directly with pQCD calculations, because the latter are predictions for the partonic jet cross sections. Hence, the theoretical predictions have to be corrected for the fragmentation of final-state partons into hadrons.

The hadronisation correction factors, $h_i = \sigma_i^{\mathrm{hadron}}/\sigma_i^{\mathrm{parton}}$, where $\sigma_i^{\mathrm{hadron}}$ is the jet cross section in bin i on hadron level and $\sigma_i^{\mathrm{parton}}$ the jet cross section on parton level,

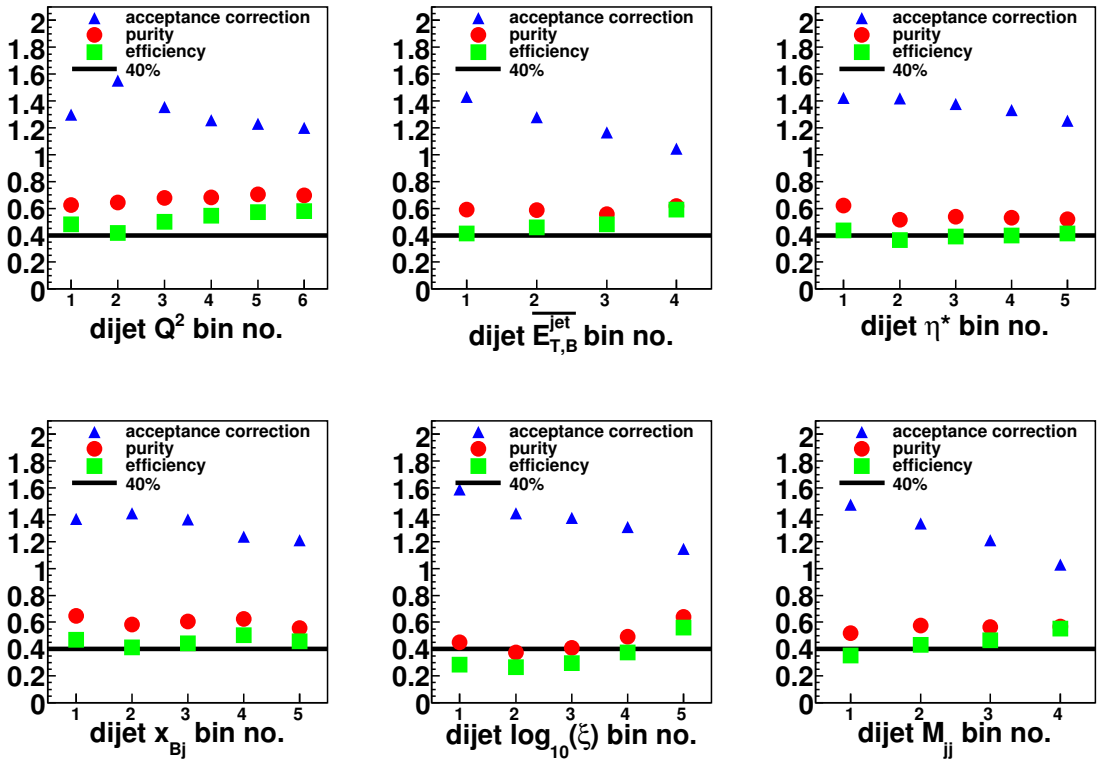

Figure 7.16: Efficiencies, purities and acceptance corrections for the single-inclusive dijet cross sections.

were determined with ARIADNE and LEPTO separately. The applied correction was calculated by averaging the individual results from LEPTO and ARIADNE; half of the difference between these two was treated as hadronisation uncertainty.

Figures 7.18 and 7.19 show the hadronisation corrections for the single-inclusive dijet and trijet production. For dijet production the size of the correction is typically about 5%, and about 15% for the trijet production. The resulting uncertainty was mostly less than 2% (3.5%) for the production of dijets (trijets). The plots for the double-differential measurements can be found in appendix A.3. Unless otherwise stated, the term "NLO" will from here on refer to the fully corrected theory predictions including hadronisation and electro-weak effects.

7.5. Cross Section Determination

The single-differential[3] inclusive cross-section $\frac{d\sigma}{dx}$ of the observable x in bin i is obtained using the relation

$$\frac{d\sigma_i}{dx} = \frac{N_i}{L \cdot k_i} \cdot C_i^A \cdot C_i^{\mathrm{QED}}, \tag{7.11}$$

[3]A similar definition can be found for double-differential cross sections.

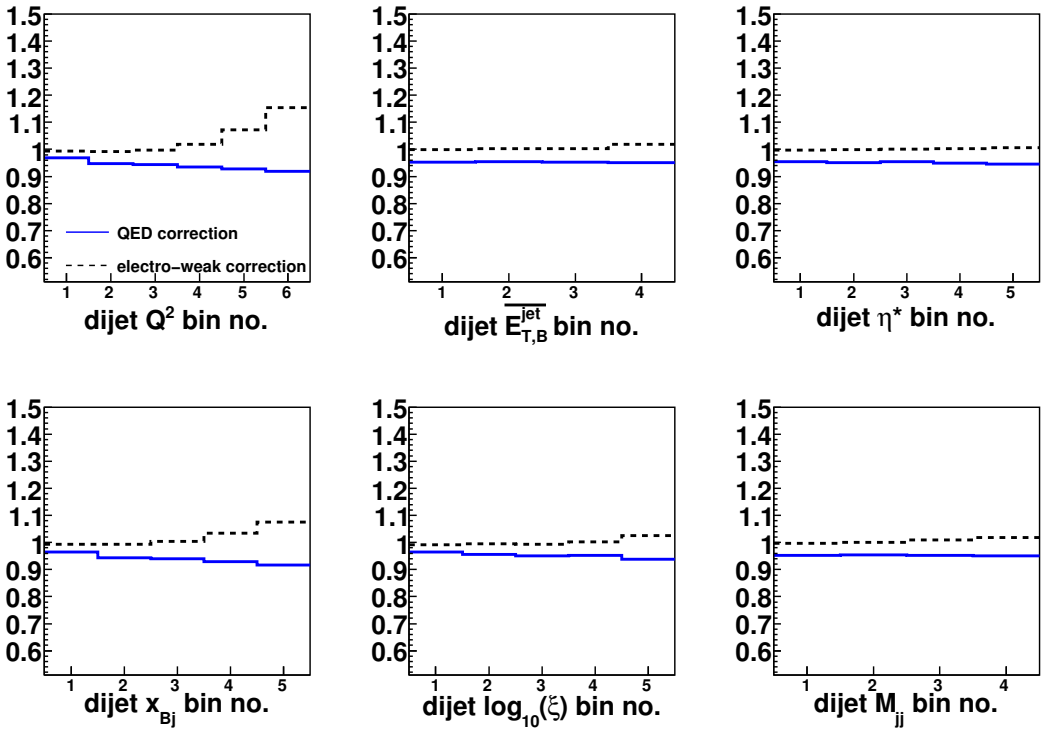

Figure 7.17: Electro-weak and QED corrections for the single-inclusive dijet cross sections. The corrections correspond to the full data sample including electron and positron data.

where N_i is the number of selected data events, L the integrated luminosity of the data sample, C_i^A the acceptance correction, k_i the bin width and C_i^{QED} the correction that accounts for QED effects. The statistical uncertainty of $\frac{d\sigma_i}{dx}$ can be calculated by applying an error propagation method, which gives with $\Xi_i = \frac{d\sigma_i}{dx}$ and the statistical uncertainties of the acceptance correction, ΔC_i^A, and the statistical uncertainty of the data, ΔN_i, the following statistical uncertainty of the cross section:

$$\Delta\Xi_i = \sqrt{\left(\frac{\Delta N_i}{L \cdot k_i} \cdot C_i^A \cdot C_i^{\mathrm{QED}}\right)^2 + \left(\frac{N_i}{L \cdot k_i} \cdot \Delta C_i^A \cdot C_i^{\mathrm{QED}}\right)^2} \tag{7.12}$$

The quantity ΔN_i was approximated with $\Delta N_i = \left(\sum_j w_j^2\right)^{\frac{1}{2}}$, where w_j is the weight of event j.

The cross-section ratio $R_{3/2}$ between trijet and dijet cross sections is obtained by using equation 7.11:

$$R_{3/2}^i = \frac{N_i^{3\mathrm{jet}} \cdot C_i^{A,3\mathrm{jet}} \cdot C_i^{\mathrm{QED},3\mathrm{jet}}}{N_i^{2\mathrm{jet}} \cdot C_i^{A,2\mathrm{jet}} \cdot C_i^{\mathrm{QED},2\mathrm{jet}}}. \tag{7.13}$$

The quantities $N_i^{3\mathrm{jet}}$ and $N_i^{2\mathrm{jet}}$ in this formula are statistically correlated and it is necessary to transform them into uncorrelated variables. If u is the number of

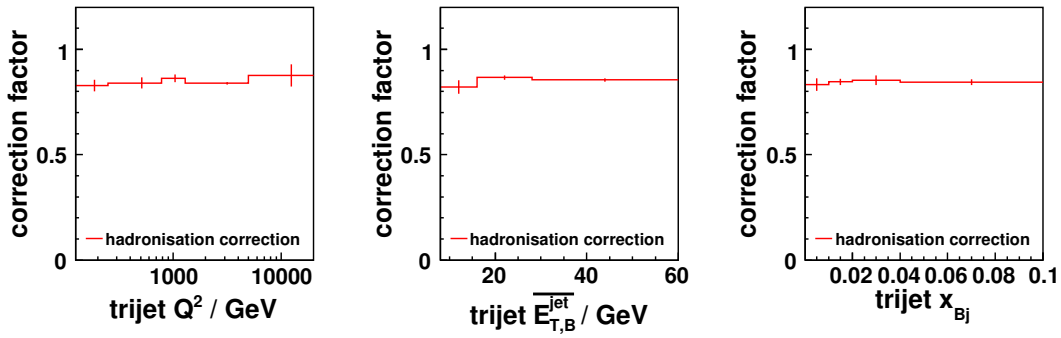

Figure 7.18: Hadronisation correction factors for the single-inclusive trijet cross sections.

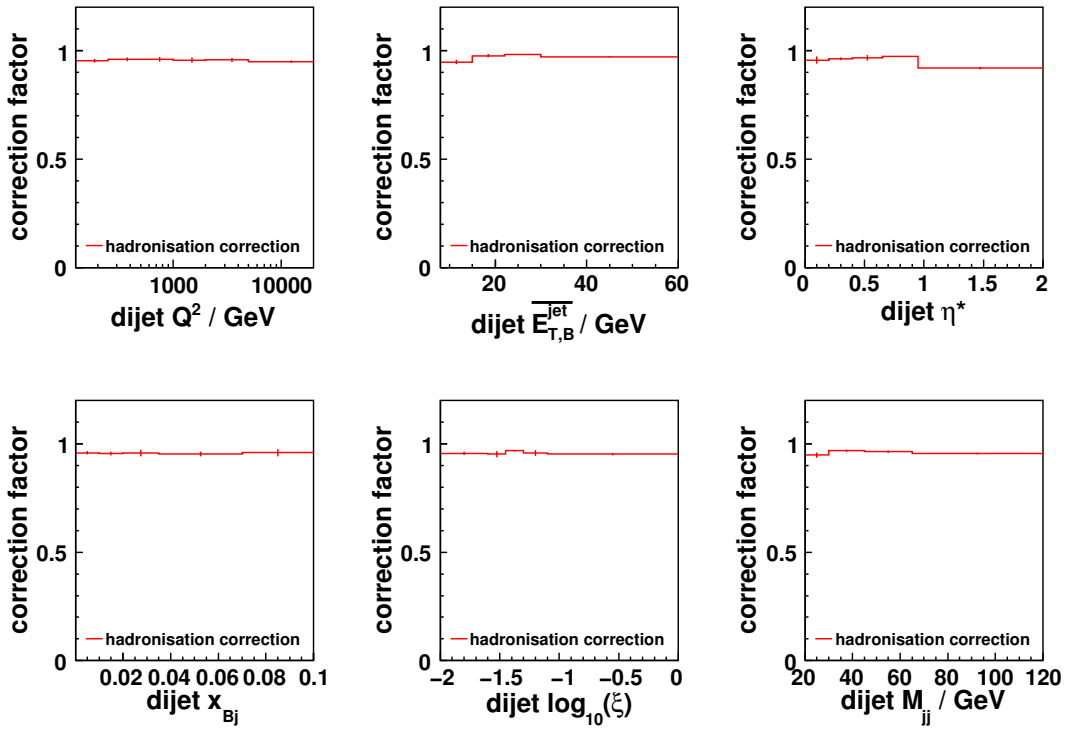

Figure 7.19: Hadronisation correction factors for the single-inclusive dijet cross sections.

exclusively selected dijet events, v the number of exclusively selected trijet events and w the number of events that were selected as a dijet as well as a trijet event, then 7.13 can be transformed to

$$R^i_{3/2} = \frac{(w+v)\cdot C_i^{A,3\text{jet}}\cdot C_i^{\text{QED},3\text{jet}}}{(u+w)\cdot C_i^{A,2\text{jet}}\cdot C_i^{\text{QED},2\text{jet}}}. \tag{7.14}$$

With error propagation the uncertainty $\Delta R^i_{3/2}$ can be derived from equation 7.14. The uncertainties of u, v and w were approximated with Poisson statistics. The correlation of the acceptance corrections $C_i^{A,3\text{jet}}$ and $C_i^{A,2\text{jet}}$ was neglected.

8. Systematic Uncertainties

Besides the statistical uncertainties of the measurement systematic uncertainties have influenced significantly the experimental precision. It emerged that the size of the systematic uncertainties was dominating the total experimental uncertainty in most of the jet phase-space regions investigated. Statistical uncertainties can be reduced with a longer measurement time of the experiment. Systematic uncertainties can only be reduced with an improved understanding of the detector or modelling of the underlying physical processes. Usually with an increased data statistic further and more detailed systematic studies are possible which results possibly in reduced systematic uncertainties.

The measurement results were compared to theoretical calculations, which usually have a limited predictive power arising from a lack of higher-order contributions.

The size of both the systematic experimental and the theoretical uncertainties were estimated using reasonable assumptions. The estimations and the sizes of these uncertainties are discussed in this chapter.

8.1. Experimental Uncertainties

The following sources of systematic experimental uncertainties were investigated for the jet measurement:

- $\mathbf{z_{vtx}}$ **Reweighting:** In chapter 6.2 a reweighting procedure which has improved the 2006/2007 e^+ data z_{vtx} description by the Monte Carlo simulation was presented. The effect on the dijet cross-section normalisation was found to be approximately +0.9% for that particular data sample. The systematic uncertainty arising from this reweighting procedure was estimated by repeating the determination of the reweighting function by fitting histograms with 300 instead of 200 bins. The systematic influence on the 2006/2007 e^+ dijet cross sections was less than 0.2% and, therefore, the influence on the combined cross sections was neglected.

- **Polarisation:** The relative uncertainty in the measured polarisation was 3.6% using the LPOL and 4.2% using the TPOL. For the final selection, the TPOL was used for 52% of the run period from the years 2004–2007. The combined, luminosity-weighted systematic error on the polarisation measurement was 3.9%. The data polarisation was scaled by ±3.9% and new correction factors were determined (see chapter 6.1). The effect on the cross sections was negligible.

- **Track Veto Correction:** In order to estimate the systematic uncertainty due to the track-veto correction procedure described in chapter 6.4 the correction procedure was adjusted slightly. Instead of imposing a correction as a function

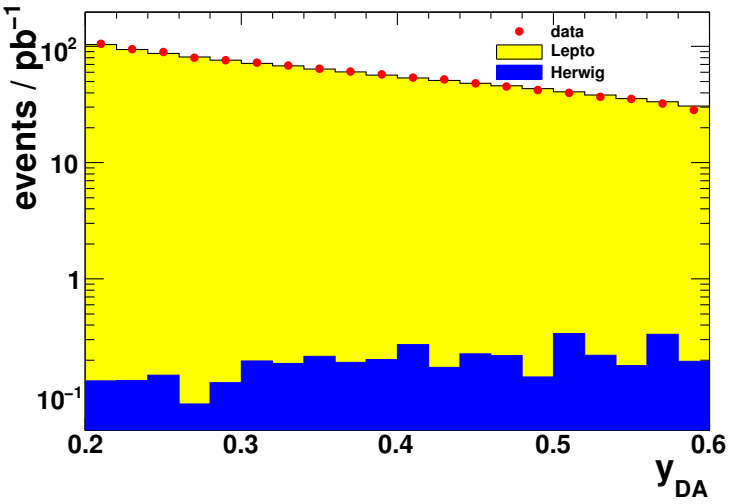

Figure 8.1: The photoproduction contribution to the inclusive DIS sample estimated with HERWIG.

of the kinematic variable y_{DA}, correction values in bins of the online CTD-FLT vertex-track multiplicity were determined. The effect on the combined cross sections was found to be typically less than 1% with slightly larger values in statistically limited regions of the phase space.

- **Acceptance Correction:** The detector acceptance was accounted for by using Monte Carlo simulations (see chapter 7.2). An investigation of the acceptance correction with two different Monte Carlo models for the parton cascade showed discrepancies between the results. In order to estimate the systematic effect arising from this dependence, the data were unfolded with ARIADNE instead of LEPTO. As a consequence the inclusive dijet cross sections changed by typically 2% in the lower Q^2 range and by up to about 6% in the higher Q^2 region. The systematic effect on the trijet cross sections was found to be significantly larger due to the occurrence of three jets. One of these jets was generated solely by the parton cascade and not by the hard matrix element. Except for the lower Q^2 region, the uncertainties on these cross sections were about 10%. Owing to the large difference of these systematic uncertainties for the production of dijets and trijets the uncertainties did basically not cancel in the cross section ratio, $R_{3/2}$, between trijet and dijet cross sections, in contrast to other uncertainties like that coming from the luminosity measurement.

- **Hadronic Energy Scale:** One of the dominating systematic uncertainties in jet measurements at ZEUS was the uncertainty on the energy scale of the jets. This uncertainty was discussed in detail in chapter 6.3, and a correction was introduced which has reduced the observed uncertainty. It was demonstrated by using various different methods that the energy scale uncertainty for jets with a transverse energy of $E^{\mathrm{jet}}_{T,\mathrm{lab}} > 10$ GeV was below 1% and 3% for jets with $E^{\mathrm{jet}}_{T,\mathrm{lab}} < 10$ GeV. These uncertainties were propagated to the jet cross sections by scaling the jet energy in the Monte Carlo simulation by $\pm 1\%$ in case of jets with $E^{\mathrm{jet}}_{T,\mathrm{lab}} > 10$ GeV and $\pm 3\%$ for jets with $E^{\mathrm{jet}}_{T,\mathrm{lab}} < 10$ GeV. Since each cut on the energy of the hadronic final state increases the cross-section dependence

on the energy scale, the systematic effect on the dijet cross sections was found to be significantly smaller than the effect on the trijet cross sections. Whereas the first have changed by approximately $\pm 4\%$ and $\pm 6\%$ in some regions of the phase space, the latter have changed by $4 - 10\%$.

- **Electron Energy Scale:** The uncertainty in the absolute energy scale of the electron candidate was estimated to be $\pm 1\%$ [188] ($\pm 2\%$ [189]) for the data taken in the years 1998–2000 (2004–2007). Therefore, the energy of the electron in the Monte Carlo simulation was varied by this amount. The contribution to the systematic uncertainty of the measurement was well below $\pm 1\%$.

- **Electron Identification:** The program SINISTRA that was used for the electron identification was replaced by the EM-algorithm [169]. The cross sections in general showed relative variations of about $\pm 1\%$; in regions with limited data statistic of up to $\pm 2\%$.

- **Photoproduction Background:** The systematic influence of background events arising from photoproduction in which an electromagnetic energy deposit in the calorimeter was wrongly identified as an electron candidate was estimated with the HERWIG [190] Monte Carlo program. The utilised Monte Carlo sample consisted of direct and resolved photoproduction events.

  Figure 8.1 shows the data distribution after an inclusive DIS event selection, the LEPTO signal distribution and the HERWIG background Monte Carlo distribution as a function of the inelasticity variable y. The estimated integrated contribution to the inclusive DIS event selection coming from photoproduction processes was found to be less than 0.3% and, hence have been neglected.

- **Cuts:** In chapter 5 the event selection was described and several cuts that have restricted the measurement to regions in which the Monte Carlo simulations have described the data reasonably well were introduced. In order to estimate the systematic impact on the jet cross sections of the actual chosen cut values the various cuts were varied in the data and the Monte Carlo simulation according to their resolutions. The introduced systematic uncertainties will be described in the following:
  - $\mathbf{E^{jet}_{T,lab}}$ **Cut:** The cut on the jet transverse energy in the laboratory frame, $E^{\mathrm{jet}}_{T,\mathrm{lab}}$, was raised and lowered from 3 GeV to 4 and 2 GeV. The influence on the inclusive dijet cross sections was approximately $0.5 - 1.5\%$, whereas for the trijet production the effect was slightly larger ($\approx 2\%$).
  - $\mathbf{E_{el}}$ **Cut:** The cut on the energy of the scattered electron was changed by $\pm 1\%$. The relative effect on the cross sections was well below 0.5%.
  - $(\mathbf{E - p_z})$ **Cuts:** Both cuts on the longitudinally momentum balance, $(E - p_z)$, were simultaneously changed by $\pm 6\%$ which resulted in a 1% change of the jet cross sections.
  - $\mathbf{p_T/\sqrt{E_T}}$ **Cut:** The cut on $p_T/\sqrt{E_T}$ was changed from 2.5 to 2 and 3 $\sqrt{\mathrm{GeV}}$ and the relative change of the cross sections was found to be smaller than 0.5%.

– **z_{vtx} Cut:** The variation of the cuts on the longitudinal vertex position, z_{vtx}, of the *ep* interaction by ±5% exhibited only a very small impact (< 0.5% change of the cross sections).

– **RCAL Radius Cut:** The geometry radius cut on the reconstructed electron position for events in which the electron was found in the RCAL was adjusted by ±2 cm. Only events with a scattered electron close to the crack region between the RCAL and BCAL were affected by this variation. Thus, the systematic effect was basically concentrated in the second Q^2 bin and amounted to < 0.5%.

– **DCA Cut:** The cut on the distance of closest approach between the extrapolated track position on the calorimeter surface and the measured electron island was changed from 10 to 8 cm [176, 184, 188, 189, 191]. The systematic uncertainty corresponding to this variation was typically well within ±1%.

Type	**Variation**	**Applied to ...**
jet energy scale	±3% $E_{T,\mathrm{lab}}^{\mathrm{jet}} < 10$ GeV, ±1% $E_{T,\mathrm{lab}}^{\mathrm{jet}} > 10$ GeV	Monte Carlo
e energy scale	±1%(1998–2000), ±2% (2004–2007)	Monte Carlo
Event Selection Cleaning Cuts		
E_{el} cut	±1%	data & Monte Carlo
$E - p_z$ cut	±6%	data & Monte Carlo
$p_T/\sqrt{E_T}$ cut	changed to 2 and 3 GeV	data & Monte Carlo
z_{vtx} cut	±5%	data & Monte Carlo
RCAL-radius cut	±2 cm	data & Monte Carlo
DCA cut	changed to 8 cm	data & Monte Carlo
Jet Selection Cleaning Cuts		
E_T^{lab}-cut	changed to 2 and 4 GeV	data & Monte Carlo
Additional		
γp background	Herwig	neglected
acceptance correction	Ariadne	data
electron identification	EM-algorithm	data & Monte Carlo
polarisation	polarisation scaled by ±3.9%	data
track-veto correction		Monte Carlo
z_{vtx} reweighting		Monte Carlo (neglected)

Table 8.1: Estimation of systematic uncertainties with variations of the analysis.

The performed checks for the estimation of the systematic uncertainties are summarised in table 8.1. The individual systematic contributions to the cross-section measurements for the inclusive dijet (trijet) production are depicted in figure 8.3 (8.4).

The total uncorrelated systematic uncertainty, δ_{syst}, was obtained by adding the described individual contributions not associated with the absolute energy scale of

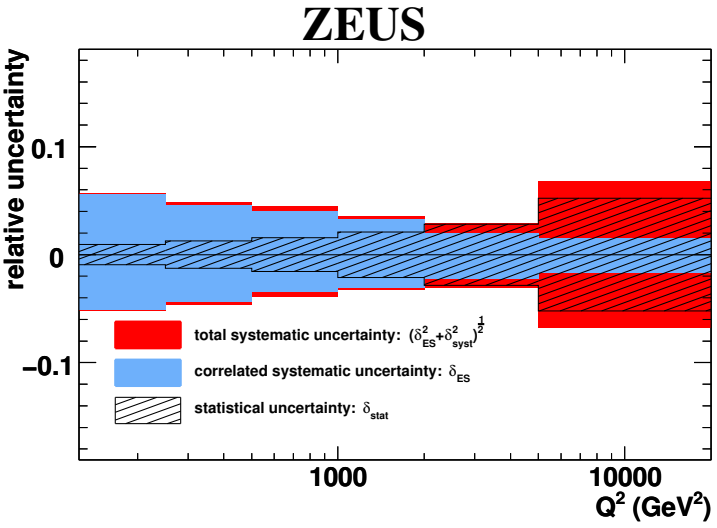

Figure 8.2: The statistical uncertainty, δ_{stat}, the correlated systematic uncertainty associated with the energy scale of the jets, δ_{ES}, and the quadratic sum of the correlated and uncorrelated, δ_{syst}, systematic uncertainties, $\sqrt{\delta^2_{\text{ES}} + \delta^2_{\text{syst}}}$, as a function of Q^2 for inclusive dijet production.

the jets in quadrature. In case of a single-sided effect the contributions were added symmetrically. The correlated systematic uncertainty, δ_{ES}, caused by the uncertainty in the absolute energy scale of the jets, was kept separately. In addition, there was an overall normalisation uncertainty of $\pm 2.2\%$ for the 1998–2000 and of $\pm 2.6\%$ for the 2004–2007 data. Therefore, the combined, luminosity-weighted systematic error on the luminosity measurement was $\pm 2.5\%$, which was not included in the cross-sections figures or the tables.

In figure 8.2 the statistical uncertainty, δ_{stat}, the correlated systematic uncertainty associated with the energy scale of the jets, δ_{ES}, and the quadratic sum of the correlated and uncorrelated, δ_{syst}, systematic uncertainties, $\sqrt{\delta^2_{\text{ES}} + \delta^2_{\text{syst}}}$, as a function of Q^2 or $\log_{10}(\xi)$ in Q^2 regions, respectively, is shown for inclusive dijet production. In general, in the bulk of the dijet phase space the measurement was limited by systematic uncertainties and not by the data statistics. The statistical uncertainty of the single-differential measurement increases from about 1% in the lowest Q^2 interval to approximately 5%, where it becomes comparable to the systematic uncertainty. Only a very weak dependence of the systematic uncertainties on $\log_{10}(\xi)$ is observed.

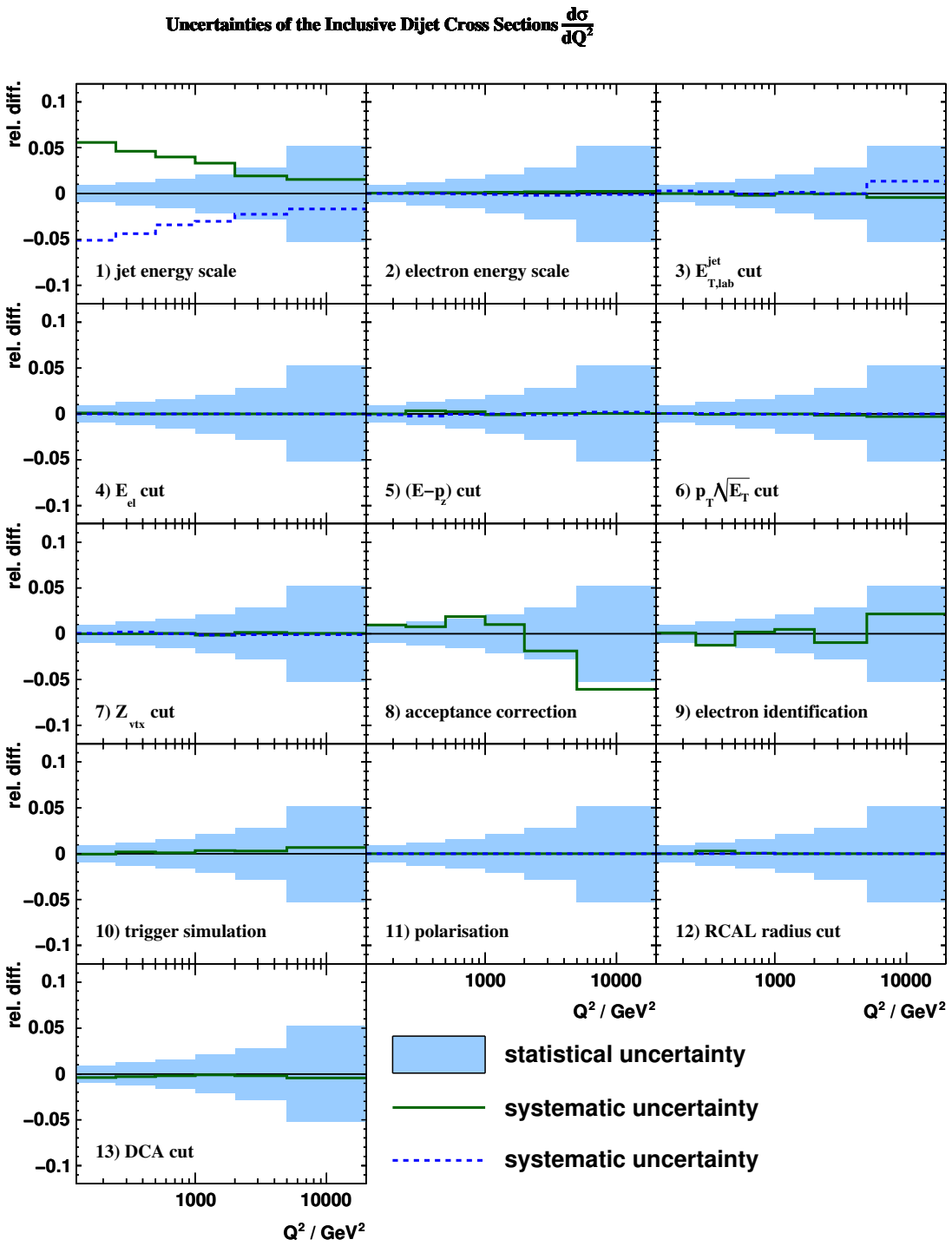

Figure 8.3: Relative change of the inclusive dijet cross section, $\frac{d\sigma}{dQ^2}$, for several sources of uncertainty.

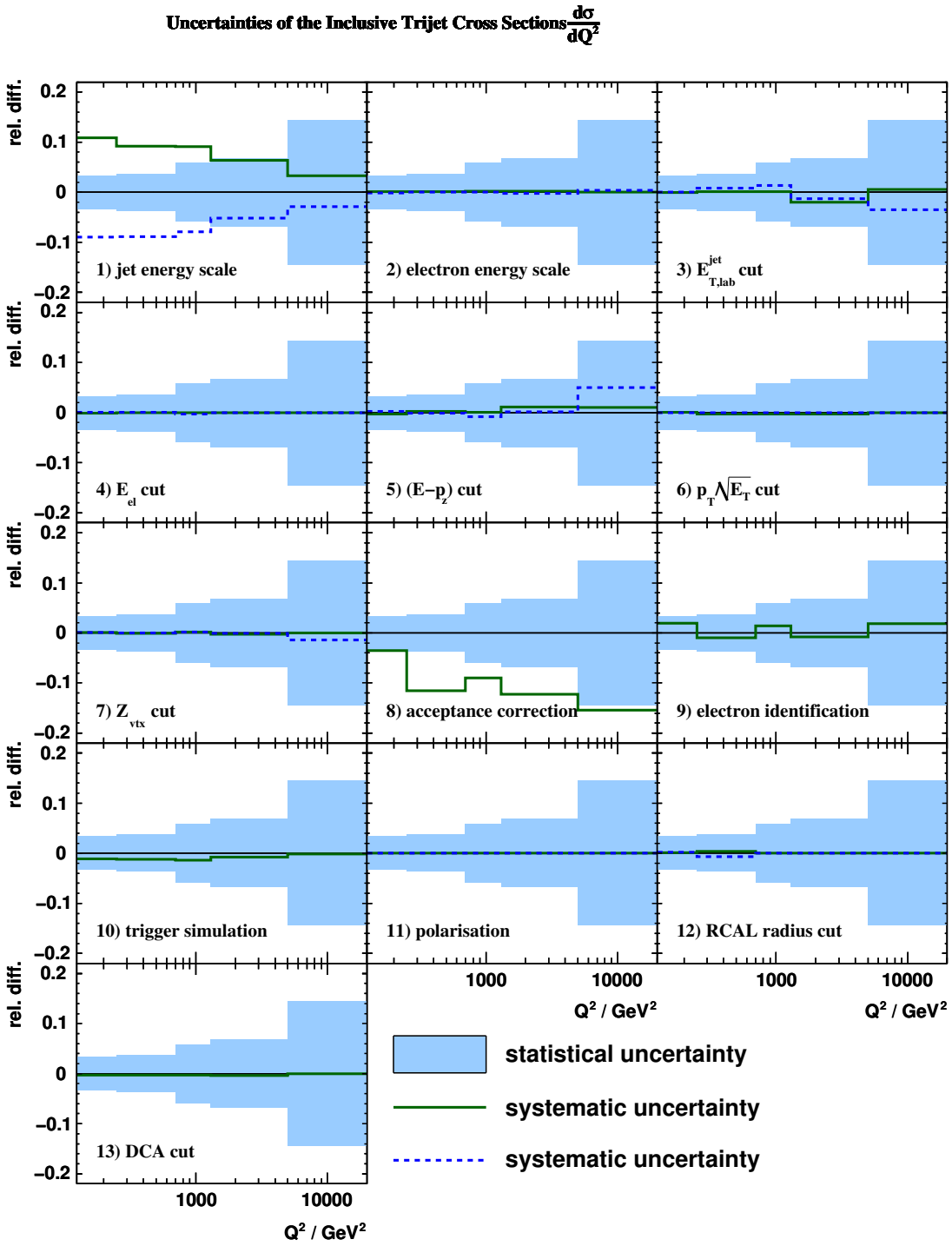

Figure 8.4: Relative change of the inclusive trijet cross section, $\frac{d\sigma}{dQ^2}$, for several sources of uncertainty.

8.2. Theoretical Uncertainties

In order to estimate systematic uncertainties of the theoretical predictions the settings of the QCD calculations were modified:

- **Renormalisation Scale:** The relative change of the inclusive dijet cross-section prediction as a function of several renormalisation scale choices, N, for the dijet selection obtained by applying an invariant mass cut and for the dijet selection with an asymmetric transverse energy cut was investigated and is presented in figures 8.5 and 8.5 for two different Q^2 ranges. The observed dependence for the selection which uses an invariant mass cut to ensure infrared insensitivity was found to be weaker than the dependence for the asymmetric transverse-energy cut-based selection. Therefore, the uncertainty of the NLO QCD calculations due to terms beyond NLO that are missing in the calculations is significantly smaller for the invariant-mass-cut selection.

  The uncertainty was estimated by varying μ_R by a factor of two up and down. Since in some regions of the phase space the change of the cross sections with respect to the central value was quite asymmetric the change that showed the larger deviation was considered for both the positive and negative uncertainty.

  The estimated uncertainty on the dijet cross sections was below $\pm 6\%$ at low Q^2 and low $\overline{E_{T,\mathrm{B}}^{\mathrm{jet}}}$ and decreased to below $\pm 3\%$ in the highest Q^2 region. For the production of trijets the dependence on the actual chosen value of μ_R was significantly larger and amounted to about $\pm 14\%$ in the low-Q^2 region investigated, whereas in the higher-Q^2 region the uncertainty was slightly smaller ($\pm 10\%$).

- **Uncertainty on the Strong Coupling:** The uncertainty on the QCD calculations due to that on $\alpha_s(M_Z)$ was estimated by repeating the calculations using two additional sets of proton PDFs, CTEQ6.6A3 and CTEQ6.6A2, determined assuming $\alpha_s(M_Z) = 0.114$ and 0.122, respectively. The difference between the calculations using these sets and CTEQ6.6 was scaled by a factor of 0.25 to reflect the uncertainty on α_s [65], which is 0.001. The resulting uncertainty on the dijet cross sections was mostly below $\pm 3\%$. Since the depencence of trijet cross sections in NLO on α_s is stronger ($O(\alpha_s^3)$) the resulting cross-section uncertainty is larger ($\approx \pm 5\%$).

- **Hadronisation:** The uncertainty on the modelling of the parton shower was estimated as half the difference between the multiplicative correction factors calculated from the LEPTO and ARIADNE models as described in chapter 7.4. These uncertainties were translated to cross-section uncertainties with the application of an error propagation method. The resulting uncertainties on the dijet (trijet) cross sections were in general less than $\pm 2\%$ ($\pm 4\%$).

- **PDF Uncertainty:** The uncertainty due to the proton PDFs was estimated by repeating the calculations using 44 additional sets from the CTEQ6.6 analysis, which takes into account the statistical and correlated systematic experimental

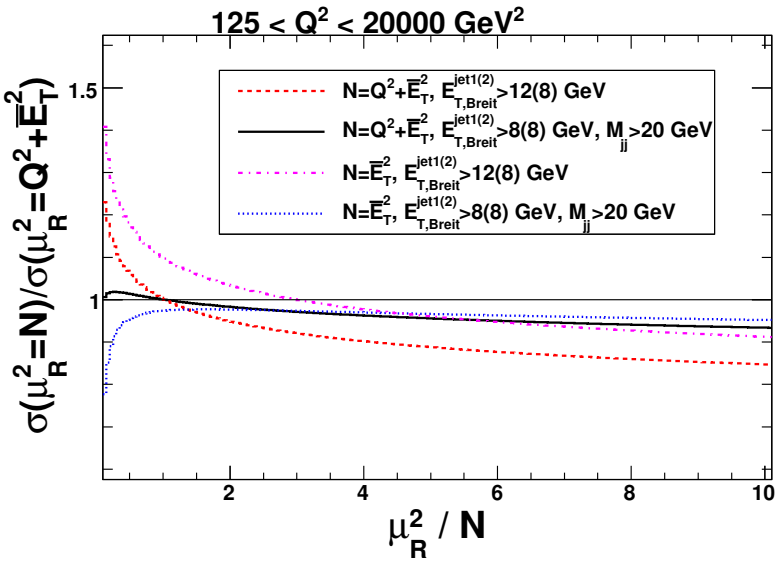

Figure 8.5: The relative change of the inclusive dijet cross-section prediction as functions of several renormalisation scale choices for two different dijet-selection scenarios in the region $125 < Q^2 < 20000$ GeV^2.

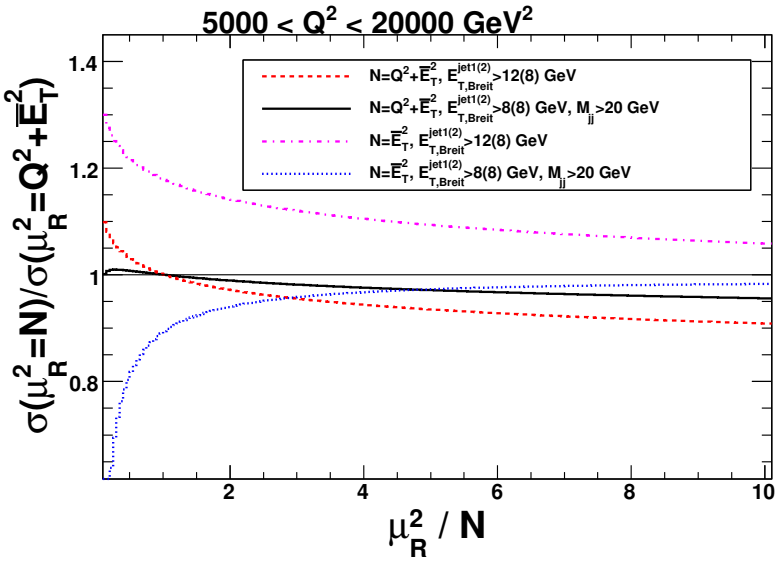

Figure 8.6: The relative change of the inclusive dijet cross-section prediction as functions of several renormalisation scale choices for two different dijet-selection scenarios in the region $5000 < Q^2 < 20000$ GeV^2.

uncertainties of each data set used in the determination of the proton PDFs. The uncertainty in the cross sections was about $\pm 4\%$ at low Q^2 and decreased to around $\pm 2\%$ at high Q^2. Comparable uncertainties for the dijet and trijet cross sections were observed.

- **Factorisation Scale:** The uncertainty of the theoretical predictions due to the choice of μ_F was determined by varying the factorisation scale in the range

$$\frac{Q}{2} < \mu_F < 2 \cdot Q \tag{8.1}$$

in the calculations.

For the dijet cross sections the influence was negligible and for the trijets it was less than $\pm 2\%$. This weak dependence is partly caused by the weak dependence of the parton densities in the range $0.008 < \xi < 0.3$ on the factorisation scale, μ_F, as indicated in figure 8.7.

- **Infrared Sensitivity:** As described in chapter 4.2.2 a special type of cut was required to ensure the insensitivity of the theoretical predictions to infrared cut-offs. This insensitivity was verified with the DISENT program by determining the total inclusive dijet cross section as a function of the applied cut on the invariant dijet mass, M_{jj}, in all analysis bins separately.

  Figure 8.8 presents as examples the total inclusive dijet cross section as a function of the M_{jj} cut in regions of Q^2 and η^*, respectively. The applied cut on M_{jj} for the final cross-section predictions is indicated as a vertical line. Except for the last two η^* bins where the distributions are not monotonically decreasing functions, the unphysical behaviour of the predictions were found to be located below the applied cut value. Therefore, except for these two bins, the theoretical predictions were found to be infrared safe.

  Furthermore, the correlation between the invariant dijet mass, M_{jj}, and η^* was investigated in order to study the behaviour of the M_{jj} cut in more detail. The variable $\cos\theta^*$ corresponds to the angle between the axis of the incoming boson and that of the outgoing quark in the boson-parton centre-of-mass frame and is defined as

  $$\cos\theta^* = \tanh\eta^* \tag{8.2}$$

  and with the quantity

  $$\cosh(\eta_1 - \eta_2) = \frac{1+\cos^2\theta^*}{1-\cos^2\theta^*} \tag{8.3}$$

  the equation

  $$M_{jj}^2 = 2 \cdot E_T^{\text{jet1}} \cdot E_T^{\text{jet2}} \cdot [\cosh(\eta_1 - \eta_2) - \cos\Delta\phi_{jj}] \tag{8.4}$$

  is obtained, where $E_T^{\text{jet1,2}}$ represents the jet transverse energies, $\eta_{1,2}$ the jet pseudorapidities and $\Delta\phi_{jj}$ the azimuthal difference between the two hardest jets in the event.

  In figure 8.9, the correlation between the invariant dijet mass, M_{jj}, and η^* for the production of dijets on hadron level is depicted – omitting the cut on M_{jj}. The vertical lines indicate the binning in η^* for the measurement of the single-differential dijet cross-sections $d\sigma/d\eta^*$. In addition, a horizontal line at $M_{jj} = 20$ GeV represents the value of the cut that was imposed for the cross-section measurement. The three kinematic configurations $E_{T,\text{B}}^{\text{jet1,2}} = 8$ GeV with $0 < \Delta\phi_{jj} < \pi$, $E_{T,\text{B}}^{\text{jet1}} \cdot E_{T,\text{B}}^{\text{jet2}} = 8 \cdot 8$ GeV^2 with $\Delta\phi_{jj} = \pi$ and $E_{T,\text{B}}^{\text{jet1,2}} = 8$ GeV with $\Delta\phi_{jj} = \pi$ of the two hardest jets in the event are displayed as filled areas or as a dashed line by applying equation 8.4. Starting with the fourth η^* bin, the cut on the invariant dijet mass tends to not suppress events with $\Delta\phi_{jj} \to \pi$ or with $\Delta E_{T,\text{B}}^{\text{jet1,2}} \to 0$ GeV anymore. Therefore, in this region of the dijet phase space a mismatch of virtual and real contributions occurs, which leads to the observed unphysical behaviour of the theoretical predictions shown in figure 8.8.

The total theoretical uncertainty was determined by symmetrically adding in quadrature the individual contributions from the renormalisation and factorisation

scale dependence, from the uncertainty on α_s, from the hadronisation uncertainty and from the PDF uncertainty. Figure 8.10 shows for the single-inclusive dijet and trijet cross sections the relative size of the systematic contributions as a function of Q^2.

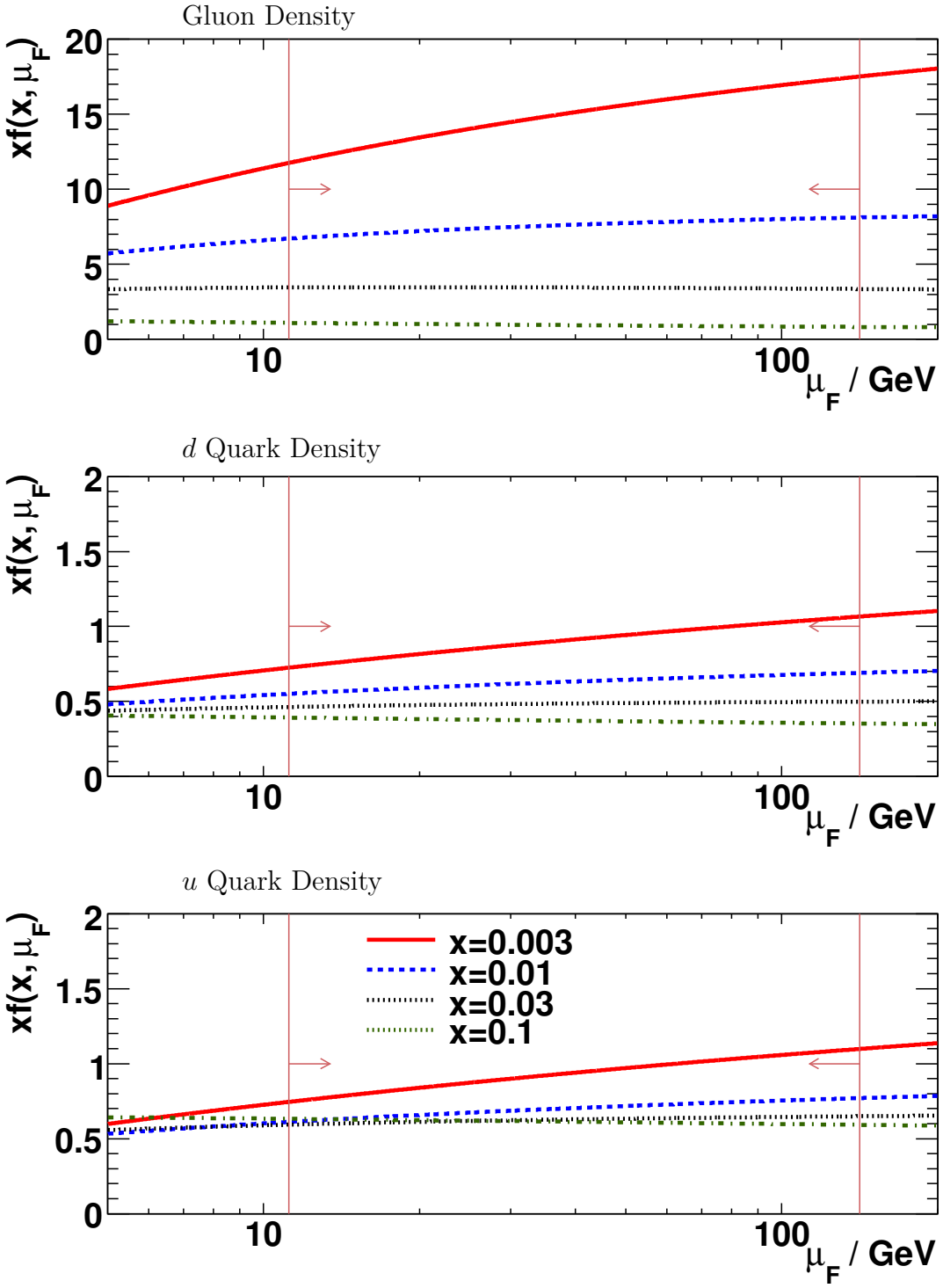

Figure 8.7: The dependence of the gluon, u and d quark density on the factorisation scale, μ_F, for four different fixed values of x.

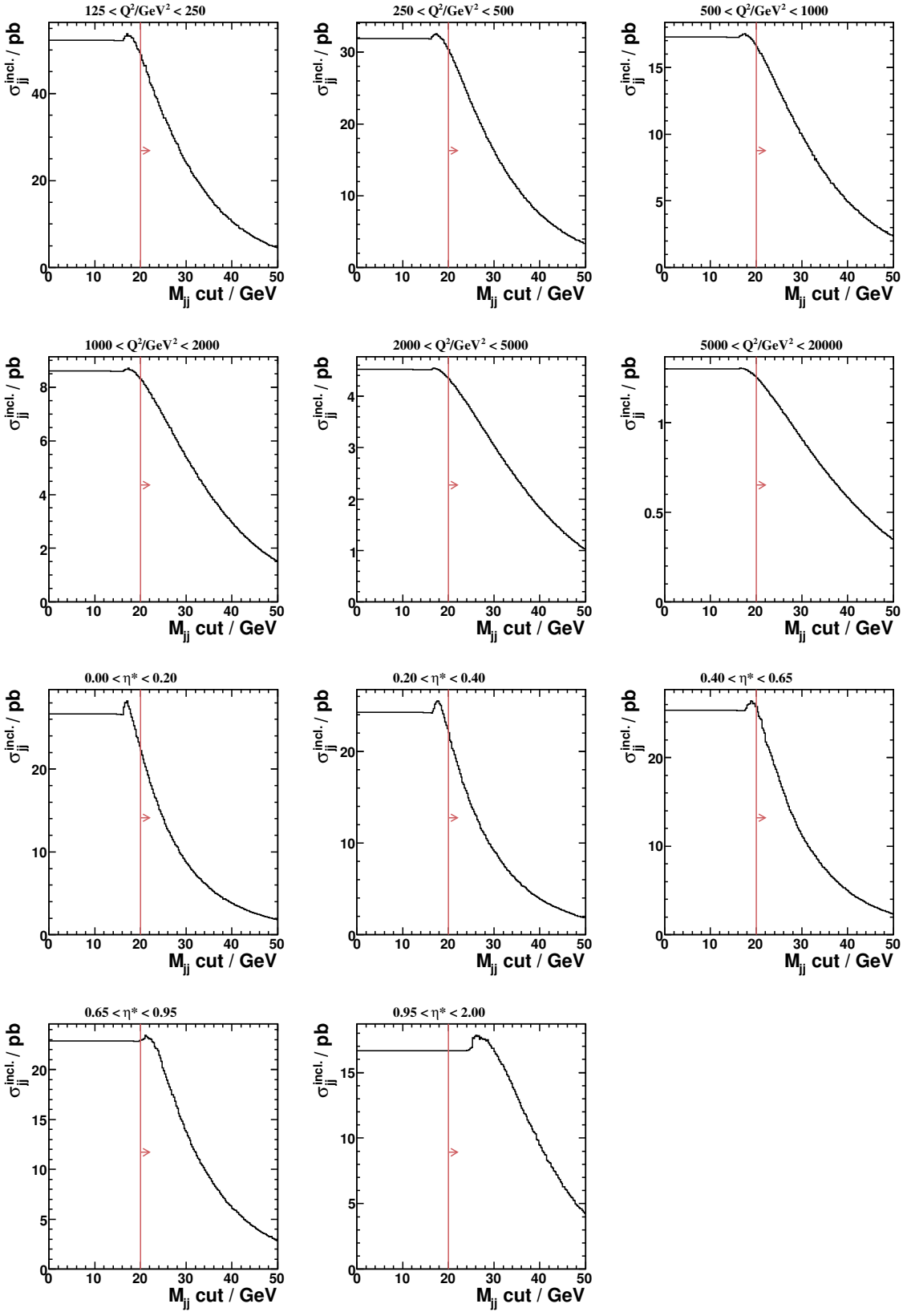

Figure 8.8: The total inclusive dijet cross section as a function of the invariant mass cut, M_{jj}, in several regions of Q^2 or η^*, respectively.

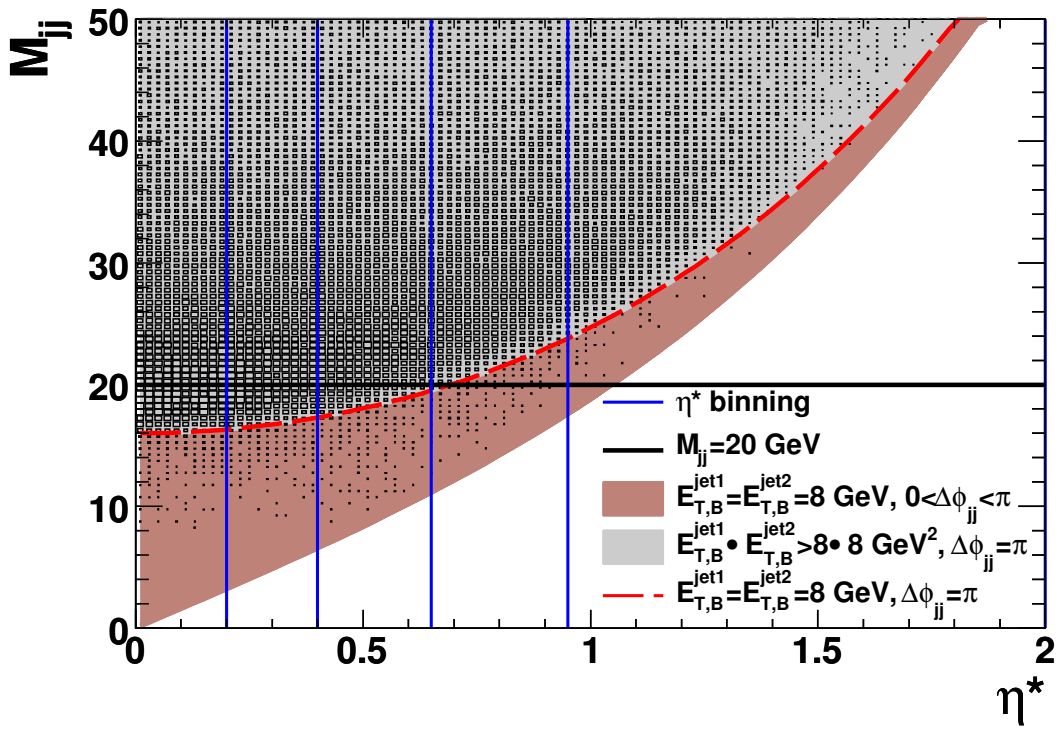

Figure 8.9: Correlation between the invariant dijet mass, M_{jj}, and $\eta^* = |\eta_1 - \eta_2|/2$ for dijet production on hadron level. Several kinematic configuration of the two hardest jets in the event are indicated as filled areas or as a dashed line.

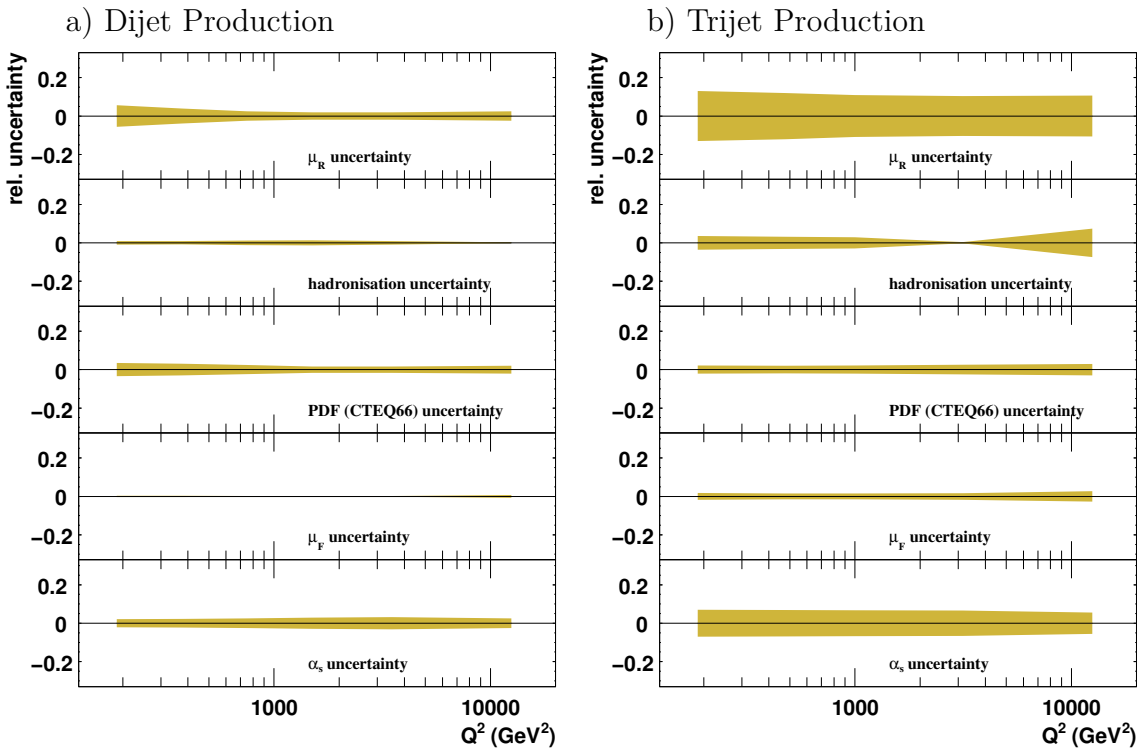

Figure 8.10: Sources of theoretical uncertainties for the inclusive cross section, $\frac{d\sigma}{dQ^2}$, for a) dijet and b) trijet production.

9. Results

In this chapter, the results of the jet measurements in deep-inelastic electron-proton scattering are presented. Single-differential and double-differential inclusive jet cross sections for dijet and trijet production were measured and the double-differential cross-section ratios, $R_{3/2}$, between the cross sections for dijet and trijet production were determined. The latter were exploited for an extraction of the strong coupling, α_s.

The differential inclusive jet cross sections were measured at large squared momentum transfer, Q^2, in the region $125 < Q^2 < 20000$ GeV^2 and in the range $0.2 < y < 0.6$ of the inelasticity of the scattering process, y. The jets were reconstructed using the k_T cluster algorithm in the longitudinally invariant inclusive mode in the Breit reference frame. The cross sections referred to jets with transverse energies $E^{\text{jet}}_{T,\text{B}} > 8$ GeV in the pseudorapidity range $-1 < \eta^{\text{jet}}_{\text{LAB}} < 2.5$. The invariant dijet mass of the two hardest jets in the event was required to be greater than 20 GeV.

Single-differential inclusive dijet cross sections were measured as functions of the variables Q^2, x_{Bj}, $\log_{10}(\xi)$, M_{jj}, η^* and $\overline{E^{\text{jet}}_{T,\text{B}}}$, which were defined in chapter 4.3. Additionally, the dijet cross-sections $d\sigma/d\log_{10}(\xi)$ and $d\sigma/d\overline{E^{\text{jet}}_{T,\text{B}}}$ were studied in different regions of Q^2. The results for the inclusive dijet cross-section measurement are currently in the ZEUS-internal publishing procedure[1] and expected to be submitted to the journal soon [23].

Differential inclusive trijet cross sections were determined in regions of Q^2, x_{Bj} and $\overline{E^{\text{jet}}_{T,\text{B}}}$ and double-differentially as functions of $\overline{E^{\text{jet}}_{T,\text{B}}}$ and Q^2. The latter and the corresponding cross sections for dijet production were used for a determination of the cross-section ratios $R_{3/2}$.

The data were corrected for detector and QED radiative effects and the running of the fine-structure constant, α_{em}, as discussed in chapter 6 and 7. The measurements were compared to NLO QCD predictions as implemented in the NLOJET++ program[2] using the CTEQ6.6 parametrisation [81] of the proton PDFs. These theoretical predictions for the partonic jet cross sections were corrected for the effect of hadronisation exploiting the Monte Carlo simulations LEPTO and ARIADNE as described in chapter 7.4. Neither NLOJET++ nor the alternatively used DISENT program include the contributions from electro-weak effects, so that, the theory had to be corrected for the influence of the Z^0 boson on the jet cross sections (see section 7.3 for more details).

The figures in this chapter that present the results for the jet cross-section measurements show the data as points; the inner uncertainty bars indicate the statistical uncertainty and the outer bars the quadratic sum of the statistical and uncorrelated systematic uncertainty. The shaded band shows the systematic uncertainty arising

[1] At the time of writing this thesis, the publication draft was in the "post-reading phase".

[2] A complete list of the used settings for the theoretical calculations can be found in chapter 4.2.1.

from the energy-scale uncertainty of the jets. Since this uncertainty is correlated between the individual bins, it is indicated separately. The theoretical predictions are presented as solid lines for the renormalisation scale $\mu_R^2 = Q^2 + \overline{E_{T,\mathrm{B}}^{\mathrm{jet}}}^2$, as dashed lines for $\mu_R^2 = Q^2$ and as dotted lines for the choice $\mu_R^2 = \overline{E_{T,\mathrm{B}}^{\mathrm{jet}}}^2$. In the lower part of the figures, the relative difference with respect to the theory with $\mu_R^2 = Q^2 + \overline{E_{T,\mathrm{B}}^{\mathrm{jet}}}^2$ is displayed. Furthermore, the total theoretical uncertainty (see section 8.2) is presented as a hatched band.

First, the results for the measurement of the inclusive dijet and trijet cross sections are discussed in the chapters 9.1 and 9.2. Moreover, results for the determination of the cross-section ratio $R_{3/2}$ are presented in chapter 9.2 and used for an extraction of the strong coupling, α_s, in chapter 9.3. The latter is compared to the values of α_s determined in other analyses and experiments. The results of the measurements are summarised in tables given in appendix A.4.

9.1. Inclusive Dijet Cross Sections

In this section, the measurements of the inclusive dijet cross sections are shown and discussed.

9.1.1. Dijet Cross Sections as Functions of Q^2

Figure 9.1 shows on the left-hand side the single-differential dijet cross-section $d\sigma/dQ^2$. The cross section falls over more than three orders of magnitude in the phase-space region investigated.

The systematic uncertainties are significantly larger than the statistical uncertainties, except for the last Q^2 bin where they become comparable. The statistical uncertainties amount to about $1-2\%$ ($\approx 6\%$) at low (high) values of Q^2. The relative cross-section uncertainty coming from the uncertainty on the energy scale of the jets decreases from about 6% at lower values of Q^2 to typically $1-2\%$ in the last Q^2 bin. The model dependence of the acceptance correction causes a systematic uncertainty which is mostly the dominant contribution in the region $2000 < Q^2 < 20000$ GeV^2.

The total uncertainty of the theory prediction adds up to $7-8/\%$ in the first interval of Q^2 and then shrinks to 4% in the region $5000 < Q^2 < 20000$ GeV^2, reflecting the decreasing renormalisation scale dependence of the predictions. The relative uncertainty due to that on the proton PDFs amounts to approximately $\approx 3\%$ over the whole investigated Q^2 range. With increasing virtuality, Q^2, the theoretical prediction with $\mu_R^2 = \overline{E_{T,\mathrm{B}}^{\mathrm{jet}}}^2$ starts to differ from the predictions obtained with the default renormalisation scale, $\mu_R^2 = Q^2 + \overline{E_{T,\mathrm{B}}^{\mathrm{jet}}}^2$, indicating that Q^2 becomes the dominant scale of the involved physical processes in that particular corner of phase space.

Within the experimental and theoretical uncertainties, the pQCD predictions with $\mu_R^2 = Q^2 + \overline{E_{T,\mathrm{B}}^{\mathrm{jet}}}^2$ describe the data in shape and normalisation very well.

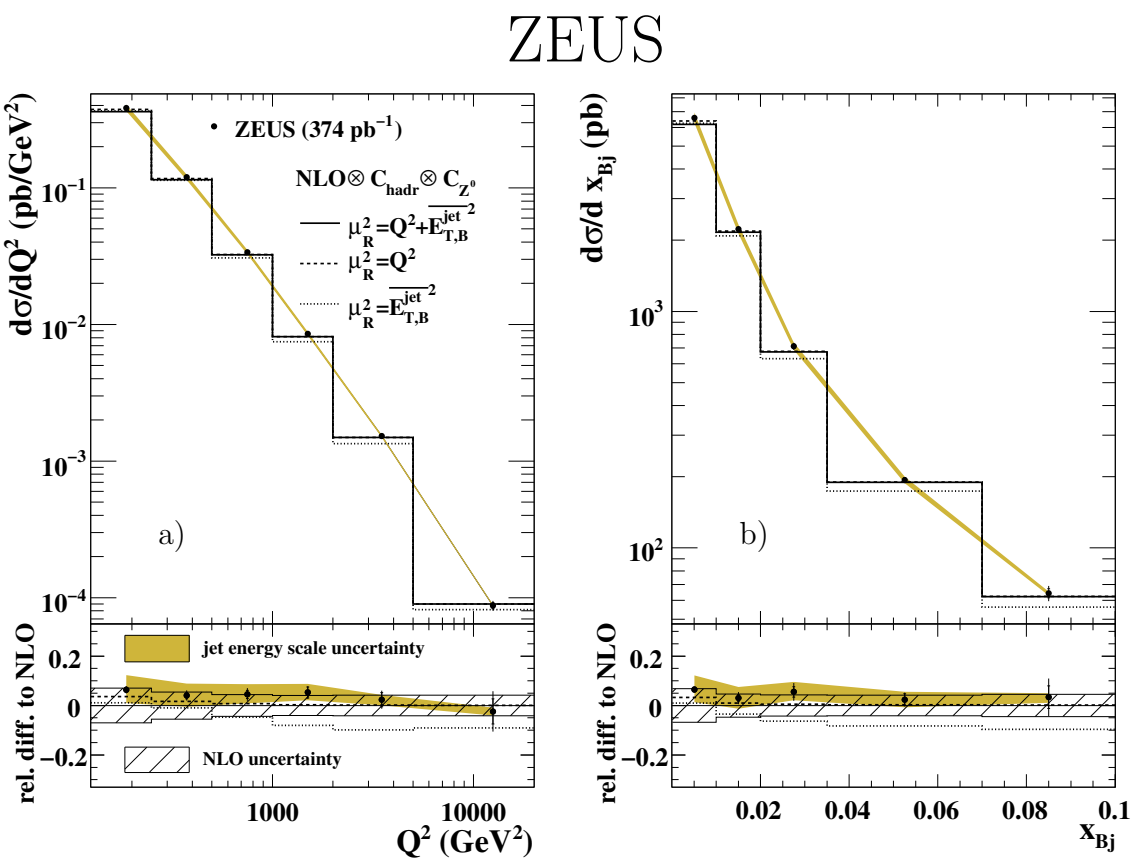

Figure 9.1: The measured single-differential cross-sections (a) $d\sigma/dQ^2$ and (b) $d\sigma/dx_{\mathrm{Bj}}$ for inclusive *dijet* production with $E_{T,\mathrm{B}}^{\mathrm{jet}} > 8$ GeV, $M_{jj} > 20$ GeV and $-1 < \eta_{\mathrm{LAB}}^{\mathrm{jet}} < 2.5$ (dots), in the kinematic range given by $0.2 < y < 0.6$ and $125 < Q^2 < 20000$ GeV^2. The inner error bars represent the statistical uncertainty. The outer error bars show the statistical and systematic uncertainties, not associated with the uncertainty in the absolute energy scale of the jets, added in quadrature. The shaded bands display the uncertainties due to the absolute energy scale of the jets. The NLO QCD calculations with $\mu_R^2 = Q^2 + \overline{E_{T,\mathrm{B}}^{\mathrm{jet}}}^2$ (solid lines), $\mu_R^2 = Q^2$ (dashed lines) and $\mu_R^2 = \overline{E_{T,\mathrm{B}}^{\mathrm{jet}}}^2$ (dotted lines), corrected for hadronisation effects and Z^0 exchange and using the CTEQ6.6 parameterisations of the proton PDFs, are also shown. The lower parts of the figures show the relative differences with respect to the NLO QCD calculations with three different μ_R scales. The hatched bands display the total theoretical uncertainty.

9.1.2. Dijet Cross Sections as Functions of x_{Bj}

Figure 9.1 shows on the right-hand side the single-differential dijet cross-section $d\sigma/dx_{\mathrm{Bj}}$. The cross section decreases with increasing x_{Bj} over two orders of magnitude due to the decreasing parton densities in the proton.

The statistical uncertainty in the lower x_{Bj} region is very small ($< 1\%$) and increases to almost 4.5% in the last x_{Bj} interval of the measurement. Over the whole investigated range the measurement is dominated by systematic uncertainties. The relative uncertainty arising from the jet energy scale uncertainty decreases from about 5% at low-x_{Bj} values to typically 2% in the high-x_{Bj} region. The model dependence

of the acceptance correction contributes significantly mostly in the higher x_{Bj} range, where it becomes the dominant uncorrelated systematic uncertainty.

The relative size of the theoretical uncertainties is approximately constant as a function of x_{Bj} and amounts to $\pm 6\%$. The relative difference between the theoretical calculations determined with the default renormalisation scale, $\mu_R^2 = Q^2 + \overline{E_{T,\mathrm{B}}^{\mathrm{jet}}}^2$, and obtained with $\mu_R^2 = \overline{E_{T,\mathrm{B}}^{\mathrm{jet}}}^2$ rises with increasing x_{Bj}, indicating that the high-x_{Bj} region is dominated by events with high values of Q^2.

9.1.3. Dijet Cross Sections as Functions of $\overline{E_{T,\mathrm{B}}^{\mathrm{jet}}}$

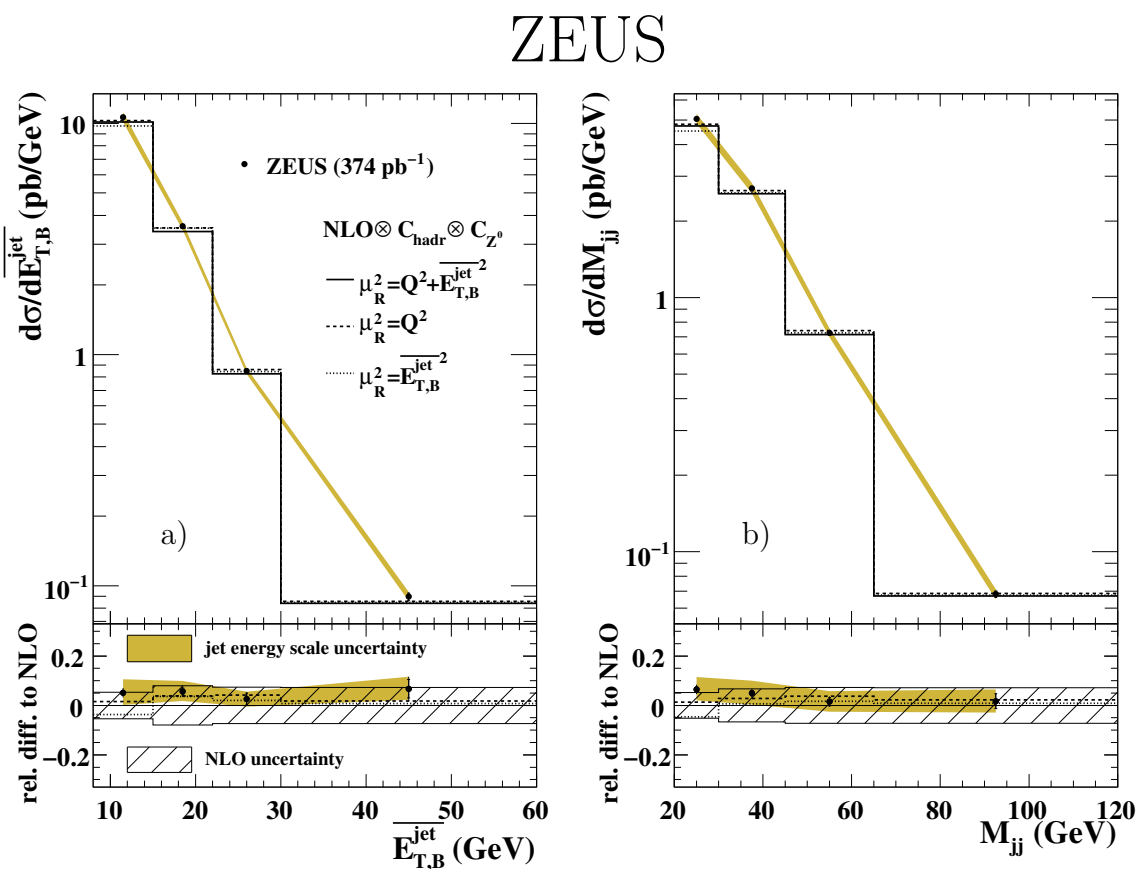

Figure 9.2: The measured differential cross-sections (a) $d\sigma/d\overline{E_{T,\mathrm{B}}^{\mathrm{jet}}}$ and (b) $d\sigma/dM_{jj}$ for inclusive *dijet* production. Other details as in the caption to Fig. 9.1.

Figure 9.2 a) presents the single-differential dijet cross-section $d\sigma/d\overline{E_{T,\mathrm{B}}^{\mathrm{jet}}}$. The measurement decreases by two orders of magnitude which results in larger statistical uncertainties ($\approx 3.5\%$) at high values of $\overline{E_{T,\mathrm{B}}^{\mathrm{jet}}}$; in the low-$\overline{E_{T,\mathrm{B}}^{\mathrm{jet}}}$ range the statistical uncertainty is typically below 1.5%. In the region of large $\overline{E_{T,\mathrm{B}}^{\mathrm{jet}}}$ the statistical uncertainty starts to become comparable to the systematic uncertainties. In the last interval of $\overline{E_{T,\mathrm{B}}^{\mathrm{jet}}}$, the uncertainty arising from the model dependence of the acceptance correction is also sizeable ($3-4\%$). The uncorrelated (correlated) systematic uncertainty amounts to about $\pm 2\%$ ($\pm 5\%$) in the low-$\overline{E_{T,\mathrm{B}}^{\mathrm{jet}}}$ region.

In general, the agreement between the measurement and the theory calculated with the three different renormalisation scale choices is reasonable. However, in the first $\overline{E_{T,\mathrm{B}}^{\mathrm{jet}}}$ bin a small deviation between the various theoretical predictions can be noted. This behaviour is in particular coming from the fact that the average transverse energy of the jets in that region is small compared to the Q^2 term in μ_R^2.

9.1.4. Dijet Cross Sections as Functions of M_{jj}

Figure 9.2 b) shows the single-differential dijet cross-section as a function of M_{jj}. The cross section falls over two orders of magnitude with a statistical precision of $\pm 1\%$ ($\pm 3\%$) at low (high) values of M_{jj}. Measured invariant dijet masses of up to 120 GeV were experimentally accesible. The correlated systematic uncertainty due to the uncertainty on the jet energy scale is approximately constant over the whole investigated range of the invariant dijet mass and amounts to $4-5\%$, whereas the size of the uncorrelated systematics slightly decreases from 2% to $< 1\%$ with increasing M_{jj}.

The theoretical uncertainties due to the α_s uncertainty increase with rising M_{jj}. In the highest investigated M_{jj} interval, the size of this uncertainty is about $\pm 3\%$ and comparable to the other theoretical uncertainties considered. Within the uncertainties, the data are reasonably well described by pQCD in NLO, with a small trend to a better description at higher M_{jj} values. As for the dijet cross-section $d\sigma/d\overline{E_{T,\mathrm{B}}^{\mathrm{jet}}}$, small deviations between the three chosen renormalisation scales are visible in the low-M_{jj} region where the average jet transverse energies are small compared to Q^2. For $M_{jj} > 65$ GeV the difference between the theoretical predictions for the different μ_R choices can be neglected.

9.1.5. Dijet Cross Sections as Functions of η^*

The differential dijet cross-section $d\sigma/d\eta^*$ is depicted on the left-hand side in figure 9.3. The cross sections in the first three η^* bins decrease only slowly with increasing η^*, whereas the drop in the last two intervals is much more pronounced. This behaviour is related to the phase space cut on the invariant dijet mass as illustrated in figure 8.9 in chapter 8.2.

The size of the η^* bins were chosen such that the relative statistical uncertainty in each bin has a comparable size. Relative statistical uncertainties of $1-2\%$ were achieved. Furthermore, the correlated systematic uncertainty that reflects the uncertainty on the jet energy scale is the main source of systematic uncertainty, with slightly smaller relative sizes at higher values of η^*.

In the first three η^* bins, the pQCD calculations describe the data in shape and normalisation very well. Except for these first three bins, the theoretical predictions were removed from the plot due to their sensitivity to infrared cut-offs as described in chapter 8.2 and as depicted in figures 8.8 and 8.9. A potential remedy for future developments and techniques applied to theoretical predictions might be all-order resummed calculations. These calculations are not sensitive to infrared contributions in this particular region of the investigated dijet phase space.

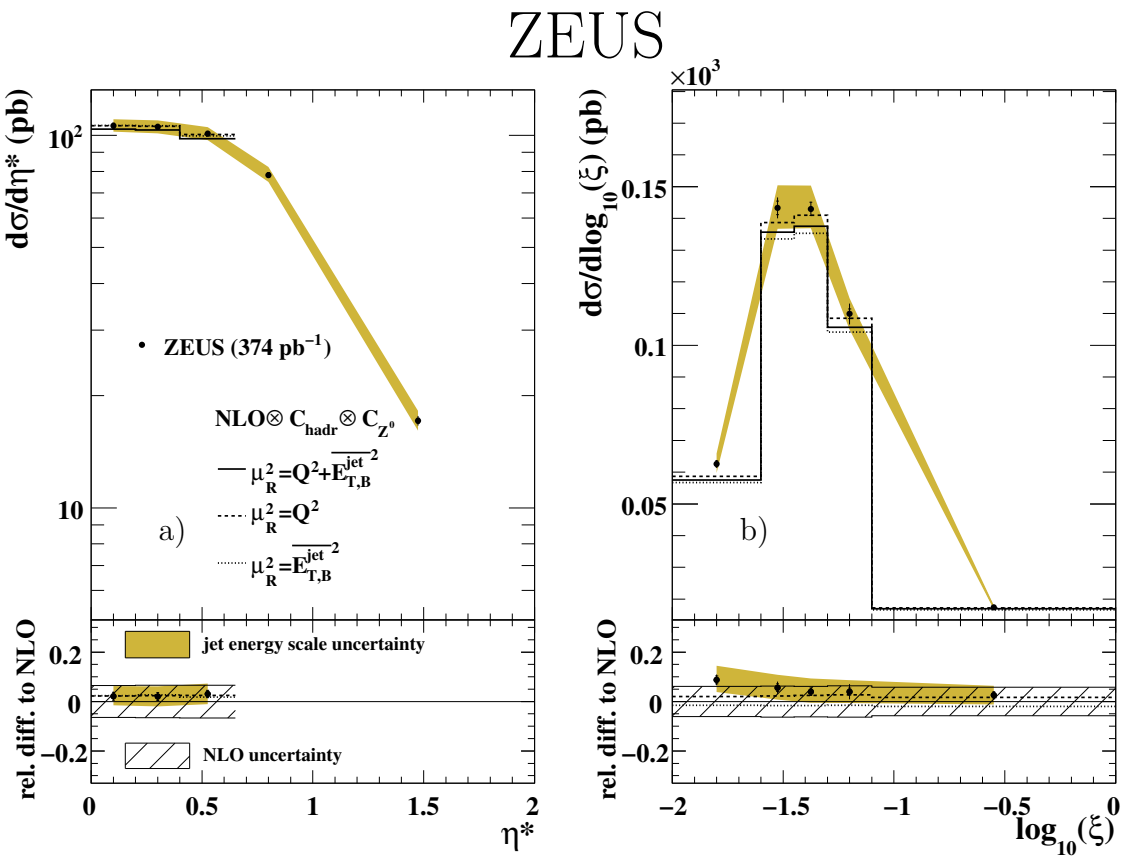

Figure 9.3: The measured differential cross-sections (a) $d\sigma/d\eta^*$ and (b) $d\sigma/d\log_{10}(\xi)$ for inclusive *dijet* production. Other details as in the caption to Fig. 9.1.

9.1.6. Dijet Cross Sections as Functions of $\log_{10}(\xi)$

Figure 9.3 shows on the right-hand side the single-differential dijet cross-section $d\sigma/d\log_{10}(\xi)$. The dijet cross section increases with increasing $\log_{10}(\xi)$ due to the suppression by the phase space selection cuts on the transverse energies of the two hardest jets in the final state, showing a maximum around $\xi \approx 0.3$. Since the variable ξ represents the fractional proton momentum carried by the initial state parton, the dijet cross sections are directly proportional to the size of the parton densities in the proton. Thus, the falling of the cross section with increasing $\log_{10}(\xi)$ reflects the decreasing quark and gluon densities at higher values of the fractional proton momentum.

The experimental systematic uncertainties are dominated by the uncertainty that corresponds to the uncertainty on the jet energy scale. Within the uncertainties, the agreement between the measurement and the theoretical predictions is good, while a small systematic trend towards a better agreement at higher values of $\log_{10}(\xi)$ can be noted. The difference between the three theoretical predictions obtained with different choices of the renormalisation scale appears to be constant over the full investigated $\log_{10}(\xi)$ range.

9.1.7. Dijet Cross Sections as Functions of $\log_{10}(\xi)$ or $\overline{E^{\mathrm{jet}}_{T,\mathrm{B}}}$ in Regions of Q^2

Figure 9.4 shows the inclusive dijet cross-section $d\sigma/d\log_{10}(\xi)$ in six different regions of the virtuality Q^2. The relative differences to the NLO QCD calculations are depicted in figure 9.5. The cross sections exhibit maxima the positions of which are functions of $\log_{10}(\xi)$. In the higher Q^2 region, the positions of the maxima tend to move to higher ξ values. The shapes of the distributions are similar to the shape of the distribution that was integrated over the full studied Q^2 range (figure 9.3b); the increase at lower ξ values is related to the transverse energy selection cuts applied to the jets whereas the decrease towards larger $\log_{10}(\xi)$ originates from the suppression coming from the decreasing parton densities in the proton.

The experimental uncertainties in the lower Q^2 region are dominated by the systematic influence coming from the jet energy scale uncertainty. The effect of this uncertainty on the cross sections is in the order of 6% in the lower Q^2 region and decreases to about 2% in the range $5000 < Q^2 < 20000$ GeV^2. In this Q^2 range, the statistical uncertainties have a size of about $10 - 12\%$ and tend to dominate the other experimental uncertainties, since the uncorrelated uncertainties in this region are only in the order of $6 - 10\%$ and are mainly induced by the dependence of the acceptance correction on the modelling of the parton cascade.

The theoretical uncertainties in the lower Q^2 region amount to approximately 7% and decrease to typically 4% in the region $5000 < Q^2 < 20000$ GeV^2. No distinct dependence on $\log_{10}(\xi)$ can be noted. The shape of the theoretical prediction with $\mu_R^2 = \overline{E^{\mathrm{jet}}_{T,\mathrm{B}}}^2$ starts to deviate with increasing Q^2 from the predictions obtained with the default renormalisation scale choice, because with increasing Q^2 the discrepancy between the terms $\overline{E^{\mathrm{jet}}_{T,\mathrm{B}}}^2$ and $Q^2 + \overline{E^{\mathrm{jet}}_{T,\mathrm{B}}}^2$ becomes sizeable. This observed difference between the various predictions is more pronounced at smaller $\log_{10}(\xi)$ values because in this region the selection cuts on the transverse energies of the final state jets dictate the shape of the distributions. In general, the theoretical predictions describe these data distributions very well in normalisation and shape.

The inclusive dijet cross-section $d\sigma/d\overline{E^{\mathrm{jet}}_{T,\mathrm{B}}}$ was measured in different regions of Q^2; the outcome is illustrated in figure 9.6. The differential cross section falls over two to three orders of magnitude with harder $\overline{E^{\mathrm{jet}}_{T,\mathrm{B}}}$ spectra for larger values of Q^2.

The correlated uncertainty due to the jet energy scale uncertainty exhibits only a very weak dependence on the average jet transverse energy; it amounts to about 5% in the low-Q^2 region, and decreases towards larger values of Q^2. In the region $125 < Q^2 < 250$ GeV^2 the statistical uncertainty of the measurement ranges from about 1% at low $\overline{E^{\mathrm{jet}}_{T,\mathrm{B}}}$ to approximately $6 - 7\%$ at higher values of $\overline{E^{\mathrm{jet}}_{T,\mathrm{B}}}$. In general, the measurement in the region $\overline{E^{\mathrm{jet}}_{T,\mathrm{B}}} > 22$ GeV is limited by the data statistics.

The theoretical uncertainties have a typical size of 7% in the lower Q^2 range investigated and slightly smaller uncertainties (5%) at large Q^2. Except for the first $\overline{E^{\mathrm{jet}}_{T,\mathrm{B}}}$ bin, the size of the theoretical uncertainties is only weakly dependent on $\overline{E^{\mathrm{jet}}_{T,\mathrm{B}}}$. The agreement between the data and the theoretical calculations obtained with the default renormalisation scale, $\mu_R^2 = Q^2 + \overline{E^{\mathrm{jet}}_{T,\mathrm{B}}}^2$, is reasonable. In the region

$8 < \overline{E^{\text{jet}}_{T,\text{B}}} < 15$ GeV and $Q^2 > 500$ GeV^2, the cross-section predictions with $\mu_R^2 = \overline{E^{\text{jet}}_{T,\text{B}}}^2$ are significantly smaller than the predictions with $\mu_R^2 = Q^2 + \overline{E^{\text{jet}}_{T,\text{B}}}^2$ and $\mu_R^2 = Q^2$, respectively. This indicates once again that in this region of the dijet phase space, the choice $\mu_R^2 = \overline{E^{\text{jet}}_{T,\text{B}}}^2$ is not the appropriate scale for the description of the involved physical processes.

In order to demonstrate the potential of the dijet data for further improvements of the understanding of the proton PDFs, figures 9.8 and 9.9 present as functions of the variables $\log_{10}(\xi)$ and $\overline{E^{\text{jet}}_{T,\text{B}}}$ in different regions of Q^2, the theoretical predictions from CTEQ6.6 for the fraction of events which are initiated by a gluon from the proton. This fractional gluon contribution ranges from about 75% at $125 < Q^2 < 250$ GeV^2 and small $\log_{10}(\xi)$ to only about 3% at highest Q^2 values above 5000 GeV^2, where ξ is approximately confined to values above 0.1. In the lower Q^2 regions investigated, the gluon fraction is also significant for large ξ values above 0.3.

In figure 9.10 the relative CTEQ6.6 PDF uncertainties, the relative uncertainty due to missing higher orders estimated by a variation of the renormalisation scale[3] and the theoretical predictions from the PDF sets MSTW2008 [82], ZEUS-JETS [22] and ZEUS-S [192] are depicted. The corresponding uncertainties for the latter three PDF sets are not drawn. In the ZEUS-S PDF extraction the inclusive DIS cross section measurement from HERA where the gluon density in the proton contributes only indirectly via scaling violations was considered together with fixed-target data. However, in the ZEUS-JETS PDF analysis direct photoproduction jet data [15] and inclusive jet data [3] in DIS were included in the fit in order to increase the sensitivity to the gluon PDF. Therefore, the deviations of the predictions obtained with those two sets are more pronounced in the lower Q^2 region, where the fractional contribution from gluon-induced processes to the dijet cross section is significantly larger than in the higher Q^2 regime (figure 9.8). Additionally, the experimental precision[4], the CTEQ6.6 PDF uncertainties and the observed spread between the various PDF sets are in some regions of the considered dijet phase space larger than the uncertainty arising from missing higher orders in the QCD calculations. This indicates that the presented dijet data are sensitive to the gluon density. Therefore, the data have the potential to provide further powerful constrains on the gluon PDF.

[3] More details can be found in chapter 8.2.

[4] As an example the experimental precision is indicated in figure 8.2 in chapter 8.

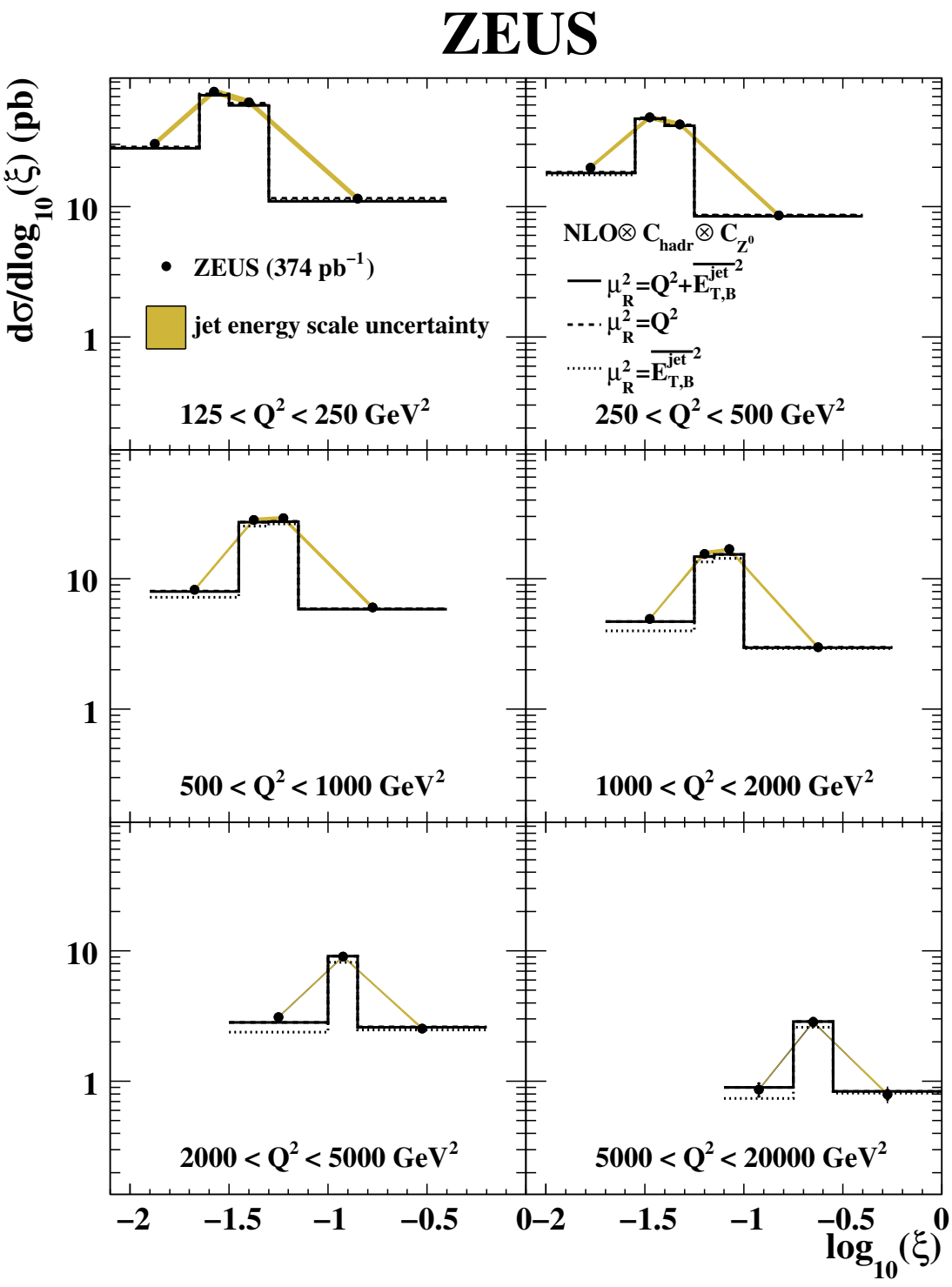

Figure 9.4: The measured differential cross-section $d\sigma/d\log_{10}(\xi)$ for inclusive *dijet* production in different regions of Q^2. Other details as in the caption to Fig. 9.1.

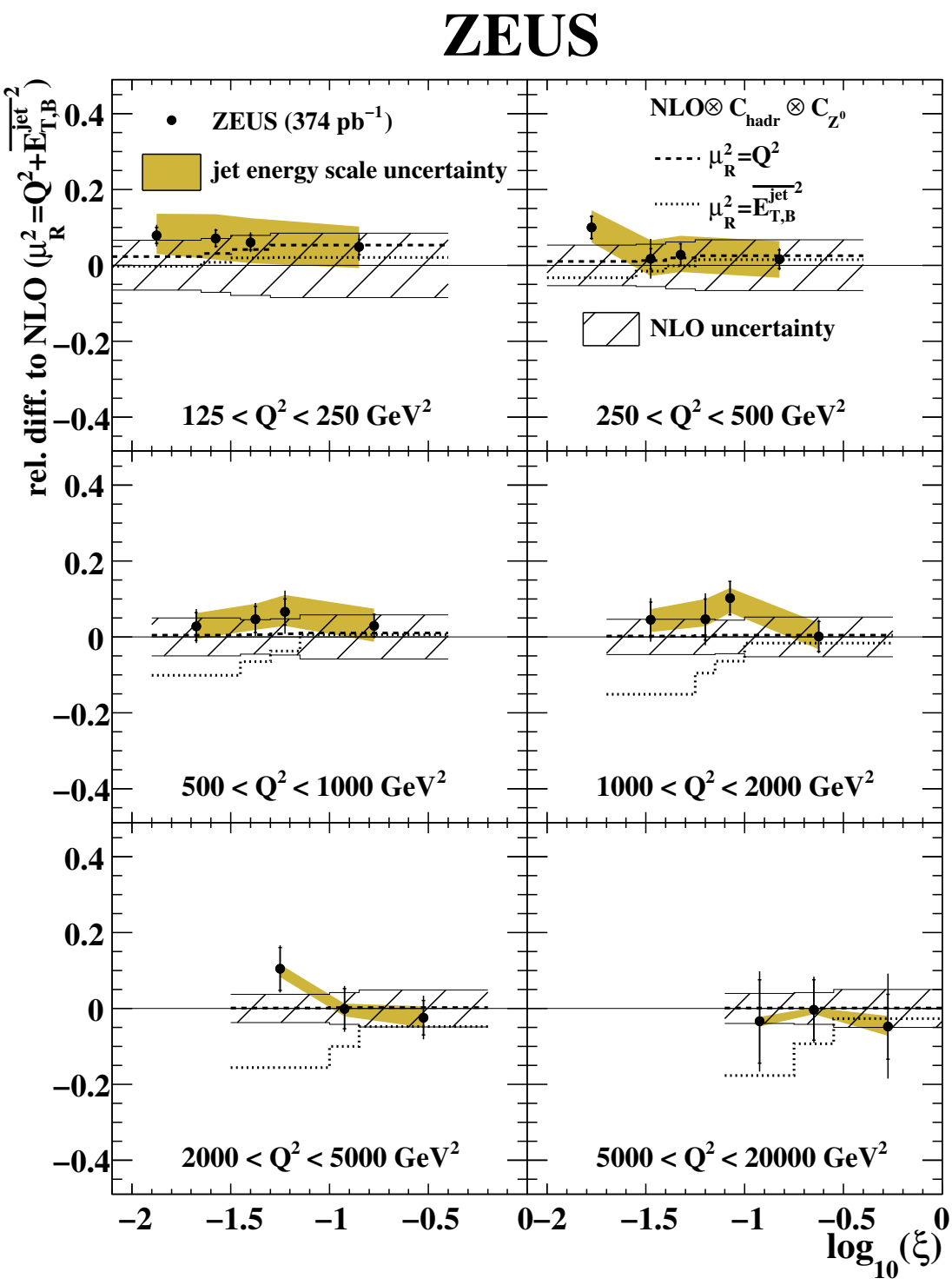

Figure 9.5: Relative differences between the measured differential cross-section $d\sigma/d\log_{10}(\xi)$ for inclusive *dijet* production presented in Fig. 9.4 and the NLO QCD calculations with $\mu_R^2 = Q^2 + \overline{E_{T,\mathrm{B}}^{\mathrm{jet}}}^2$. Other details as in the caption to Fig. 9.1.

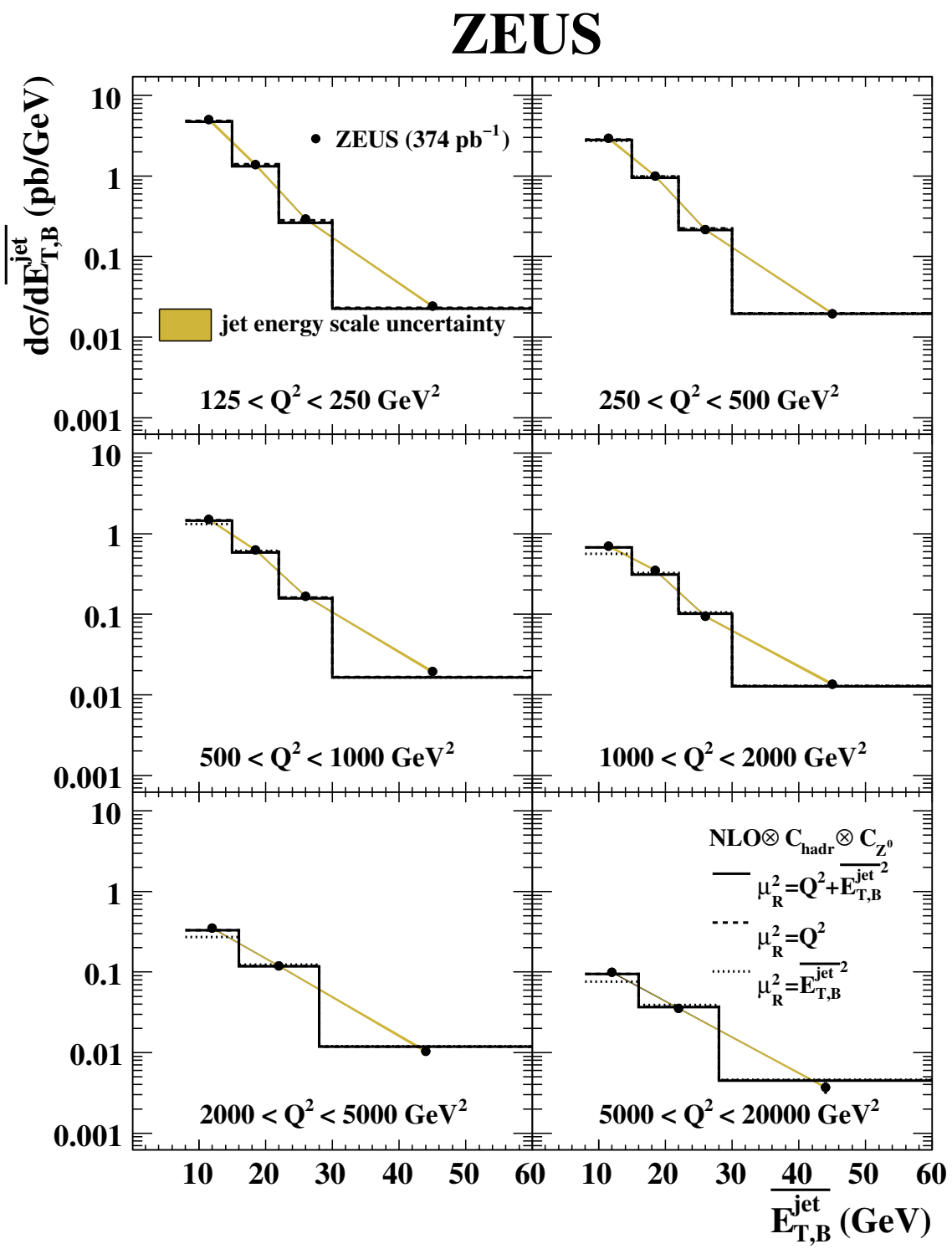

Figure 9.6: The measured differential cross-section $d\sigma/d\overline{E^{\rm jet}_{T,\rm B}}$ for inclusive *dijet* production in different regions of Q^2. Other details as in the caption to Fig. 9.1.

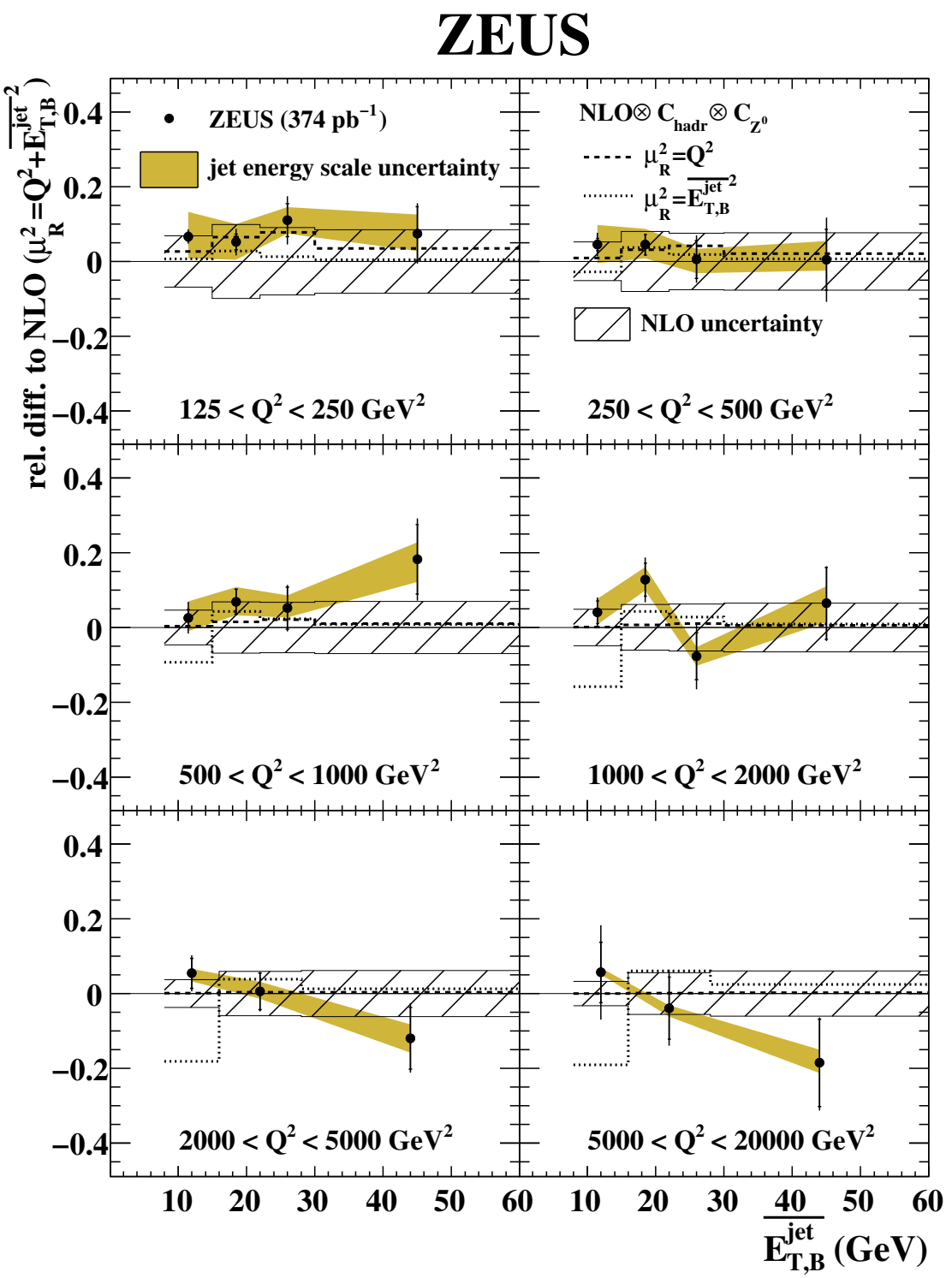

Figure 9.7: Relative differences between the measured differential cross-section $d\sigma/d\overline{E_{T,\mathrm{B}}^{\mathrm{jet}}}$ for inclusive *dijet* production presented in Fig. 9.6 and the NLO QCD calculations with $\mu_R^2 = Q^2 + \overline{E_{T,\mathrm{B}}^{\mathrm{jet}}}^2$. Other details as in the caption to Fig. 9.1.

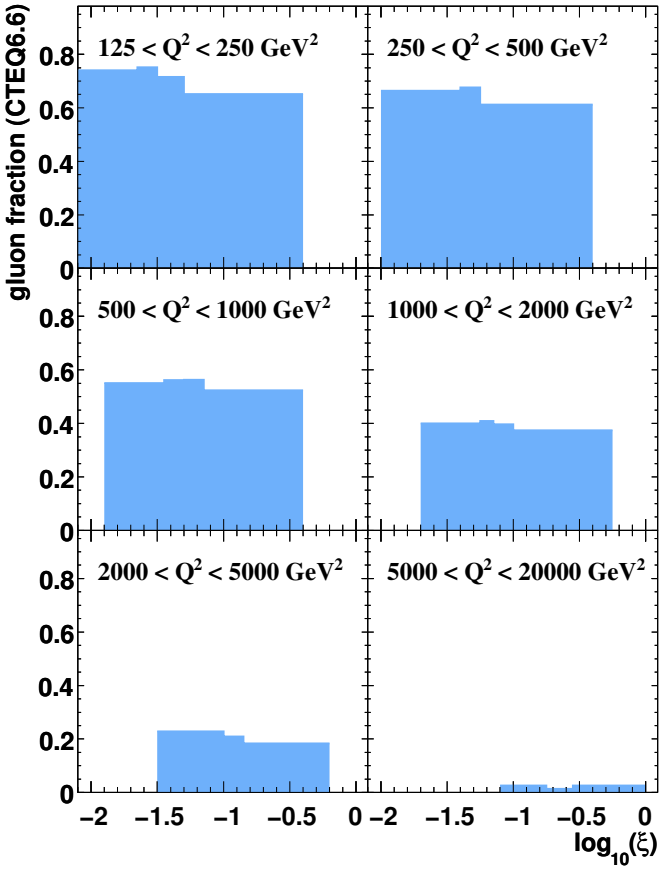

Figure 9.8: The fraction of gluon-induced *dijet* events as a function of $\log_{10}(\xi)$ in different regions of Q^2.

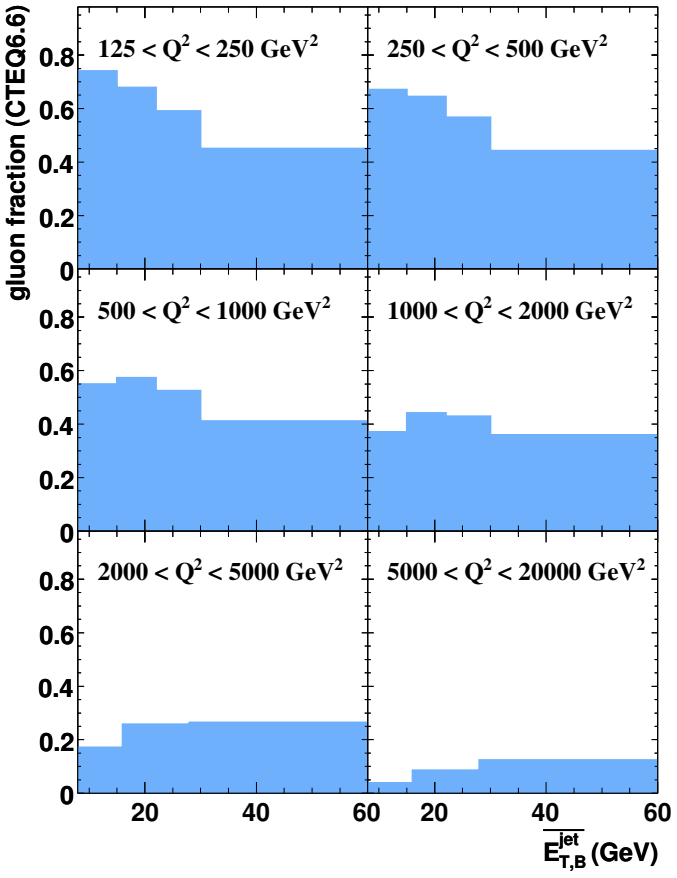

Figure 9.9: The fraction of gluon-induced *dijet* events as a function of $\overline{E_{T,\mathrm{B}}^{\mathrm{jet}}}$ in different regions of Q^2.

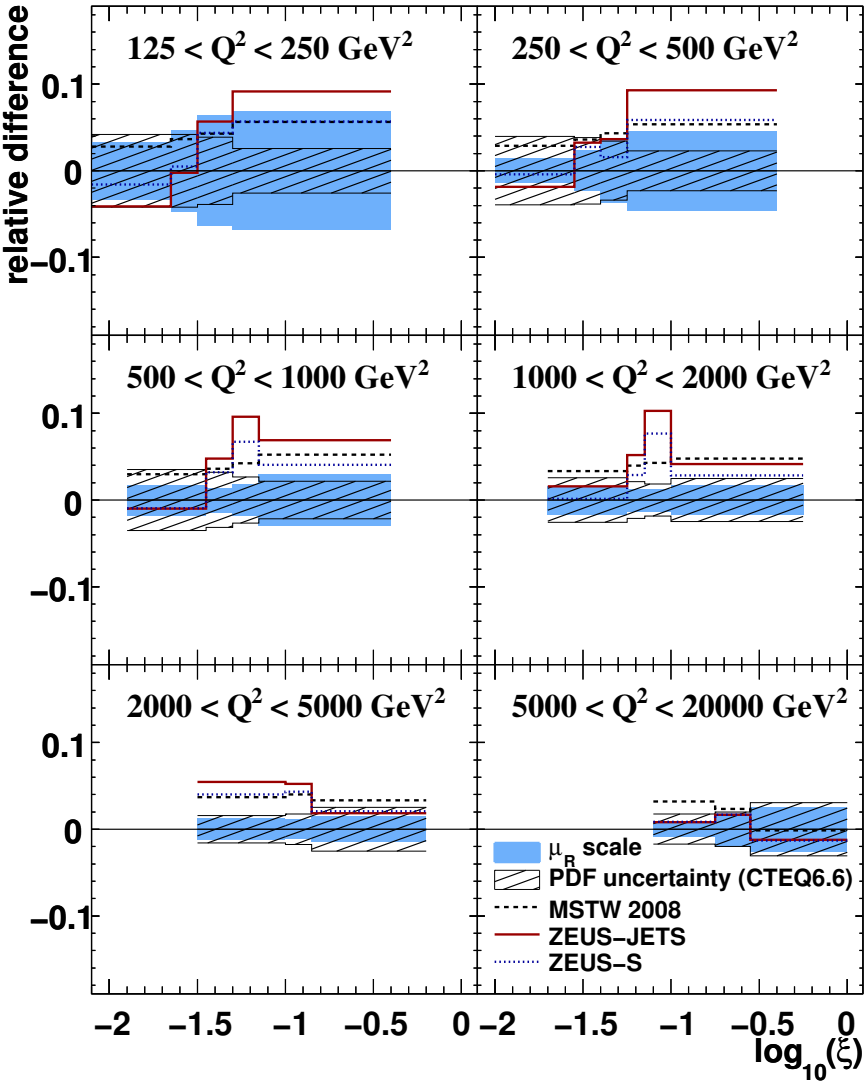

Figure 9.10: The relative CTEQ6.6 PDF uncertainty, the relative uncertainty due to missing higher orders estimated by a variation of μ_R and the theoretical predictions from different PDF sets relative to those obtained with CTEQ6.6 for inclusive *dijet* production as a function of $\log_{10}(\xi)$ in different regions of Q^2.

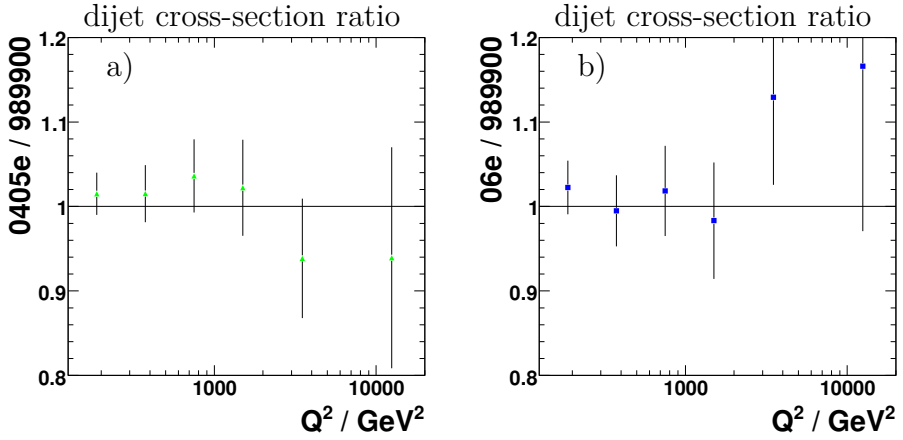

Figure 9.11: The dijet cross-section ratios as a function of Q^2 for the a) 2004–2005 e^- and b) 2006 e^- periods with respect to the data from the years 1998–2000. The data were corrected for electro-weak effects.

9.1.8. Comparison Between the Data-Taking Periods

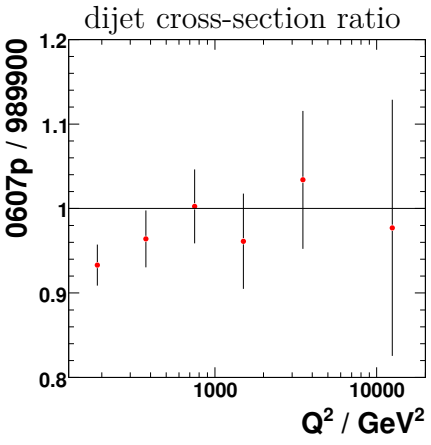

Figure 9.12: The dijet cross-section ratios as a function of Q^2 for the 2006–2007 e^+ period with respect to the data from the years 1998–2000. The data were corrected for electro-weak effects.

In the presented analysis, data taken during the years 1998–2000, 2004–2006 and 2006–2007 were considered. Since the involved physical processes for jet production are time-independent, a comparison of the jet cross sections between the periods can be employed to exclude time dependent experimental effects. In figures 9.11 and 9.12 the dijet cross-section ratios for the individual data-taking periods relative to the cross sections measured during the years 1998–2000 are presented. Additionally, only for this particular study the measurements were corrected for electro-weak effects[5] in order to be able to compare the cross sections for the e^- and e^+ periods. In practice, the inverse of the electro-weak correction factors discussed in chapter 7.3 were applied to the data separately for the e^- and e^+ periods. The indicated uncertainty bars show the relative statistical uncertainty – omitting the systematic uncertainties. It can be noted that the data from the years 2004–2006 agree very well within the statistical uncertainties with the 1998–2000 data. However, the 2006–2007 data exhibit a systematic shift towards smaller cross sections in the order of approximately $\approx 4\% \pm 1.2\%$ compared to the 1998–2000 data. Since the 2006–2007 data contribute approximately 1/4 to the full combined data luminosity, the effect on the combined cross section would be $\approx 1\%$, which is negligible compared to $\approx 5\%$ systematic uncertainty.

9.2. Inclusive Trijet Cross Sections and the Cross-Section Ratio $R_{3/2}$

In this section, the measurements of the inclusive trijet cross sections and the determination of the cross-section ratio, $R_{3/2}$, are presented and discussed.

9.2.1. Trijet Cross Sections as Functions of Q^2

Figure 9.13 a) presents the single-differential inclusive trijet cross-section as a function of Q^2. The cross section decreases by about three orders of magnitude.

[5] In general, the theoretical predictions were corrected for the contributions from the Z^0 boson.

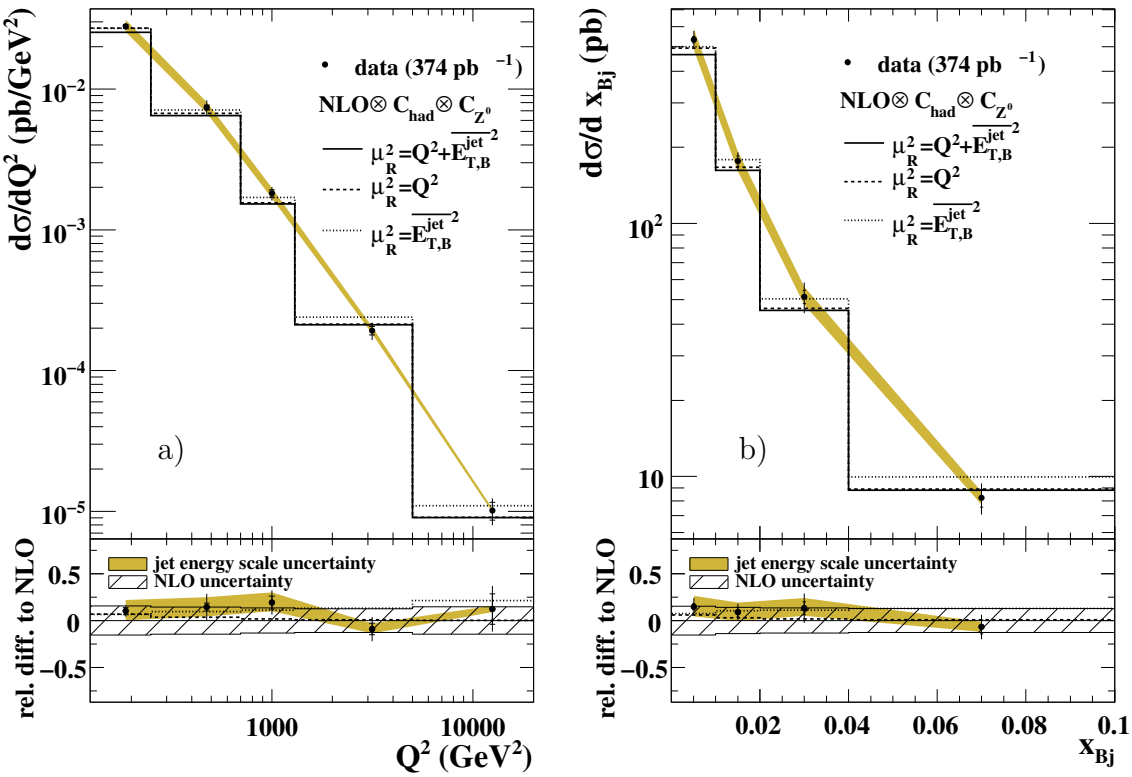

Figure 9.13: The measured differential cross-sections (a) $d\sigma/dQ^2$ and (b) $d\sigma/dx_{\mathrm{Bj}}$ for inclusive *trijet* production. Other details as in the caption to Fig. 9.1.

The statistical uncertainties in the Q^2 region $125 < Q^2 < 700$ GeV^2 amount to about 3% and are in this region smaller than the correlated systematic uncertainties ($\approx 10\%$) coming from the jet energy scale. Towards larger values of Q^2 the statistical uncertainty increases up to 15%, where it becomes comparable to the uncorrelated systematic uncertainty. The main source of uncorrelated systematic uncertainties is introduced by the model dependence of the acceptance correction. Except for the first Q^2 bin, this uncertainty has a size of about $10 - 15\%$.

Typically, the theoretical uncertainties have a size of 10% to 15% and show no distinct Q^2 dependence. The main source of theoretical uncertainties is coming from the choice of the renormalisation scale and from the uncertainty on the value of α_s. The latter is caused by the stronger dependence ($O(\alpha_s^3)$) of the trijet production in NLO compared to the dijet production on the value of α_s. The PDF uncertainties contribute with a comparable size ($\approx$ 3%) as for the dijet cross sections to the predictions for trijet production. The estimated cross-section uncertainty due to the hadronisation correction amounts to $3 - 4\%$. Due to the more complicated multi-jet final state, this uncertainty is larger than the corresponding uncertainty for dijet production. As already discussed for the production of dijets in chapter 9.1.1, the prediction with $\mu_R^2 = \overline{E_{T,\mathrm{B}}^{\mathrm{jet}}}^2$ significantly deviates in the high Q^2 regime from the predictions obtained with the default renormalisation scale. However, within the

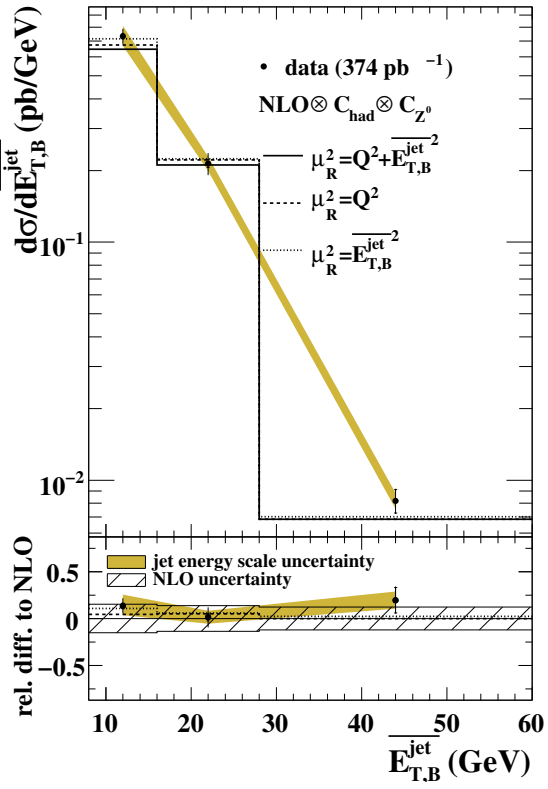

Figure 9.14: The measured differential cross-section $d\sigma/d\overline{E_{T,\mathrm{B}}^{\mathrm{jet}}}$ for inclusive *trijet* production. Other details as in the caption to Fig. 9.1.

uncertainties the NLO pQCD predictions with all three considered renormalisation scales describe the measurement of trijet production as a function of Q^2.

9.2.2. Trijet Cross Sections as Functions of x_{Bj}

The single-differential inclusive trijet cross-section $d\sigma/dx_{\mathrm{Bj}}$ is shown in figure 9.13 on the right-hand side. Due to the suppression by the decreasing parton densities in the proton at higher momentum fractions, the cross section decreases with increasing x_{Bj} over two orders of magnitude.

The experimental correlated systematic uncertainties amount to 6% (10%) in the high (low) x_{Bj} regime. Their size is comparable to the uncorrelated systematic uncertainties. The statistical precision of the data amounts to $\approx 3\%$ at low x_{Bj}. In contrast, at large x_{Bj} values it becomes as large as 8%.

The NLO QCD calculations describe the data within uncertainties reasonably well. Their uncertainties amount to about 15%. No systematic deviation between the data and the theory is visible.

9.2.3. Trijet Cross Sections as Functions of $\overline{E_{T,B}^{jet}}$

In figure 9.14 the single-differential trijet cross-section $d\sigma/d\overline{E_{T,\mathrm{B}}^{\mathrm{jet}}}$ is depicted. The cross section falls over slightly more than one order of magnitude.

The uncertainties related the jet energy scale and the model dependence of the acceptance correction are the largest contribution to the total systematic uncertainty

of the trijet production measurement. These uncertainties amount to about $8 - 10\%$.

Within the theoretical uncertainties the NLO predictions with all three renormalisation scales describe the data reasonably well.

9.2.4. Trijet Cross Sections as Functions of $\overline{E^{jet}_{T,B}}$ in Regions of Q^2

The two figures 9.15 and 9.16 present the double-differential trijet cross-section $d\sigma/d\overline{E^{jet}_{T,B}}$ in different regions of Q^2 and the relative difference to the NLO QCD calculations. The cross section falls over two to three orders of magnitude in the phase-space region investigated, exhibiting a harder $\overline{E^{jet}_{T,B}}$ spectrum for larger values of Q^2.

The experimental correlated uncertainty amounts to approximately 10% in the region $125 < Q^2 < 1300$ GeV^2, with slightly smaller uncertainties at $\overline{E^{jet}_{T,B}} > 28$ GeV. In the highest investigated Q^2 interval, this uncertainty is sligthly smaller ($\approx 5\%$). Except for the range $8 < \overline{E^{jet}_{T,B}} < 28$ GeV, the statistical uncertainties are of comparable size. The uncertainty related to the acceptance correction has a relative size of $10 - 15\%$. Besides the jet energy scale uncertainty, it is the dominant systematic uncertainty.

The total theoretical uncertainty has a size of about $\pm 15\%$ and decreases to 12% at high $\overline{E^{jet}_{T,B}}$. Similarly to the single-differential trijet cross sections the theoretical uncertainties are dominated by the renormalisation-scale dependence and the α_s uncertainty.

9.2.5. The Cross-Section Ratio $R_{3/2}$ as a Function of $\overline{E^{jet}_{T,B}}$ in Regions of Q^2

Figure 9.17 depicts the cross-section ratio $R_{3/2}$ as a function of $\overline{E^{jet}_{T,B}}$ in different regions of Q^2. First, the ratio increases, shows a maximum around 20 GeV and then falls for larger $\overline{E^{jet}_{T,B}}$ values. The shape of the distributions is caused by the phase-space selection cuts. In particular, the cut on the invariant dijet mass M_{jj} causes the observed maxima.

The statistical uncertainties of the measurement are slightly smaller than those for the measurement of the corresponding trijet cross sections (figures 9.15 and 9.16). The correlated uncertainties coming from the jet energy scale are slightly smaller (7%).

The theoretical uncertainties have typically a size of 5%; in some bins up to 10%. Within the uncertainties the theory is describing the measurement.

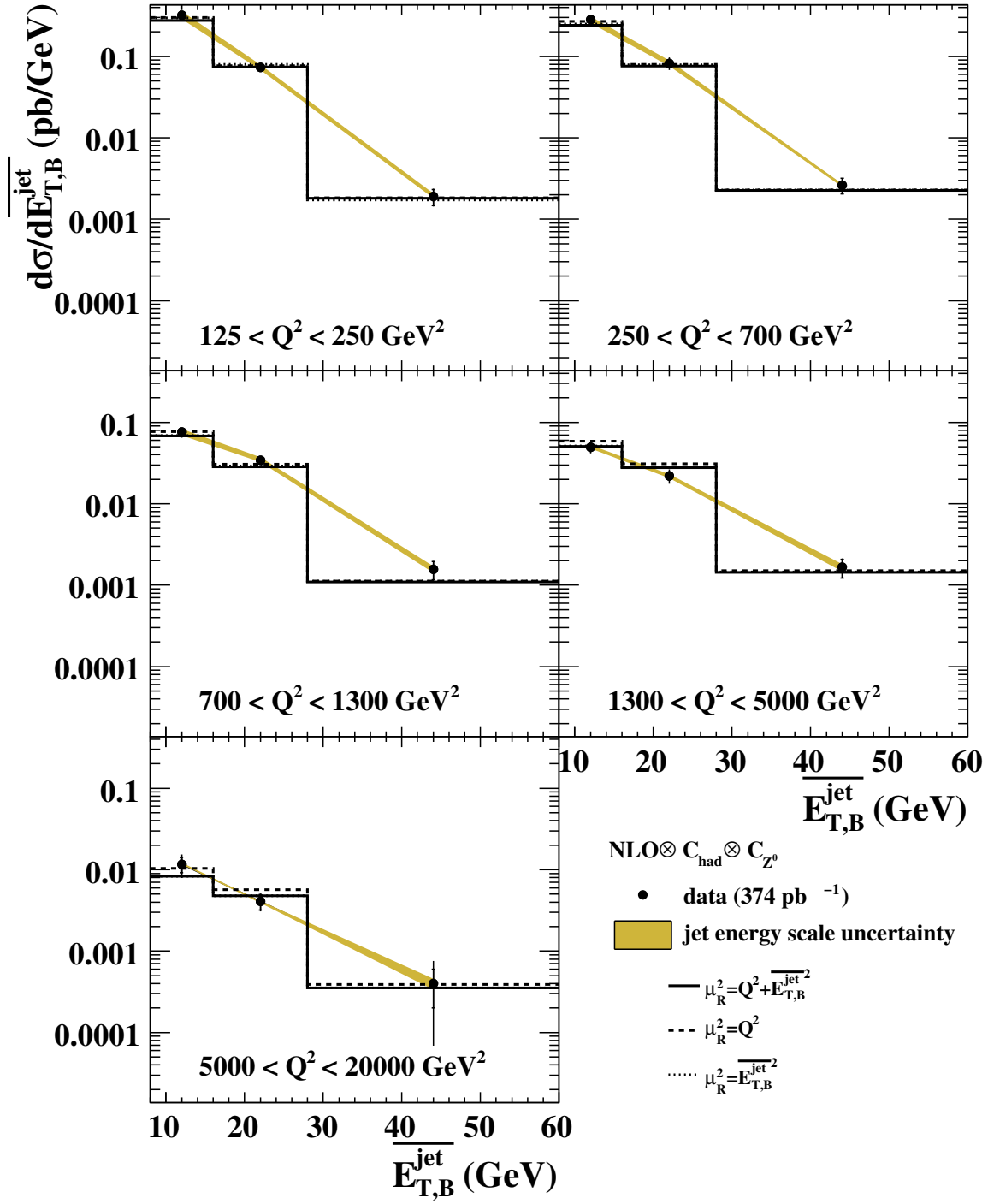

Figure 9.15: The measured differential cross-section $d\sigma/d\overline{E^{\rm jet}_{T,\rm B}}$ for *trijet* production in different regions of Q^2. Other details as in the caption to Fig. 9.1.

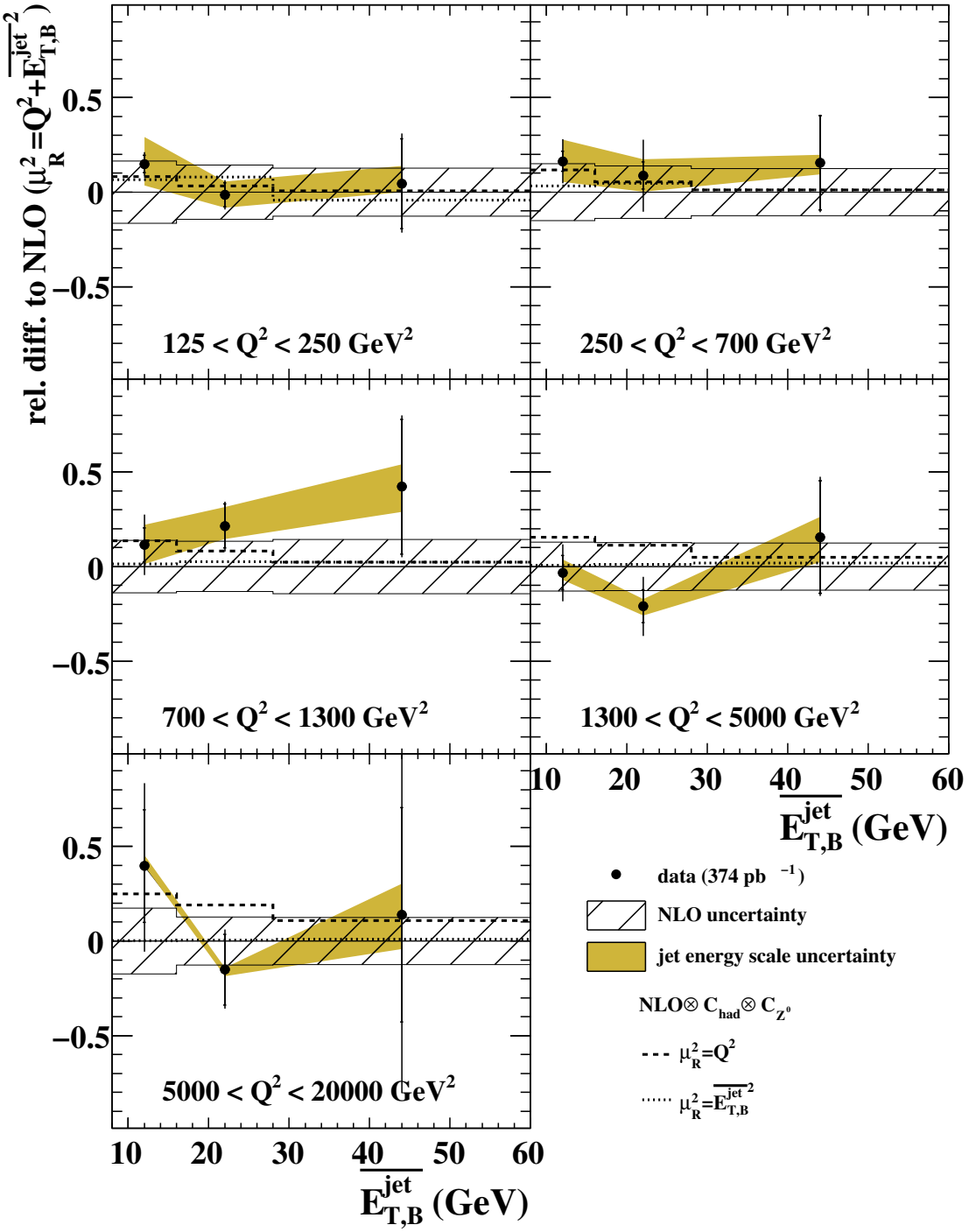

Figure 9.16: Relative differences between the measured differential cross-section $d\sigma/d\overline{E_{T,\mathrm{B}}^{\mathrm{jet}}}$ for *trijet* production presented in Fig. 9.15 and the NLO QCD calculations with $\mu_R^2 = Q^2 + \overline{E_{T,\mathrm{B}}^{\mathrm{jet}}}^2$. Other details as in the caption to Fig. 9.1.

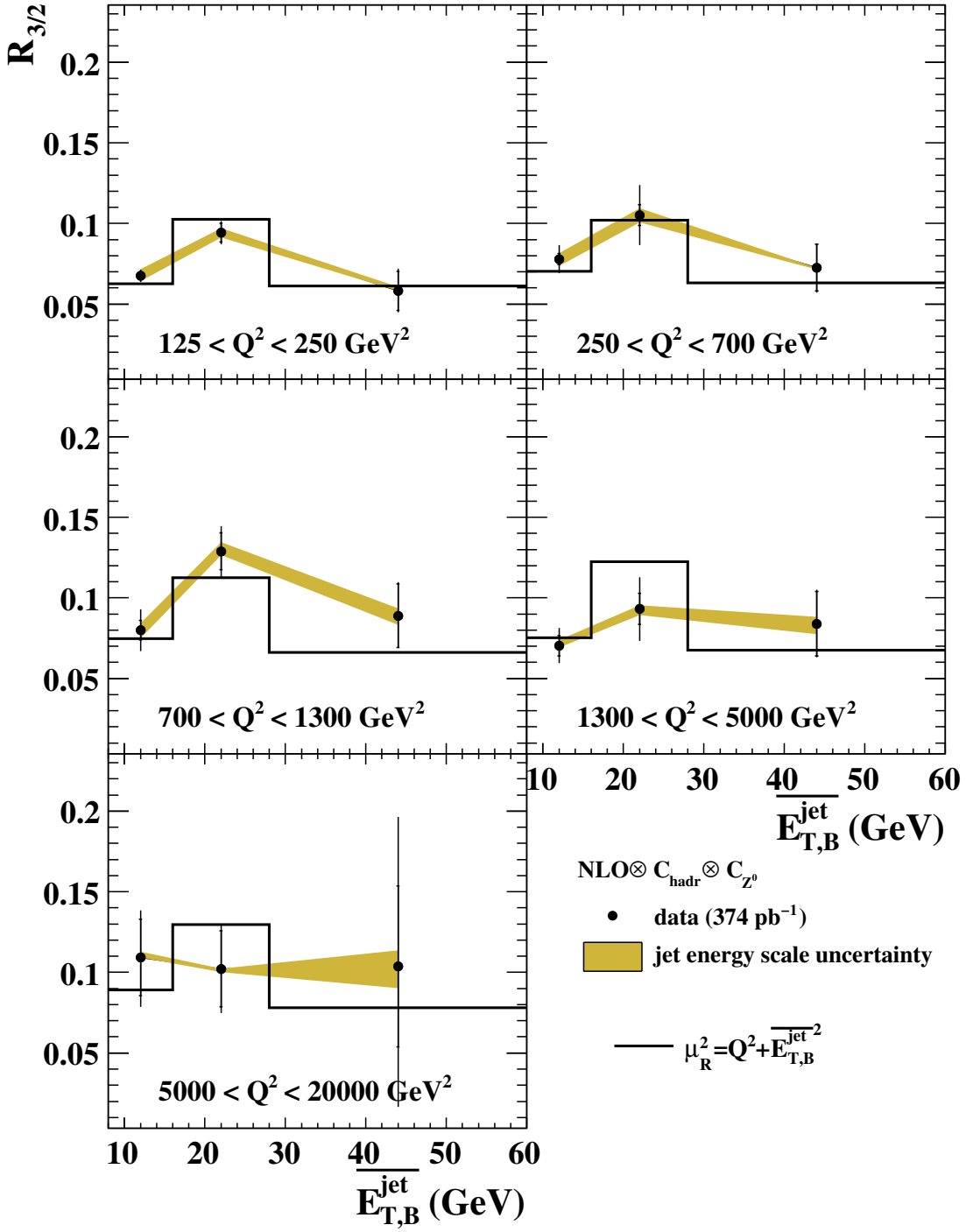

Figure 9.17: The measured differential cross-section ratio, $R_{3/2}$, as a function of $\overline{E^{\text{jet}}_{T,\text{B}}}$ in different regions of Q^2. Other details as in the caption to Fig. 9.1.

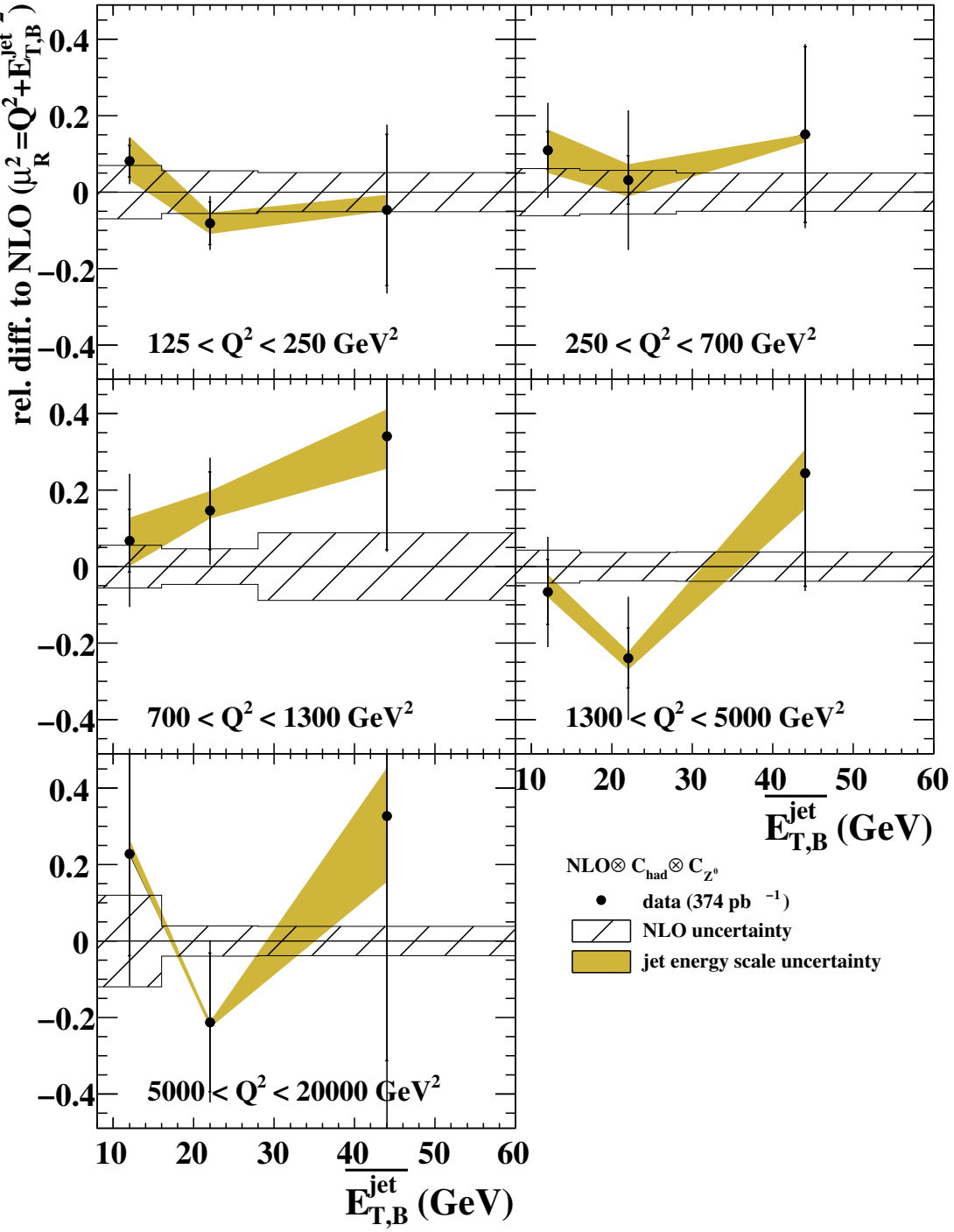

Figure 9.18: Relative differences between the measured differential cross-section ratio, $R_{3/2}$, as a function of $\overline{E_{T,\mathrm{B}}^{\mathrm{jet}}}$ presented in Fig. 9.17 and the NLO QCD calculations with $\mu_R^2 = Q^2 + \overline{E_{T,\mathrm{B}}^{\mathrm{jet}}}^2$. Other details as in the caption to Fig. 9.1.

9.3. Extraction of the Strong Coupling

In the previous sections 9.1 and 9.2, the measurements of dijet and trijet cross sections as well as the cross-section ratios, $R_{3/2}$, were presented, and the agreement between the data and the theoretical predictions in NLO was found to be reasonable. In this chapter the data are used for an extraction of the value of the strong coupling, α_s, for which QCD only predicts the scale dependence. The applied extraction method and the results are described and discussed.

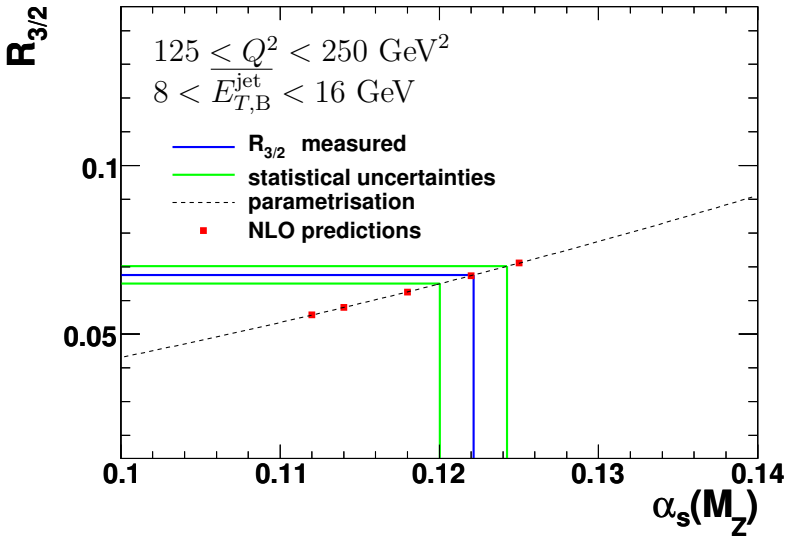

Figure 9.19: The α_s extraction method using the cross-section ratio, $R_{3/2}$, in the region $125 < Q^2 < 250$ GeV^2 and $8 < \overline{E^{\text{jet}}_{T,\text{B}}} < 16$ GeV.

The sensitivity of the jet cross sections to the value of $\alpha_s(M_Z)$ was studied by calculating with NLOJET++ the relative difference of the NLO predictions for dijet and trijet production and for the cross-section ratio $R_{3/2}$ with respect to the results obtained assuming $\alpha_s(M_Z) = 0.118$ in different regions of Q^2 and $\overline{E^{\text{jet}}_{T,\text{B}}}$. The outcome of this study is depicted in figure 9.21; it shows that trijet production is, as expected, more sensitive to α_s than dijet production. At larger values of $\overline{E^{\text{jet}}_{T,\text{B}}}$, the dependence of $R_{3/2}$ on α_s is comparable to the α_s dependence of dijet production. With decreasing Q^2, the relative difference of the ratio $R_{3/2}$ is more similar to the relative difference of the trijet cross section, indicating that an α_s extraction in the lower Q^2 region can potentially have a reduced total experimental uncertainty.

The measured differential cross-section ratios, $R_{3/2}$, presented in section 9.2 were used to determine $\alpha_s(M_Z)$ in order to profit from the enhanced sensitivity to α_s and from the partial cancellation of correlated systematic uncertainties. The method applied in this analysis was similar to the one used in previous jet studies at ZEUS [3, 4, 62, 63] and consisted of the following steps:

- The NLO QCD calculations were performed with the five PDF sets [81] CTEQ6.6A4, CTEQ6.6A3, CTEQ6.6, CTEQ6.6A2 and CTEQ6.6A1 which were determined from global fits assuming the values 0.112, 0.114, 0.118, 0.122 and 0.125 for $\alpha_s(M_Z)$. The actual used value of $\alpha_s(M_Z)$ in the QCD calculations was that associated with the corresponding PDF set.

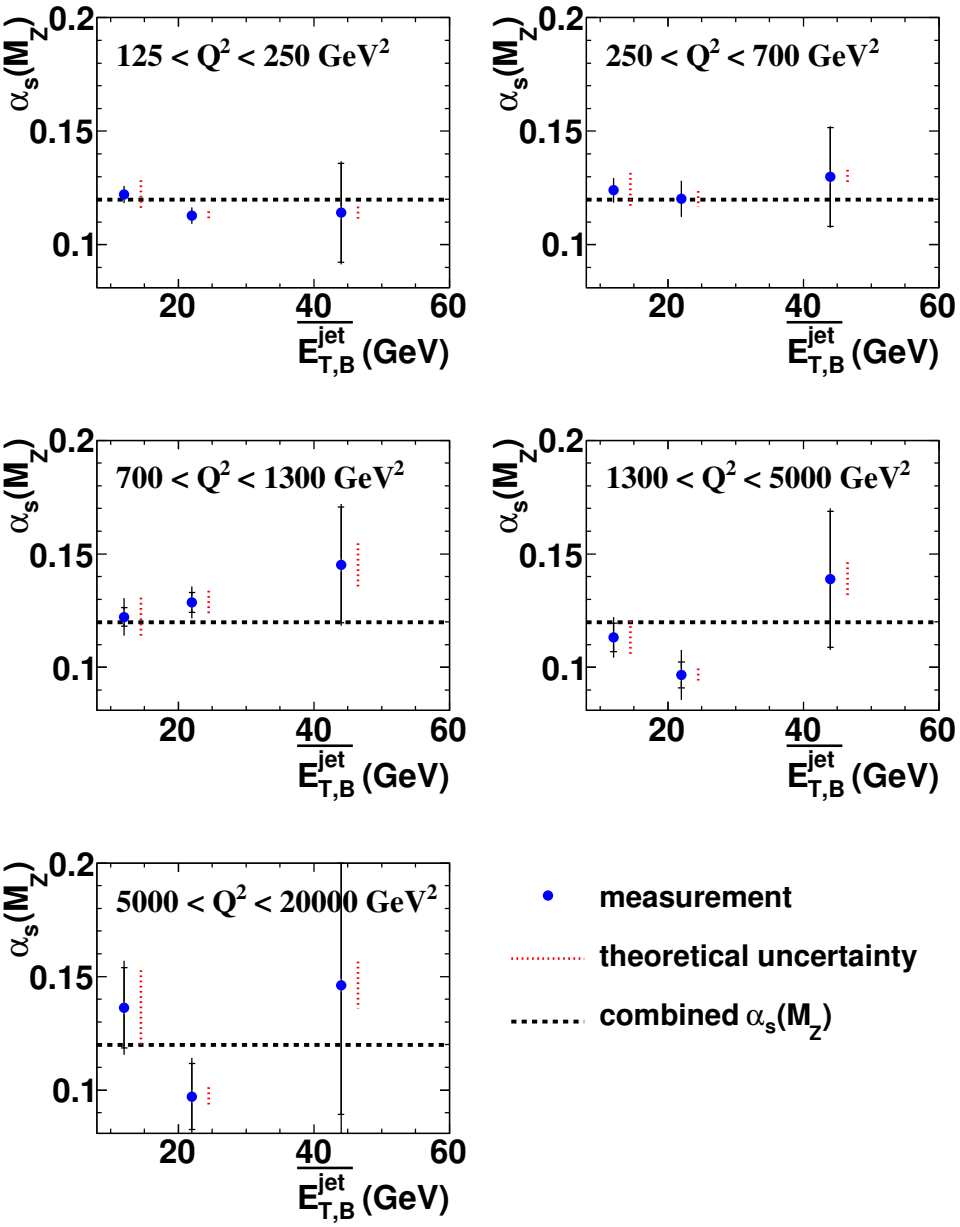

Figure 9.20: The extracted $\alpha_s(M_Z)$ values for each measured data point and the combined value.

- The dependence of $R_{3/2}$ on the value of $\alpha_s(M_Z)$ was parameterised in each analysis bin i with the polynomial function

$$R^i_{3/2} = a_i \cdot \alpha_s(M_Z) + b_i \cdot \alpha_s(M_Z)^2 . \tag{9.1}$$

  The variables a_i and b_i were obtained by a χ^2 fit to the theoretical predictions. This method treats correctly the explicit dependence arising from the partonic cross sections and the implicit dependence coming from the PDFs. The correlation between the PDFs and α_s is thus preserved.

Figure 9.19 shows an examples for the quantity $R_{3/2}$ as a function of $\alpha_s(M_Z)$, the parameterisation of the dependence and the extracted value of α_s with its uncertainty in the region $125 < Q^2 < 250$ GeV^2 and $8 < \overline{E_{T,\mathrm{B}}^{\mathrm{jet}}} < 16$ GeV.

- Afterwards, the combined value of $\alpha_s(M_Z)$ was determined from a combined χ^2 fit to all 15 data points performed with MINUIT. The statistical uncertainty defined as the range where χ^2 changes by 1 was obtained from the fitting procedure, whereas the experimental and systematic uncertainties were estimated by repeating the fit for each experimental and theoretical systematic check presented in the chapters 8.1 and 8.2 except for that coming from the uncertainty on α_s. The difference with respect to the central extracted α_s value has defined the corresponding uncertainty. The individual uncertainties were added in quadrature and transformed to symmetric uncertainties.

Figure 9.20 depicts the individual extracted $\alpha_s(M_Z)$ values for each studied data point in comparison with the combined $\alpha_s(M_Z)$ which is indicated as dashed lines. The agreement between the data points is reasonable within the combined[6] statistical and systematic experimental uncertainties ($\chi^2/\mathrm{ndf} = 1.03$).

Figure 9.22 shows the results for several extractions of the strong coupling, $\alpha_s(M_Z)$, from jets in photoproduction [6, 62], from jets at low [21] and high Q^2 [5, 63] and from four-jet rates [64] in e^+e^- interactions. The α_s values extracted in this analysis from $R_{3/2}$ for the full jet phase space investigated and for several restricted phase-space regions are also shown.

All α_s values extracted in this analysis are within the uncertainties consistent with the world average α_s value of 0.1189 ± 0.0010 [65]. An extraction restricted to the lower Q^2 part of the studied phase space gave the smallest total theoretical and systematic experimental uncertainties. The smaller size of the systematic experimental uncertainties in this region is partially caused by the fact that the dependence of $R_{3/2}$ on the actual α_s value at lower Q^2 is stronger and more similar to the dependence of the trijet predictions as depicted in figure 9.21. The following value of α_s with the smallest in this analysis achievable total uncertainty was extracted from the region $125 < Q^2 < 250$ GeV^2 with a fit to three data points:

$$\alpha_s(M_Z) = 0.1187 \pm 0.0014\,(\mathrm{stat.}) \pm 0.0031\,(\mathrm{exp.}) \pm 0.0040\,(\mathrm{th.}) \qquad (9.2)$$

The relative statistical uncertainty is approximately 1.2%, the relative systematic experimental uncertainty was found to be 2.6% and the relative theoretical uncertainty was determined to be 3.4%, giving a total relative uncertainty of about 4.4%. The value of χ^2 per degree of freedom was 1.2. Since the extraction was at least partially limited by the statistics of the data, the precision of the α_s extraction can possibly be improved by extending the analysis to the low-Q^2 region.

[6] The statistical and systematic experimental uncertainties were added in quadrature.

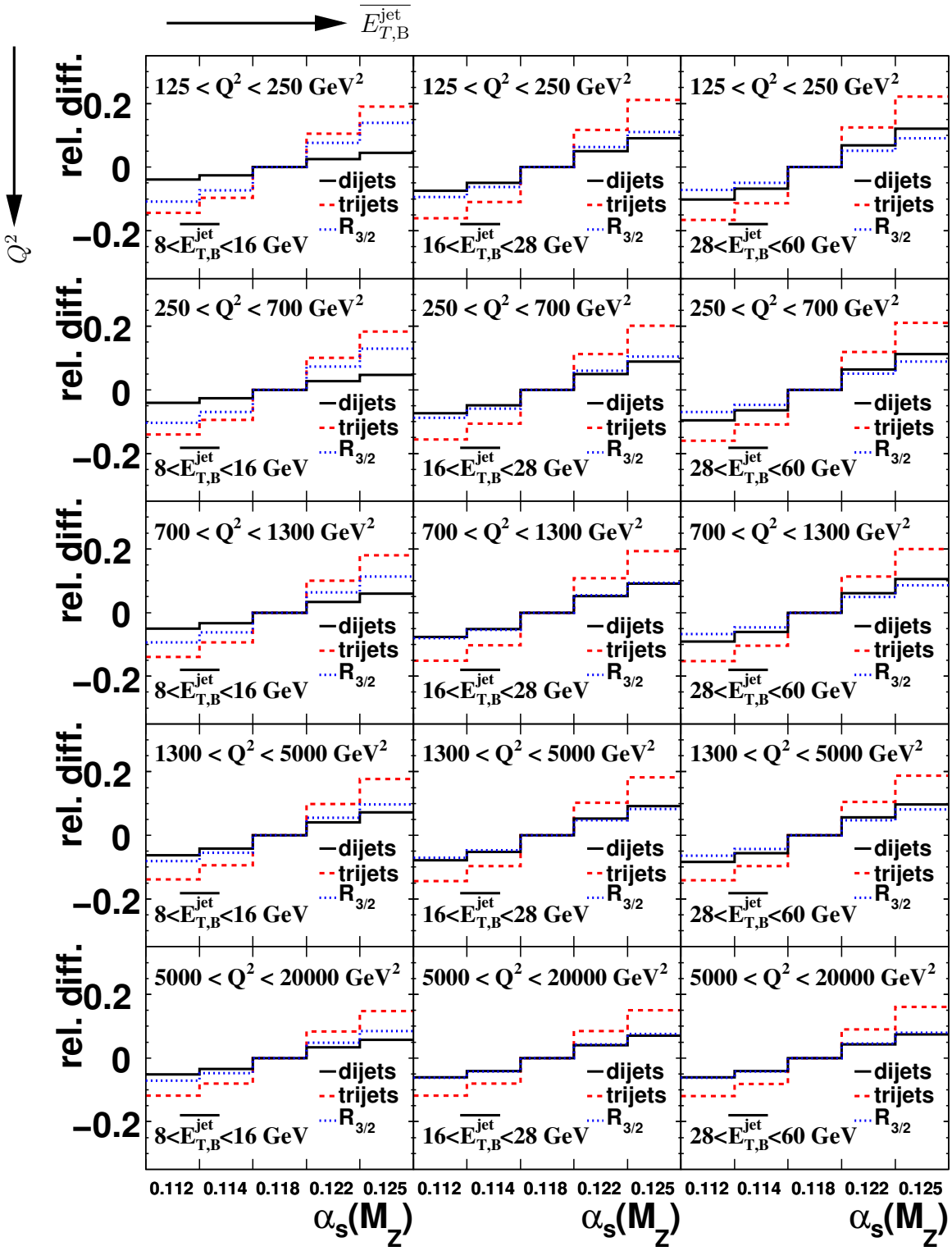

Figure 9.21: The relative difference of the NLO predictions for dijet (solid lines), trijet (dashed lines) production and the cross-section ratio $R_{3/2}$ (dotted lines) with respect to the result of the calculation with $\alpha_s(M_Z) = 0.118$ as a function of $\alpha_s(M_Z)$ in different regions of Q^2 and $\overline{E^{\text{jet}}_{T,\text{B}}}$.

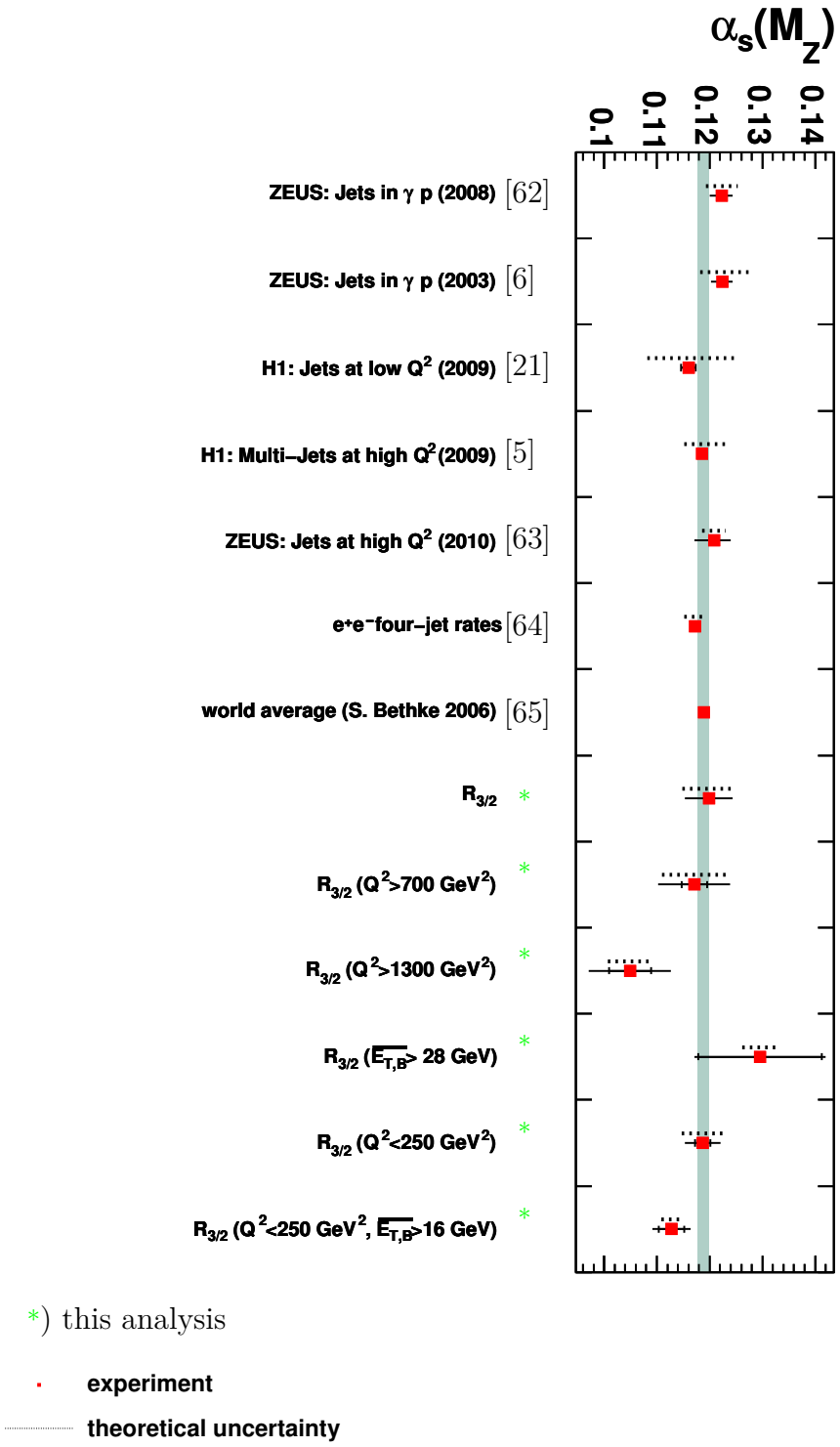

Figure 9.22: Comparison of the results from various α_s extraction. The filled vertical area indicates the world average value of α_s.

10. Summary and Conclusion

Differential cross sections for dijet and trijet production in deep-inelastic electron-proton scattering at HERA as functions of several kinematic and jet variables were measured and compared to next-to-leading order theoretical predictions. These jet measurements probe an extended region of the phase space compared to previous jet analyses at ZEUS. The analysed data sample was taken with the ZEUS detector and corresponded to an integrated luminosity of 374 pb^{-1}. The presented dijet and trijet measurements were performed with a data sample which was more than a factor of 4.5 larger than in previous comparable analyses at ZEUS.

In this thesis, differential jet cross sections were measured with beam energies of 27.5 GeV for the electrons/positrons and 920 GeV for the protons in the kinematic region of the virtuality, $125 < Q^2 < 20000$ GeV^2, and the inelasticity, $0.2 < y < 0.6$.

The k_t jet algorithm in the longitudinally invariant inclusive mode was applied to the measured final-state objects, which were assumed to be massless, in the boson-quark collinear frame, the Breit reference frame. In data and on Monte Carlo reconstruction level, the signals from the smallest calorimeter units – the cells – were used as inputs to the cluster algorithm. The cross sections referred to jets with $E^{\text{jet}}_{T,\text{B}} > 8$ GeV and $-1 < \eta^{\text{jet}}_{\text{LAB}} < 2.5$, where the first variable is the transverse jet energy in the Breit frame and the latter the jet pseudorapidity in the laboratory frame. For the selection of dijet (trijet) events it was required that at least the two (three) highest-transverse-energy jets exceed the transverse-energy threshold. Additionally, the invariant dijet mass of the two highest-transverse-energy jets in the event was required to be greater than 20 GeV. The latter cut was also imposed for the selection of trijet events.

Starting from the year 2004, HERA provided lepton beams with longitudinal polarisation resulting in a small average polarisation of $\approx -3\%$. Therefore, the data analysed in the presented thesis were corrected with the HECTOR program such that the measurement corresponded to unpolarised cross sections. The data were neither corrected for Z^0 exchange nor for γ/Z^0 interference.

The longitudinal vertex distribution of the ep interaction in the Monte Carlo simulations for the 2006–2007 positron data was reweighted in order to improve the description of the data.

Several corrections were applied to the measured jets in order to improve the jet energy calibration and reconstruction. The hadronic energy scale was investigated by utilising single-jet events in which the transverse momentum between the final-state electron and the jet is balanced. A correction for the jet energy scale in the Monte Carlo was derived and the uncertainty on the scale was estimated by comparing the jets composed from calorimeter information only with tracking information and by utilising the momentum balance of dijet events with respect to the final-state electron. It was demonstrated that the energy-scale uncertainty for jets with $E^{\text{jet}}_{T,\text{lab}} > 10$ GeV ($3 < E^{\text{jet}}_{T,\text{lab}} < 10$ GeV) was $\pm 1\%$ ($\pm 3\%$). After improving the calibration of the jet sample, the reconstructed jets were compared with jets on hadron level and corrected

for the influence of detector effects as function of the jet pseudorapidity. This correction helped to improve the purity and the efficiency of the jet sample.

The first-level trigger efficiency was investigated with the aid of an unbiased trigger chain. It was found that there was a trigger efficiency mismatch starting from the year 2004 between the data and the Monte Carlo simulations caused by the track-veto requirements of the utilised trigger chain. For the 2006–2007 positron data, the size of this effect was slightly reduced by using a Monte Carlo simulation with an improved simulation of the CTD gas gain. However, the remaining observed discrepancy was accounted for with a correction procedure which randomly removed Monte Carlo events until the Monte Carlo simulations described the observed data efficiency.

After applying the full dijet selection, the Monte Carlo simulations were reweighted in order to agree with the the observed Q^2 dependence in the data.

After applying all the described corrections, the two Monte Carlo simulations LEPTO and ARIADNE described the shape of all relevant data distributions reasonably well. This good agreement was the basis for correcting the data for acceptance effects with the aid of a bin-by-bin unfolding procedure as determined with the LEPTO Monte Carlo simulation. Additionally, the data were corrected for QED radiative and loop effects and the running of α_{em}.

The programs utilised for the theoretical predictions have only provided calculations for the partonic cross section. Therefore, the theory was corrected for the non-perturbative effect of hadronisation by exploiting the average between the hadronisation correction factors of the two Monte Carlo simulations LEPTO and ARIADNE. The size of the hadronisation corrections was typically ≈ 0.95 for dijet and $\approx 0.8 - 0.85$ for trijet production.

The programs used for the fixed-order calculations did not include the contribution from electro-weak effects; thus, the theory was corrected for the influence of the Z^0 boson on the DIS cross sections. These correction factors were extracted from Monte Carlo simulations and defined as the cross-section ratio between the Monte Carlo prediction with electro-weak effects and without these effects.

Several sources of experimental and theoretical systematic uncertainties were investigated and their influence on the jet cross-section measurement was studied. In the bulk of the dijet phase space, the experimental systematic uncertainty with the largest contribution was the uncertainty of the jet energy scale. For the measurement of dijet production, the model dependence of the acceptance correction in the high-Q^2 region was the largest experimental uncertainty. In contrast, the uncertainties of the trijet-cross-section measurement were dominated by the uncertainty coming from the model dependence of the acceptance correction and by the uncertainty of the jet energy scale. The larger dependence on the parton-cascade model was caused by the fact that both Monte Carlo simulations only made use of a leading-order prediction for dijet production. Higher orders were approximated with the application of the parton cascade.

In order to perform a comprehensive and stringent study of the pQCD predictions, differential dijet cross sections were measured as functions of Q^2, x_{Bj}, η^*, M_{jj}, $\overline{E^{\mathrm{jet}}_{T,\mathrm{B}}}$ and ξ. Since the latter variable, ξ, is related to the momentum fraction carried by the struck quark, its sensitivity to the PDFs was used to investigate the contributions

from gluon-induced events. Owing to this sensitivity, the differential dijet cross section as function of ξ was also measured in different regions of Q^2 in order to test the scale dependence of the PDFs. In addition, the inclusive dijet cross section as a function of $\overline{E_{T,\mathrm{B}}^{\mathrm{jet}}}$ in different regions of Q^2 was measured in order to study the energy scale dependence of the jet cross sections.

In general, the precision of the dijet measurement was limited by systematic uncertainties – especially the jet energy scale uncertainty and the uncertainty coming from the phenomenological modelling of the parton cascade in the Monte Carlo simulations utilised for the unfolding procedure had sizable effects on the dijet cross sections. In the high-η^* region, the fixed-order QCD predictions in NLO were found to be sensitive to infrared cut-offs. Except for this particular region, the agreement between the data and the theoretical calculations was good for all investigated observables in normalisation as well as in shape, confirming that pQCD in NLO has the predictive power to describe dijet production in DIS at HERA.

Furthermore, the dijet data showed a potential for providing further powerful constraints on the parton density functions of the proton due to the sensitivity of the measurement to the gluon density and due to the achieved experimental precision. In some regions of the dijet phase space the estimated PDF uncertainty and the spread between the predictions obtained with various PDF sets were found to be larger than the uncertainty introduced by missing higher orders in the calculations. In addition, the sensitivity to the gluon density was studied with the NLOJET++ program by determining the relative fraction of boson-gluon-fusion events. In the lower Q^2 region, about 60% to 75% of the events are gluon-induced. Moreover, in this region, the spread between the predictions from various PDF sets was found to be largest.

The differential inclusive trijet cross sections were measured as functions of Q^2, x_{Bj} and $\overline{E_{T,\mathrm{B}}^{\mathrm{jet}}}$. The trijet cross sections as a function of $\overline{E_{T,\mathrm{B}}^{\mathrm{jet}}}$ were also studied in various regions of Q^2 in order to investigate the scale dependence of trijet production.

The measurement of single- and double-differential trijet cross sections suffered from larger systematic uncertainties compared to those for the production of dijets. However, the agreement between the measurement and the theory was found to be good within these uncertainties. Therefore, the theory of pQCD in NLO is able to describe multi-jet final states in DIS at HERA.

A partial reduction of systematic uncertainties was achieved by determining the double-differential cross-section ratio, $R_{3/2}$, between trijet and dijet cross sections as a function of $\overline{E_{T,\mathrm{B}}^{\mathrm{jet}}}$ in regions of Q^2. In particular, the normalisation uncertainty due to the luminosity measurement completely cancelled and the uncertainty due to the jet energy scale was slightly reduced. This cross-section ratio was used for an extraction of the strong coupling, α_s, which was found to be compatible within the uncertainties with the world average value. By restricting the extraction to the region $125 < Q^2 < 250$ GeV, an α_s value with a total uncertainty of $\pm 4.4\%$ was obtained,

$$\alpha_s\left(M_Z\right) = 0.1187 \pm 0.0014\,(\mathrm{stat.}) \pm 0.0031\,(\mathrm{exp.}) \pm 0.0040\,(\mathrm{th.})\,. \tag{10.1}$$

The extracted value of α_s indicates that a further reduction of experimental systematic uncertainties is necessary in order to be competitive with the extractions from other processes and experiments. A study of the dependence of the cross sections and

of $R_{3/2}$ on α_s has indicated that an α_s extraction at lower values of Q^2 than considered in this analysis could give smaller total uncertainties due to a stronger dependence of the cross-section ratio on α_s in the lower Q^2 range.

The results for the inclusive dijet cross-section measurement are currently in the ZEUS-internal publishing procedure[1] and expected to be submitted to the journal soon [23].

Owing to the high precision of the data, the measurement has provided a stringent and powerful test of perturbative QCD in NLO. The theory of pQCD is able to describe all multi-jet observables presented in this thesis in the investigated phase-space region at HERA.

In a recent publication [5], the H1 collaboration presented a measurement of multi-jet production at high Q^2. The jet cross sections were normalised to the cross section of neutral-current deep-inelastic scattering and correspond to an integrated luminosity of 395 pb^{-1}. Since the phase space in which this measurement was performed differs from the one studied in this analysis and due to the normalisation of the jet cross sections, it is not easily possible to compare the results with those presented in this thesis. However, the H1 and ZEUS collaborations are planning to agree on a common phase-space region in order to be able to combine the jet measurements. The combination would presumably result in a reduction of systematic uncertainties like the jet-energy-scale uncertainty due to cross-calibration effects between the two experiments as seen in previous combinations [80]. Furthermore, it is planned to implement the combined jet cross sections into global PDF fits.

[1] At the time of writing this thesis, the publication draft was in the "post-reading phase".

Part II.

Test Beam Measurements with the EUDET Pixel Telescope

11. Introduction

The next planned high-energy collider is a linear electron-positron collider – the "International Linear Collider" (ILC) [26] or the "Compact Linear Collider" (CLIC) [27] – operated at a centre-of-mass energy of about $500 - 1000$ GeV (ILC) or up-to 3 TeV (CLIC).

Crucial requirement in many physics analyses at the ILC will be the reconstruction of secondary vertices arising from the decay of (heavy) c- and b-quarks and τ-leptons [193] very close to the primary interaction point. Events with these topologies can be used e.g. for the measurement of quark charges or for tagging b-quarks in jets in order to discriminate events in which top quarks decayed from background processes [194].

The vertex detector [195] for the track and vertex reconstruction foreseen for the ILC must have a polar-angle coverage as hermetic as possible and the innermost layer has to be as close to the interaction point as possible. In order to reduce the impact of multiple scattering the layer thickness of the vertex detector – including cooling – has to be very thin ($0.1\%X_0$ per layer). It has to be capable to cope with the ILC bremstrahlung background and the average power consumption has to be moderate in order to reduce the amount of cooling needed. The readout of the vertex-detector sensors must be adapted to the proposed bunch-crossing structure of the ILC. The sensors installed in the vertex detector must have a very high granularity in order to provide a spatial resolution of < 5 μm [196] obtained with pixel sensors with a pitch of < 20 μm.

At the moment, several different technologies are developed and investigated for the ILC vertex detector such as CCD [197], CMOS [198, 199] or DEPFET [200] sensors and others.

In order to support the research and development of such technologies, the EUDET project, supported by the "European Union" in the "6^{th} Framework Programme" (FP6), would like to enhance the available test-beam infrastructure. The subproject JRA1 is intended to provide a high-resolution pixel telescope that can be operated in a magnetic field of 1.2 T. It should be noted that this telescope is not restricted to developments and studies for the ILC.

It was decided to follow a two stage approach: First, a so-called "demonstrator telescope" was constructed quickly using well-established analog sensors. This telescope was available already 18 month after the start of the project. Since these analog sensors have not matched the design requirements of the project, the telescope was upgraded with new sensors in late Summer 2009 in order to reach the final resolution and readout rate.

In this thesis, some of the required changes for the upgrade to the final telescope and the first analysis of data taken with the upgraded EUDET telescope are described and discussed. First, in chapter 12 the experimental setup is introduced and the analysed data samples are specified. In chapter 13 some of the adjustments to the data-acquisition software are described. After briefly describing the main parts of the

offline analysis-software in chapter 14, the results of the data analysis are presented in chapter 15 and finally summarised in chapter 16.

12. Experimental Setup

The EUDET telescope is designed to be used in a wide range of detector research and development studies. Therefore, the telescope has to provide a flexible and portable infrastructure in order to be able to investigate quite different devices-under-test (DUTs) with low-energetic electrons ($1 - 6$ GeV) at DESY as well as with high-energy (> 100 GeV) hadron beams at the SPS facility at CERN under varying beam conditions.

The telescope consists of two arms each equipped with three sensors kept at a stable temperature by a cooling system [201]. The positions of the sensors along the beam axis can be adapted to the respective requirements. Between the two arms an optional mechanical x-y-support stage that allows to position the DUT with a few micrometer precision is installed.

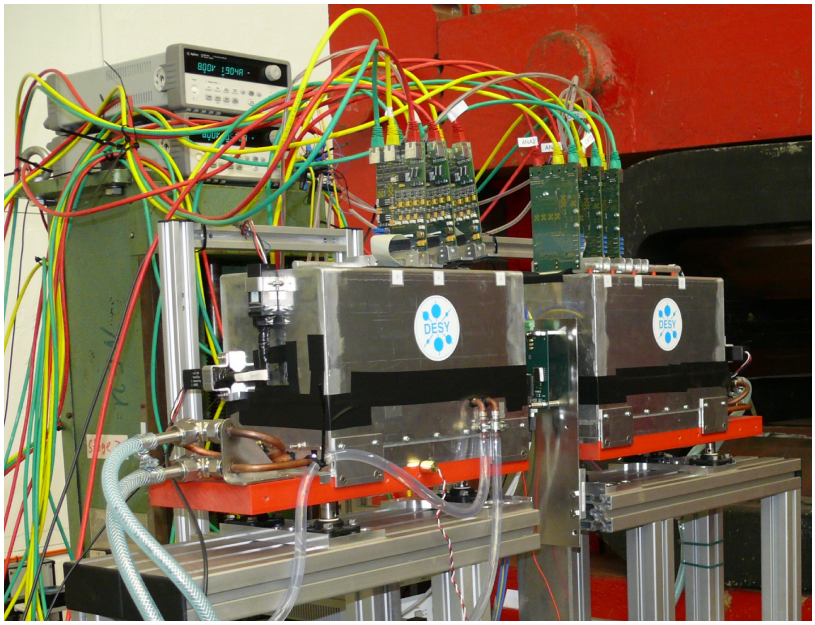

Figure 12.1: The telescope installed at DESY. A DUT [202] is installed in between the two boxes (figure taken from [203]).

A photograph of the EUDET telescope together with an installed DUT [202, 203] taken during a test-beam measurement at DESY is shown in figure 12.1. In this exemplary picture, the DUT is a high-voltage "Complementary Metal Oxide Semiconductor" (CMOS) monolithic detector placed in between the two telescope arms.

In figure 12.2 the hardware components of the telescope and their interconnections are illustrated. The sensors are read-out by dedicated data-reduction boards that transfer their data to a computer where the data-acquisition software is running. A trigger system including four scintillators connected to photomultiplier tubes allows to trigger on particles passing the telescope.

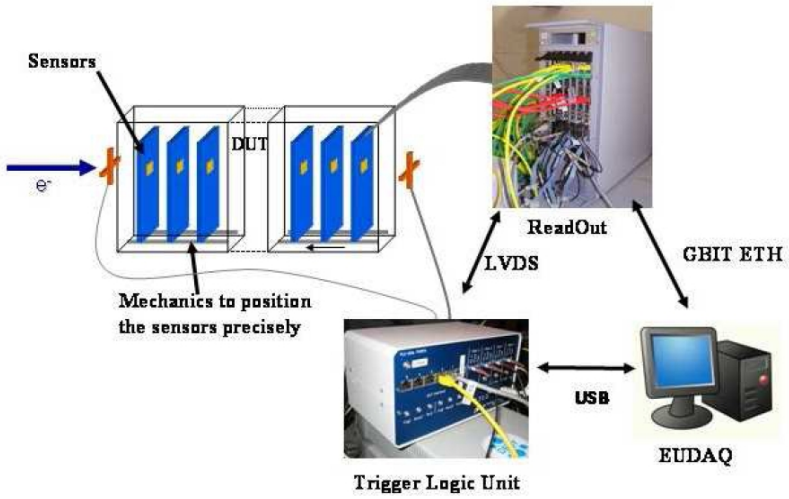

Figure 12.2: Schematic overview of the main telescope components (figure taken from [204]).

In this chapter, the main hardware components[1] of the telescope are described and finally the analysed data sample is specified.

12.1. Hardware

In this section, the sensors, the readout hardware and the trigger system are described.

12.1.1. The Sensors

The sensors for the telescope have to provide a single-point resolution of $2-3$ μm with a minimum of material in order to reach a reasonably good telescope resolution even at lower beam energies of $1-6$ GeV where the contribution from multiple scattering becomes large.

At the time when the telescope concept was developed, the "Monolithic Active Pixel Sensors" (MAPS) [198, 205] technology was the only available vertex-detector technology[2] for future collider experiments that could provide $\approx 2\text{cm}^2$ large sensors. In particular, the MIMOSA[3] detector series [199] successfully developed, fabricated and extensively studied at the CNRS-IPHC institute in Strasbourg, was utilsed for the telescope.

12.1.1.1. Monolithic Active Pixel Sensor

Monolithic CMOS detectors offer the possibility to integrate read-out circuits onto the sensors.

A cross section of a "Monolithic Active Pixel Sensor" is sketched in figure 12.3. The sensor is fabricated on a lightly-doped p-epitaxial layer grown on a highly-doped p^{++} substrate. The pixel readout circuit is embedded in a p-well on top of the epitaxial layer. The charge-collecting diode is formed by a junction between the n^+-doped implant

[1] The data-acquisition system is discussed in chapter 13.
[2] A general-purpose overview of various pixel-detector technologies can be found in [206].
[3] MIMOSA stands for "Minimum Ionizing MOS Active Pixel Sensor".

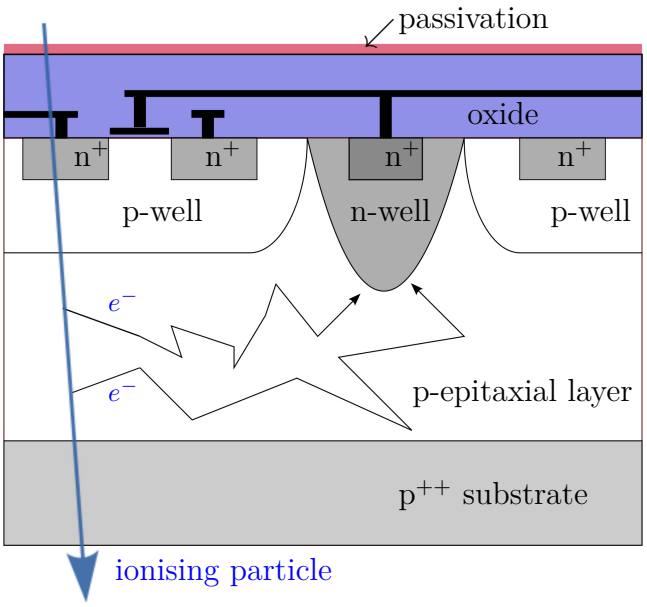

Figure 12.3: Schematic cross section of a "Monolithic Active Pixel Sensor" (MAPS).

and the p-epitaxial layer. Therefore, the sensor is only depleted directly underneath the charge-collecting n-well diode. Due to the large doping difference between the epitaxial layer and the p-well and the p^{++} substrate, respectively, potential barriers at the boundaries are created. A passing ionising particles creates electron-hole pairs in the sensor material and those electrons produced in the epitaxial layer diffuse towards the charge-collecting n-well diode, where the electronic signal is measured. In the p^{++} substrate, usually made of "low quality" silicon, the recombination time of charge carriers is short compared to the corresponding time in the lightly-doped epitaxial layer.

Since the sensitive volume is placed directly underneath the electronics and the generated charge is kept in this volume by potential barriers, a "fill factor", which is the fraction of the pixel area that is sensitive, of 100% can be achieved.

The MAPS detectors have several additional advantages compared to other technologies: CMOS pixel detectors are potentially very cheap because standard cost-effective processing technologies can be used. Since the readout circuit in each pixel is only active during readout and due to the fact that no additional external bias voltage is applied, the power consumption is typically relatively small. Despite the small signal, sufficient signal-to-noise ratios can be obtained due to the very low input capacitances. The granularity of the pixel matrix is fine providing a good spatial resolution of a few micrometer for tracking detectors. Since the epitaxial layer is very thin ($< 20\ \mu$m) and the substrate can be thinned, the amount of multiple scattering of passing particles in the detector material can be limited. Owing to the thin epitaxial layer the posititon resolution is also good for large incident angles.

The main disadvantages are the restriction to n-MOS transistors for the pixel circuit limiting the complexity of the integrated electronics and the sensitivity to radiation damage. Another disadvantage is in some environments the relatively large integration time compared to other technologies and the slower charge collection time.

12.1.1.2. Mimosa Sensors

The pixel sensors for the telescope have been fabricated using the AMS 0.35 OPTO process. On each pixel of the MAPS sensors utilised in the EUDET telescope a so-called self-biased on-pixel amplifier [207, 208] is implemented. This mechanism clears the pixel signal and compensates for leakage current. The clearing process is slow compared to the readout frequency. Thus, the generated signal charge remains for several readout cycles in the pixel. The application of "Correlated Double Sampling" (CDS) avoids double counting of the signal by determining the difference of two or three successive read-out pixel signals. Owing to this approach an explicit reset of the pixel matrix is not nessesary.

The MIMOSA sensors typically provide a signal-to-noise ratio for minimum ionising particles (MIPS) of $20 - 40$ and a detection efficiency for MIPS depending on the thresholds of $> 99\%$.

The "demonstrator telescope" was equipped with MIMOTEL prototypes [209] with a pixel pitch of 30 μm in both directions providing an active area of 7.7×7.7 mm^2 that consists of a 256×256 pixel array. In addition, a high-resolution plane (MIMOSA 18) with a pixel pitch of 10 μm can be used at the expense of a slower readout rate. This high-resolution sensor consists of 512×512 pixel providing a sensitive area of $5 \cdot 5$ mm^2. Simulation studies [210] and test-beam measurements [211] have demonstrated that the usage of one of these high-resolution planes in the telescope can significantly improve the intrinsic telescope resolution. The readout time of the MIMOTEL (MIMOSA 18) sensors is 800 μs (3 ms) which is in this architecture equal to the time over which signals are integrated.

However, an integrated data-reduction architecture (e.g. CDS, zero suppression) on the sensor is missing for the two sensors described above. Therefore, these sensors do not fulfil the readout performance requirements of the final telescope.

In order to cope faster with the accumulated data an on-sensor CDS, an integrated zero suppression, and the possibility to provide a fully binary output was implemented in the MIMOSA 26 sensors [212, 213]. These sensors were in particular developed for the operation in the final EUDET telescope.

The MIMOSA 26 sensor is a combination of the MIMOSA 22 sensor [214] and the SUZE01 chip [215] that performs online data sparsification. The sensor is subdivided into 1152 columns of 576 pixels with a pitch of 18.4 μm providing a high granularity. The sensitive area of the sensors is approximately 21×10.6 mm^2.

On each pixel an amplification and CDS circuit is implemented. The sensor is read-out in a column-parallel mode with a pixel-readout frequency of 80 MHz which results in a integration time of about 112 μs. Each column is equipped with a discriminator that performs an offset compensation and a second column double sampling. Furthermore, the data are pipelined and sparsified by zero-suppression stages. The data sparsification allows a faster data throughput and due to the small integration time the hit multiplicity is reduced. A data compression factor of 10 to 1000 can be achieved [216].

In this analysis, the analog pixel signals were available in the data from the MIMOTEL sensors, while the pixel signals for the MIMOSA 26 data were purely binary.

12.1.2. The Data Reduction Boards

The pixel sensors were read-out by custom-made "EUDET Data Reduction Boards" (EUDRBs) [217, 218]. The EUDRBs were adapted to the readout of several different versions of Mimosa sensors.

The operation of the EUDRBs is controlled by a "Field Programmable Gate Array" (FPGA). A mother/daughter-board approach was chosen in order to maximise the flexibility. The sensor specific components have been implemented on removable and interchangeable daughter cards, while on the motherboards the memory and computing elements were placed.

The EUDRBs perform CDS, pedestal subtraction and zero suppression with a configurable threshold. Owing to this approach the size of the transfered data can be reduced compared to a full-frame readout where all pixel signals are transferred without further data processing.

Each sensor is read-out by one EUDRB, while the data of the individual EUDRBs are transfered through a VME bus to a VME CPU (PowerPC MVME6100) and from there via Ethernet to the data-acquisition software (chapter 13 for more details). Detectors with JTAG programmable features can be configured with the EUDRBs as well. One EUDRB has to be configured as timing master and must be connected to the trigger system (chapter 12.1.3). This timing master distributes the trigger signal to the other EUDRBs.

Furthermore, the sensors can be read-out either asynchronously or synchronously. While the first readout was typically used for the demonstrator telescope equipped with either MimoTEL or Mimosa 18 sensors, the latter was used for the readout of the final telescope. The MimoTEL telescope was read-out asynchronously because a higher noise level was observed when running synchronously [219].

12.1.3. The Trigger Logic Unit

In order to provide a simple and easy to use trigger system, a dedicated "Trigger Logic Unit" (TLU) [220–224] was developed in the EUDET JRA1 project. The TLU was designed to be as flexible as possible whilst only few restrictions on the user of the TLU were introduced.

The dedicated trigger system is based on an USB programmable FPGA board and it provides coaxial connector interfaces that accept NIM, TTL or photo-multiplier level pulses for the generation of a beam-trigger. In addition to the beam-trigger, the TLU can be run in a self-triggered mode as well. The trigger signal is distributed via RJ45 and/or LEMO connectors to the connected DUTs.

Several handshake modes are available for the communication between the connected hardware and the TLU: 1) Without handshake the TLU is not interpreting busy signals from the DUTs; the trigger line is set for a fixed length of time. 2) In contrast, in the trigger-handshake mode the trigger line is set and the connected DUTs raise the busy signal until they are available for new trigger signals. 3) The trigger/data-handshake mode is similar to the trigger-handshake mode. In addition, the connected DUTs can read-out the trigger number while holding the busy signal. The latter is used for the connection of the EUDRBs to the trigger

system and it's the recommended method for the DUT integration.

12.2. The Data Samples

The data studied in this analysis were taken with the EUDET pixel telescope mounted at the H6 beam line at the SPS facility at CERN. The beam line was configured to provide 120 GeV hadrons. The beam size was approximately ≈ 3 cm (FWHM) and the beam intensity has been tuned such that about one particle per readout cycle was observed. Two slightly different experimental setups were used:

- **July 2009 Test Beam:** The goal of this test-beam measurement was the integration of the MIMOSA 26 sensors into the available telescope data-acquisition system and the analysis of the combined data. Therefore, three of these sensors were integrated as DUT layers into the telescope, whereas for the telescope MIMOTEL sensors were used. The integration was done such that the three MIMOSA 26 were read-out with three EUDRBs integrated in one VME crate. With this approach the performance of the sensors for the final telescope could be studied before the final upgrade of the whole telescope.

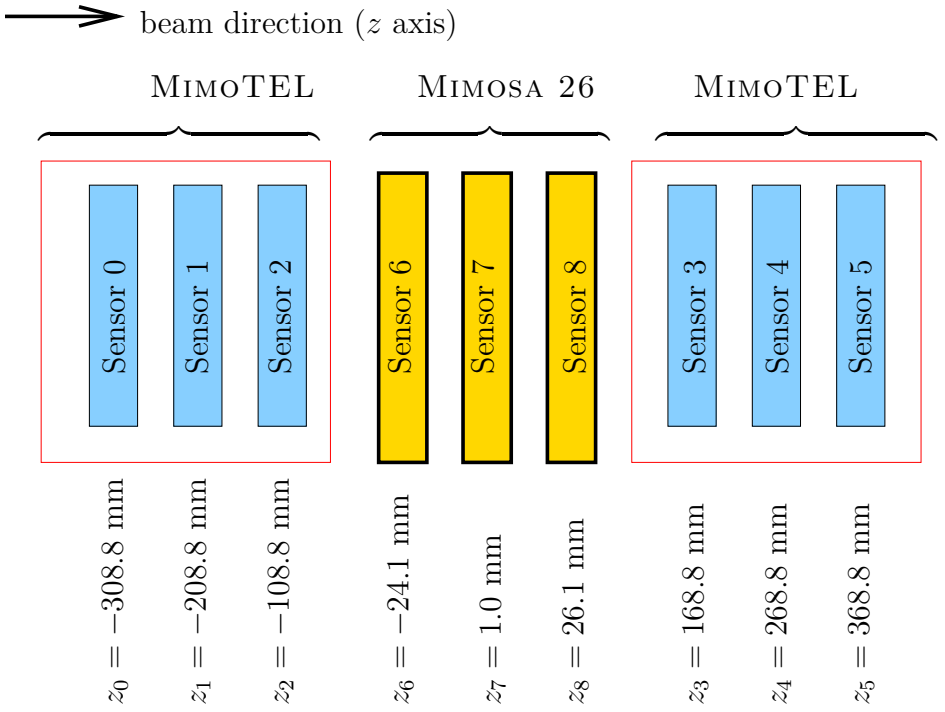

Figure 12.4: The experimental setup for the July 2009 test-beam measurement. Three MIMOSA 26 sensors were treated as DUTs.

Figure 12.4 illustrates the experimental setup of this test-beam measurement schematically. The MIMOSA 26 sensors were configured with a signal-to-noise threshold setting of $S/N > 12$ in order to reduce the fake rate coming from noise hits in the first data. The analysed data sample consisted of approximately 100000 events with an average track multiplicity of 1.

- **September 2009 Test Beam:** During September 2009, the six MIMOTEL telescope sensors were replaced by MIMOSA 26 sensors. These sensors were read-out with in total six EUDRBs, while always three of them were integrated in one VME crate in order to avoid VME-bus throughput limitations. One of the sensors (sensor 5) could not be used due to an electrical connection problem.

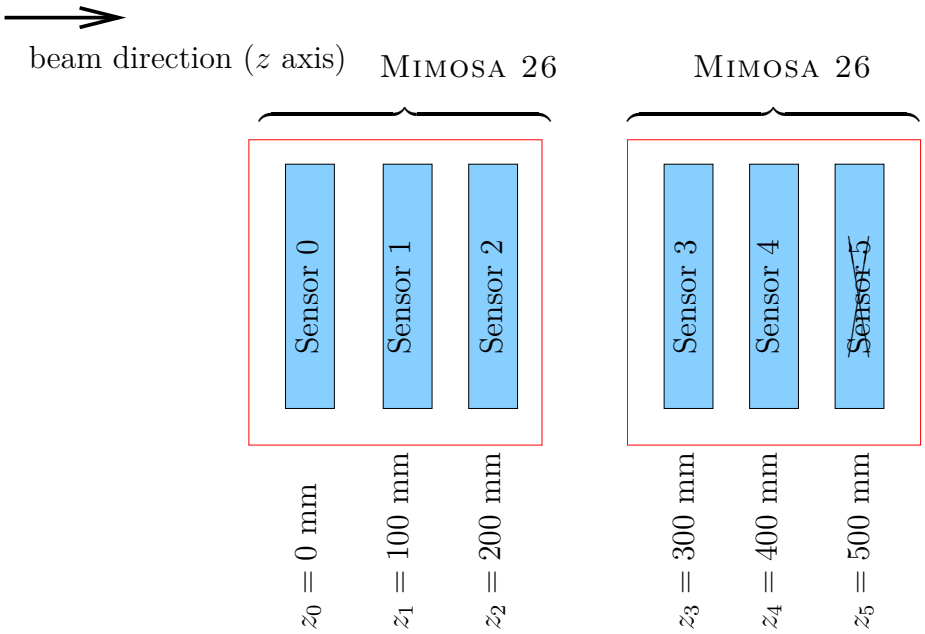

Figure 12.5: The experimental setup for the September 2009 test-beam measurement. Sensor 5 was not used.

During the data taking a data-taking peak rate of approximately 990 Hz was achieved. In contrast to the July data taking, the sensors were configured with a lower signal-to-noise threshold of $S/N > 10$ in order to improve the resolution and detection efficiency. The analysed data sample consisted of approximately 1.5 million events with about $1 - 2$ tracks per event.

Since the system was rather new, the higher threshold settings were used as mentioned above. Today, the telescope sensors are configured with thresholds of $S/N > 8$ or even $S/N > 6$.

13. The Data Acquisition Software

The EUDET pixel telescope has a flexible data-acquisition software (EUDAQ) [225–227] that was designed to be modular and portable. The software makes use of several individual independent programs (producer) that are connected with each other over the network as shown in figure 13.1. The hardware of the telescope and of the possibly connected DUTs is read-out by separate producer tasks that are connected to the "run control" and to the "data collector". The latter receives the data streams, builds the events and stores the data on the storage device. The "log collector" provides an interface for the producers for the collection of logging messages.

One part of the EUDAQ software is the online-monitoring system (RootMonitor) that makes use of the object-oriented data analysis framework ROOT [228] implemented in C++. The RootMonitor was successfully tested and used during past test-beam campaigns of the telescope at DESY and at CERN.

During the work for this thesis, the usability and performance of the RootMonitor was improved. Therefore, in this chapter an overview of some of the RootMonitor developments is given.

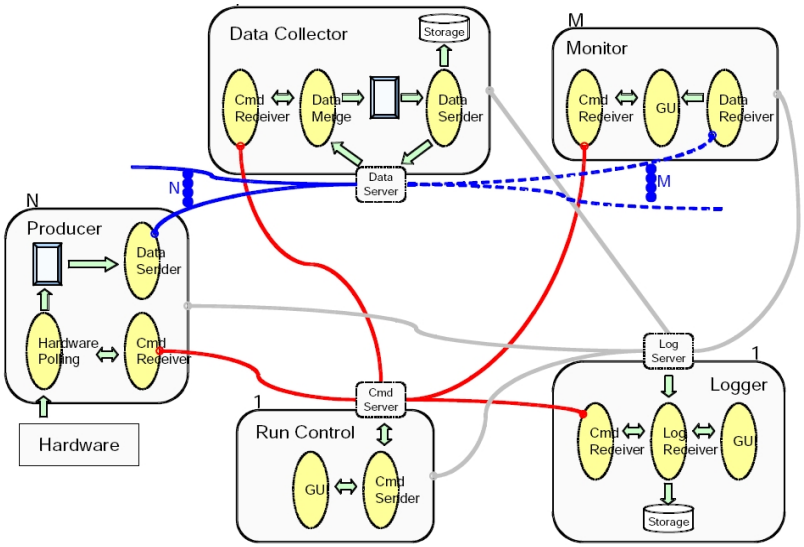

Figure 13.1: The schematic layout of the EUDAQ software. Several individual producer tasks are connected over the network (figure taken from [229]).

13.1. Event Reconstruction

Several reconstruction algorithms are used for the event reconstruction in order to monitor the data quality.

The RootMonitor can be used together with the EUDAQ system during data taking as well as a stand-alone application reading and analysing raw data files.

The RootMonitor is able to handle different sensor types for the various telescope planes. The sensor types must be specified in a dedicated configuration file.

The reconstruction algorithms account for different sensors types automatically. It is also possible to specify an additional file that contains for the DUT the pedestal and noise values.

In order to roughly estimate the noise of the MimoTEL or Mimosa 18 sensors, the root mean squares of the signal values are determined. This information is used in the cluster-reconstruction algorithm. The signal values are calculated with the application of a correlated double-sampling method (CDS) as provided by the EUDAQ library. In addition, every 50. events a combined CDS distribution for each sensor plane is determined and the noise for the corresponding sensor is extracted (section 13.2.1).

13.1.1. Cluster Reconstruction

The RootMonitor provides a simple fixed-frame cluster-reconstruction algorithm e.g. for MimoTEL sensors. Seed pixel candidates are identified and starting from the pixel with the highest signal-to-noise ratio clusters are constructed by joining neighbouring pixel to the cluster if certain thresholds are fulfilled. In this analysis, the possibility to adjust these thresholds in the graphical user interface was implemented. In addition, the algorithm was generalised in order to cope with different cluster sizes – 3×3 and 5×5.

In this analysis, for the Mimosa 26 sensors an additional cluster algorithm was implemented. This algorithm starts from one hit candidate and then assigns all 8 neighbouring hit pixels to the cluster. This procedure is repeated until all hit pixel are joined into clusters. In order to reduce the impact of noisy pixels, an algorithm that identifies these pixels stores the information for all hit pixels and if for 200 events the pixel fired in more than 15% of the events such pixels are marked as noisy. This threshold was roughly tuned by using the data from a sensors that had a known structure of bad pixels.

Moreover, two different methods for the cluster-position reconstruction are available in the RootMonitor. Either the position of the seed pixel is used or the centre-of-gravity for each cluster is determined. The latter is a signal-weighted average of the pixel positions belonging to the cluster.

13.2. The Graphical User Interface

In this section the graphical user interface (GUI) of the RootMonitor is described and some of the available histograms. These histograms are intended for the control of the data quality during data taking.

13.2.1. Available Histograms

Some of the important histograms are described in the following:

- **Time Dependence of Noise:** As previously described, the time dependence of the noise is monitored. This is in particular interesting for the monitoring of the telescope cooling. This information is only available if the telescope runs

in raw mode and if the telescope sensor planes are MimoTEL or Mimosa 18 sensors. Figure 13.2 shows the time dependence of the noise in ADC counts, which is in this case almost constant. The different sensor planes are indicated with different colours.

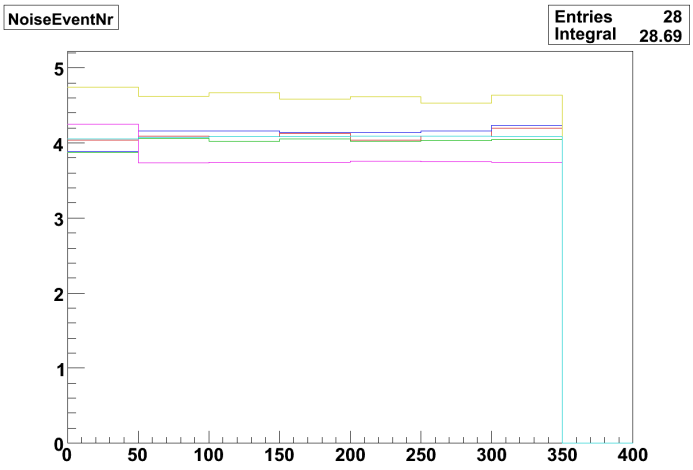

Figure 13.2: The noise for each sensor plane as a function of time (event number) in ADC counts.

- **Cluster Correlations:** During the assembly of the experimental setup it is typically difficult to position the telescope inside the beam. In order to allow an easier positioning correlation plots were implemented in the RootMonitor.

  Beam particles passing the telescope planes create clusters in the sensors. These clusters are spatially correlated between the individual planes. Therefore, for neighbouring sensors the reconstructed position in x and y direction for all possible pairs of cluster was filled into 2-dimensional histograms. Correlations can be identified as straight lines in these histograms.

  As an example, figure 13.3 depicts the x and y correlation plots for pairs of neighbouring planes as well as the correlation between the first and the last plane. Deviations from a diagonal line can be interpreted as telescope misalignment. In this example, the orientation of the sensors in the second arm differs from the orientation in the first arm. Thus, the slope of the line is not the same in all histograms. Additionally, the sensor 3 has a smaller pixel pitch.

  In the case of a DUT the RootMonitor is able to provide correlation plots that show the cluster position correlation between the DUT and the telescope. This can be seen in figure 13.4 where, as an example, correlations between the telescope planes and a DEPFET sensor [230] are depicted.

  Previously, the correlation of cluster positions in different sensor planes was described. These histograms are only helpful if the influence of multiple scattering is sufficiently small and if the multiplicity is low.

  In order to provide additional correlation histograms the correlation between the number of reconstructed hits in the sensor planes was implemented in the RootMonitor. Figure 13.5 illustrates the correlation that can be observed as a cloud following a diagonal line. In this example, the offset in some of the

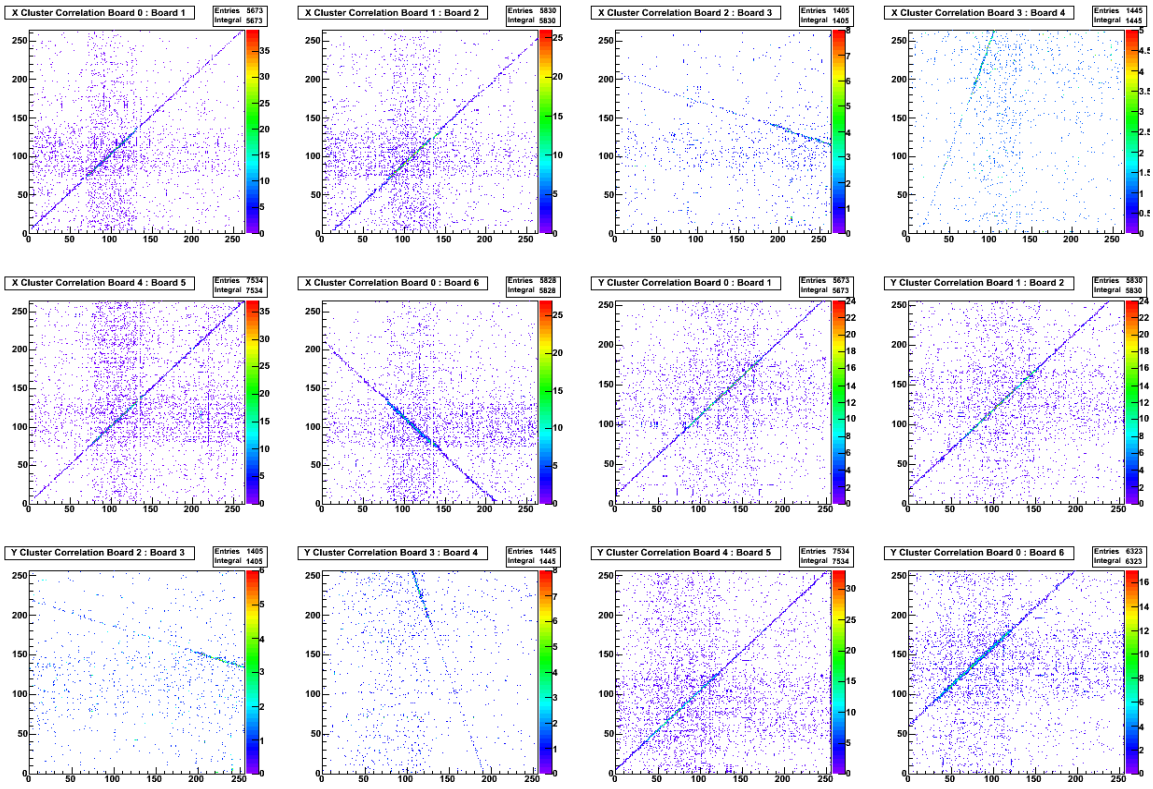

Figure 13.3: Cluster position correlation between pairs of sensor planes. In this example, sensor no. 3 has a smaller pixel pitch.

plots is caused by the different amount of sensor noise. The number of bins can be adjusted via the GUI in order to match to the data multiplicity.

- **CDS Lego:** The "CDS Lego" plots were implemented in order to observe particle hits on an event-by-event basis. Every N^{th} event the corresponding plots for all sensor plane are filled with the current signal values. The variable N can be adjusted in the GUI.

  Figure 13.6 shows as an example CDS values for two sensors for event number 40 where one hit can be seen.

13.2.2. Configuration Menu

Sometimes it is necessary to change reconstruction parameters online without modifying the source code of the RootMonitor. In order to ensure a better usability, the possibility to change online via the GUI parameters was implemented.

In figure 13.7 a screen shot of the configuration tab is depicted. In this menu several parameters can be adjusted. On the right-hand side a list of check boxes is provided. These check boxes can be used in order to enable or disable pads of histograms. The check boxes are grouped into three parts depending on where the corresponding histograms are shown. After pushing the "Apply" button the configuration is updated and all canvasses are divided dynamically depending on

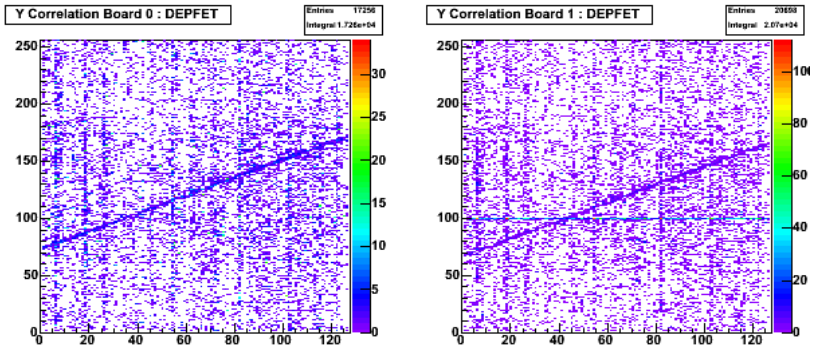

Figure 13.4: Examples for cluster position correlations between telescope sensors and a DEPFET sensor operating as DUT.

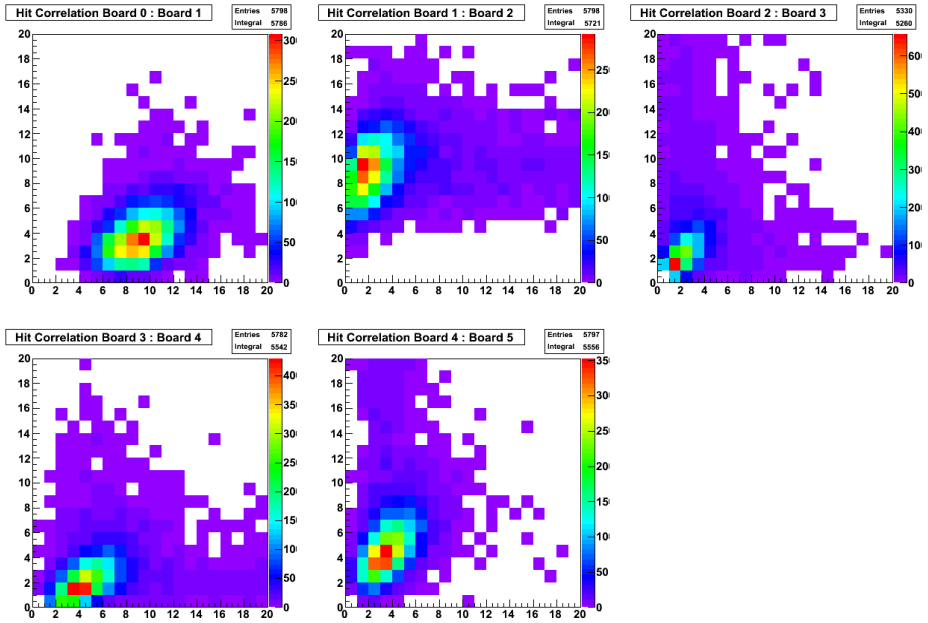

Figure 13.5: Correlation between the number of hits in neighbouring telescope planes.

the number of active pads. Histograms belonging to disabled pads are filled in the background. Thus, the information is not lost. If currently not needed pads are disabled, then the performance of the RootMonitor GUI increases. Furthermore, the number of enabled pads is counted, the canvasses are then suitably divided and the stacks of histograms are drawn using the corresponding drawing options. It is also possible to refresh the histogram view.

In the window header the current file name, the run and event numbers are depicted. It is possible to reduce the number of processed events and change the time interval after which the RootMonitor is forced to update the histogram drawings.

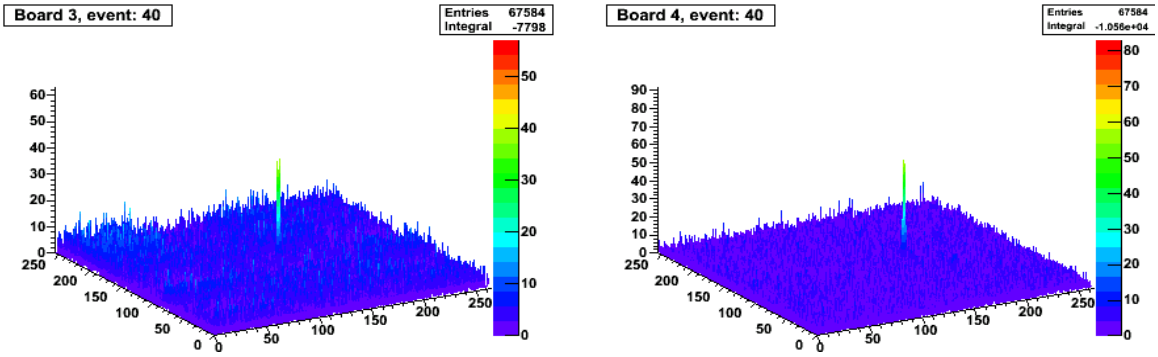

Figure 13.6: The CDS value for sensor plane number 3 and 4 and event number 40.

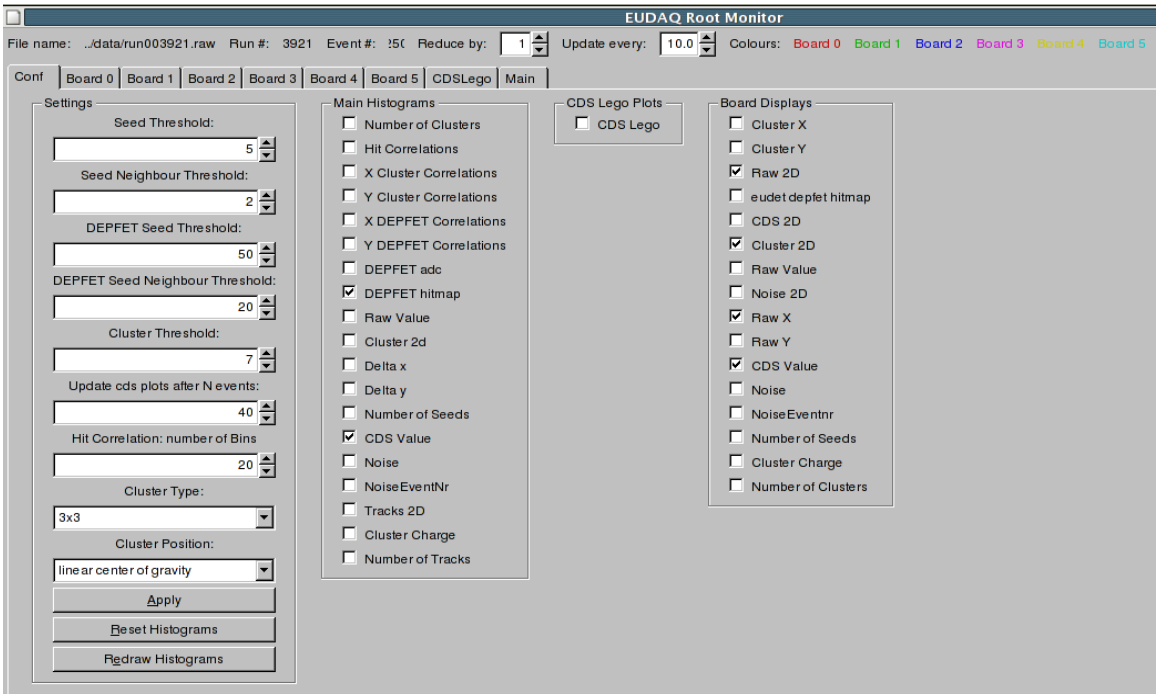

Figure 13.7: The configuration menu, where one can change online reconstruction parameters. It is also possible to enable or disable pads of histograms.

14. The Offline Analysis Software

The offline analysis software (EUTelescope) [231, 232] for the telescope data is based on Marlin [233–235] and LCIO [236, 237]. Even though EUTelescope was primarily developed for the analysis of the telescope data, it can also be adopted to the analysis of other data sets.

The EUTelescope software makes use of the Marlin analysis framework which divides the analysis in several individual small tasks – called "processors". The behaviour of these processors can be controlled with XML steering files. The data are stored in the LCIO format which was developed to provide a persistency data model and interface. The data are grouped into so-called "collections". Typically a Marlin processor takes as input several data or database collections, analyses the input collections, creates several histograms and produces potentially an output collection that can be either stored on the disk or used as an input for other processors. It is possible to perform each analysis step separately as well as the full chain at once.

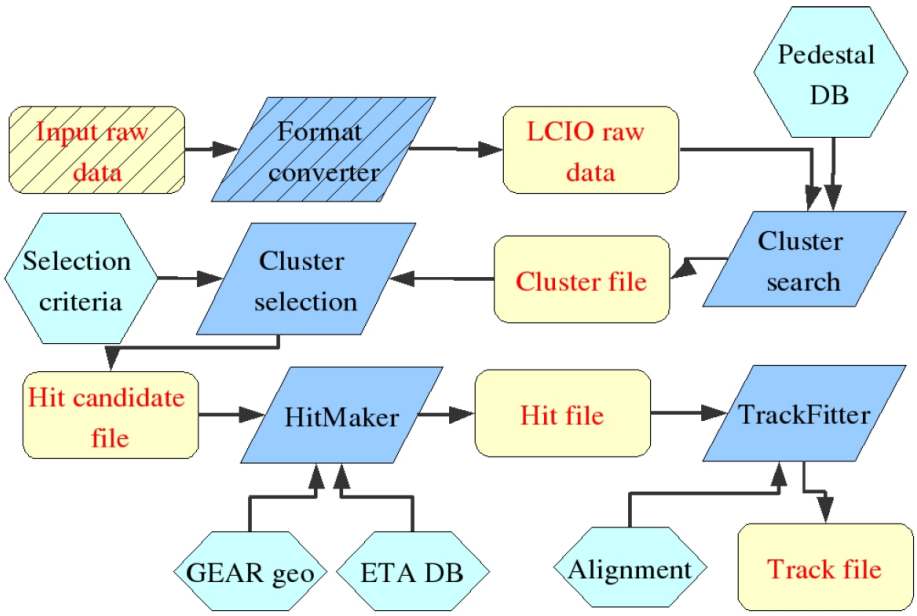

Figure 14.1: The schematic layout of the EUTelescope software (figure taken from [231]).

Figure 13.1 shows the schematic layout of the EUTelescope analysis chain. The first step of the data analysis is the conversion of the raw data files into the LCIO format. In general, this conversion is performed by making use of the corresponding functionality provided by the EUDAQ software[1], but it can be extended to convert

[1] A detailed description how the conversion has to be done in the EUDAQ library can be found in [227].

any other data set. After the conversion, depending on the data type and the requirements, pedestal and noise information are determined and hit pixels are grouped into clusters by applying loose selection and quality cuts. This collection of cluster candidates can be used in conjunction with an additional processor that applies some filtering criteria to obtain a collection of filtered clusters. Afterwards, the cluster coordinates are transformed from the local reference frame to the global telescope reference frame using the geometry description provided by the GEAR [238] package. After determining the alignment constants of the individual planes, the fitter reconstructs tracks using this collection of corrected hits. These tracks can be used for an extrapolation to the DUT surface in order to determine the predicted positions of hits in the DUT plane.

During the work for this thesis, the new MIMOSA 26 sensors were fully integrated into EUTELESCOPE. In order to implement these sensors in the software, several processors and algorithms had to be adapted to the different data format. In the following, some of the major changes needed for the analysis of data taken with these new sensors are briefly discussed.

14.1. Clustering

One of the first steps in the data analysis is the search for cluster candidates. The EUTELESCOPE software provides several different algorithms like the "fixed frame clustering" that merges all neighbouring hit pixel that fulfil certain criteria to a cluster candidate. The size of these cluster can be specified in the steering file. Contrary to this algorithm the "sparse clustering" is not based on a fixed size and shape of the cluster. It utilises the distance between the pixel and the seed pixel[2] for the clustering. Therefore, these cluster mostly do not have a regular shape or size.

All the provided clustering algorithms use data collections that provide for each pixel the signal in ADC counts and the noise information. Since the new MIMOSA 26 sensors only provide binary information and no noise information, a new algorithm had to be developed – the "digital fixed frame algorithm".

In the EUTELESCOPE software package each cluster type is implemented as an individual C++ class. Since all cluster types have to provide the same functionality in order to be usable in the analysis framework, a generic abstract base class (EUTELVIRTUALCLUSTER) with several general virtual methods is implemented in the software. The classes for different cluster types inherit from this abstract class and all the virtual member methods are overridden with the necessary implementations.

The required changes needed for the MIMOSA 26 sensors were implemented by introducing an additional cluster type – called "EUTELDFFCLUSTER". This new cluster type provides all necessary member functions – for instance methods like the centre-of-gravity shift – in order to be fully operational in the analysis framework. The corresponding "digital fixed frame algorithm" creating these digital clusters is briefly described in the following:

- For all hit pixels the number of neighbouring hit pixels, N, is determined,

[2]The seed pixel is defined as the pixel with the highest signal-to-noise ratio of the cluster.

whereas diagonal neighbours are ignored.

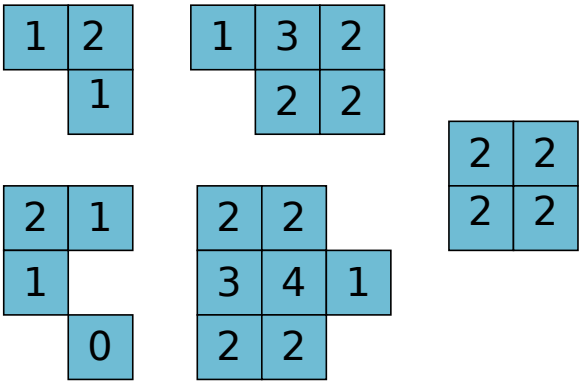

Figure 14.2: The "digital fixed frame algorithm": As examples five different cluster are shown. The indicated numbers represent the number of neighbouring pixel (ignoring diagonal neighbours).

Figure 14.2 illustrates as examples five cluster. The indicated numbers indicate the number of neighbours. The pixel with the largest N in a group of pixel is more likely to be the seed pixel than those pixel with smaller N. In case of symmetric clusters with more seed candidates the pixel that is read-out first is taken as seed.

- The list of hit pixel obtained in the previous step is sorted with decreasing N in order to determine the seed candidates. For pairs of pixel with equal N, the pixel with the larger number of diagonal neighbours is preferred.

- The resulting list is processed starting from the seed candidate with the greatest N.

- All hit pixel in a fixed $x \times y$ frame around the seed pixel are merged into the cluster and removed from the pixel collection and from the list of seed candidates. The size of the cluster can be specified in the corresponding steering file.

- Additionally, it is possible to reject all cluster that do not exceed a certain amount of hit pixel. By default this cut is disabled and was not used at all in the analysis presented here.

The described algorithm was fully integrated into EUTelescope and it can be used not only for Mimosa 26 data but also for other data.

14.2. Alignment

In order to be able to reconstruct tracks with the telescope and to extrapolate these tracks to the DUT plane, the geometrical positions of the sensor planes have to be known with a precision which is significantly better than the resolution. The EUTelescope software packages provides a processor (EuTelMille) that uses Millepede [239, 240] for the determination of the alignment constants in order to reduce the bias and the uncertainty of the fitted track parameters and to minimize the χ^2 of the tracks.

Each parametrisation of a track depends on local parameters that vary between the tracks and on global parameters – the alignment constants. The processor EuTelMille takes as an input a collection of hits and then for all combination of hits straight lines are fitted to these groups of hits independently in x and y direction. In order to suppress fake tracks resulting from combinatoric background, cuts on the residual distributions for all sensor planes can be specified in the corresponding steering file. The derivatives of the tracks with respect to all local and global parameters are stored in a binary file that can be read by Millepede. The Millepede software determines in a simultaneous linear-least-squares fit of all local and global track parameters the alignment constants for the sensor planes. Determined are shifts in x and y direction and rotations around the z direction. Usually the alignment constants of the first and the last plane are fixed in this determination in order to define the coordinate system and to obtain a stable fit result.

Since the number of planes that could be aligned with this software package was fixed to six and only planes belonging to the telescope were considered in this processor, some improvements of the EuTelMille processor had to be implemented:

- The EuTelMille processor was adjusted such that it can handle an arbitrary number of planes. All related cuts and steering parameters were adjusted accordingly.

- The possibility was implemented to use hits stored in several individual collections. The EuTelMille processor merges all hits from the individual collections together and performs the alignment for all planes simultaneously. This implementation together with the previously described modification enables EuTelMille also for the alignment of the DUT.

- Additionally, the possibility to use a combination of a hit and a track collection for the alignment of the DUT was implemented. The track collection can be created for instance with the analytical track fitter (see section 15.1.4 for more details) after aligning the telescope planes. These tracks can be exploited in the alignment processor in order to determine the alignment constants of the DUT. In this case, the alignment constants of the telescope typically have to be fixed in the fitting procedure.

After the implementation of these modifications the alignment package was suited for the data analysed for this thesis, where up-to nine sensor planes were used.

During the analysis of the Mimosa 26 data a distinct residual structure, as shown in figure 14.3a, was observed when using the alignment processor. In order to investigate this structure, a very simple "toy" Monte Carlo study was performed. In this Monte Carlo approach five sensor planes were arbitrarily misaligned – ignoring rotations. Afterwards, particles were generated with a small beam spread and hits were created in the five telescope planes. The influence of multiple scattering was neglected. Since the Mimosa 26 sensors provide binary data, the hit information was digitized using a pixel pitch of 18.4 μm. A detection efficiency of 95% per plane was assumed. Straight-line tracks were fitted to all combinations of hits and filled into residual histograms. The result of this study is depicted in figure 14.3b. It can be noted

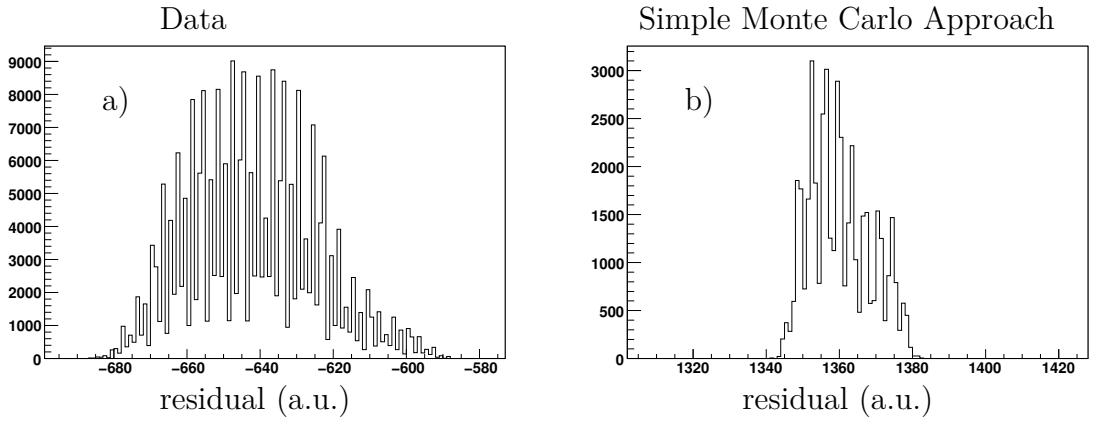

Figure 14.3: Residual between the measured hit position and the predicted hit position in the central sensor plane for a) data and b) a simple Monte Carlo model.

that the general structure of the observed data residuals can be reproduced, whereas the details differ between the data and the Monte Carlo approach. Presumably, this disagreement is caused by an oversimplified Monte Carlo model. The spiky structure of the residuals is more pronounced for smaller beam spreads and for sensors in the central part of the telescope. This behaviour was also observed in the data.

15. Results

In this chapter, the analysis results for the data (chapter 12.2 for more details) taken in July and September 2009 at the SPS facility at CERN is presented and discussed. Both data samples were taken with a beam of 120 GeV hadrons.

15.1. July 2009 Test Beam

During the July 2009 test beam three MIMOSA 26 sensors were operated as DUTs in the telescope. A signal-to-noise threshold of $S/N > 12$ was applied to the MIMOSA 26 sensors. The telescope consisted of six MIMOTEL sensors.

15.1.1. Pedestal and Noise

During the data taking several dedicated small data samples for the determination of the pedestal and noise values of the MIMOTEL sensors were taken. For these data samples the EUDRBs were configured to provide the information for the full sensor matrices without applying any online zero suppression. The particle beam was turned off and the sensors were read-out with a fixed frequency. The pedestal value for every pixel separately was determined with the corresponding EUTELESCOPE processor by calculating the average signal in every pixel – rejecting the largest upward and downward fluctuations. The noise was defined as the root mean square (RMS) of the pedestal fluctuation.

Figure 15.1 shows two-dimensional histograms of the noise and pedestal values for sensor 3 as well as the distribution of these quantities. Except for the last sub-matrix of the sensor, the noise was determined to be around 3 ADCs, whereas the pedestal was found to be very close to zero. The reason is that the pixels are self-biased (section 12.1.1.2). The higher noise values in the last sub-matrix were caused by the read-out system and not by the sensors itself.

After the determination of the pedestal and noise values and after marking dead and noisy pixels this information was loaded into the EUDRBs. Afterwards, the EUDRBs applied a zero-suppression algorithm online during the data taking. Only the signals of those pixel were not suppressed that have exceed a signal-to-noise ratio of 2. Additionally, the signals of pixels inside a 5×5 area around these pixel were included in the data stream from the EUDRBs.

In the offline analysis, the pedestal values were subtracted from the signal and the signals were corrected for common-mode shifts.

15.1.2. Cluster Reconstruction

As described in the previous chapter 14.1, clusters were reconstructed in the reference-telescope sensors (the analog sensors) with the application of the "fixed frame clustering"

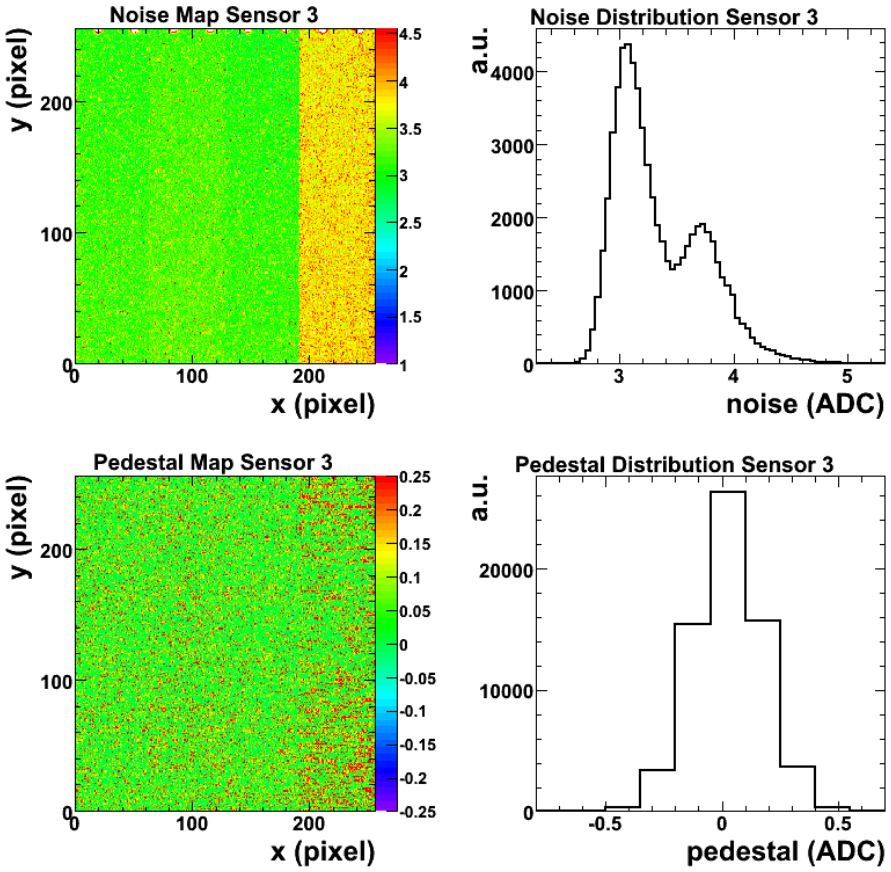

Figure 15.1: As an example the noise and pedestal values for sensor 3.

algorithm. For each sensor, cuts on the seed and cluster signal-to-noise ratios were applied in order to suppress noise. These cut values were adapted for each sensor separately as indicated in figure 15.2, where the seed signal-to-noise distribution before the application of cuts is depicted for sensor 2. The vertical lines illustrate the applied cuts. The peak on the left-hand side of the distribution below the indicated cut is the contribution from noise, whereas the peak on the right-hand side is related to the signals of particles.

For the reference telescope, cluster-signal distributions for parts of the data are presented in figure 15.3 after applying signal-to-noise cuts. Shown are also the fit results of Landau distributions[1] to the data. The data show reasonable cluster-signal spectra even though the fit does not agree perfectly with the data. It should be noted that during the data taking, an increasing detector noise was observed possibly caused by a non-constant temperature of the cooling water.

In contrast to the reference sensors, the "digital fixed frame algorithm" was used for the Mimosa 26 (the DUT) data.

[1]Landau distributions describe the fluctuations in the energy loss of charged particles in thin layers of material.

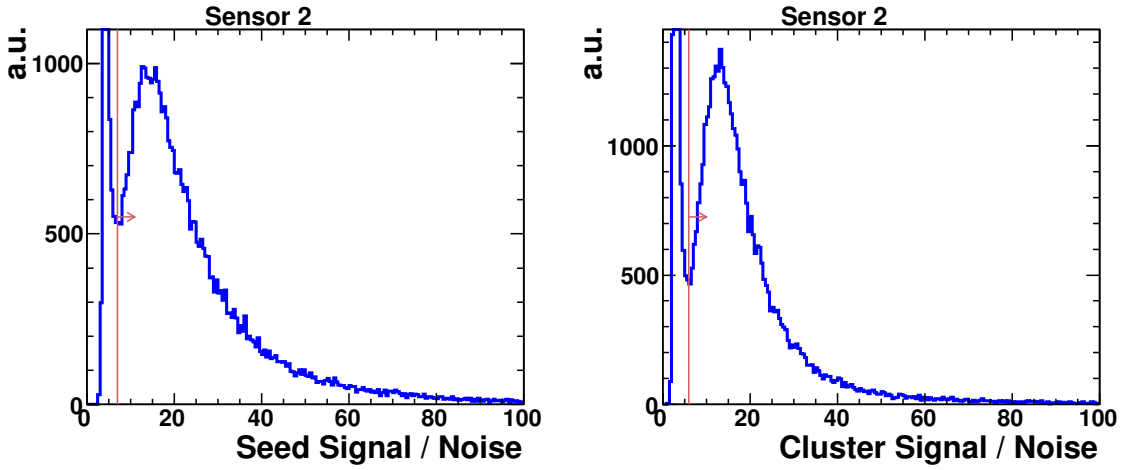

Figure 15.2: The seed and cluster signal-to-noise ratios. The vertical line indicates the applied cut values.

15.1.3. The η-Algorithm

The η-algorithm is a widely used standard method for the correction of non-linear charge-collection effects. The algorithm utilises the centre-of-gravity (CoG) shift within the seed pixel of clusters. These shifts should be uniformly distributed over the whole seed-pixel area, because the particle impact position inside the seed pixel is uniformly distributed.

The η correction discussed here was only applied to the data of the reference telescope and not to the binary Mimosa 26 data, because with the applied threshold settings these data mainly consisted of single-pixel cluster. Therefore, a more detailed investigation of this correction with the new sensors was not possible.

Figure 15.4a shows for a small subset of the data the CoG shift separately in x and y direction. The η-algorithm integrates these distributions and the obtained function is normalised to the highest value and shifted by -0.5 as depicted in figure 15.4b, where η is shown as a function of the CoG shift. The discrete step at CoG equal to 0 is caused by the occurrence of single-pixel cluster. Figure 15.4c (15.4d) presents the correlation between the CoG shift in x and y direction before (after) the application of the η correction. The corrected distributions are much more uniform than the uncorrected ones.

In figure 15.5 the distribution of reconstructed hits on one of the Mimosa 26 sensors is illustrated. The rectangular area with a higher density of hits is related to the trigger window (the geometrical overlap of the four used scintillators).

15.1.4. Alignment and Track Reconstruction

After transforming the cluster coordinates from the local reference frame to the global reference frame of the telescope, the alignment constants of the telescope planes and the three Mimosa 26 sensors were determined with an approach that consisted of two iterations:

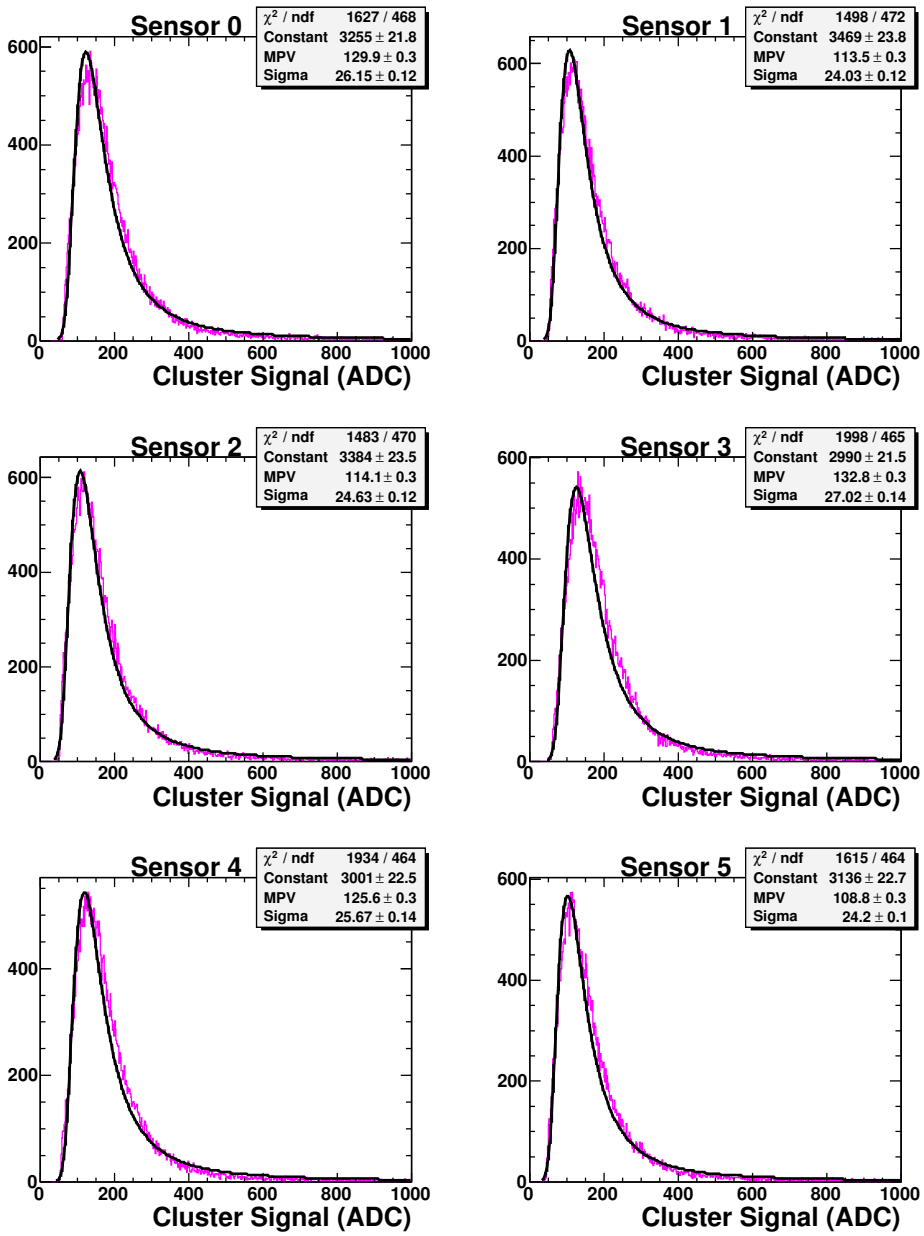

Figure 15.3: The cluster signal after applying cuts on the seed and cluster signal-to-noise ratios.

1. Only the telescope planes were aligned – the three DUT sensors were excluded from the alignment.

2. The alignment corrections were applied to the telescope planes and these planes were fixed in the fit. Afterwards, the three DUT sensors were included in the alignment procedure and their constants were extracted.

The procedure described above was repeated once in order to improve the alignment, because small rotational misalignments were observed.

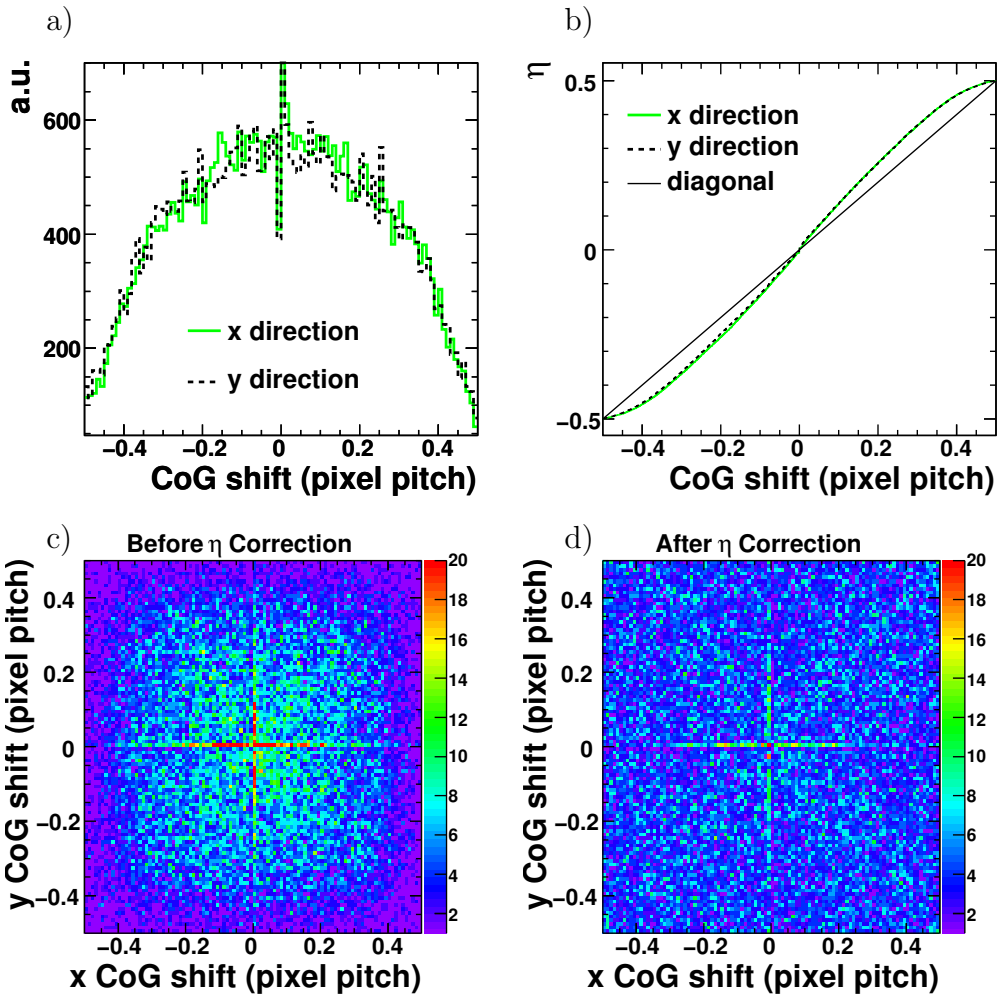

Figure 15.4: a) The centre-of-gravity (CoG) shift distribution in x and y direction. b) The η-function in x and y direction. c) Correlation between the CoG shift in x and y direction before applying the η correction. d) CoG shift correlation after applying the η correction.

Owing to the used approach the alignment of the telescope was performed independently from the DUT alignment. For the telescope planes typical sizes of the alignment corrections were < 0.5 mm for shifts in x and y direction and a few millirad for the rotation around the z axis. Since the positioning of the DUT in the telescope acceptance region is typically more difficult, the alignment constants for the DUTs were found to be significantly larger – about 4 mm (1 mm) for shifts in x (y) direction.

The algorithm for the track reconstruction utilised in this analysis makes use of an analytical track-finding approach [210] as provided by the EUTelescope software. This algorithm takes into account the multiple scattering of particles in the detector material in the definition of the corresponding χ^2 function. The algorithm assumes that the scattering angles of the particles are small, that the sensor planes are parallel to each other, that the beam has only a small angular spread, that the beam is perpendicular to the telescope planes, that the energy loss of particles in the sensor

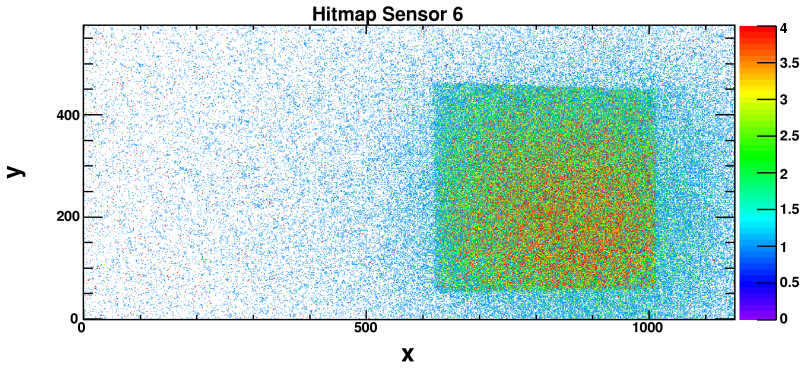

Figure 15.5: The distribution of reconstructed hits on one of the MIMOSA 26 sensors.

material can be neglected and that the thickness of the material in which the particles can scatter is small compared to the distance of the individual planes.

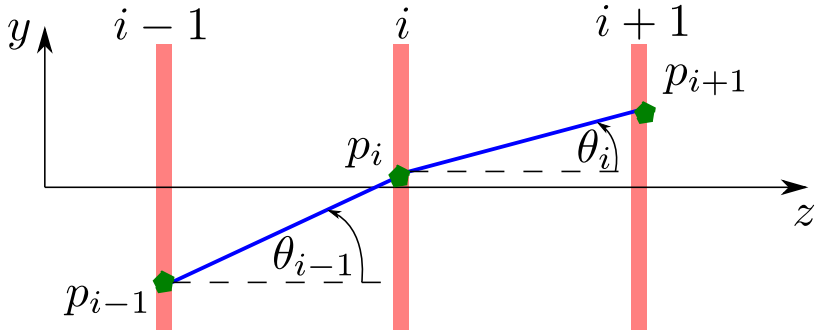

Figure 15.6: The definition of the variables θ_i and θ_{i-1} used in the track reconstruction algorithm.

The tracks are then reconstructed by minimising a χ^2 function according to

$$\Delta\chi_i^2 = \left(\frac{y_i - p_i}{\sigma_i}\right)^2 + \left(\frac{\theta_i - \theta_{i-1}}{\Delta\theta_i}\right)^2, \tag{15.1}$$

where $\Delta\chi_i^2$ is the contribution arising from plane i, y_i the measured particle position and p_i the predicted position. The angles θ_i and θ_{i-1} correspond to the angle between the nominal beam direction (the z axis) and the track direction as shown in figure 15.6. In the first and the last plane the term due to multiple scattering is omitted. The quantity $\Delta\theta_i$ is the expected width of the distribution of the scattering angle. This variable can be determined for small scattering angles [241] according to

$$\Delta\theta = \frac{13.6\ \text{MeV}}{\beta cp} \cdot z\sqrt{\frac{dx}{X_0}}\left[1 + 0.038 \cdot \ln\left(\frac{dx}{X_0}\right)\right], \tag{15.2}$$

where βc is the velocity, p the momentum, z the charge of the beam particle, X_0 the radiation length of the material and dx the thickness of the material. The analytical fitter extracts the necessary information like the radiation length from the corresponding GEAR file. The quantity X_0 was set in this analysis to 9.36 cm, which is the radiation length of silicon. For inactive material only the last term in equation 15.1 contributes to the total χ^2. The track parameters are determined analytically.

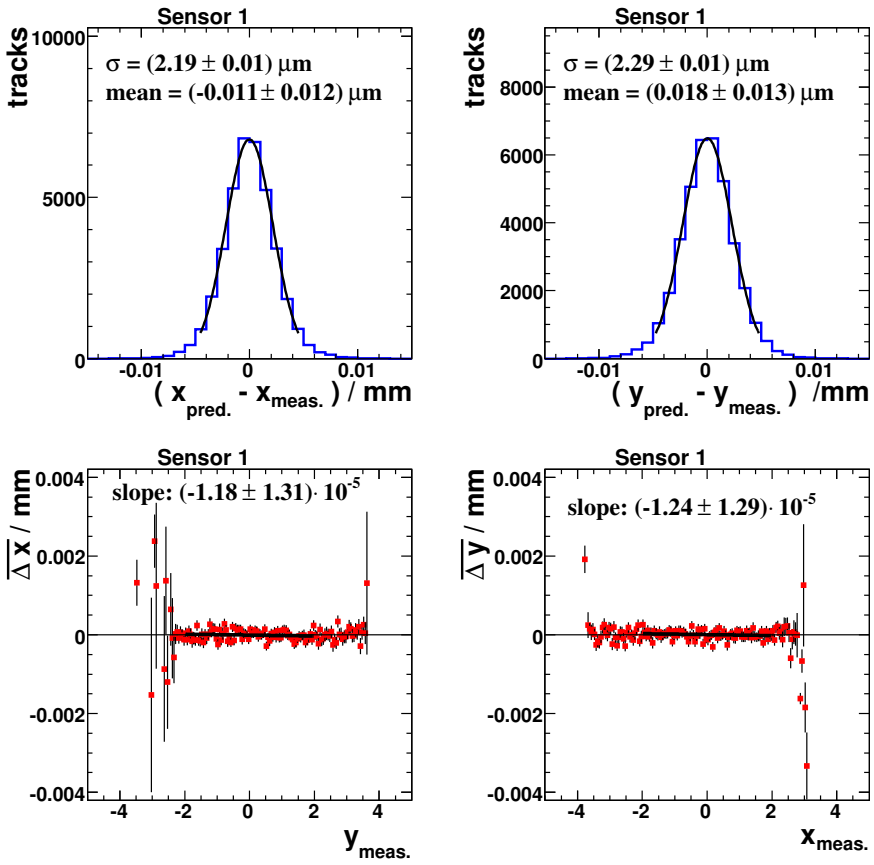

Figure 15.7: Investigation of the telescope alignment for telescope sensor 1. Shown are residual plots in x and y direction and $\overline{\Delta x}$ ($\overline{\Delta y}$) as a function of $y_{\text{meas.}}$ ($x_{\text{meas.}}$).

In order to investigate the alignment of the telescope sensors, a track reconstruction was performed with the requirement that only those tracks were considered with one reconstructed hit in each plane. The three MIMOSA 26 sensors were treated as passive layers and not included in the fit. Afterwards, (biased) residual distributions between the coordinates of the measured hit and the predicted position for the telescope planes were determined as shown in figure 15.7 for sensor 1. Similar figures for the other telescope sensors are shown in appendix A.5. These residuals are shifted in general by less than 0.1 μm with respect to the origin. In addition, in these figures the average residual $\overline{\Delta x}$ ($\overline{\Delta y}$) as a function of y (x) is depicted. The slope of these distributions can be exploited in order to roughly estimate the misalignment related to rotations around the z axis. Therefore, straight lines were fitted to these distributions. Since the values for the slopes as extracted from the fit and the determined fit uncertainties have a comparable size, the result of the alignment procedure was reasonable.

Figures 15.8, 15.10 and 15.10 show the residual distributions and the quantity $\overline{\Delta x}$ ($\overline{\Delta y}$) as a function of y (x) for the three DUT planes. These planes were *not* included in the fit. Therefore, hits in the DUT planes were assigned to the track if the distance between the hit and the predicted hit position was smaller than 100 μm. The residual distributions were first fitted with Gaussian functions without restricting the fit range.

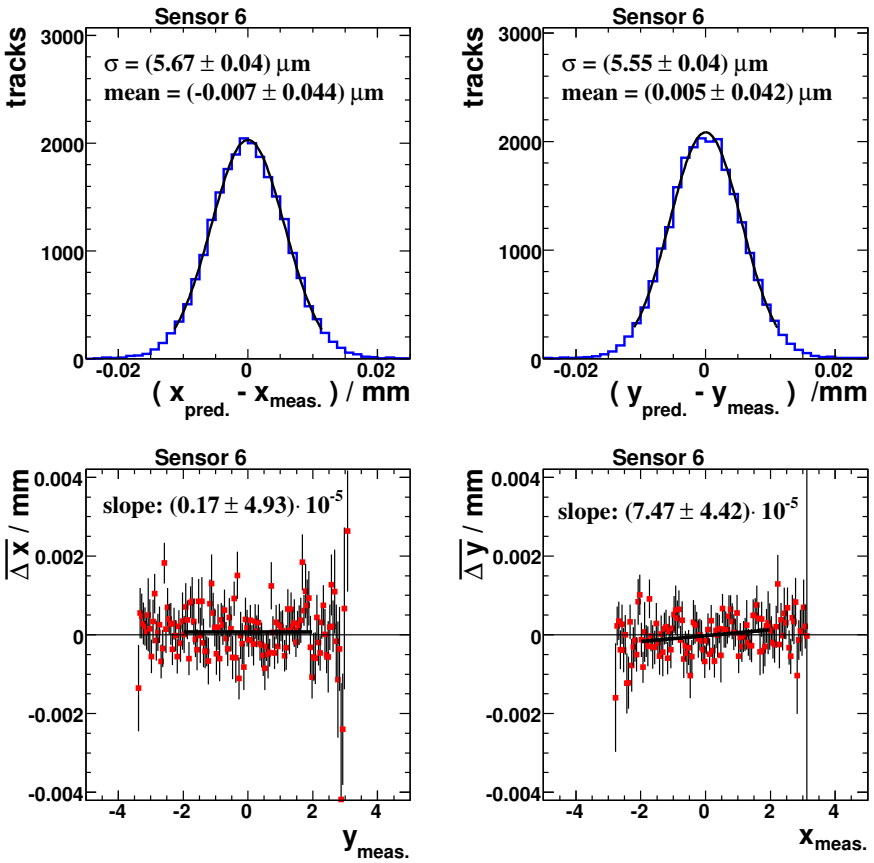

Figure 15.8: The observed residuals and the quantity $\overline{\Delta x}$ ($\overline{\Delta y}$) as a function of y (x) for the MIMOSA 26 sensor 6. The sensors was not included in the track fit.

Afterwards, the fit was repeated and restricted to the range $[-2\sigma, 2\sigma]$. The obtained values for the resolutions are depicted in the figures as well. The positions of the maxima are shifted by typically less than 0.03 μm with respect to the origin. The alignment procedure has also sufficiently accounted for rotational misalignments of the three DUT planes within the uncertainties.

The observed (measured) resolutions in the DUT planes consisted of convolutions of the reference-telescope resolution, the single-point resolution of the MIMOSA 26 sensor and the contribution from multiple scattering, which was in the analysed data samples negligible. Therefore, the MIMOSA 26 single-point resolution, σ_{M26}, can be expressed according to

$$\sigma^2_{\mathrm{M26}} = \sigma^2_{\mathrm{meas.}} - \sigma^2_{\mathrm{tel.}} - \cancel{\sigma^2_{\mathrm{MS}}}, \tag{15.3}$$

where $\sigma_{\mathrm{meas.}}$ represents the measured resolution, σ_{MS} the contribution from multiple scattering and $\sigma_{\mathrm{tel.}}$ the intrinsic telescope resolution. The latter can be determined from the single-point resolution of the telescope sensors:

$$\sigma^2_{\mathrm{tel}} = k \cdot \sigma^2_{\mathrm{MimoTEL}} \tag{15.4}$$

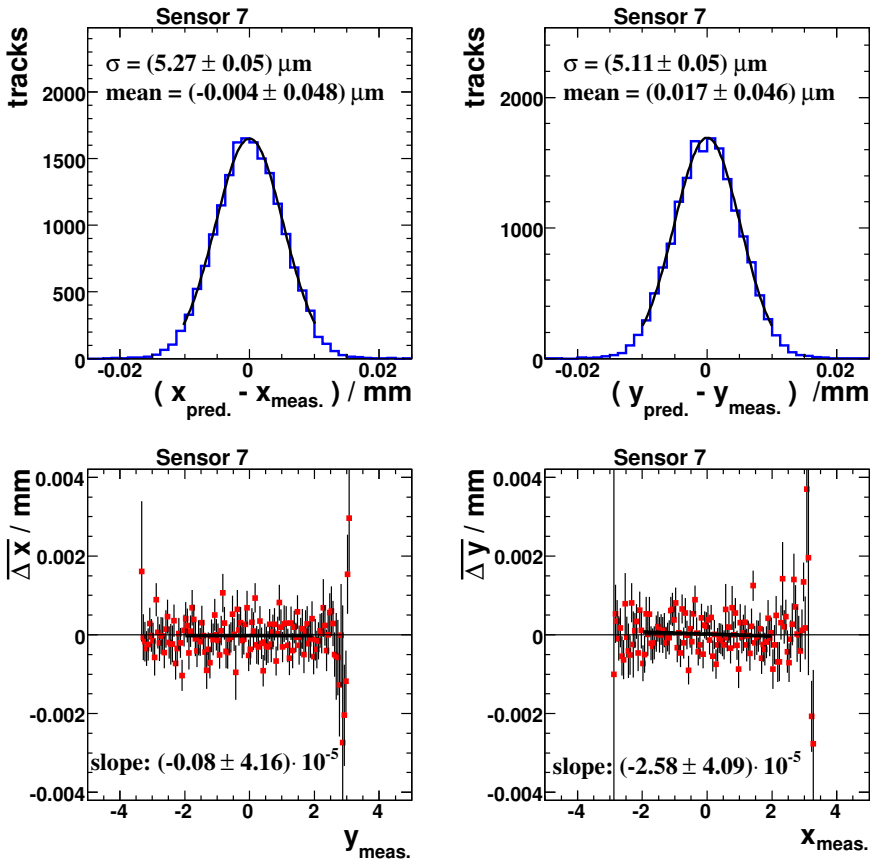

Figure 15.9: The observed residuals and the quantity $\overline{\Delta x}$ ($\overline{\Delta y}$) as a function of y (x) for the MIMOSA 26 sensor 6. The sensors was not included in the track fit.

The variable k is a geometrical scaling factor [210, 211] that can be calculated according to

$$k = \frac{\sum_i^N z_i^2}{N \sum_i^N z_i^2 - \left(\sum_i^N z_i\right)^2}, \tag{15.5}$$

where the variable z_i is the z position of plane i under the assumption that the DUT is placed at the origin of the coordinate system, $z = 0$. In this determination the contributions from multiple scattering were neglected due to the high-energetic (120 GeV) beam particles and due to the small sensor thickness (< 700 μm).

With a single-point resolution of the telescope planes of $\sigma_{\text{MimoTEL}} \approx 3.5$ μm the observed resolution can be used for an extraction of the MIMOSA 26 single-point resolution as depicted in table 15.1.4. Statistical uncertainties are not given because the spread between the sensors and between the x and y direction indicates that the measurement was dominated by not-understood systematic uncertainties.

Owing to the used threshold settings most of the clusters were single-pixel cluster as shown in figure 15.11, where for clusters assigned to tracks the pixel multiplicity is depicted. The amount of single-pixel cluster has ranged from about 55% to 75%. Even though all three MIMOSA 26 sensors were configured with the same threshold

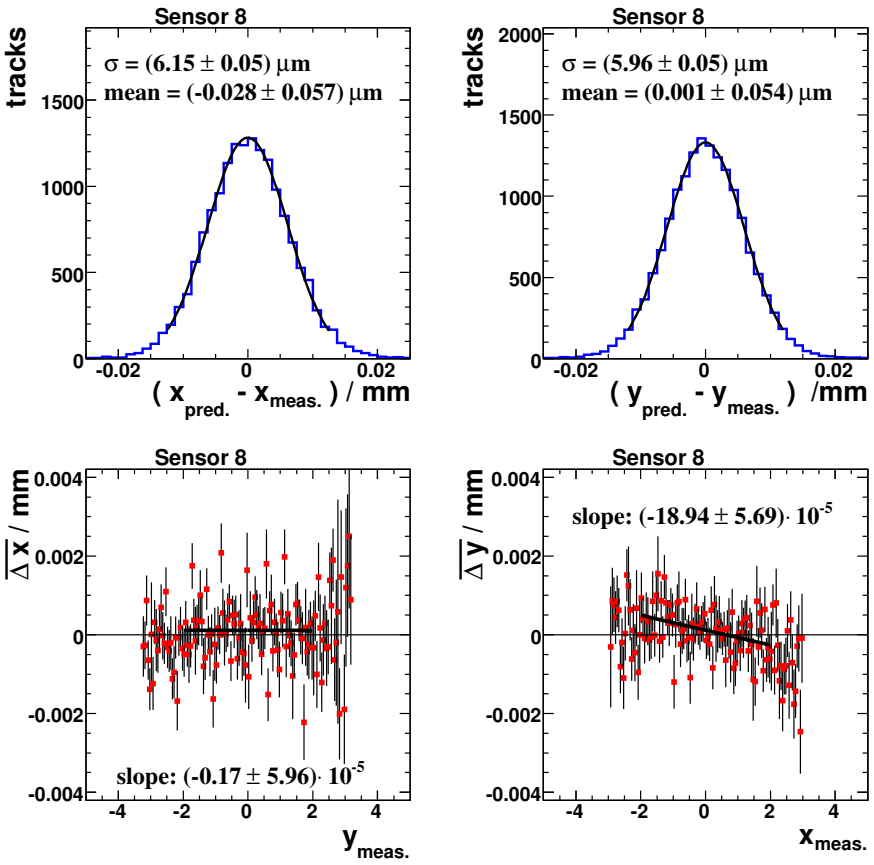

Figure 15.10: The observed residuals and the quantity $\overline{\Delta x}$ ($\overline{\Delta y}$) as a function of y (x) for the MIMOSA 26 sensor 6. The sensors was not included in the track fit.

settings, significant differences between the sensors are visible. Since these differences possibly have a large impact on the obtained results for the resolutions, a deeper understanding of this effect is mandatory for a more precise extraction of the resolution. A further possible improvement would be the consideration of multiple scattering.

For a data sample that consists of single-pixel clusters only, the resolution can be calculated according to [206]

$$\sigma_{\text{dig}} = \frac{P}{\sqrt{12}} = \frac{18.4\ \mu\text{m}}{\sqrt{12}} = 5.31\ \mu\text{m}, \tag{15.6}$$

where P represents the pixel pitch, which is 18.4 μm for MIMOSA 26. Since the investigated data were dominated by single-pixel cluster the extracted resolutions are roughly similar to σ_{dig}.

During the analysis of the data it was observed that part of the data were affected by a jitter of the x coordinate[2] of the clusters. During one run it occasionally happened that the x coordinates of all pixel in the data stream were shifted by exactly one pixel pitch. This effect was observed in the data of all three MIMOSA 26 sensors simultaneously.

[2]The y coordinate was not affected.

Sensor ID	σ_x	σ_y	k
Sensor 6	5.48 μm	5.35 μm	0.174
Sensor 7	5.07 μm	4.90 μm	0.169
Sensor 8	5.98 μm	5.78 μm	0.168

Table 15.1: The single-point resolutions and the geometrical scaling factor, k, for the three MIMOSA 26 sensors determined with a signal-to-noise threshold of $S/N > 12$.

In order to illustrate this effect, figure 15.12 shows the residual distribution in the x direction in one of the MIMOSA 26 sensors. A distinct second peak with exactly one pixel pitch distance is visible. Later after the data-taking it was found that the shielding of the electrical cables connected to the sensors was insufficient resulting in unpredictable and unstable behaviour of the whole data-acquisition system [219]. Possibly this could have caused the observed jitter. Therefore, it was decided to restrict the analysis to the part of the data where this effect was not observed.

15.2. September 2009 Test Beam

During the September 2009 test beam the sensors of the telescope were upgraded to six MIMOSA 26 sensors of which five could be used. A signal-to-noise threshold of $S/N > 10$ was applied to the MIMOSA 26 sensors. In this section the results of the data analysis are presented.

The data taken during the September 2009 test beam were affected by two TLU problems: 1) From time to time the synchronisation between the two VME crates was lost. 2) Since the read trigger numbers were always equal to zero, this synchronisation problem could not be fixed offline.

In order to recover at least part of the data, the spatial correlation between the cluster positions in neighbouring planes was investigated. Therefore, the data were chopped into several small sets and for each set the cluster correlations were investigated. Only those data that have exhibited a clear correlation were further analysed. Additionally, the data set that was taken directly before the first set without visible correlation was also removed from the analysis. Owing to this procedure about 200000 out of 1.5 million events could be recovered and analysed.

The track reconstruction was performed as described in the previous section by using four of the five available sensor planes. The hits in the sensor plane not used in the track fit were assigned to the track if the distance between the predicted track position and the hit position was smaller than 100 μm. Figures 15.13 and 15.14 present the extracted residual distributions for each sensor plane separately. For each distribution the corresponding sensor plane was removed from the track reconstruction. These distributions were fitted with Gaussian functions and the resolution, $\sigma_{\text{meas.}}$, was extracted as described in the previous section. Since the measured resolutions for the x and y direction differ significantly, a systematic uncertainty of 0.10 μm estimated from the spread was assigned to the extracted resolutions. Therefore, this systematic uncertainty was considered in the extraction of the single-point resolution of the MIMOSA 26 sensor. Different resolutions for the x and y direction were also observed in previous analyses [242].

The prediction for the measured resolution can be calculated from the single-point

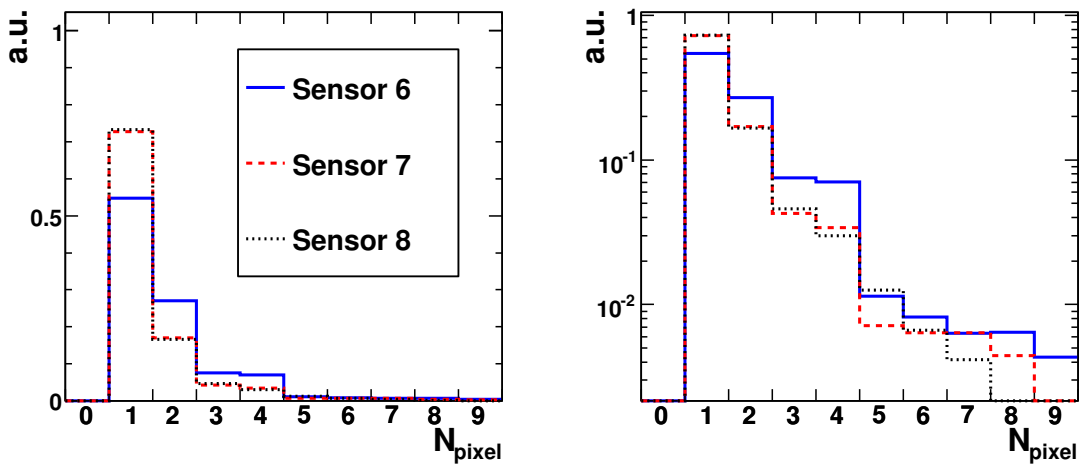

Figure 15.11: Pixel multiplicity per cluster for the three MIMOSA 26 sensors.

resolution of the MIMOSA 26 sensor, σ_{M26}, and the geometrical scaling factor, k, according to

$$\sigma^2_{\text{meas.}} = \sigma^2_{\text{M26}} + \sigma^2_{\text{tel.}} + \cancel{\sigma^2_{\text{MS}}}, \tag{15.7}$$

and

$$\sigma^2_{\text{tel}} = k \cdot \sigma^2_{\text{M26}}, \tag{15.8}$$

under the assumption that all telescope sensors have the same single-point resolution and that $\sigma_{\text{MS}} = 0$.

Figure 15.15 shows the prediction for the measured resolution, $\sigma_{\text{meas.}}$, as a function of the z coordinate for different values of σ_{M26} in comparison with the measured values extracted from the residual distributions shown in figures 15.13 and 15.14. The combined single-point resolution of the MIMOSA 26 sensors was extracted from that figure with a χ^2 minimisation method ($\chi^2/\text{ndf} \approx 1.2$). The extracted value for the single-point resolution was determined to be $\sigma_{\text{M26}} = [4.35 \pm 0.10\,(sys)]$ μm and is indicated in the figure as a filled band. Within the systematic uncertainties the agreement between the measurement and the prediction of its dependence on the sensor position is reasonable. The quality of the track reconstruction is illustrated in figure 15.16 where the distribution of the quantity χ^2 of the tracks is shown. The data are compared with the expected χ^2 distribution [243] for four degrees of freedom[3]. The expected χ^2 distribution agrees with the data reasonably well. The obtained single-point resolution for the applied threshold setting agrees within the uncertainties with the results from the MIMOSA 26 developers [212, 213] with a tendency towards smaller values. Since multiple scattering was neglected, a possibly slightly smaller single-point resolution can be extracted by taking this effect into account.

[3]In total four planes with 8 measurements were used in the track reconstruction. The number of fitted parameters was equal to 10 and the number of used constrains on multiple scattering was 6 (three inner sensor planes).

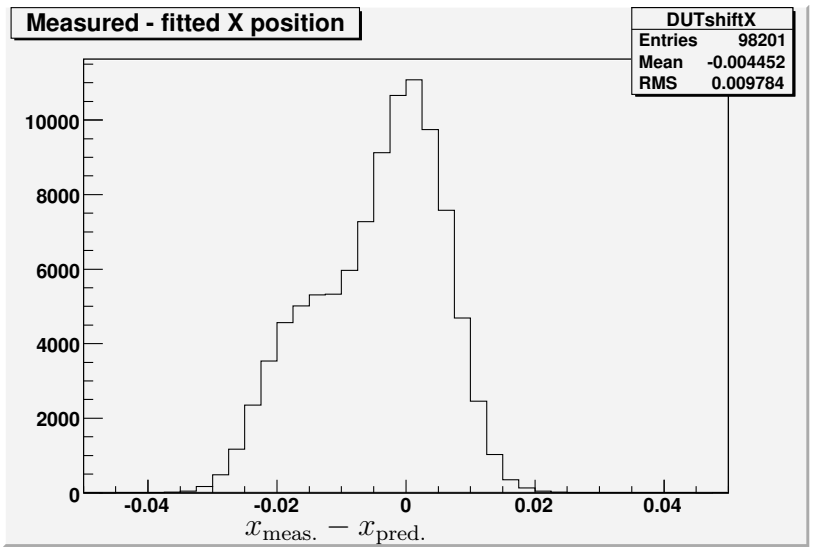

Figure 15.12: The Residual distribution in x direction for one MIMOSA 26 sensor.

The extracted single-point resolution can be utilised to calculate the intrinsic telescope resolution for the employed threshold setting and the used geometrical setup. For the investigated setup with four planes used in the track reconstruction and with a signal-to-noise threshold of $S/N > 10$ the intrinsic telescope resolution in the central sensor plane was determined to be (2.22 ± 0.05) μm. This resolution can significantly be improved by performing the track reconstruction with six planes instead of four and by applying a lower threshold setting during the data taking. For a telescope setup (threshold $S/N > 10$) with six planes where the distance between neighbouring planes is equal to 10 cm, an intrinsic telescope resolution of $1.9 - 2.0$ μm in the DUT layer centered between the two arms can be reached.

In addition to the determination of the resolution, the detection efficiency of the central sensor plane (sensor 2) was investigated. The efficiency was determined with the ratio of number of hits assigned to tracks over the total number of predicted hits. Measured hits were assigned to tracks if the distance between the measured and predicted hit position was smaller than 100 μm. Figure 15.17 shows the efficiency in x and y direction, fake hit rate and the predicted track positions. The fake hit rate was determined by using for the central sensor plane data from the previous event. These hits were assigned to the track if the distance was smaller than 100 μm. This rate was in general between 10^{-4} and 10^{-3} and, therefore, significantly larger than the expectation of 10^{-5} [213]. The reason could be that during the data taking a larger amount of electronic noise in the system than expected was observed. The dip at $x \approx -5$ mm in the plot that shows the predicted track positions is caused by sensor 0, because the dip disappears after removing sensor 0 from the track reconstruction. After the test beam campaign it was found that the JTAG programming of sensor 0 was insufficient [219] which could have caused such a behaviour.

The detection efficiency for the signal-to-noise threshold $S/N > 10$ was determined to be approximately $\approx 95.5\%$ in the region of the trigger window, which is larger than the expectation [212, 213] of 94%. The location of the trigger window is clearly visible in the efficiency histogram.

One possible explanation [219, 244] that could explain the different efficiencies

in the region of the trigger window and outside this window can be the following: As a consequence of the rolling-shutter mode, each pixel contains the signals that correspond to a time which is equal to the integration time of the sensors (≈ 110 μs). Hence, the effective sensitive time window for each pixel is shifted relative to the others. Moreover, in the offline analysis during conversion two frames are combined such that the data from the current frame is taken up to the pivot row. The remaining parts are taken from the previous frame. Those parts taken are called in the following "active" and the discarded parts "inactive". For particles passing the detector in coincidence with the trigger signal the whole sensor matrix is "active". The relative fraction of the "inactive" area increases the more the particles moves in time away from the trigger signal. Since the sensors read-out by EUDRBs in one VME crate are read-out synchronously, the pixel address in pixel units is for those sensors identical (typically in the range ± 1 pixel units). However, relative transverse shifts of the sensors result in different geometrical pivot row positions in the (x, y)-coordinate system. Hence, particles passing one sensor in the "active" part of the matrix can possibly pass the other sensors in the "inactive" parts. Due to the fact that the relative fraction of the "active" area is for out-of-time particles much smaller than for particles passing in coincidence with the trigger signal the sensors, the efficiency for the detection of out-of-time hits is slightly smaller. The same behaviour should not only occur for small shifts but also for tracks with an angle with respect to the z axis and for a tilted/rotated telescope.

Since the average track multiplicity per event is about ≈ 1.2 and the efficiency difference between particles in the region of the trigger window and out-of-time particles is about $\sim 4\%$, the contributions from out-of-time particles to the measured efficiency in the region of the trigger window, where the observed efficiency is a weighted average, amounts to approximately $\approx 1\%$.

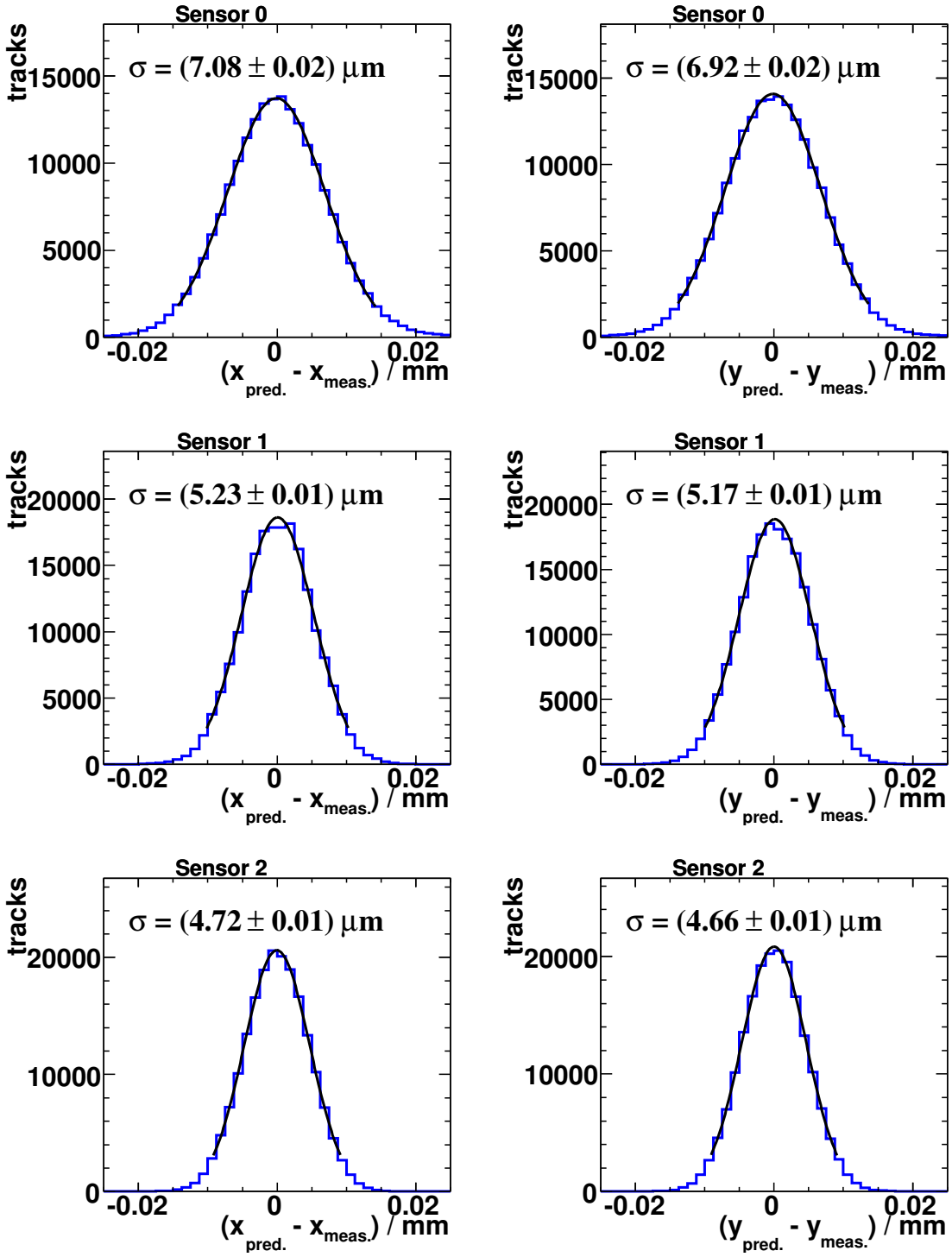

Figure 15.13: Residual distributions in x and y direction for the September 2009 data. The corresponding sensors were treated as passive layers in the track reconstruction.

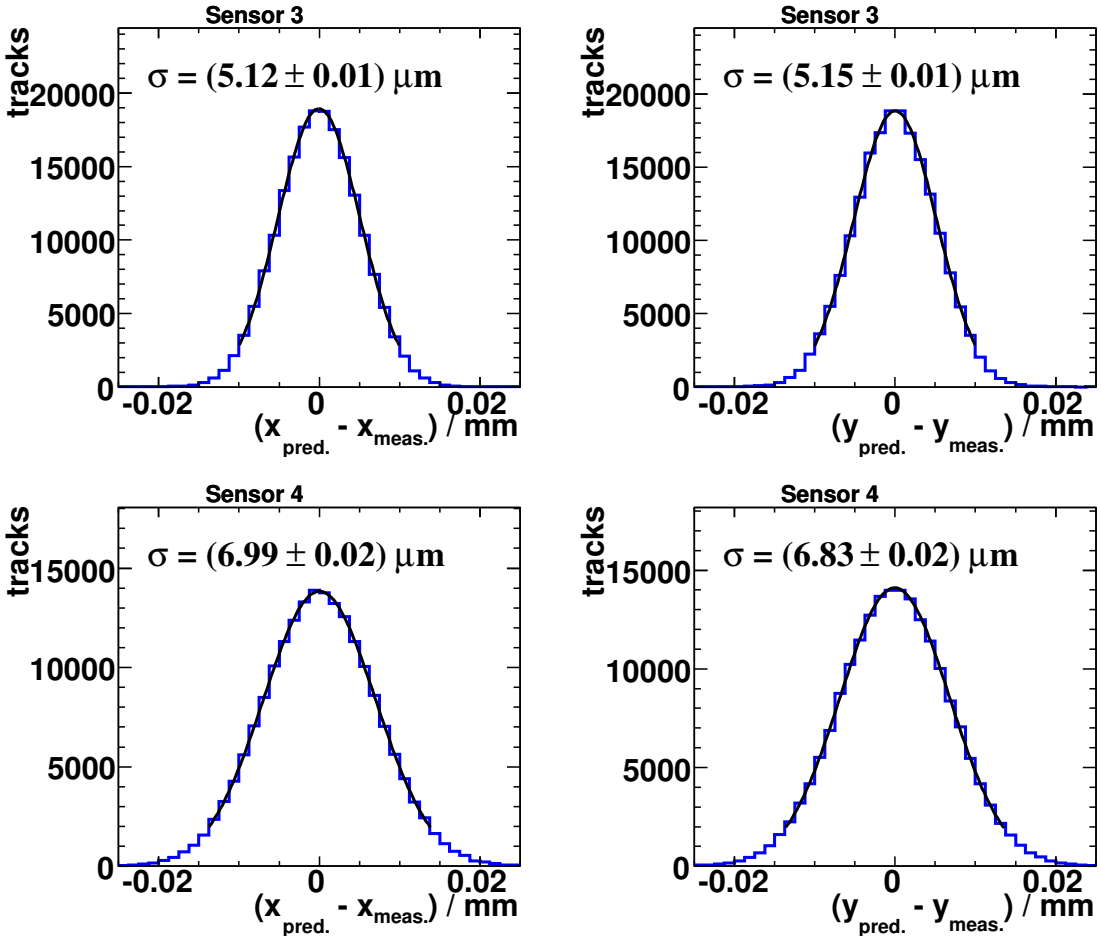

Figure 15.14: Residual distributions in x and y direction for the September 2009 data. The corresponding sensors were treated as passive layers in the track reconstruction.

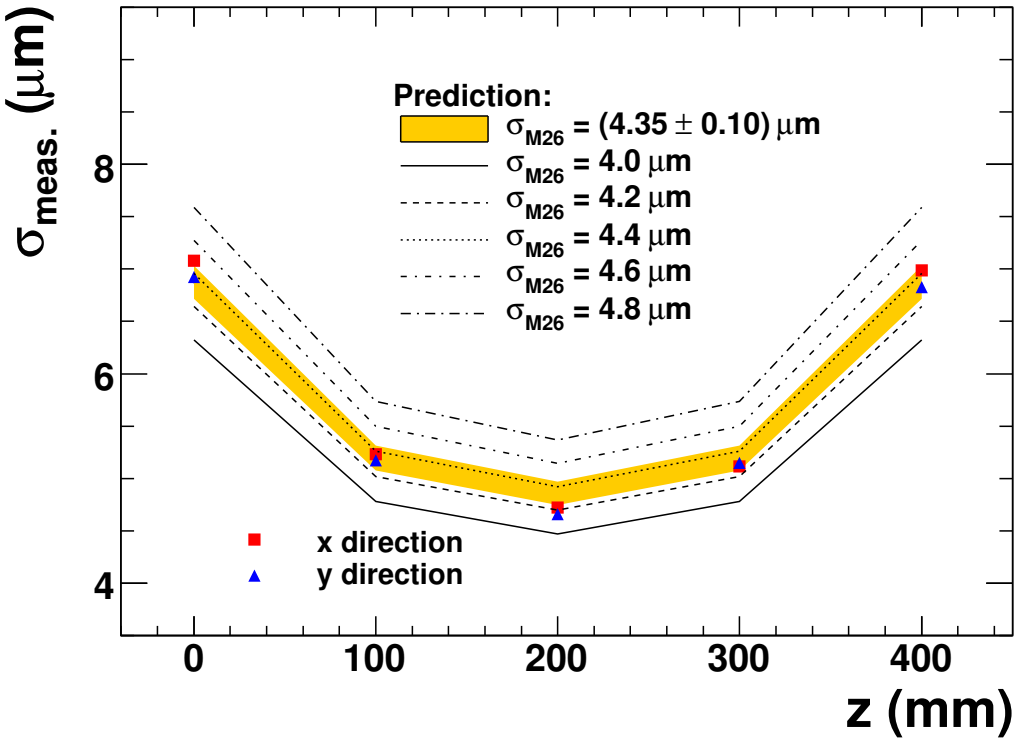

Figure 15.15: The measured resolution, $\sigma_{\text{meas.}}$, as a function of the z coordinate. The corresponding sensor plane for each data point was treated as passive layer in the track reconstruction.

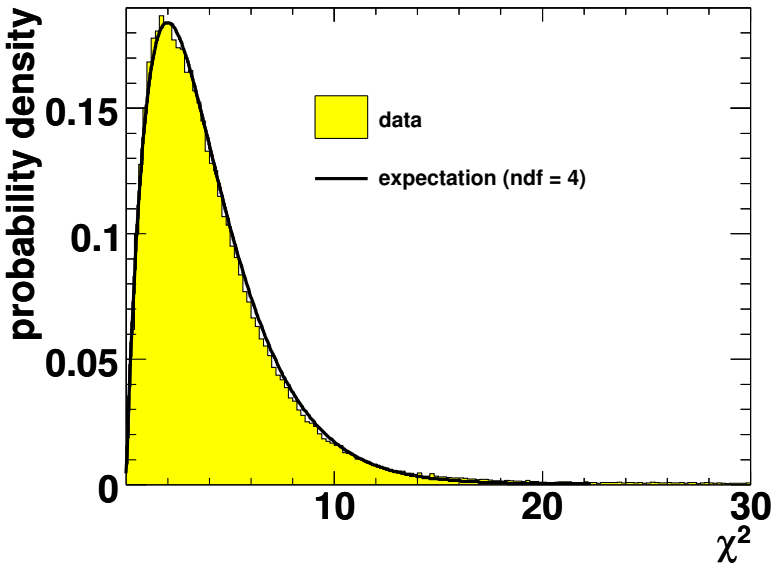

Figure 15.16: Distribution of the quantity χ^2 for reconstructed tracks in comparison with the expectation for four degrees of freedom (ndf).

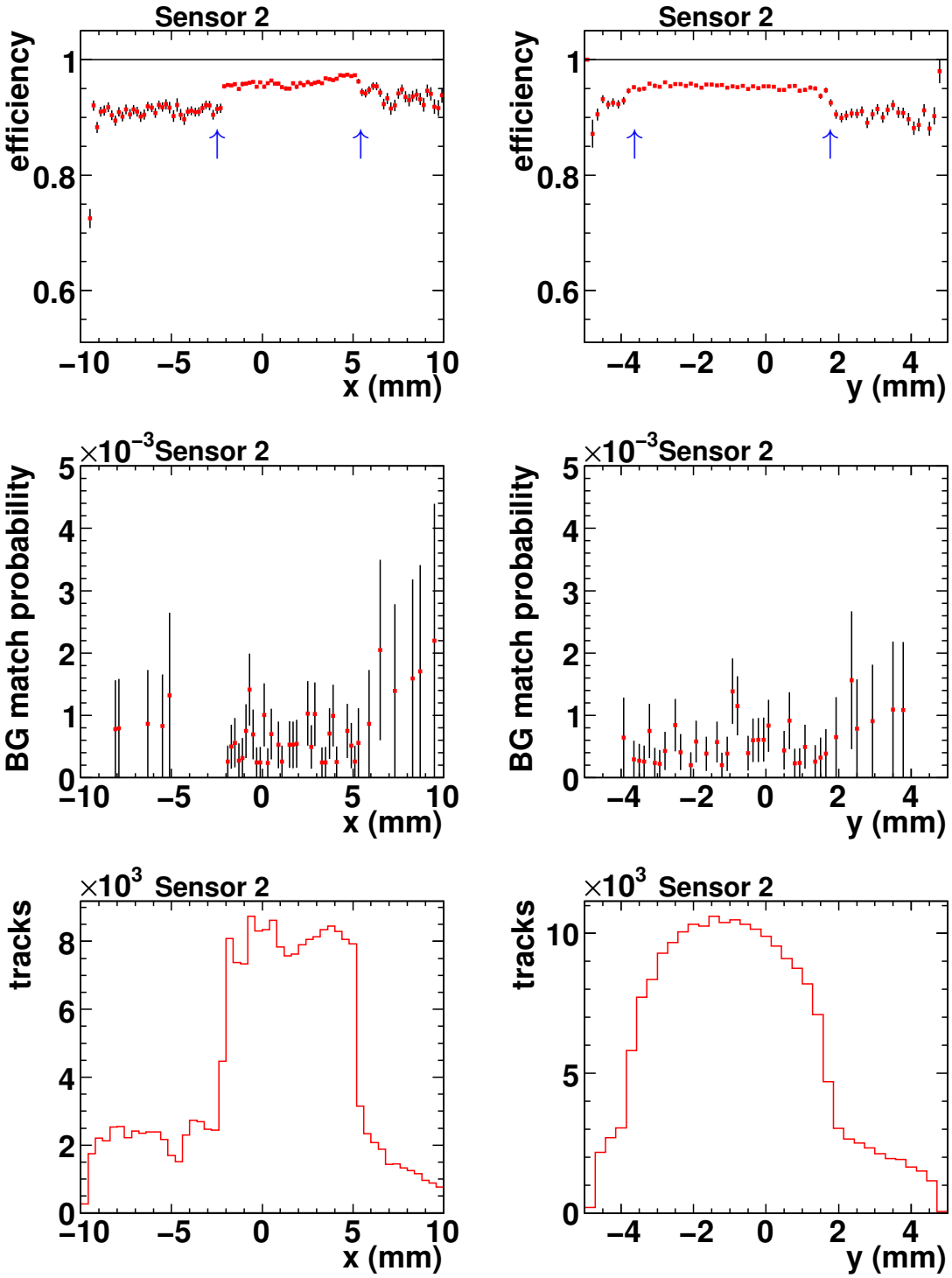

Figure 15.17: The detection efficiency in x and y direction, the probability to match background (BG) hits to the reconstructed track and the predicted track positions in the sensor plane. In the efficiency plots the position of the trigger window is indicated with small arrows.

16. Summary and Conclusion

The EUDET high-resolution test-beam telescope was designed to be used in a wide range of detector research and development studies. The provided infrastructure is flexible and portable in order to allow the investigation of rather different devices-under-test. The telescope can be used at high-energy hadron beams (e.g. > 100 GeV at the SPS facility at CERN) as well as at low-energetic electron beams ($1 - 6$ GeV at DESY). The telescope consists of two arms each equipped with three pixel sensors; the device-under-test can be installed for instance between the two arms.

In the EUDET project a two stage approach for the construction of the telescope was chosen: First, the so-called "demonstrator telescope" was constructed equipped with well established analog sensors (MimoTEL). Afterwards, the telescope was upgraded in Summer 2009 to sensors with binary output (Mimosa 26) in order to match the design requirements – in particular to reach a higher readout rate of about 1 kHz.

In this thesis, the usability, flexibility and performance of the online-monitoring system was improved by introducing new histograms, adjusting the reconstruction algorithms and by implementing new elements into the graphical user interface. Additionally, the offline-analysis software was adapted to cope with the new binary Mimosa 26 sensors installed in the final telescope.

The very first analysis of two different data samples taken with these new sensors in the EUDET telescope was presented:

- First, a data sample was analysed in which the "demonstrator telescope" was used as a reference system. Three Mimosa 26 were installed as devices-under-test. These devices-under-test were configured with signal-to-noise thresholds of $S/N > 12$ resulting in a data sample dominated by single-pixel clusters. The offline analysis software was successfully adapted to the new requirements of binary sensors. For the applied threshold setting a Mimosa 26 single-point resolution of about 5.3 μm was determined.

- The second analysed data sample consisted of data taken with the final telescope upgraded to six Mimosa 26 sensors, of which five could be used. The applied threshold setting was $S/N > 10$ in order to improve the resolution and detection efficiency. The measured residual widths were found to be consistent with a single-point resolution of $\sigma_{\mathrm{M26}} = [4.35 \pm 0.10\,(sys)]$ μm. Therefore, a telescope equipped with six sensors can reach an intrinsic telescope resolution in the order of $1.9 - 2.0$ μm for a threshold of $S/N > 10$. The detection efficiency was determined to be approximately 95%, while the fake rate was found to be below 10^{-3}.

The EUDET telescope was upgraded successfully to the final version over the Summer 2009. Since then it was successfully used by several different groups and it will extensively be utilised in the future.

A. Appendix

A.1. Jet Energy Corrections

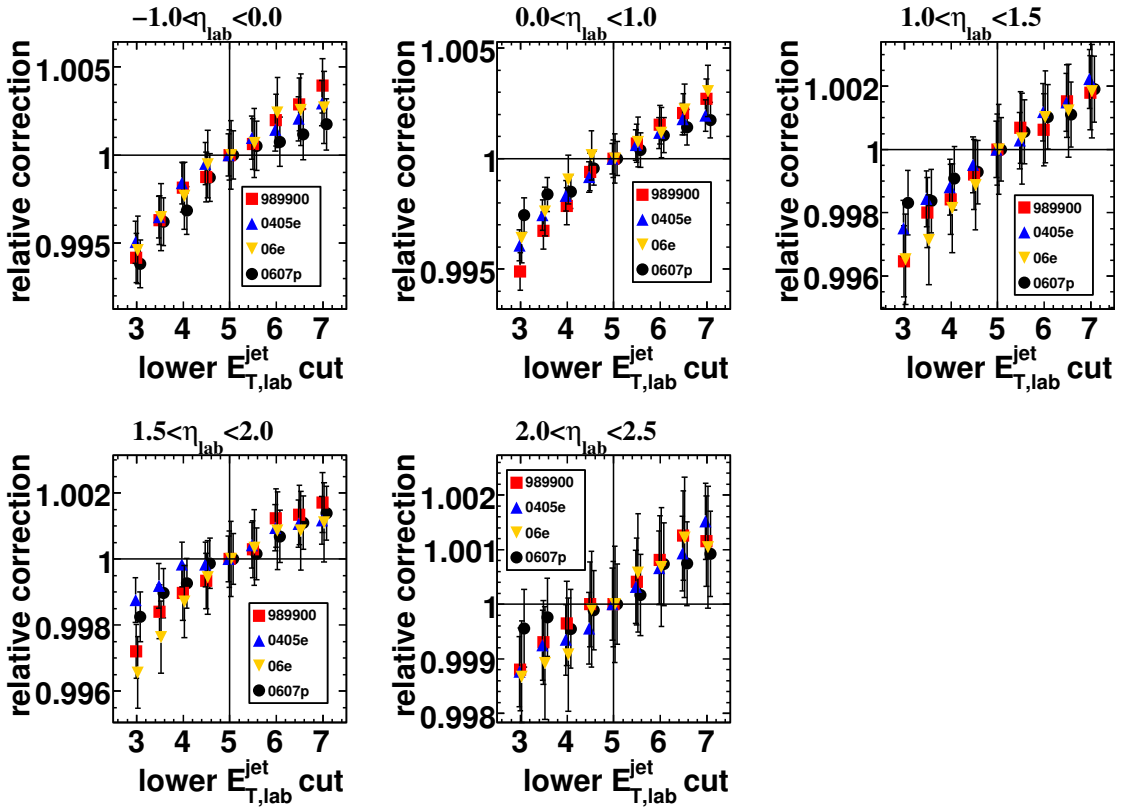

Figure A.1: The relative change of the hadronic energy scale correction factors as a function of the lower $E_{T,\mathrm{lab}}^{\mathrm{jet}}$ cut for all data-taking periods in different regions of $\eta_{\mathrm{lab}}^{\mathrm{jet}}$.

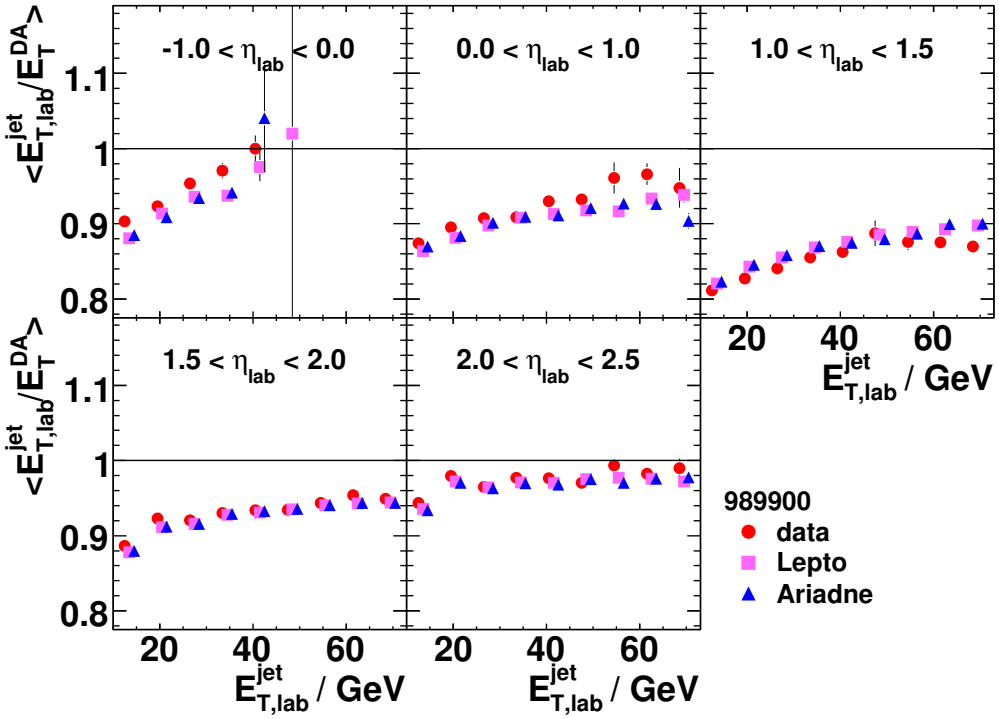

Figure A.2: The ratio $< \frac{E^{\rm jet}_{T,\rm lab}}{E^{DA}_{T,\rm lab}} >$ as a function of the jet transverse energy ***before*** the calibration in five pseudorapidity regions.

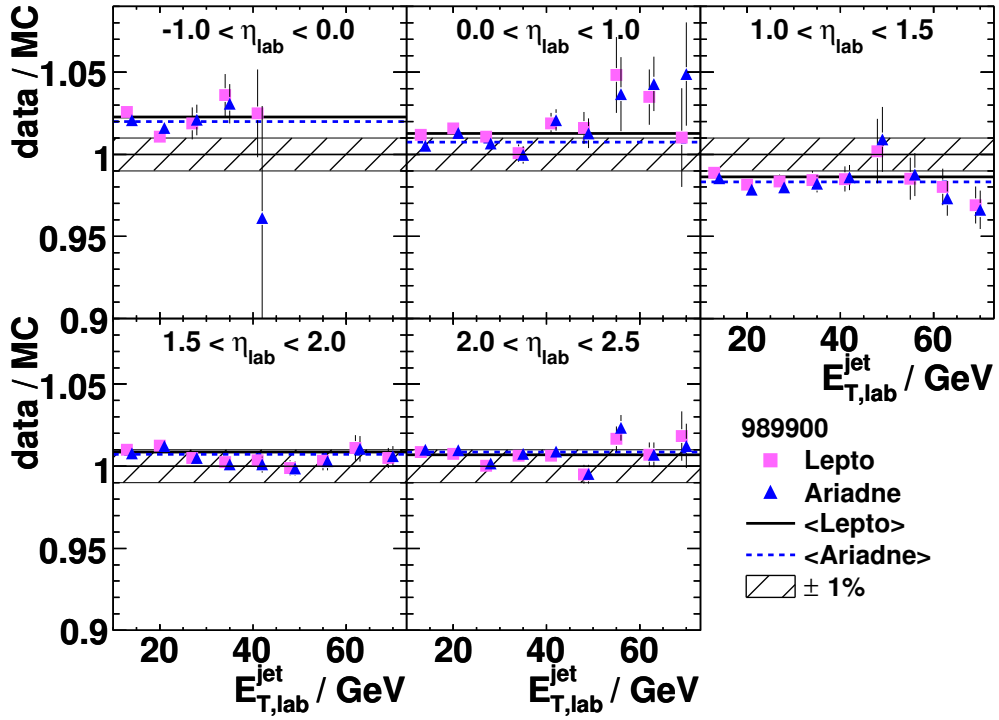

Figure A.3: The double ratio between the data and the MCs as a function of the jet transverse energy, $E^{\rm jet}_{T,\rm lab}$, in five regions of the pseudorapidity, $\eta^{\rm jet}_{\rm lab}$, ***before*** the jet energy scale correction. The hatched area indicates the 1% uncertainty region on the jet energy scale. The horizontal lines depict the average double ratio for ARIADNE and LEPTO in each $\eta^{\rm jet}_{\rm lab}$ interval separately.

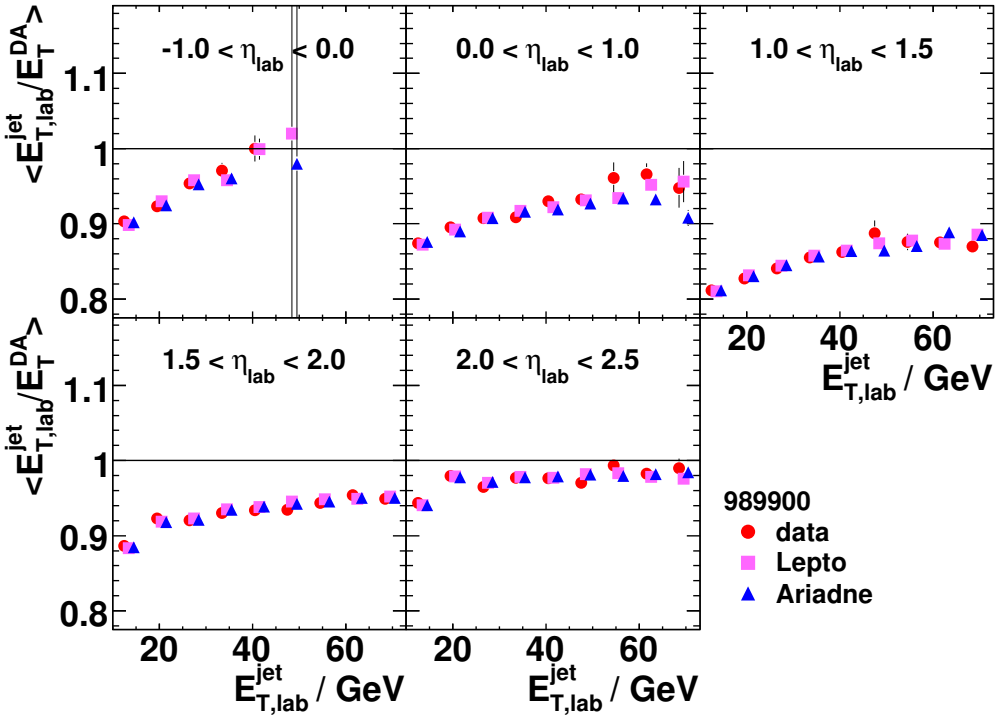

Figure A.4: The ratio $< \frac{E^{\mathrm{jet}}_{T,\mathrm{lab}}}{E^{DA}_{T,\mathrm{lab}}} >$ as a function of the jet transverse energy ***after*** the calibration in five pseudorapidity regions.

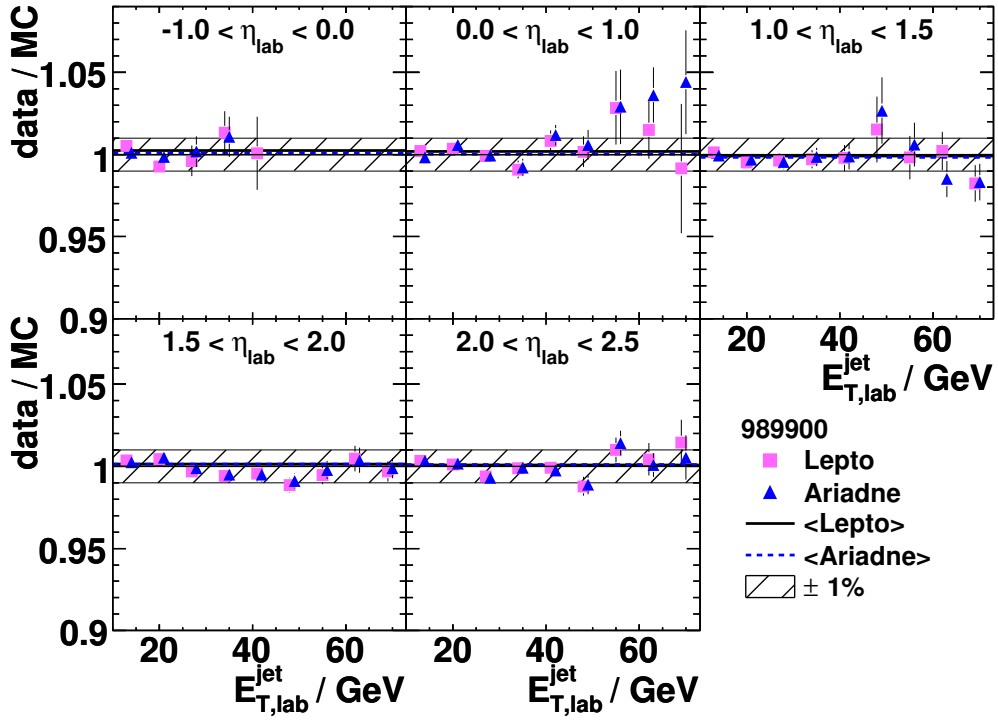

Figure A.5: The double ratio ***after*** the jet energy scale correction. Other details as in the caption to figure A.3.

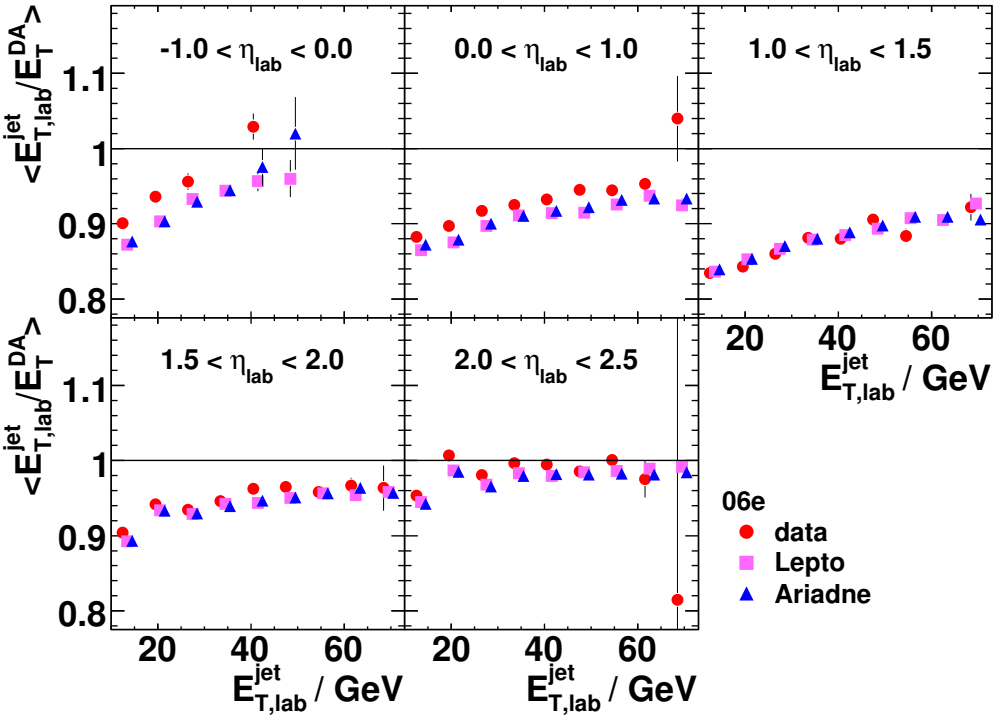

Figure A.6: The ratio $< \frac{E^{\mathrm{jet}}_{T,\mathrm{lab}}}{E^{DA}_{T,\mathrm{lab}}} >$ as a function of the jet transverse energy ***after*** the calibration in five pseudorapidity regions.

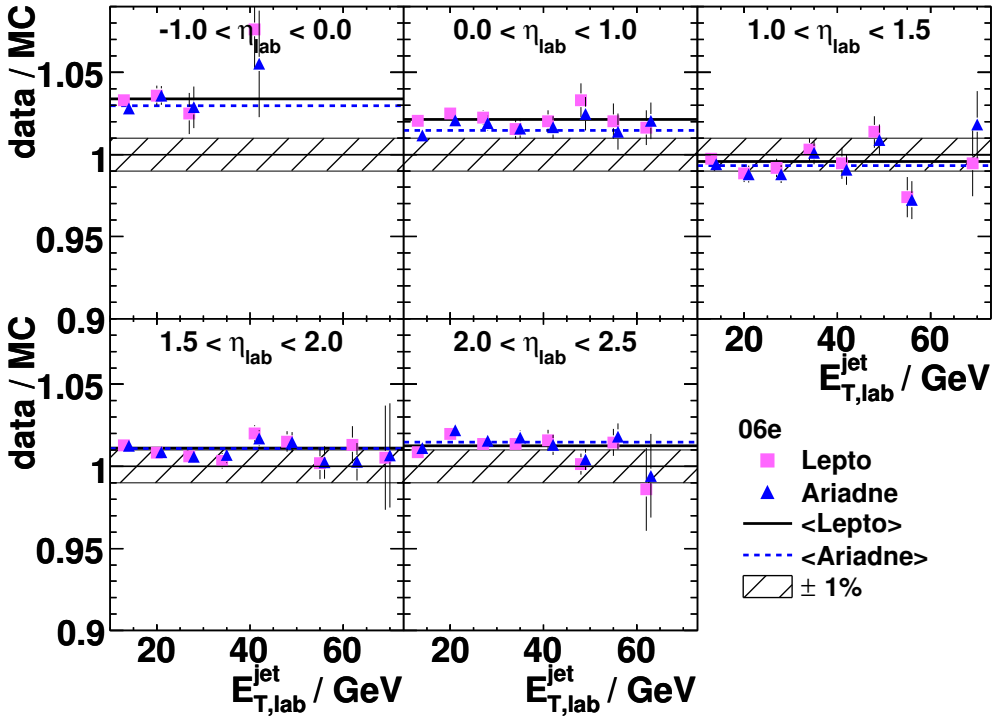

Figure A.7: The double ratio ***before*** the jet energy scale correction. Other details as in the caption to figure A.3.

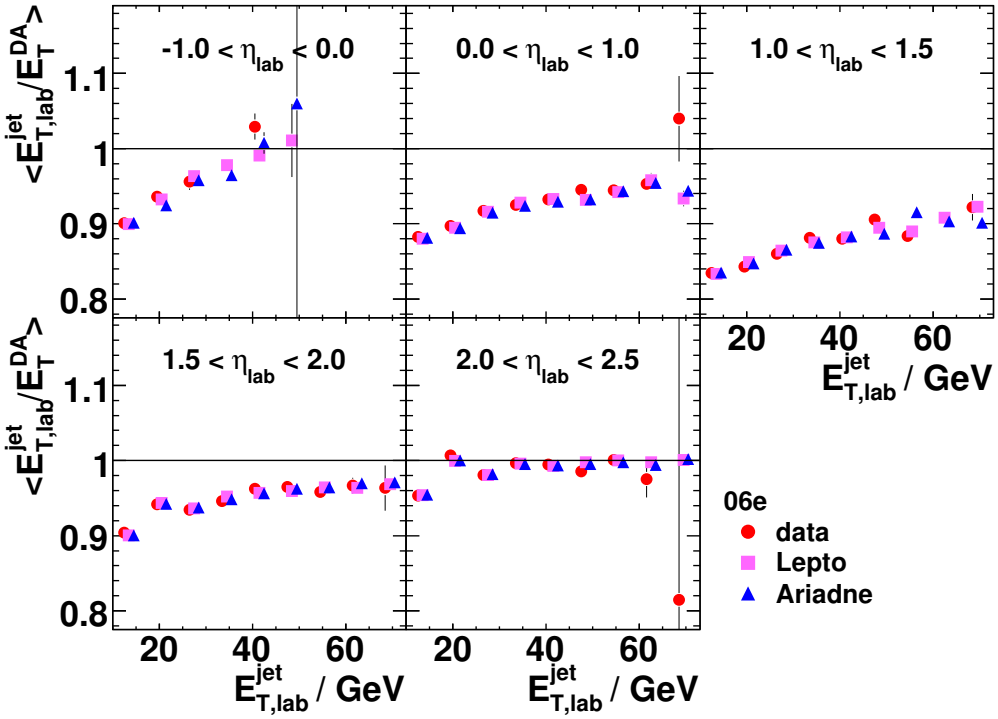

Figure A.8: The ratio $< \frac{E^{\mathrm{jet}}_{T,\mathrm{lab}}}{E^{DA}_{T,\mathrm{lab}}} >$ as a function of the jet transverse energy ***after*** the calibration in five pseudorapidity regions.

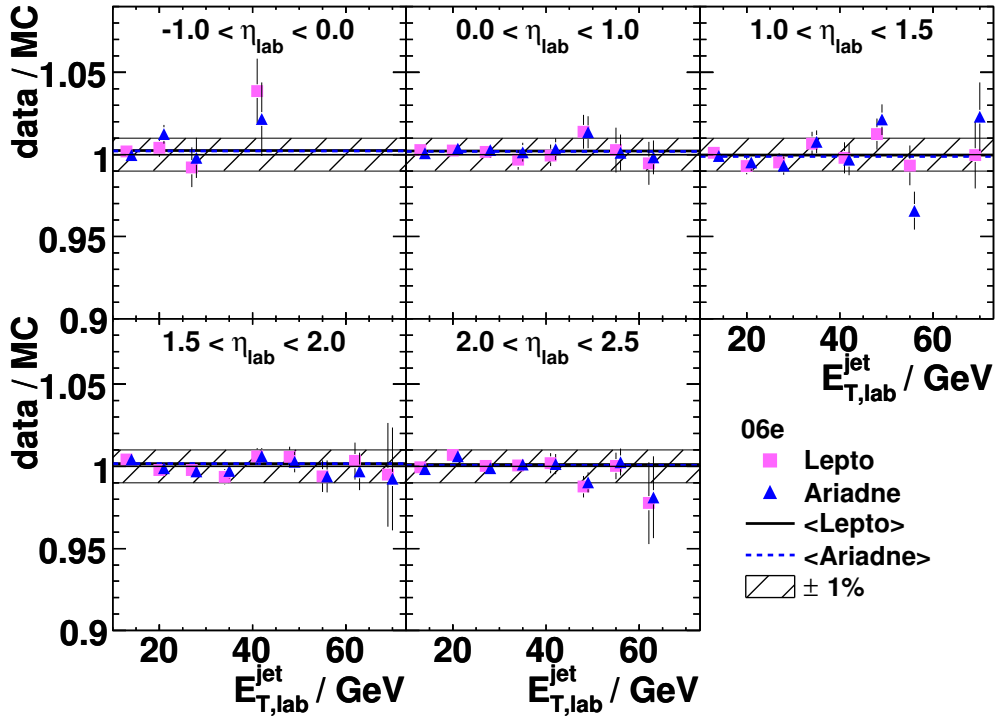

Figure A.9: The double ratio ***after*** the jet energy scale correction. Other details as in the caption to figure A.3.

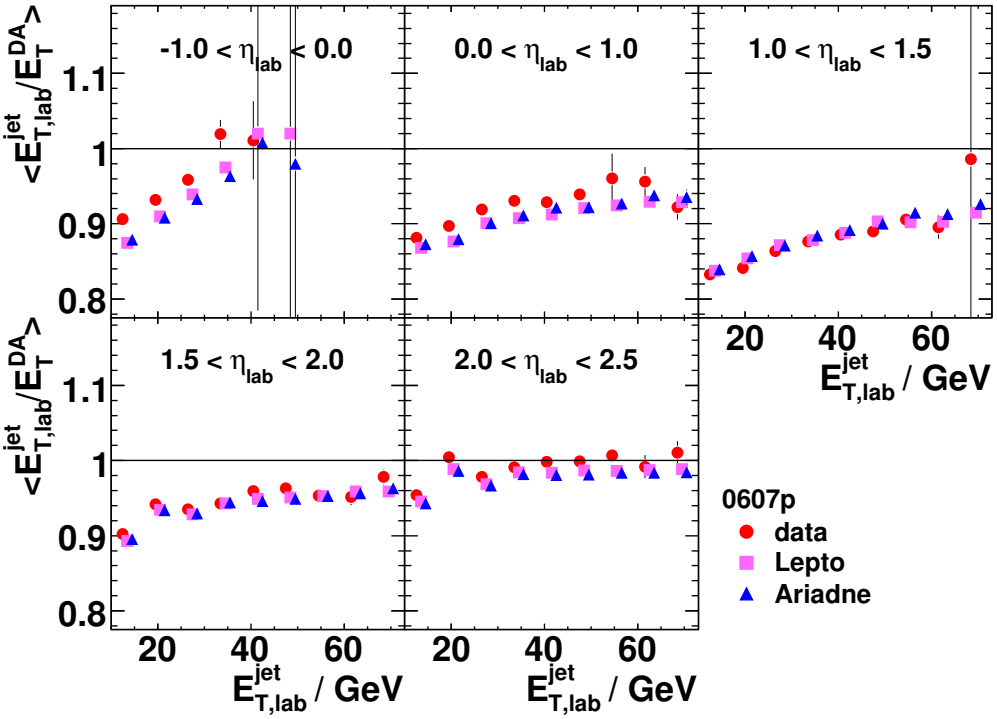

Figure A.10: The ratio $< \frac{E^{\mathrm{jet}}_{T,\mathrm{lab}}}{E^{DA}_{T,\mathrm{lab}}} >$ as a function of the jet transverse energy ***after*** the calibration in five pseudorapidity regions.

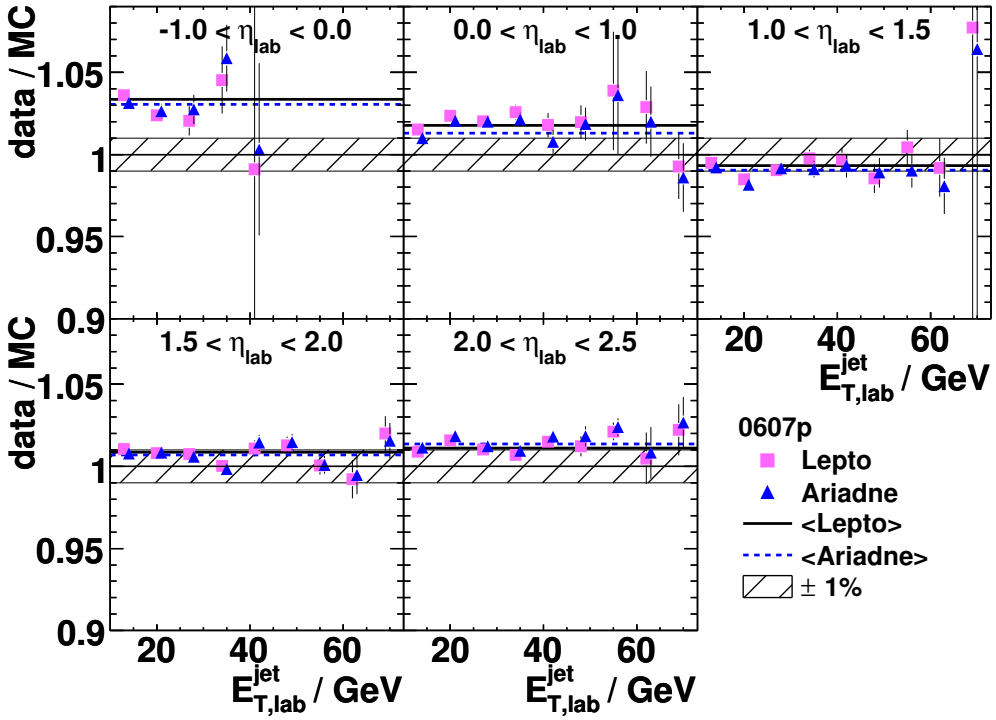

Figure A.11: The double ratio ***before*** the jet energy scale correction. Other details as in the caption to figure A.3.

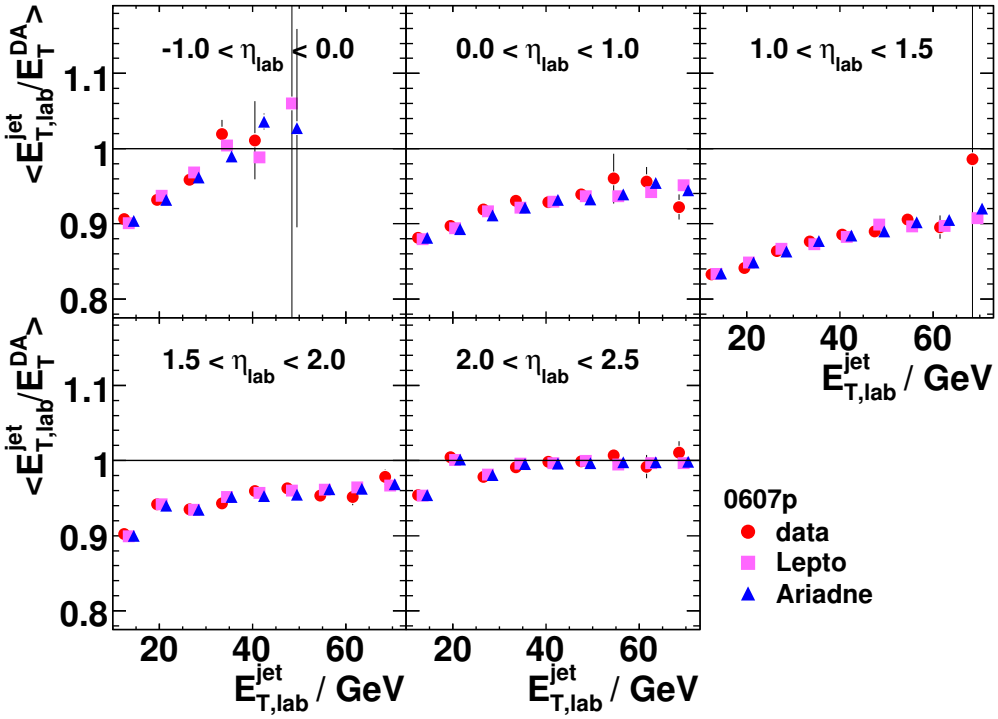

Figure A.12: The ratio $< \frac{E^{\mathrm{jet}}_{T,\mathrm{lab}}}{E^{DA}_{T,\mathrm{lab}}} >$ as a function of the jet transverse energy ***after*** the calibration in five pseudorapidity regions.

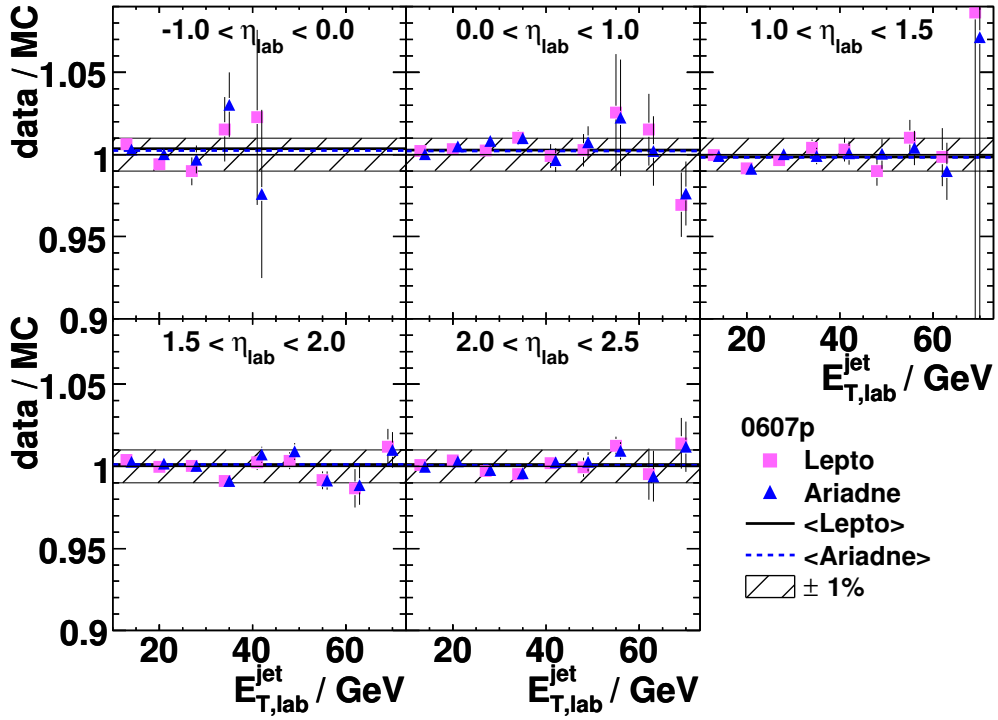

Figure A.13: The double ratio ***after*** the jet energy scale correction. Other details as in the caption to figure A.3.

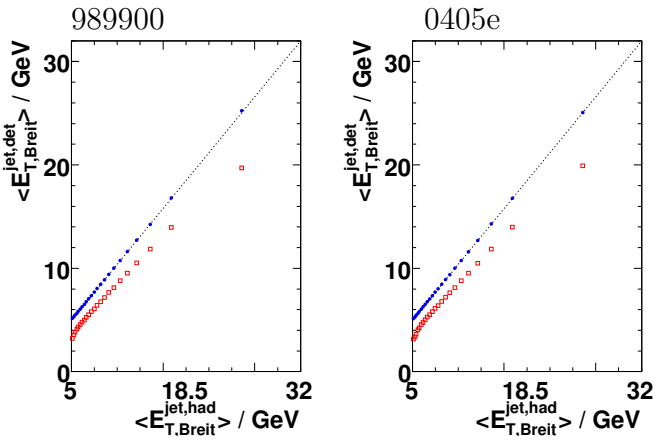

Figure A.14: The average detector level $\left\langle E_{T,\mathrm{Breit}}^{\mathrm{jet,det}} \right\rangle$ as a function of $\left\langle E_{T,\mathrm{Breit}}^{\mathrm{jet,had}} \right\rangle$ in the range $-1 < \eta_{\mathrm{lab}}^{\mathrm{jet}} < 2.5$ for LEPTO before and after applying a correction for inactive material in front of the calorimeter.

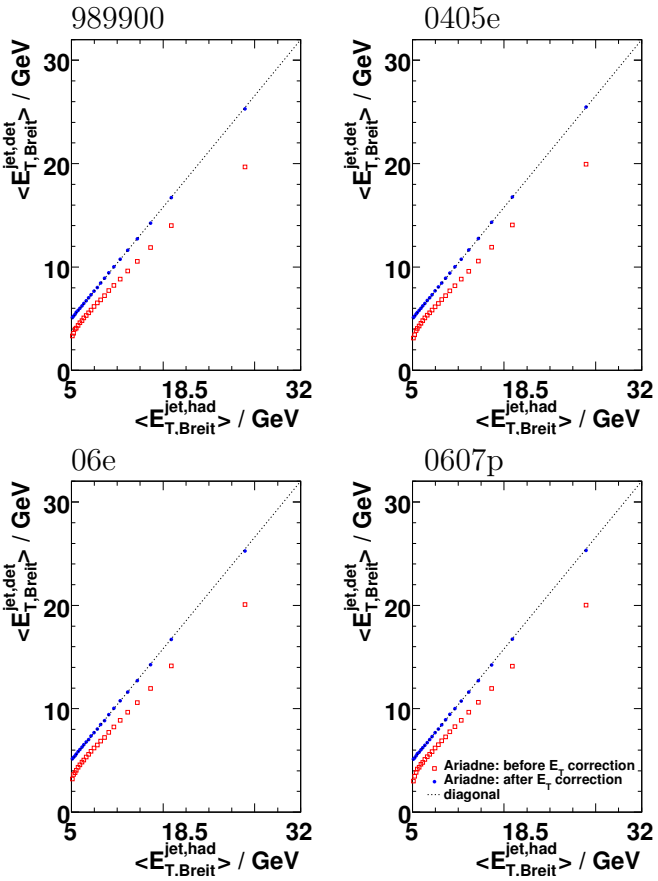

Figure A.15: The average detector level $\left\langle E_{T,\mathrm{Breit}}^{\mathrm{jet,det}} \right\rangle$ as a function of $\left\langle E_{T,\mathrm{Breit}}^{\mathrm{jet,had}} \right\rangle$ in the range $-1 < \eta_{\mathrm{lab}}^{\mathrm{jet}} < 2.5$ for ARIADNE before and after applying a correction for inactive material in front of the calorimeter.

A.2. Trigger Efficiency

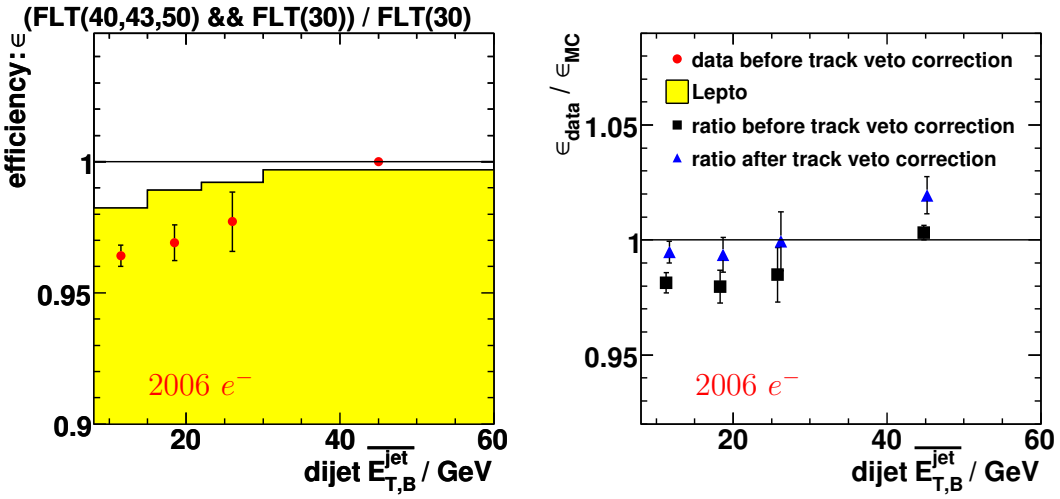

Figure A.16: The 2006 e^- trigger efficiency, ϵ, and the ratio $\epsilon_{\mathrm{data}}/\epsilon_{\mathrm{MC}}$ before and after applying the track-veto correction in regions of the average transverse energy in the Breit frame, $\overline{E^{\mathrm{jet}}_{T,\mathrm{B}}}$, of the dijet system.

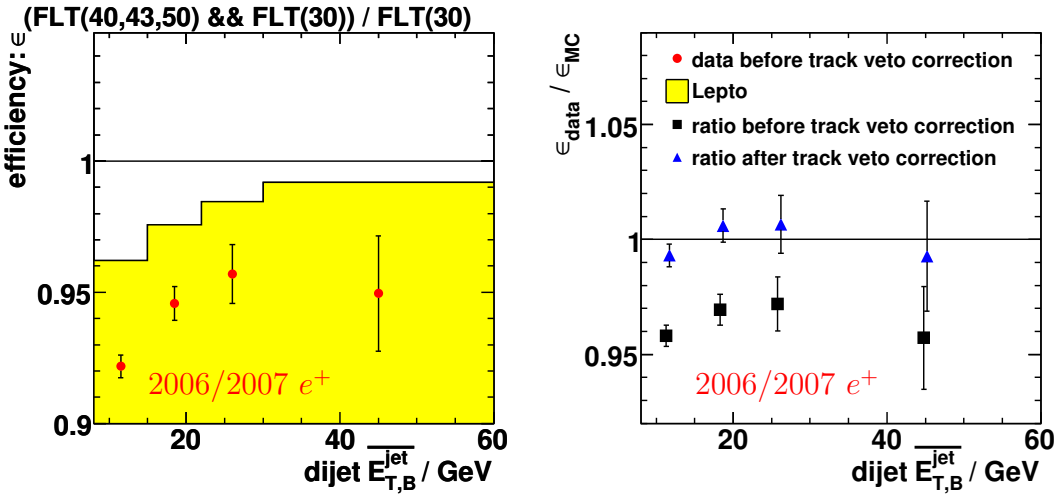

Figure A.17: The 2006/2007p e^+ trigger efficiency. Other details as in the caption to figure A.16.

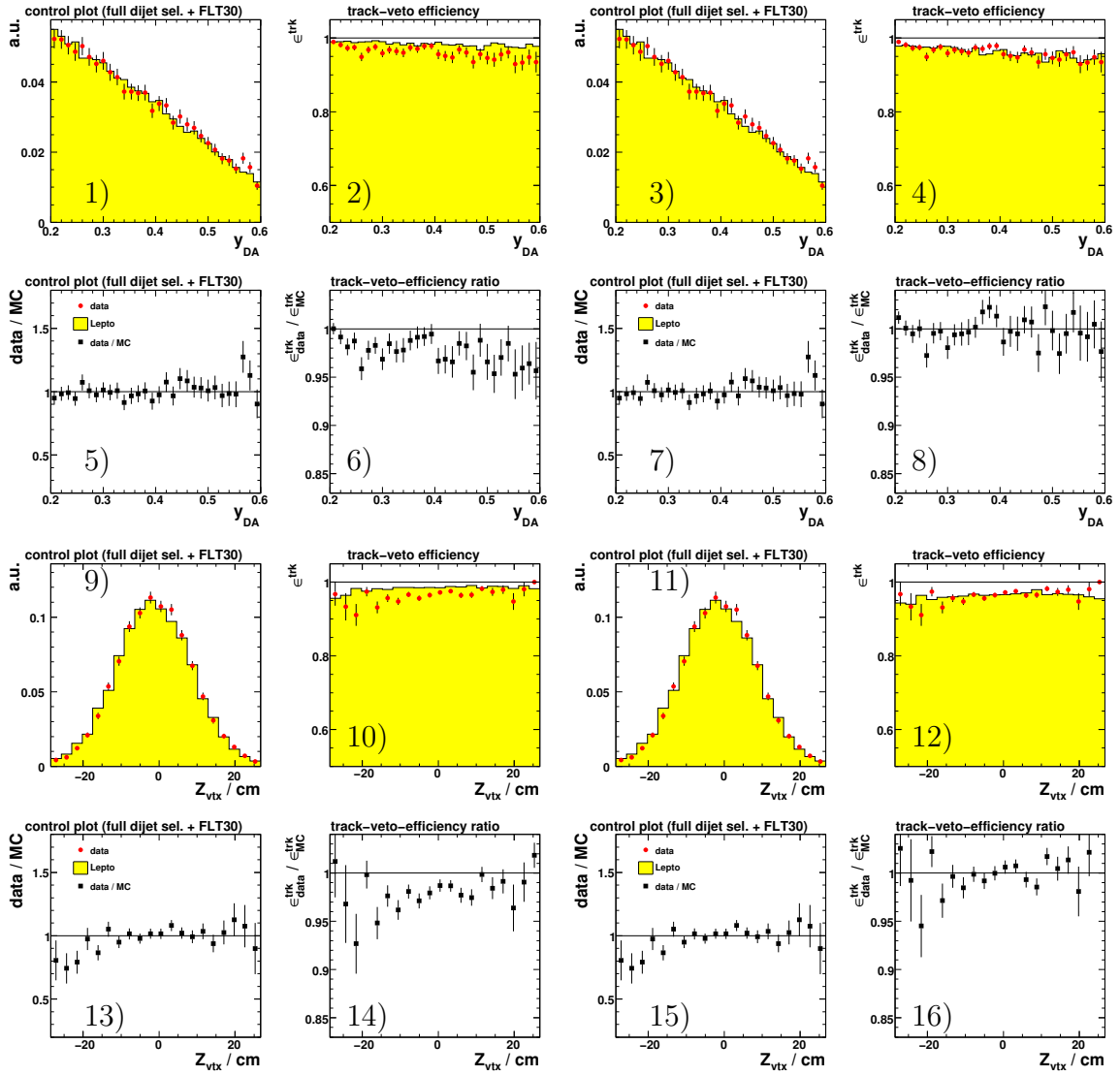

Figure A.18: Study of the 2004/2005 e^- track veto efficiency as functions of y_{DA} and z_{vtx} for data and LEPTO: 1,3,9,11) Control distributions. 2,4,10,12) The track veto efficiency ϵ^{trk}. 5,7,13,15) Ratio of the individual control distributions. 6,8,14,16) Ratio of the track veto efficiencies $\epsilon^{\mathrm{trk}}_{\mathrm{data}}/\epsilon^{\mathrm{trk}}_{\mathrm{MC}}$. Figures 3,4,7,8,11,12,15,16 show the distributions after applying the track-veto correction.

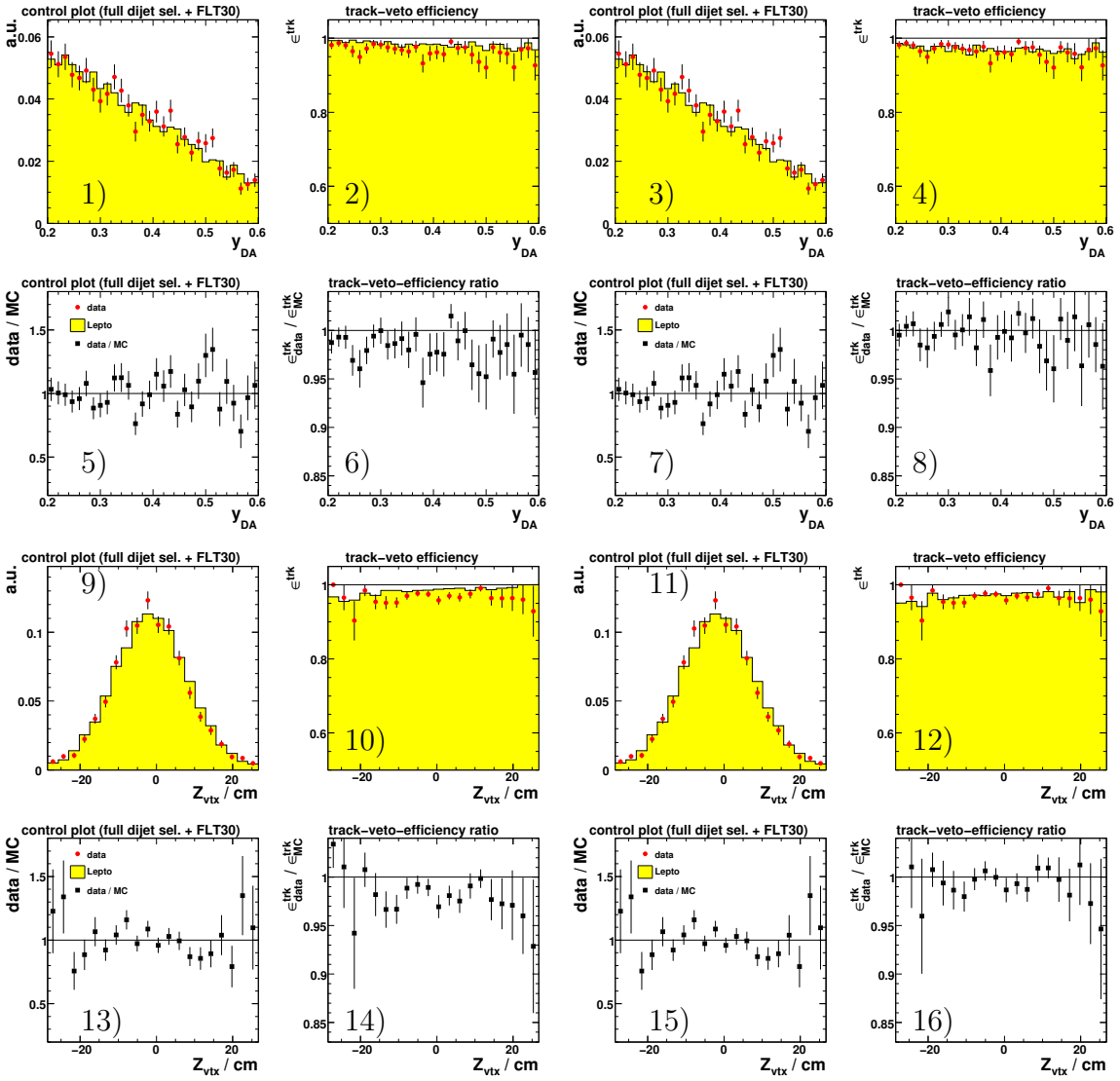

Figure A.19: Study of the 2006 e^- track veto efficiency as functions of y_{DA} and z_{vtx} for data and LEPTO: 1,3,9,11) Control distributions. 2,4,10,12) The track veto efficiency ϵ^{trk}. 5,7,13,15) Ratio of the individual control distributions. 6,8,14,16) Ratio of the track veto efficiencies $\epsilon^{\mathrm{trk}}_{\mathrm{data}}/\epsilon^{\mathrm{trk}}_{\mathrm{MC}}$. Figures 3,4,7,8,11,12,15,16 show the distributions after applying the track-veto correction.

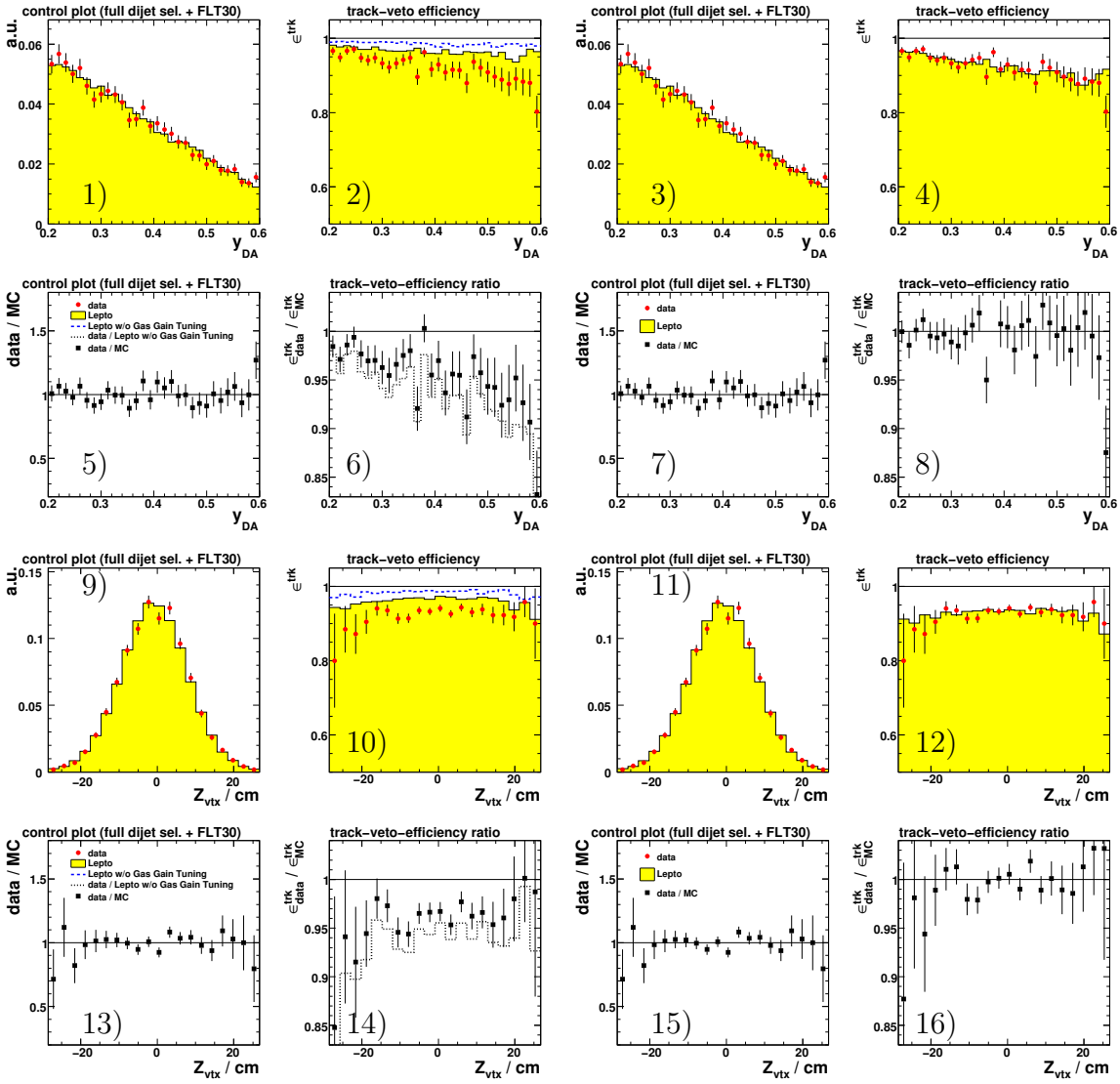

Figure A.20: Study of the 2006/2007 e^+ track veto efficiency as functions of y_{DA} and z_{vtx} for data and LEPTO: 1,3,9,11) Control distributions. 2,4,10,12) The track veto efficiency ϵ^{trk}. 5,7,13,15) Ratio of the individual control distributions. 6,8,14,16) Ratio of the track veto efficiencies $\epsilon^{\mathrm{trk}}_{\mathrm{data}}/\epsilon^{\mathrm{trk}}_{\mathrm{MC}}$. Figures 3,4,7,8,11,12,15,16 show the distributions after applying the track-veto correction.

A.3. Data Unfolding and Theory Corrections

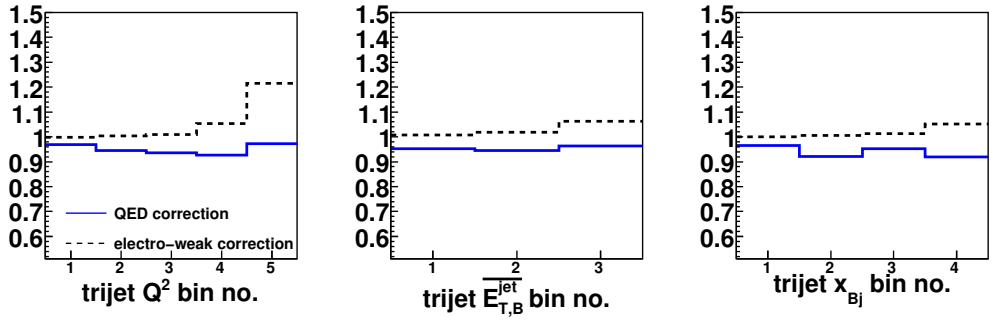

Figure A.21: Electro-weak and QED corrections for the inclusive trijet cross-sections $\frac{d\sigma}{dQ^2}$, $\frac{d\sigma}{d\overline{E}^{\mathrm{jet}}_{T,\mathrm{B}}}$ and $\frac{d\sigma}{dx_{Bj}}$. The fluctuation in the last Q^2 bin is caused by a limited MC statistic. However, the total experimental uncertainty of the data in that bin is about 23%.

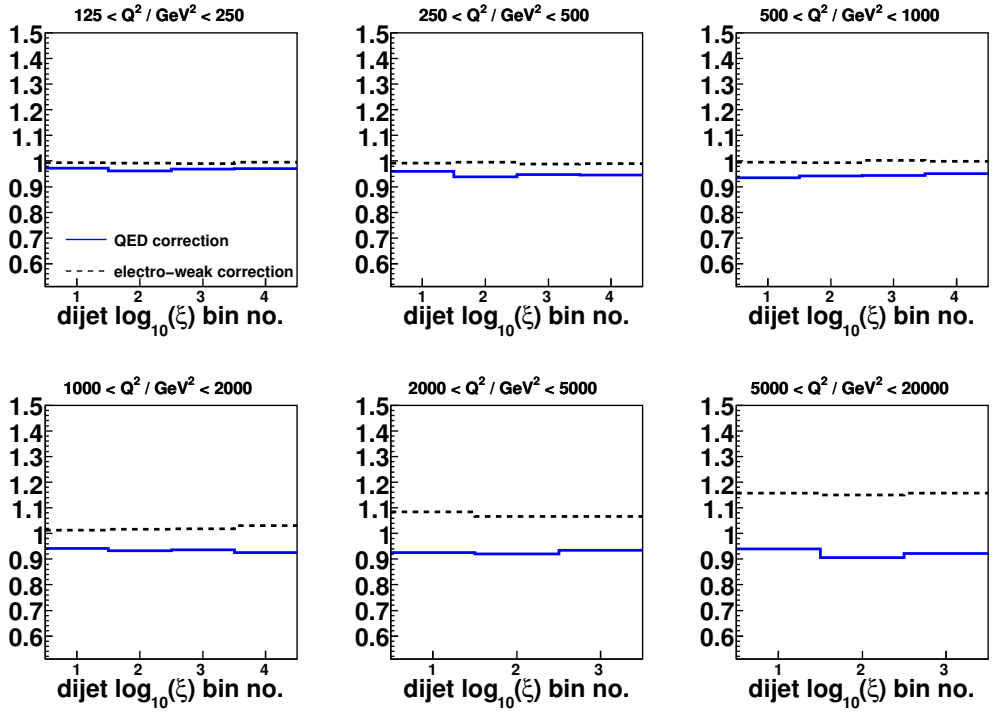

Figure A.22: Electro-weak and QED corrections for the inclusive dijet cross-sections $\frac{d\sigma}{d\log_{10}(\xi)}$ in several regions of Q^2.

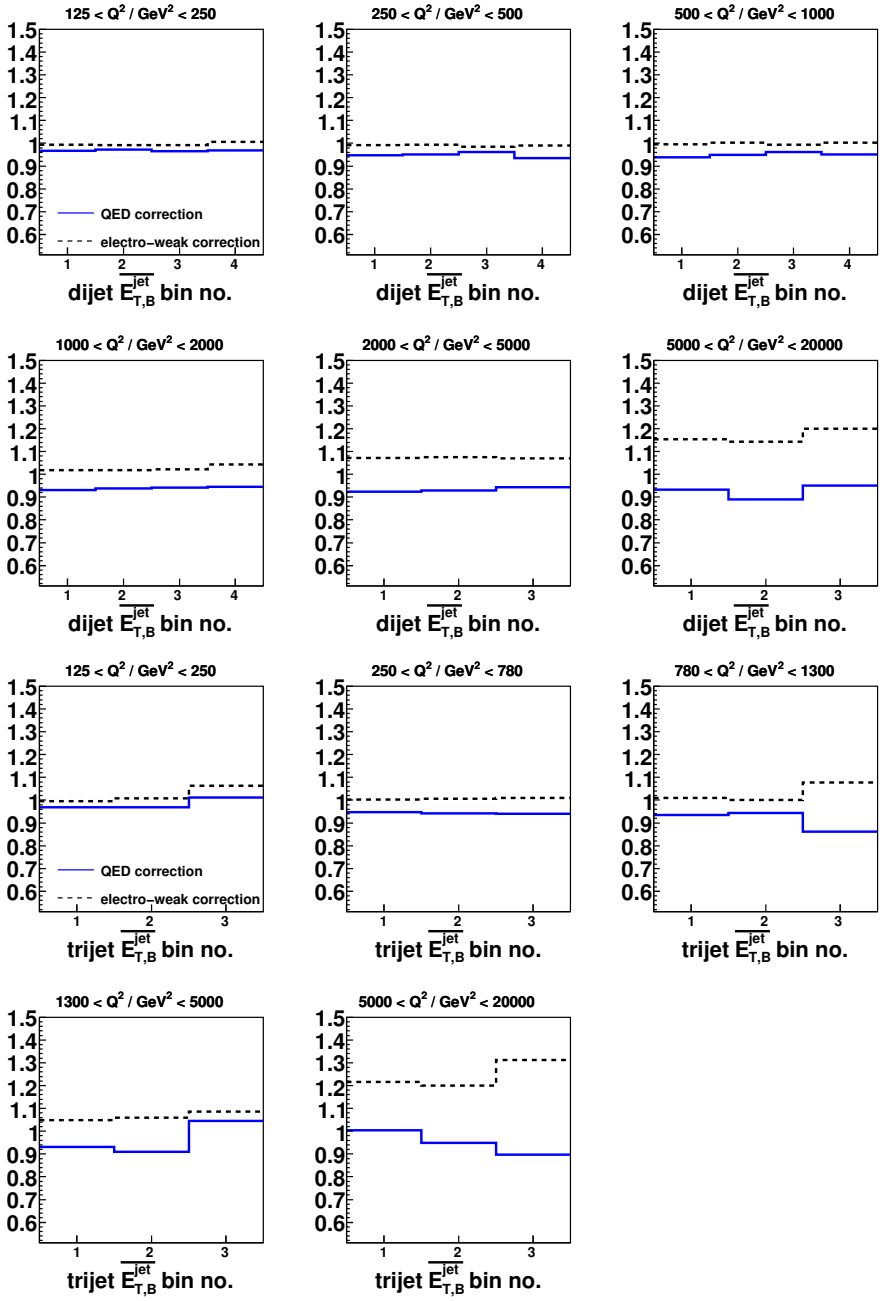

Figure A.23: Electro-weak and QED corrections for the inclusive dijet and trijet cross-sections $\frac{d\sigma}{dE^{\mathrm{jet}}_{T,\mathrm{B}}}$ in several regions of Q^2.

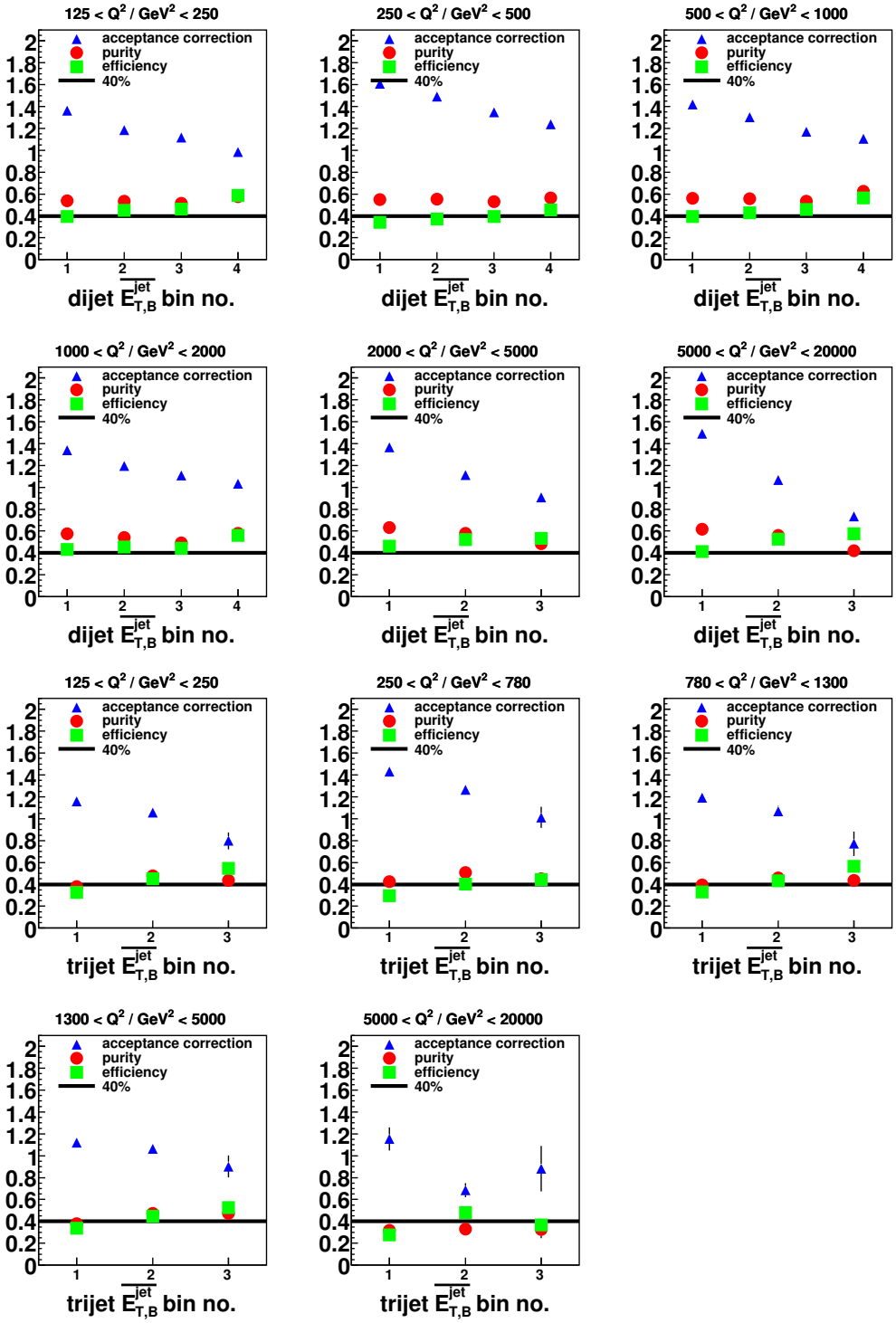

Figure A.24: Efficiencies, purities and acceptance corrections for the inclusive dijet and trijet cross-sections $\frac{d\sigma}{d\overline{E}^{\mathrm{jet}}_{T,\mathrm{B}}}$ in regions of Q^2.

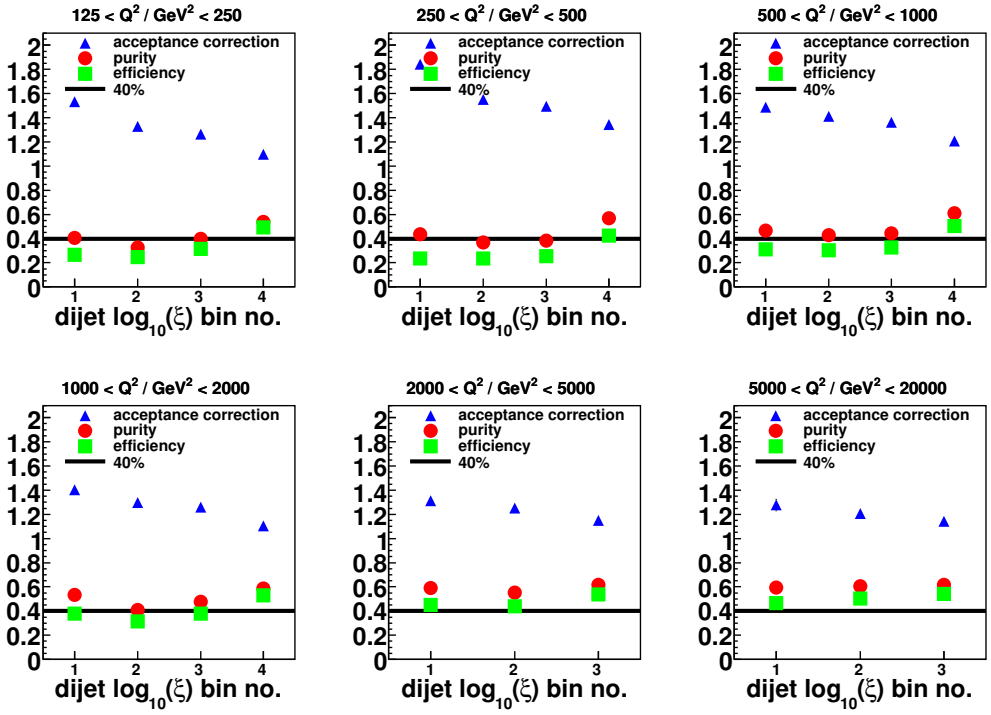

Figure A.25: Efficiencies, purities and acceptance corrections for the inclusive dijet cross-sections $\frac{d\sigma}{d\log_{10}(\xi)}$ in regions of Q^2.

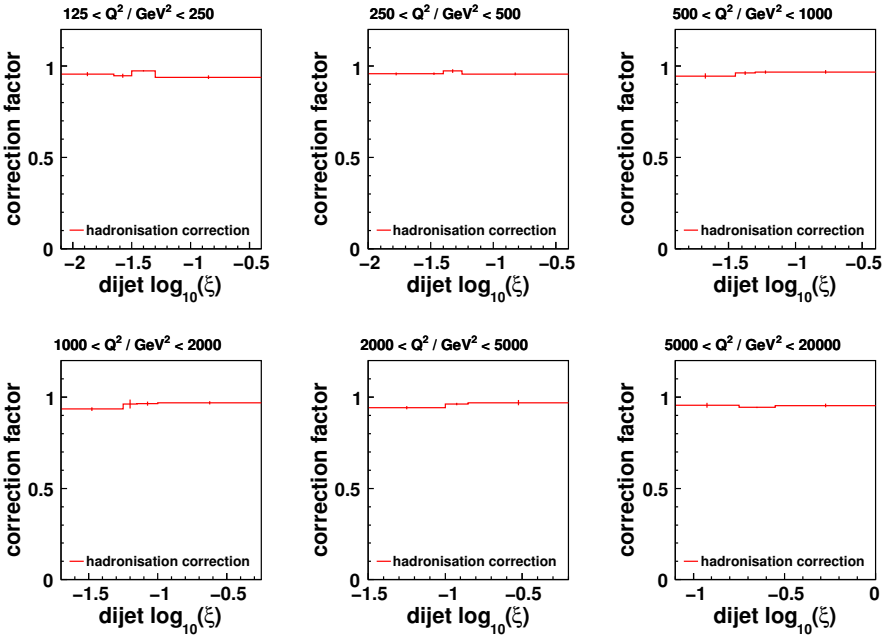

Figure A.26: Hadronisation correction factors for the dijet cross-section $\frac{d\sigma}{d\log_{10}(\xi)}$ in several regions of Q^2.

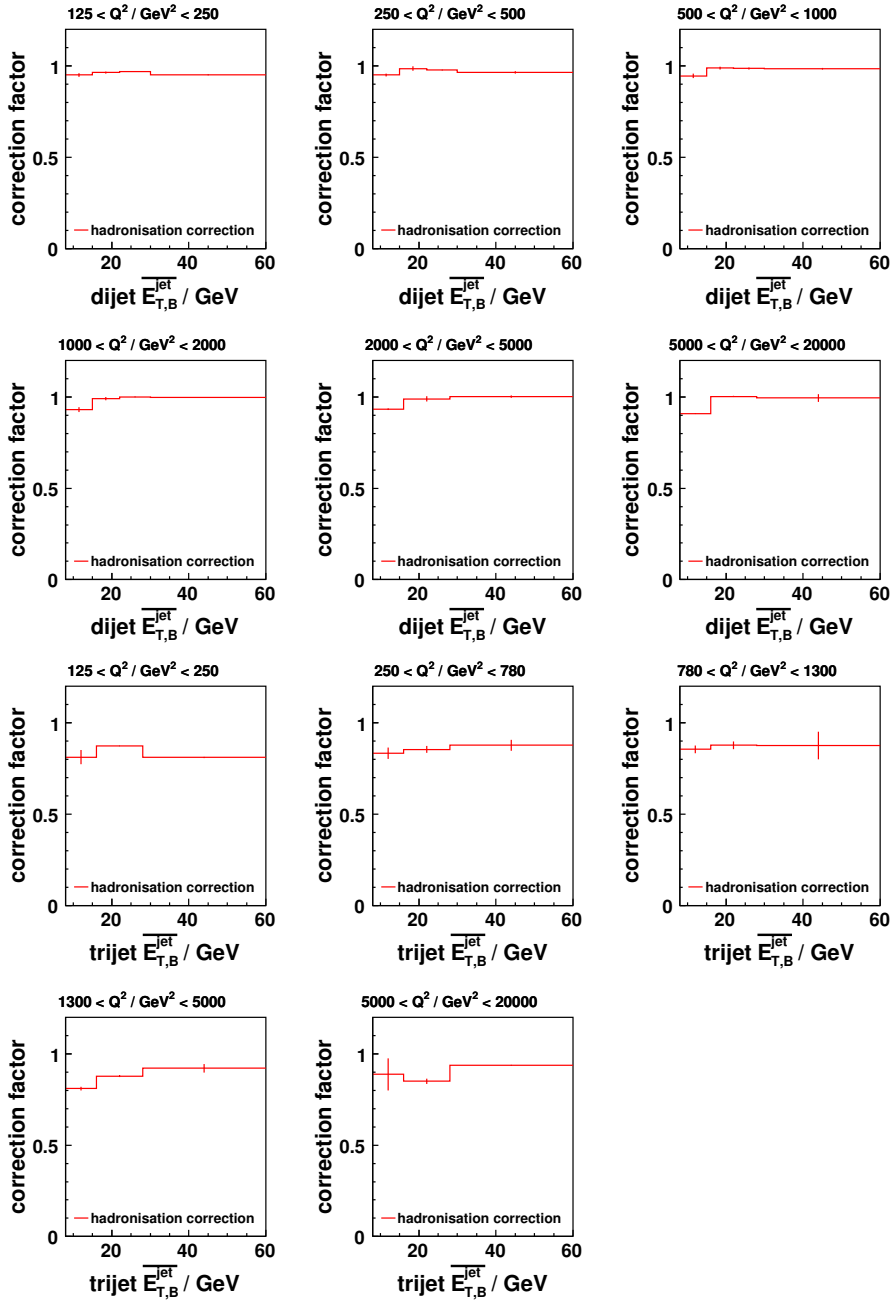

Figure A.27: Hadronisation correction factors for the inclusive dijet and trijet cross-sections $\frac{d\sigma}{d\overline{E}_T}$ in several regions of Q^2.

A.4. Cross-Section Tables

The following tables give the numerical values for the dijet and trijet cross sections presented in the previous chapter 9. The numerical values for the cross section ratio, $R_{3/2}$, are also given.

Q^2 bin $\left(\mathrm{GeV}^2\right)$	$d\sigma/dQ^2$ $(\mathrm{pb}/\mathrm{GeV}^2)$	δ_{stat}	δ_{syst}	δ_{ES}	C_{QED}	$C_{\mathrm{hadr}} \cdot C_{\mathrm{Z}^0}$
125 ... 250	0.3843	± 0.0036	$^{+0.0039}_{-0.0040}$	$^{+0.0215}_{-0.0195}$	0.97	0.95
250 ... 500	0.1193	± 0.0015	$^{+0.0019}_{-0.0018}$	$^{+0.0055}_{-0.0052}$	0.95	0.96
500 ... 1000	0.03372	± 0.00053	$^{+0.00065}_{-0.00065}$	$^{+0.00135}_{-0.00115}$	0.94	0.96
1000 ... 2000	0.00855	± 0.00018	$^{+0.00010}_{-0.00010}$	$^{+0.00029}_{-0.00026}$	0.93	0.98
2000 ... 5000	0.001523	± 0.000043	$^{+0.000033}_{-0.000033}$	$^{+0.000030}_{-0.000034}$	0.93	1.03
5000 ... 20000	0.0000875	± 0.0000046	$^{+0.0000058}_{-0.0000057}$	$^{+0.0000014}_{-0.0000015}$	0.92	1.09

Table A.1: The measured differential cross-section $\mathrm{d}\sigma/\mathrm{d}Q^2$ for inclusive dijet production. The statistical, uncorrelated systematic and jet-energy-scale (ES) uncertainties are shown separately. The multiplicative corrections, C_{QED}, which have been applied to the data and the corrections for hadronisation and Z^0 effects to be applied to the parton-level NLO QCD calculations, $C_{\mathrm{hadr}} \cdot C_{\mathrm{Z}^0}$, are shown in the last two columns.

x_{Bj} bin	$d\sigma/dx_{\mathrm{Bj}}$ (pb)	δ_{stat}	δ_{syst}	δ_{ES}	C_{QED}	$C_{\mathrm{hadr}} \cdot C_{\mathrm{Z}^0}$
0.0001 ... 0.01	6580	± 54	$^{+44}_{-45}$	$^{+351}_{-317}$	0.96	0.95
0.01 ... 0.02	2229	± 31	$^{+44}_{-44}$	$^{+98}_{-94}$	0.94	0.95
0.02 ... 0.035	711	± 14	$^{+19}_{-20}$	$^{+27}_{-23}$	0.94	0.96
0.035 ... 0.07	193.8	± 4.6	$^{+2.8}_{-2.5}$	$^{+6.1}_{-5.7}$	0.93	0.99
0.07 ... 0.1	64.4	± 2.8	$^{+3.8}_{-3.8}$	$^{+1.0}_{-1.4}$	0.92	1.03

Table A.2: Inclusive dijet cross-sections $d\sigma/dx_{\mathrm{Bj}}$. Other details as in the caption to Table A.1.

$\overline{E_{T,\mathrm{B}}^{\mathrm{jet}}}$ bin (GeV)	$d\sigma/d\overline{E_{T,\mathrm{B}}^{\mathrm{jet}}}$ (pb/GeV)	δ_{stat}	δ_{syst}	δ_{ES}	C_{QED}	$C_{\mathrm{hadr}} \cdot C_{\mathrm{Z^0}}$
8 ... 15	10.65	± 0.083	$^{+0.174}_{-0.174}$	$^{+0.549}_{-0.495}$	0.95	0.95
15 ... 22	3.595	± 0.046	$^{+0.060}_{-0.062}$	$^{+0.142}_{-0.134}$	0.95	0.98
22 ... 30	0.848	± 0.020	$^{+0.011}_{-0.010}$	$^{+0.025}_{-0.026}$	0.95	0.99
30 ... 60	0.0896	± 0.0031	$^{+0.0027}_{-0.0027}$	$^{+0.0041}_{-0.0038}$	0.95	0.99

Table A.3: Inclusive dijet cross-sections $d\sigma/d\overline{E_{T,\mathrm{B}}^{\mathrm{jet}}}$. Other details as in the caption to Table A.1.

M_{jj} bin (GeV)	$d\sigma/dM_{jj}$ (pb/GeV)	δ_{stat}	δ_{syst}	δ_{ES}	C_{QED}	$C_{\mathrm{hadr}} \cdot C_{\mathrm{Z^0}}$
20 ... 30	5.048	± 0.049	$^{+0.079}_{-0.079}$	$^{+0.236}_{-0.212}$	0.95	0.95
30 ... 45	2.693	± 0.028	$^{+0.038}_{-0.038}$	$^{+0.130}_{-0.121}$	0.95	0.97
45 ... 65	0.726	± 0.012	$^{+0.009}_{-0.010}$	$^{+0.031}_{-0.029}$	0.95	0.98
65 ... 120	0.0681	± 0.0020	$^{+0.0005}_{-0.0005}$	$^{+0.0032}_{-0.0031}$	0.95	0.97

Table A.4: Inclusive dijet cross-sections $d\sigma/dM_{jj}$. Other details as in the caption to Table A.1.

$\log_{10}(\xi)$ bin	$d\sigma/d\log_{10}(\xi)$ (pb)	δ_{stat}	δ_{syst}	δ_{ES}	C_{QED}	$C_{\mathrm{hadr}} \cdot C_{\mathrm{Z^0}}$
-2 ... -1.6	62.63	± 0.91	$^{+0.81}_{-0.86}$	$^{+3.27}_{-2.83}$	0.97	0.95
-1.6 ... -1.45	143.3	± 2.1	$^{+2.5}_{-2.5}$	$^{+7.1}_{-6.6}$	0.96	0.95
-1.45 ... -1.3	143.0	± 2.1	$^{+1.0}_{-0.8}$	$^{+7.3}_{-6.1}$	0.95	0.96
-1.3 ... -1.1	109.9	± 1.5	$^{+2.9}_{-3.0}$	$^{+4.9}_{-4.9}$	0.95	0.96
-1.1 ... 0	17.40	± 0.24	$^{+0.11}_{-0.13}$	$^{+0.65}_{-0.63}$	0.94	0.98

Table A.5: Inclusive dijet cross-sections $d\sigma/d\log_{10}(\xi)$. Other details as in the caption to Table A.1.

η^* bin	$d\sigma/d\eta^*$ (pb)	δ_{stat}	δ_{syst}	δ_{ES}	C_{QED}	$C_{\mathrm{hadr}} \cdot C_{\mathrm{Z^0}}$
0 ... 0.2	106.1	± 1.6	$^{+0.9}_{-0.8}$	$^{+4.3}_{-3.8}$	0.95	0.96
0.2 ... 0.4	105.4	± 1.6	$^{+0.9}_{-0.9}$	$^{+4.3}_{-4.1}$	0.95	0.96
0.4 ... 0.65	101.0	± 1.4	$^{+0.6}_{-0.7}$	$^{+4.1}_{-4.0}$	0.96	0.97
0.65 ... 0.95	78.2	± 1.1	$^{+0.3}_{-0.4}$	$^{+4.0}_{-3.3}$	0.95	0.98
0.95 ... 2	17.14	± 0.27	$^{+0.42}_{-0.42}$	$^{+1.06}_{-1.02}$	0.95	0.93

Table A.6: Inclusive dijet cross-sections $d\sigma/d\eta^*$. Other details as in the caption to Table A.1.

$\log_{10}(\xi)$ bin	$d\sigma/d\log_{10}(\xi)$ (pb)	δ_{stat}	δ_{syst}	δ_{ES}	C_{QED}	$C_{\text{hadr}} \cdot C_{\text{Z}^0}$
$125 < Q^2 < 250$ GeV^2						
$-2.1 \ldots -1.65$	30.34	± 0.60	$^{+0.51}_{-0.55}$	$^{+1.58}_{-1.38}$	0.97	0.95
$-1.65 \ldots -1.5$	76.2	± 1.5	$^{+1.0}_{-0.9}$	$^{+4.5}_{-4.0}$	0.96	0.94
$-1.5 \ldots -1.3$	63.2	± 1.2	$^{+1.1}_{-1.0}$	$^{+3.8}_{-3.3}$	0.97	0.97
$-1.3 \ldots -0.4$	11.53	± 0.22	$^{+0.31}_{-0.33}$	$^{+0.60}_{-0.61}$	0.97	0.94
$250 < Q^2 < 500$ GeV^2						
$-2 \ldots -1.55$	19.93	± 0.52	$^{+0.29}_{-0.27}$	$^{+0.82}_{-0.71}$	0.96	0.95
$-1.55 \ldots -1.4$	48.2	± 1.3	$^{+2.1}_{-2.1}$	$^{+2.3}_{-2.2}$	0.94	0.96
$-1.4 \ldots -1.25$	42.8	± 1.2	$^{+0.5}_{-0.4}$	$^{+2.1}_{-1.9}$	0.95	0.96
$-1.25 \ldots -0.4$	8.56	± 0.21	$^{+0.13}_{-0.14}$	$^{+0.40}_{-0.41}$	0.95	0.95
$500 < Q^2 < 1000$ GeV^2						
$-1.9 \ldots -1.45$	8.21	± 0.29	$^{+0.22}_{-0.19}$	$^{+0.29}_{-0.27}$	0.94	0.94
$-1.45 \ldots -1.3$	28.32	± 0.93	$^{+0.74}_{-0.72}$	$^{+1.10}_{-0.76}$	0.94	0.96
$-1.3 \ldots -1.15$	29.11	± 0.93	$^{+1.23}_{-1.27}$	$^{+1.22}_{-1.02}$	0.94	0.97
$-1.15 \ldots -0.4$	6.00	± 0.17	$^{+0.07}_{-0.08}$	$^{+0.26}_{-0.25}$	0.95	0.97
$1000 < Q^2 < 2000$ GeV^2						
$-1.7 \ldots -1.25$	4.91	± 0.22	$^{+0.16}_{-0.16}$	$^{+0.13}_{-0.15}$	0.94	0.95
$-1.25 \ldots -1.15$	15.52	± 0.80	$^{+0.64}_{-0.63}$	$^{+0.80}_{-0.27}$	0.93	0.98
$-1.15 \ldots -1$	16.87	± 0.68	$^{+0.10}_{-0.15}$	$^{+0.41}_{-0.58}$	0.94	0.98
$-1 \ldots -0.25$	2.97	± 0.12	$^{+0.06}_{-0.06}$	$^{+0.11}_{-0.10}$	0.93	1.00
$2000 < Q^2 < 5000$ GeV^2						
$-1.5 \ldots -1$	3.11	± 0.16	$^{+0.07}_{-0.08}$	$^{+0.04}_{-0.06}$	0.93	1.03
$-1 \ldots -0.85$	9.07	± 0.48	$^{+0.26}_{-0.28}$	$^{+0.12}_{-0.18}$	0.92	1.03
$-0.85 \ldots -0.2$	2.54	± 0.12	$^{+0.09}_{-0.09}$	$^{+0.08}_{-0.07}$	0.93	1.04
$5000 < Q^2 < 20000$ GeV^2						
$-1.1 \ldots -0.75$	0.865	± 0.099	$^{+0.065}_{-0.065}$	$^{+0.011}_{-0.013}$	0.94	1.10
$-0.75 \ldots -0.55$	2.85	± 0.23	$^{+0.10}_{-0.10}$	$^{+0.02}_{-0.03}$	0.91	1.08
$-0.55 \ldots 0$	0.794	± 0.071	$^{+0.092}_{-0.090}$	$^{+0.023}_{-0.020}$	0.92	1.10

Table A.7: Inclusive dijet cross-sections $d\sigma/d\log_{10}(\xi)$ in different regions of Q^2. Other details as in the caption to Table A.1.

$\overline{E^{\text{jet}}_{T,\text{B}}}$ bin (GeV)	$d\sigma/\overline{E^{\text{jet}}_{T,\text{B}}}$ (pb/GeV)	δ_{stat}	δ_{syst}	δ_{ES}	C_{QED}	$C_{\text{hadr}} \cdot C_{\text{Z}^0}$
$125 < Q^2 < 250$ GeV^2						
8 ... 15	5.050	± 0.057	$^{+0.071}_{-0.070}$	$^{+0.311}_{-0.274}$	0.97	0.95
15 ... 22	1.385	± 0.028	$^{+0.037}_{-0.038}$	$^{+0.063}_{-0.062}$	0.97	0.96
22 ... 30	0.292	± 0.012	$^{+0.012}_{-0.013}$	$^{+0.009}_{-0.010}$	0.97	0.96
30 ... 60	0.0241	± 0.0016	$^{+0.0009}_{-0.0008}$	$^{+0.0011}_{-0.0010}$	0.97	0.95
$250 < Q^2 < 500$ GeV^2						
8 ... 15	2.937	± 0.046	$^{+0.076}_{-0.076}$	$^{+0.146}_{-0.141}$	0.95	0.95
15 ... 22	0.998	± 0.026	$^{+0.011}_{-0.011}$	$^{+0.040}_{-0.035}$	0.95	0.98
22 ... 30	0.215	± 0.011	$^{+0.008}_{-0.008}$	$^{+0.006}_{-0.008}$	0.96	0.97
30 ... 60	0.0195	± 0.0016	$^{+0.0015}_{-0.0015}$	$^{+0.0010}_{-0.0006}$	0.93	0.95
$500 < Q^2 < 1000$ GeV^2						
8 ... 15	1.502	± 0.031	$^{+0.055}_{-0.054}$	$^{+0.064}_{-0.052}$	0.94	0.95
15 ... 22	0.629	± 0.019	$^{+0.008}_{-0.009}$	$^{+0.023}_{-0.021}$	0.95	0.99
22 ... 30	0.1665	± 0.0089	$^{+0.0041}_{-0.0041}$	$^{+0.0054}_{-0.0040}$	0.96	0.98
30 ... 60	0.0194	± 0.0015	$^{+0.0010}_{-0.0010}$	$^{+0.0007}_{-0.0010}$	0.95	0.99
$1000 < Q^2 < 2000$ GeV^2						
8 ... 15	0.701	± 0.020	$^{+0.017}_{-0.017}$	$^{+0.025}_{-0.022}$	0.93	0.95
15 ... 22	0.352	± 0.014	$^{+0.012}_{-0.013}$	$^{+0.011}_{-0.009}$	0.94	1.01
22 ... 30	0.0943	± 0.0064	$^{+0.0063}_{-0.0063}$	$^{+0.0025}_{-0.0026}$	0.94	1.02
30 ... 60	0.0136	± 0.0012	$^{+0.0003}_{-0.0004}$	$^{+0.0006}_{-0.0007}$	0.94	1.04
$2000 < Q^2 < 5000$ GeV^2						
8 ... 16	0.350	± 0.013	$^{+0.009}_{-0.009}$	$^{+0.004}_{-0.007}$	0.92	1.00
16 ... 28	0.1191	± 0.0058	$^{+0.0023}_{-0.0022}$	$^{+0.0030}_{-0.0023}$	0.93	1.07
28 ... 60	0.01040	± 0.00097	$^{+0.00053}_{-0.00049}$	$^{+0.00044}_{-0.00046}$	0.94	1.08
$5000 < Q^2 < 20000$ GeV^2						
8 ... 16	0.0995	± 0.0076	$^{+0.0092}_{-0.0092}$	$^{+0.0012}_{-0.0005}$	0.93	1.05
16 ... 28	0.0354	± 0.0031	$^{+0.0023}_{-0.0021}$	$^{+0.0003}_{-0.0008}$	0.89	1.14
28 ... 60	0.00368	± 0.00053	$^{+0.00015}_{-0.00023}$	$^{+0.00016}_{-0.00012}$	0.95	1.20

Table A.8: Inclusive dijet cross-sections $d\sigma/d\overline{E^{\text{jet}}_{T,\text{B}}}$ in different regions of Q^2. Other details as in the caption to Table A.1.

Q^2 bin $\left(\mathrm{GeV}^2\right)$	$d\sigma/dQ^2$ $(\mathrm{pb}/\mathrm{GeV}^2)$	δ_{stat}	δ_{syst}	δ_{ES}	C_{QED}	$C_{\mathrm{hadr}} \cdot C_{\mathrm{Z}^0}$
125 ... 250	0.02788	± 0.00094	$^{+0.00117}_{-0.00117}$	$^{+0.00303}_{-0.00251}$	0.97	0.83
250 ... 700	0.00742	± 0.00027	$^{+0.00087}_{-0.00086}$	$^{+0.00068}_{-0.00066}$	0.95	0.84
700 ... 1300	0.00182	± 0.00011	$^{+0.00017}_{-0.00017}$	$^{+0.00017}_{-0.00014}$	0.94	0.87
1300 ... 5000	0.000192	± 0.000013	$^{+0.000024}_{-0.000024}$	$^{+0.000012}_{-0.000010}$	0.93	0.89
5000 ... 20000	0.0000102	± 0.0000015	$^{+0.0000017}_{-0.0000016}$	$^{+0.0000003}_{-0.0000003}$	0.97	1.05

Table A.9: Inclusive trijet cross-sections $d\sigma/dQ^2$. Other details as in the caption to Table A.1.

x_{Bj} bin	$d\sigma/dx_{\mathrm{Bj}}$ (pb)	δ_{stat}	δ_{syst}	δ_{ES}	C_{QED}	$C_{\mathrm{hadr}} \cdot C_{\mathrm{Z}^0}$
0.0001 ... 0.01	533	± 15	$^{+42}_{-41}$	$^{+54}_{-48}$	0.97	0.84
0.01 ... 0.02	176.4	± 8.4	$^{+12.3}_{-12.4}$	$^{+16.4}_{-15.7}$	0.92	0.85
0.02 ... 0.04	51.3	± 3.1	$^{+6.4}_{-6.4}$	$^{+4.9}_{-3.6}$	0.95	0.86
0.04 ... 0.1	8.24	± 0.66	$^{+0.95}_{-0.95}$	$^{+0.49}_{-0.49}$	0.92	0.85

Table A.10: Inclusive trijet cross-sections $d\sigma/dx_{\mathrm{Bj}}$. Other details as in the caption to Table A.1.

$\overline{E^{\mathrm{jet}}_{T,\mathrm{B}}}$ bin (GeV)	$d\sigma/d\overline{E^{\mathrm{jet}}_{T,\mathrm{B}}}$ $(\mathrm{pb}/\mathrm{GeV})$	δ_{stat}	δ_{syst}	δ_{ES}	C_{QED}	$C_{\mathrm{hadr}} \cdot C_{\mathrm{Z}^0}$
8 ... 16	0.734	± 0.020	$^{+0.049}_{-0.049}$	$^{+0.078}_{-0.066}$	0.95	0.83
16 ... 28	0.2139	± 0.0081	$^{+0.0211}_{-0.0211}$	$^{+0.0150}_{-0.0146}$	0.94	0.88
28 ... 60	0.00819	± 0.00092	$^{+0.00040}_{-0.00032}$	$^{+0.00063}_{-0.00061}$	0.96	0.91

Table A.11: Inclusive trijet cross-sections $d\sigma/d\overline{E^{\mathrm{jet}}_{T,\mathrm{B}}}$. Other details as in the caption to Table A.1.

$\overline{E^{\text{jet}}_{T,\text{B}}}$ bin (GeV)	$d\sigma/\overline{E^{\text{jet}}_{T,\text{B}}}$ (pb/GeV)	δ_{stat}	δ_{syst}	δ_{ES}	C_{QED}	$C_{\text{hadr}} \cdot C_{\text{Z}^0}$
$125 < Q^2 < 250$ GeV^2						
8 ... 16	0.319	± 0.013	$^{+0.011}_{-0.011}$	$^{+0.040}_{-0.032}$	0.97	0.81
16 ... 28	0.0730	± 0.0047	$^{+0.0032}_{-0.0032}$	$^{+0.0052}_{-0.0050}$	0.97	0.88
28 ... 60	0.00189	± 0.00043	$^{+0.00021}_{-0.00018}$	$^{+0.00017}_{-0.00008}$	1.01	0.86
$250 < Q^2 < 700$ GeV^2						
8 ... 16	0.281	± 0.013	$^{+0.025}_{-0.025}$	$^{+0.028}_{-0.027}$	0.95	0.84
16 ... 28	0.0821	± 0.0054	$^{+0.0133}_{-0.0133}$	$^{+0.0065}_{-0.0065}$	0.94	0.86
28 ... 60	0.00262	± 0.00056	$^{+0.00011}_{-0.00019}$	$^{+0.00009}_{-0.00014}$	0.94	0.88
$700 < Q^2 < 1300$ GeV^2						
8 ... 16	0.0755	± 0.0060	$^{+0.0090}_{-0.0089}$	$^{+0.0073}_{-0.0068}$	0.93	0.86
16 ... 28	0.0343	± 0.0033	$^{+0.0015}_{-0.0019}$	$^{+0.0029}_{-0.0019}$	0.94	0.88
28 ... 60	0.00156	± 0.00039	$^{+0.00013}_{-0.00012}$	$^{+0.00013}_{-0.00015}$	0.86	0.94
$1300 < Q^2 < 5000$ GeV^2						
8 ... 16	0.0492	± 0.0046	$^{+0.0061}_{-0.0061}$	$^{+0.0036}_{-0.0019}$	0.93	0.86
16 ... 28	0.0219	± 0.0024	$^{+0.0036}_{-0.0037}$	$^{+0.0011}_{-0.0014}$	0.91	0.93
28 ... 60	0.00166	± 0.00043	$^{+0.00016}_{-0.00013}$	$^{+0.00015}_{-0.00019}$	1.04	0.99
$5000 < Q^2 < 20000$ GeV^2						
8 ... 16	0.0117	± 0.0025	$^{+0.0027}_{-0.0028}$	$^{+0.0005}_{-0.0001}$	1.00	1.07
16 ... 28	0.00407	± 0.00089	$^{+0.00049}_{-0.00044}$	$^{+0.00005}_{-0.00017}$	0.95	1.01
28 ... 60	0.00040	± 0.00020	$^{+0.00029}_{-0.00027}$	$^{+0.00006}_{-0.00006}$	0.90	1.23

Table A.12: Inclusive trijet cross-sections $d\sigma/d\overline{E^{\text{jet}}_{T,\text{B}}}$ in different regions of Q^2. Other details as in the caption to Table A.1.

$\overline{E^{\text{jet}}_{T,\text{B}}}$ bin (GeV)	$d\sigma/\overline{E^{\text{jet}}_{T,\text{B}}}$ (pb/GeV)	δ_{stat}	δ_{syst}	δ_{ES}	C_{QED}	$C_{\text{hadr}} \cdot C_{\text{Z}^0}$
$125 < Q^2 < 250$ GeV^2						
8 ... 16	4.719	± 0.051	$^{+0.080}_{-0.080}$	$^{+0.287}_{-0.258}$	0.97	0.95
16 ... 28	0.774	± 0.016	$^{+0.007}_{-0.008}$	$^{+0.031}_{-0.030}$	0.97	0.96
28 ... 60	0.0325	± 0.0018	$^{+0.0007}_{-0.0007}$	$^{+0.0015}_{-0.0013}$	0.96	0.96
$250 < Q^2 < 700$ GeV^2						
8 ... 16	3.612	± 0.047	$^{+0.069}_{-0.067}$	$^{+0.172}_{-0.156}$	0.94	0.95
16 ... 28	0.781	± 0.017	$^{+0.009}_{-0.008}$	$^{+0.029}_{-0.031}$	0.96	0.98
28 ... 60	0.0361	± 0.0021	$^{+0.0010}_{-0.0010}$	$^{+0.0017}_{-0.0014}$	0.94	0.96
$700 < Q^2 < 1300$ GeV^2						
8 ... 16	0.944	± 0.022	$^{+0.031}_{-0.031}$	$^{+0.036}_{-0.027}$	0.94	0.95
16 ... 28	0.2662	± 0.0090	$^{+0.0116}_{-0.0118}$	$^{+0.0096}_{-0.0102}$	0.95	1.00
28 ... 60	0.0176	± 0.0013	$^{+0.0006}_{-0.0007}$	$^{+0.0005}_{-0.0006}$	0.93	0.99
$1300 < Q^2 < 5000$ GeV^2						
8 ... 16	0.699	± 0.019	$^{+0.003}_{-0.003}$	$^{+0.016}_{-0.016}$	0.93	0.98
16 ... 28	0.2353	± 0.0083	$^{+0.0054}_{-0.0055}$	$^{+0.0061}_{-0.0052}$	0.93	1.04
28 ... 60	0.0197	± 0.0014	$^{+0.0005}_{-0.0004}$	$^{+0.0008}_{-0.0008}$	0.95	1.08
$5000 < Q^2 < 20000$ GeV^2						
8 ... 16	0.1067	± 0.0079	$^{+0.0098}_{-0.0098}$	$^{+0.0012}_{-0.0005}$	1.00	1.05
16 ... 28	0.0398	± 0.0033	$^{+0.0025}_{-0.0023}$	$^{+0.0004}_{-0.0009}$	1.00	1.14
28 ... 60	0.00387	± 0.00053	$^{+0.00016}_{-0.00025}$	$^{+0.00017}_{-0.00013}$	1.00	1.20

Table A.13: Inclusive dijet cross-sections $d\sigma/d\overline{E^{\text{jet}}_{T,\text{B}}}$ in different regions of Q^2. These cross-section values were used in the determination of $R_{3/2}$. Other details as in the caption to Table A.1.

$\overline{E_{T,\mathrm{B}}^{\mathrm{jet}}}$ bin (GeV)	$R_{3/2}$	δ_{stat}	δ_{syst}	δ_{ES}	C_{QED}	$C_{\mathrm{hadr}} \cdot C_{\mathrm{Z^0}}$
$125 < Q^2 < 250$ GeV^2						
8 ... 16	0.0675	± 0.0026	$^{+0.0028}_{-0.0028}$	$^{+0.0040}_{-0.0032}$	1.00	0.85
16 ... 28	0.0943	± 0.0057	$^{+0.0045}_{-0.0045}$	$^{+0.0029}_{-0.0030}$	1.00	0.92
28 ... 60	0.058	± 0.012	$^{+0.006}_{-0.006}$	$^{+0.002}_{-0.001}$	1.05	0.90
$250 < Q^2 < 700$ GeV^2						
8 ... 16	0.0779	± 0.0034	$^{+0.0080}_{-0.0080}$	$^{+0.0038}_{-0.0042}$	1.00	0.88
16 ... 28	0.1051	± 0.0065	$^{+0.0174}_{-0.0174}$	$^{+0.0043}_{-0.0044}$	0.98	0.87
28 ... 60	0.073	± 0.014	$^{+0.003}_{-0.005}$	$^{+0.001}_{-0.001}$	1.00	0.91
$700 < Q^2 < 1300$ GeV^2						
8 ... 16	0.0799	± 0.0061	$^{+0.0116}_{-0.0115}$	$^{+0.0045}_{-0.0050}$	0.99	0.90
16 ... 28	0.129	± 0.011	$^{+0.011}_{-0.011}$	$^{+0.006}_{-0.002}$	1.00	0.89
28 ... 60	0.089	± 0.020	$^{+0.007}_{-0.004}$	$^{+0.005}_{-0.006}$	0.93	0.95
$1300 < Q^2 < 5000$ GeV^2						
8 ... 16	0.0704	± 0.0064	$^{+0.0088}_{-0.0088}$	$^{+0.0034}_{-0.0011}$	1.00	0.87
16 ... 28	0.0932	± 0.0097	$^{+0.0170}_{-0.0173}$	$^{+0.0021}_{-0.0038}$	0.98	0.89
28 ... 60	0.084	± 0.020	$^{+0.007}_{-0.006}$	$^{+0.004}_{-0.006}$	1.10	0.92
$5000 < Q^2 < 20000$ GeV^2						
8 ... 16	0.109	± 0.024	$^{+0.017}_{-0.020}$	$^{+0.003}_{-0.001}$	1.00	1.02
16 ... 28	0.102	± 0.024	$^{+0.015}_{-0.014}$	$^{+0.001}_{-0.002}$	0.95	0.89
28 ... 60	0.104	± 0.050	$^{+0.078}_{-0.071}$	$^{+0.010}_{-0.013}$	0.90	1.03

Table A.14: The cross-section ratio, $R_{3/2}$, in different regions of Q^2. Other details as in the caption to Table A.1.

A.5. Pixel Telescope

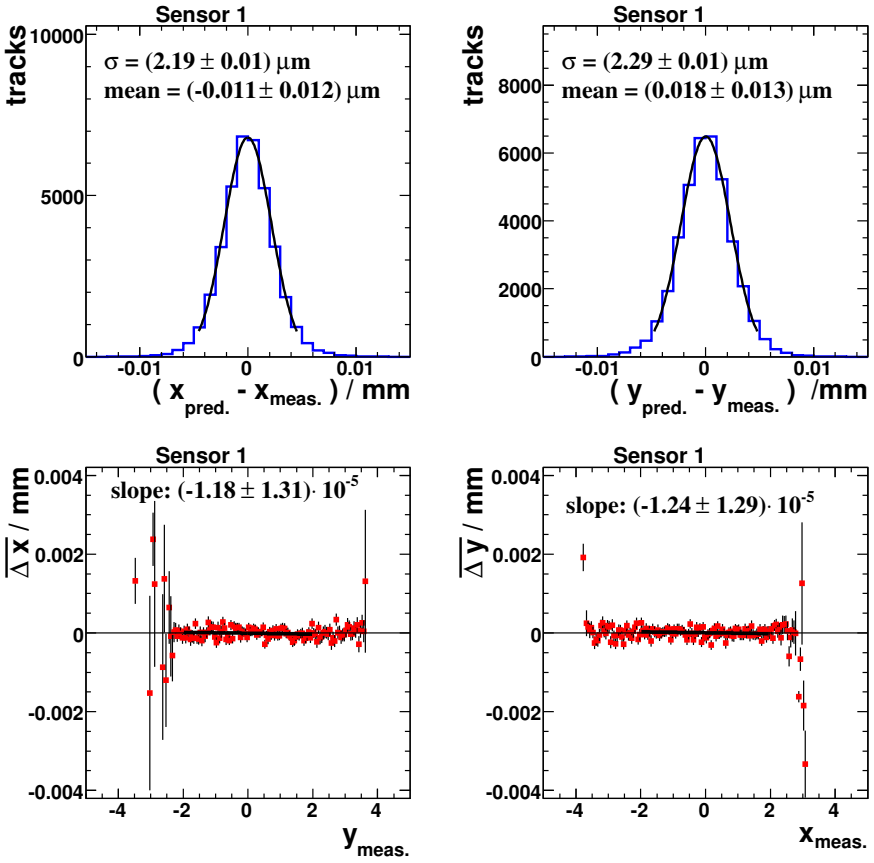

Figure A.28: Investigation of the telescope alignment for sensor 1. Shown are residual plots in x and y direction and $\overline{\Delta x}$ ($\overline{\Delta y}$) as a function of $y_{\text{meas.}}$ ($x_{\text{meas.}}$).

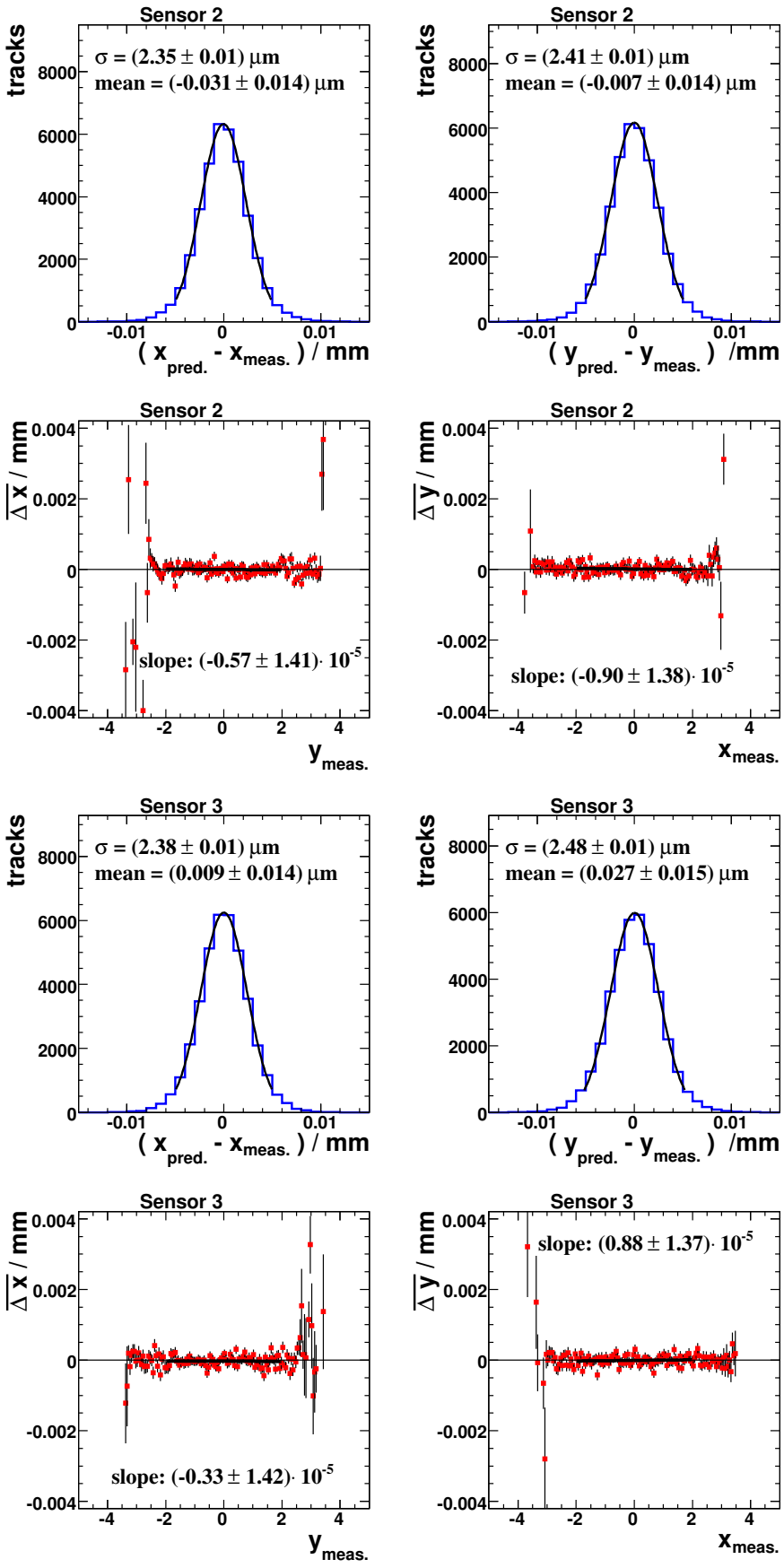

Figure A.29: Investigation of the telescope alignment for the sensors 2 and 3. Shown are residual plots in x and y direction and $\overline{\Delta x}$ ($\overline{\Delta y}$) as a function of $y_{\text{meas.}}$ ($x_{\text{meas.}}$).

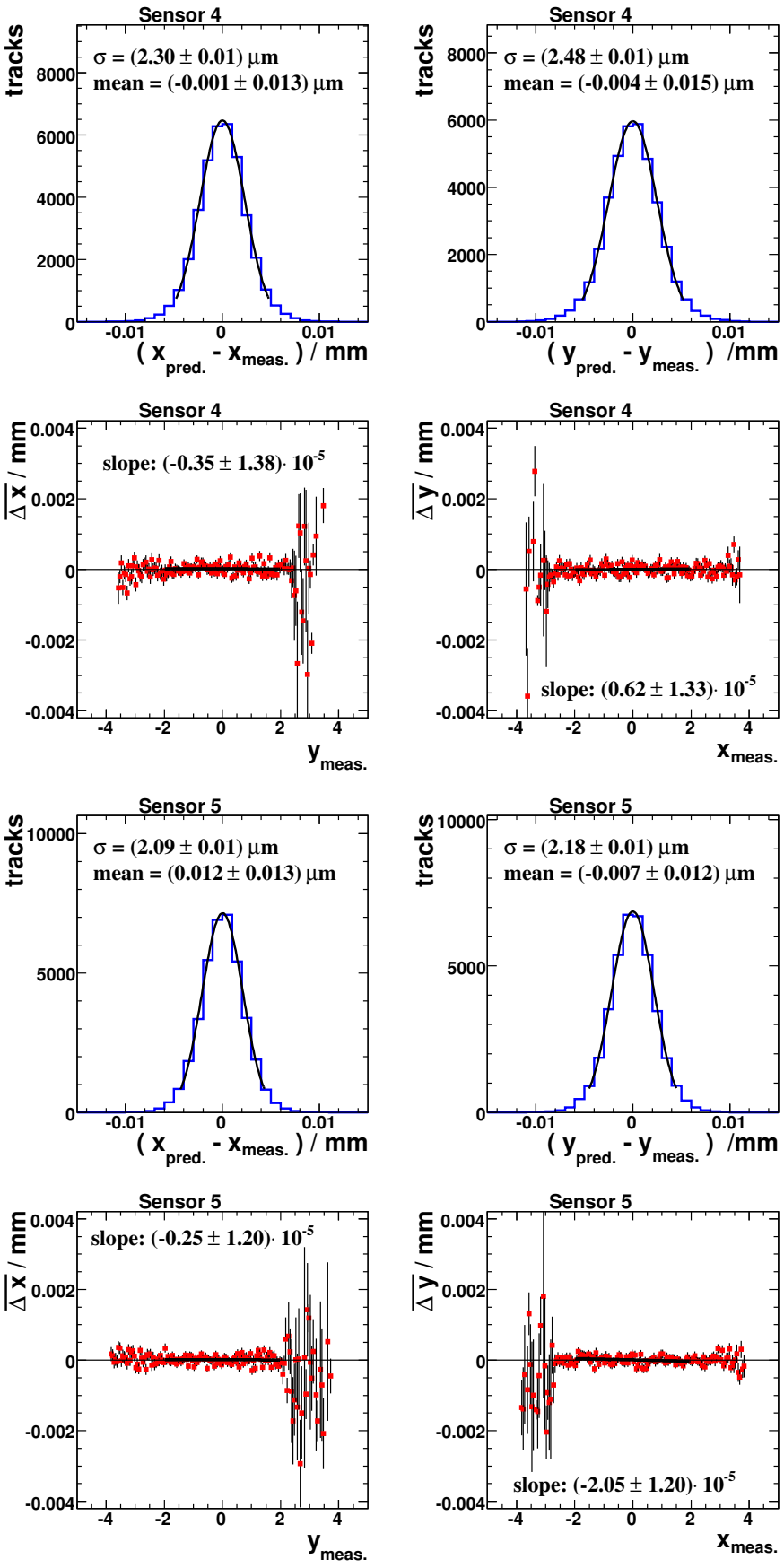

Figure A.30: Investigation of the telescope alignment for the sensors 4 and 5. Shown are residual plots in x and y direction and $\overline{\Delta x}$ ($\overline{\Delta y}$) as a function of $y_{\text{meas.}}$ ($x_{\text{meas.}}$).

Bibliography

[1] H. Geiger and E. Marsden. On a Diffuse Reflection of the α-Particles. *Proceedings of the Royal Society of London. Series A*, 82(557):495–500, 1909. doi:10.1098/rspa.1909.0054.

[2] E. Rutherford. The scattering of α and β particles by matter and the structure of the atom. *Phil. Mag.*, 21:669–688, 1911. doi:10.1080/14786440508637080.

[3] S. Chekanov et al. Inclusive jet cross sections in the Breit frame in neutral current deep inelastic scattering at HERA and determination of α_s. *Phys. Lett.*, B547:164–180, 2002. doi:10.1016/S0370-2693(02)02763-6.

[4] S. Chekanov et al. Jet-radius dependence of inclusive-jet cross sections in deep inelastic scattering at HERA. *Phys. Lett.*, B649:12–24, 2007. doi:10.1016/j.physletb.2007.03.039.

[5] F. D. Aaron et al. Jet Production in ep Collisions at High Q^2 and Determination of α_s. *Eur. Phys. J.*, C65:363–383, 2010. doi:10.1140/epjc/s10052-009-1208-7.

[6] S. Chekanov et al. Scaling violations and determination of α_s from jet production in γp interactions at HERA. *Phys. Lett.*, B560:7–23, 2003. doi:10.1016/S0370-2693(03)00380-0.

[7] A. Aktas et al. Measurement of Inclusive Jet Production in Deep-Inelastic Scattering at High Q^2 and Determination of the Strong Coupling. *Phys. Lett.*, B653:134–144, 2007. doi:10.1016/j.physletb.2007.07.050.

[8] C. Adloff et al. Measurement of inclusive jet cross-sections in deep- inelastic ep scattering at HERA. *Phys. Lett.*, B542:193–206, 2002. doi:10.1016/S0370-2693(02)02375-4.

[9] C. Adloff et al. Measurement of inclusive jet cross-sections in photoproduction at HERA. *Eur. Phys. J.*, C29:497–513, 2003. doi:10.1140/epjc/s2003-01262-9.

[10] A. Aktas et al. Inclusive dijet production at low Bjorken-x in deep inelastic scattering. *Eur. Phys. J.*, C33:477–493, 2004. doi:10.1140/epjc/s2004-01644-5.

[11] S. Chekanov et al. Multijet production in neutral current deep inelastic scattering at HERA and determination of α_s. *Eur. Phys. J.*, C44:183–193, 2005. doi:10.1140/epjc/s2005-02347-1.

[12] S. Chekanov et al. High-E_T dijet photoproduction at HERA. *Phys. Rev.*, D76: 072011, 2007. doi:10.1103/PhysRevD.76.072011.

[13] S. Chekanov et al. Multi-jet cross sections in charged current $e^- p$ scattering at HERA. *Phys. Rev.*, D78:032004, 2008. doi:10.1103/PhysRevD.78.032004.

[14] S. Chekanov et al. Three- and four-jet final states in photoproduction at HERA. *Nucl. Phys.*, B792:1–47, 2008. doi:10.1016/j.nuclphysb.2007.08.021.

[15] S. Chekanov et al. Dijet photoproduction at HERA and the structure of the photon. *Eur. Phys. J.*, C23:615–631, 2002. doi:10.1007/s100520200936.

[16] S. Chekanov et al. Inclusive-jet and dijet cross sections in deep inelastic scattering at HERA. *Nucl. Phys.*, B765:1–30, 2007.

[17] C. Adloff et al. Measurement and QCD analysis of jet cross sections in deep-inelastic positron proton collisions at $\sqrt{s}$ of 300-GeV. *Eur. Phys. J.*, C19:289–311, 2001. doi:10.1007/s100520100621.

[18] J. Breitweg et al. Measurement of dijet production in neutral current deep inelastic scattering at high Q^2 and determination of α_s. *Phys. Lett.*, B507:70–88, 2001. doi:10.1016/S0370-2693(01)00421-X.

[19] H. Abramowicz et al. Inclusive-jet cross sections in NC DIS at HERA and a comparison of the kT, anti-kT and SIScone jet algorithms. 2010.

[20] S. Chekanov et al. Angular correlations in three-jet events in ep collisions at HERA. 2008.

[21] F. D. Aaron et al. Jet Production in ep Collisions at Low Q^2 and Determination of α_s. 2010. doi:10.1140/epjc/s10052-010-1282-x.

[22] S. Chekanov et al. An NLO QCD analysis of inclusive cross-section and jet-production data from the ZEUS experiment. *Eur. Phys. J.*, C42:1–16, 2005. doi:10.1140/epjc/s2005-02293-x.

[23] H. Abramowicz et al. Inclusive dijet cross sections in deep inelastic scattering at HERA. *ZEUS-pub-10-005*, expected to be submitted to the journal soon, 2010. post-reading draft.

[24] John R. Ellis. Limits of the Standard Model. 2002. arXiv:hep-ph/0211168.

[25] The Large Hadron Collider. URL `http://lhc.web.cern.ch/lhc/`.

[26] James Brau, (Ed.) et al. ILC Reference Design Report Volume 1 - Executive Summary. 2007.

[27] R. Tomás. Overview of the Compact Linear Collider. *Phys. Rev. ST Accel. Beams*, 13(1):014801, Jan 2010. doi:10.1103/PhysRevSTAB.13.014801.

[28] Robert Hofstadter. Electron scattering and nuclear structure. *Rev. Mod. Phys.*, 28:214–254, 1956. doi:10.1103/RevModPhys.28.214.

[29] R. W. Mcallister and R. Hofstadter. ELASTIC SCATTERING OF 188-MEV ELECTRONS FROM THE PROTON AND THE ALPHA PARTICLE. *Phys. Rev.*, 102:851–856, 1956. doi:10.1103/PhysRev.102.851.

[30] W. Bartel et al. Electroproduction of pions near the Delta(1236) isobar and the form-factor of G*(M)(q^2) of the (gamma N Delta) vertex. *Phys. Lett.*, B28: 148–151, 1968. doi:10.1016/0370-2693(68)90155-X.

[31] J. D. Bjorken. Asymptotic Sum Rules at Infinite Momentum. *Phys. Rev.*, 179: 1547–1553, 1969. doi:10.1103/PhysRev.179.1547.

[32] Jerome I. Friedman and Henry W. Kendall. Deep inelastic electron scattering. *Ann. Rev. Nucl. Part. Sci.*, 22:203–254, 1972. doi:10.1146/annurev.ns.22.120172.001223.

[33] Elliott D. Bloom et al. High-Energy Inelastic *ep* Scattering at 6-Degrees and 10-Degrees. *Phys. Rev. Lett.*, 23:930–934, 1969. doi:10.1103/PhysRevLett.23.930.

[34] Martin Breidenbach et al. Observed Behavior of Highly Inelastic electron-Proton Scattering. *Phys. Rev. Lett.*, 23:935–939, 1969. doi:10.1103/PhysRevLett.23.935.

[35] Richard P. Feynman. Very high-energy collisions of hadrons. *Phys. Rev. Lett.*, 23:1415–1417, 1969. doi:10.1103/PhysRevLett.23.1415.

[36] G. Zweig. An SU(3) model for strong interaction symmetry and its breaking. CERN-TH-401.

[37] Murray Gell-Mann. A Schematic Model of Baryons and Mesons. *Phys. Lett.*, 8: 214–215, 1964. doi:10.1016/S0031-9163(64)92001-3.

[38] J. D. Bjorken and Emmanuel A. Paschos. Inelastic Electron Proton and gamma Proton Scattering, and the Structure of the Nucleon. *Phys. Rev.*, 185:1975–1982, 1969. doi:10.1103/PhysRev.185.1975.

[39] Ingo Sick. On the rms-radius of the proton. *Phys. Lett.*, B576:62–67, 2003. doi:10.1016/j.physletb.2003.09.092.

[40] Randolf Pohl et al. The size of the proton. *Nature*, 466:213Ž20132, 2010. doi:10.1038/nature09250.

[41] R. Devenish and A. Cooper-Sarkar. *Deep Inelastic Scattering*. Oxford University Press, 2003.

[42] Curtis G. Callan, Jr. and David J. Gross. High-energy electroproduction and the constitution of the electric current. *Phys. Rev. Lett.*, 22:156–159, 1969. doi:10.1103/PhysRevLett.22.156.

[43] G. Altarelli and G. Martinelli. Transverse momentum of jets in electroproduction from quantum chromodynamics. *Phys. Lett. B*, 76(1):89–94, 1978. doi:10.1016/0370-2693(78)90109-0.

[44] F. D. Aaron et al. Measurement of the Proton Structure Function F_L at Low x. *Phys. Lett.*, B665:139–146, 2008. doi:10.1016/j.physletb.2008.05.070.

[45] S. Chekanov et al. Measurement of the longitudinal proton structure function at HERA. *Phys. Lett. B*, 682(1):8–22, 2009. doi:10.1016/j.physletb.2009.10.050.

[46] ZEUS and H1 Collab. Compiled H1+ZEUS NC and CC plots for conferences. *zeus-prel-09-001*, 2009.

[47] I. J. R. Aitchison and A. J. G. Hey. Gauge theories in particle physics: A practical introduction. Vol. 1: From relativistic quantum mechanics to QED. . Bristol, UK: IOP (2003) 406 p.

[48] I. J. R. Aitchison and A. J. G. Hey. Gauge theories in particle physics: A practical introduction. Vol. 2: Non-Abelian gauge theories: QCD and the electroweak theory. . Bristol, UK: IOP (2004) 454 p.

[49] Raymond Brock et al. Handbook of perturbative QCD: Version 1.0. *Rev. Mod. Phys.*, 67:157–248, 1995. doi:10.1103/RevModPhys.67.157.

[50] R. K. Ellis, W. James Stirling, and B. R. Webber. QCD and collider physics. *Camb. Monogr. Part. Phys. Nucl. Phys. Cosmol.*, 8:1–435, 1996.

[51] R. Brandelik et al. Evidence for a Spin One Gluon in Three Jet Events. *Phys. Lett.*, B97:453, 1980. doi:10.1016/0370-2693(80)90639-5.

[52] Chen-Ning Yang and Robert L. Mills. Conservation of isotopic spin and isotopic gauge invariance. *Phys. Rev.*, 96:191–195, 1954. doi:10.1103/PhysRev.96.191.

[53] Gerard 't Hooft and M. J. G. Veltman. Regularization and Renormalization of Gauge Fields. *Nucl. Phys.*, B44:189–213, 1972. doi:10.1016/0550-3213(72)90279-9.

[54] William A. Bardeen, A. J. Buras, D. W. Duke, and T. Muta. Deep Inelastic Scattering Beyond the Leading Order in Asymptotically Free Gauge Theories. *Phys. Rev.*, D18:3998, 1978. doi:10.1103/PhysRevD.18.3998.

[55] David J. Gross and Frank Wilczek. Ultraviolet Behavior of Non-Abelian Gauge Theories. *Phys. Rev. Lett.*, 30(26):1343–1346, Jun 1973. doi:10.1103/PhysRevLett.30.1343.

[56] H. David Politzer. Reliable Perturbative Results for Strong Interactions? *Phys. Rev. Lett.*, 30(26):1346–1349, Jun 1973. doi:10.1103/PhysRevLett.30.1346.

[57] William E. Caswell. Asymptotic Behavior of Non-Abelian Gauge Theories to Two-Loop Order. *Phys. Rev. Lett.*, 33(4):244–246, Jul 1974. doi:10.1103/PhysRevLett.33.244.

[58] P. M. Stevenson. Optimized perturbation theory. *Phys. Rev. D*, 23(12):2916–2944, Jun 1981. doi:10.1103/PhysRevD.23.2916.

[59] Paul M. Stevenson. Resolution of the Renormalization Scheme Ambiguity in Perturbative QCD. *Phys. Lett.*, B100:61, 1981. doi:10.1016/0370-2693(81)90287-2.

[60] G. Grunberg. Renormalization group improved perturbative QCD. *Phys. Lett. B*, 95(1):70 – 74, 1980. doi:10.1016/0370-2693(80)90402-5.

[61] J. Collins. Choosing the renormalization/factorization scale (QCD). *Journal of Physics G: Nuclear and Particle Physics*, 17(10):1547, 1991. URL `http://stacks.iop.org/0954-3899/17/i=10/a=009`.

[62] ZEUS Collab. α_s from inclusive-jet cross sections in photoproduction at ZEUS. *ZEUS-prel-08-008*, 2008.

[63] ZEUS Collab. Inclusive-jet production in NC DIS with HERA II. *zeus-prel-10-002*, 2010.

[64] Stefan Kluth. α_S from LEP. *J. Phys. Conf. Ser.*, 110:022023, 2008. doi:10.1088/1742-6596/110/2/022023.

[65] S. Bethke. Experimental tests of asymptotic freedom. *Prog. Part. Nucl. Phys.*, 58:351–386, 2007. doi:10.1016/j.ppnp.2006.06.001.

[66] Claude Amsler et al. Review of particle physics. *Phys. Lett.*, B667:1, 2008. doi:10.1016/j.physletb.2008.07.018.

[67] B. Bistrovic et al. Understanding hadron structure from lattice QCD in the SciDAC era. *J. Phys. Conf. Ser.*, 16:150–159, 2005.

[68] John C. Collins and Davison E. Soper. The Theorems of Perturbative QCD. *Ann. Rev. Nucl. Part. Sci.*, 37:383–409, 1987.

[69] Guido Altarelli, R. Keith Ellis, G. Martinelli, and So-Young Pi. Processes Involving Fragmentation Functions Beyond the Leading Order in QCD. *Nucl. Phys.*, B160:301, 1979. doi:10.1016/0550-3213(79)90062-2.

[70] Guido Altarelli and G. Parisi. Asymptotic Freedom in Parton Language. *Nucl. Phys.*, B126:298, 1977.

[71] V. N. Gribov and L. N. Lipatov. e^+e^- pair annihilation and deep inelastic ep scattering in perturbation theory. *Sov. J. Nucl. Phys.*, 15:675–684, 1972.

[72] V. N. Gribov and L. N. Lipatov. Deep inelastic ep scattering in perturbation theory. *Sov. J. Nucl. Phys.*, 15:438–450, 1972.

[73] Yuri L. Dokshitzer. Calculation of the Structure Functions for Deep Inelastic Scattering and e^+e^- Annihilation by Perturbation Theory in Quantum Chromodynamics. *Sov. Phys. JETP*, 46:641–653, 1977.

[74] I. I. Balitsky and L. N. Lipatov. The Pomeranchuk Singularity in Quantum Chromodynamics. *Sov. J. Nucl. Phys.*, 28:822–829, 1978.

[75] E. A. Kuraev, L. N. Lipatov, and Victor S. Fadin. The Pomeranchuk Singularity in Nonabelian Gauge Theories. *Sov. Phys. JETP*, 45:199–204, 1977.

[76] Marcello Ciafaloni. Coherence Effects in Initial Jets at Small q^2/s. *Nucl. Phys.*, B296:49, 1988. doi:10.1016/0550-3213(88)90380-X.

[77] S. Catani, F. Fiorani, and G. Marchesini. QCD Coherence in Initial State Radiation. *Phys. Lett.*, B234:339, 1990. doi:10.1016/0370-2693(90)91938-8.

[78] S. Catani, F. Fiorani, and G. Marchesini. Small x Behavior of Initial State Radiation in Perturbative QCD. *Nucl. Phys.*, B336:18, 1990. doi:10.1016/0550-3213(90)90342-B.

[79] A. D. Martin. BFKL / CCFM phenomenology. Prepared for International Workshop on Deep Inelastic Scattering and Related Phenomena (DIS 96), Rome, Italy, 15- 19 Apr 1996.

[80] F. D. Aaron et al. Combined Measurement and QCD Analysis of the Inclusive ep Scattering Cross Sections at HERA. *JHEP*, 01:109, 2010. doi:10.1007/JHEP01(2010)109.

[81] Pavel M. Nadolsky et al. Implications of CTEQ global analysis for collider observables. *Phys. Rev.*, D78:013004, 2008. doi:10.1103/PhysRevD.78.013004.

[82] A. D. Martin, W. J. Stirling, R. S. Thorne, and G. Watt. Parton distributions for the LHC. *Eur. Phys. J.*, C63:189–285, 2009. doi:10.1140/epjc/s10052-009-1072-5.

[83] B. Reisert. H1 inclusive cross-section measurements and an extraction of parton distribution functions. *Mod. Phys. Lett.*, A20:1557–1571, 2005. doi:10.1142/S0217732305017706.

[84] ZEUS Collab. ZEUS09 PDF fit including HERA-II NC/CC e^-p and CC e^+p and HER/MER/LER data. *zeus-prel-09-010*, 2009.

[85] M. R. Whalley, D. Bourilkov, and R. C. Group. The Les Houches Accord PDFs (LHAPDF) and Lhaglue. 2005. URL `http://projects.hepforge.org/`.

[86] R. P. Feynman. *Photon-hadron interactions*. New York, 1972.

[87] K. H. Streng, T. F. Walsh, and P. M. Zerwas. QUARK AND GLUON JETS IN THE BREIT FRAME OF LEPTON - NUCLEON SCATTERING. *Zeit. Phys.*, C2:237, 1979. doi:10.1007/BF01474667.

[88] B. R. Webber. Factorization and jet clustering algorithms for deep inelastic scattering. *J. Phys.*, G19:1567–1575, 1993.

[89] J. E. Huth et al. Toward a standardization of jet definitions. In E. L. Berger, editor, *Research directions for the decade. Proceedings, 1990 Summer Study on High-Energy Physics, Snowmass, USA, June 25 - July 13, 1990*, page 134. World Scientific, 1992.

[90] S. Catani, Yuri L. Dokshitzer, M. H. Seymour, and B. R. Webber. Longitudinally invariant k_t clustering algorithms for hadron hadron collisions. *Nucl. Phys.*, B406:187–224, 1993. doi:10.1016/0550-3213(93)90166-M.

[91] Stephen D. Ellis and Davison E. Soper. Successive combination jet algorithm for hadron collisions. *Phys. Rev.*, D48:3160–3166, 1993. doi:10.1103/PhysRevD.48.3160.

[92] Yuri L. Dokshitzer, G. D. Leder, S. Moretti, and B. R. Webber. Better Jet Clustering Algorithms. *JHEP*, 08:001, 1997.

[93] M. Wobisch and T. Wengler. Hadronization corrections to jet cross sections in deep- inelastic scattering. 1998. hep-ph/9907280.

[94] Matteo Cacciari, Gavin P. Salam, and Gregory Soyez. The anti-k_t jet clustering algorithm. *JHEP*, 04:063, 2008. doi:10.1088/1126-6708/2008/04/063.

[95] Gavin P. Salam and Gregory Soyez. A practical Seedless Infrared-Safe Cone jet algorithm. *JHEP*, 05:086, 2007.

[96] Matteo Cacciari, Gavin P. Salam, and Gregory Soyez. The Catchment Area of Jets. *JHEP*, 04:005, 2008. doi:10.1088/1126-6708/2008/04/005.

[97] U. Schneekloth (ed.). The HERA luminosity upgrade. 1998. DESY-HERA-98-05.

[98] D. P. Barber et al. The first achievement of longitudinal spin polarization in a high-energy electron storage ring. *Phys. Lett.*, B343:436–443, 1995. doi:10.1016/0370-2693(94)01465-O.

[99] A.A.Sokolov and I.M.Ternov. On Polarization and Spin Effects in Synchrotron Radiation Theory. *Sov. Phys. Dokl.*, 8:1203, 1964.

[100] V. N. Baier and Valery A. Khoze. Determination of the transverse polarization of high- energy electrons. *Sov. J. Nucl. Phys.*, 9:238–240, 1969.

[101] D. P. Barber et al. The HERA polarimeter and the first observation of electron spin polarization at HERA. *Nucl. Instrum. Meth.*, A329:79–111, 1993. doi:10.1016/0168-9002(93)90924-7.

[102] M. Beckmann et al. The longitudinal polarimeter at HERA. *Nucl. Instrum. Meth.*, A479:334–348, 2002. doi:10.1016/S0168-9002(01)00901-9.

[103] ZEUS Collaboration. THE ZEUS DETECTOR, STATUS REPORT 1993 U.HOLM (ED.) DESY (1993) (UNPUBLISHED). URL `http://www-zeus.desy.de/bluebook/bluebook.html`.

[104] C. B. Brooks et al. Development of the ZEUS central tracking detector. *Nucl. Instrum. Meth.*, A283:477–483, 1989.

[105] N. Harnew et al. Vertex Triggering Using Time Difference Measurements in the ZEUS Central Tracking Detector. *Nucl. Instrum. Meth.*, A279:290–296, 1989.

[106] B. Foster et al. The Performance of the Zeus central tracking detector z- by-timing electronics in a transputer based data acquisition system. *Nucl. Phys. Proc. Suppl.*, 32:181–188, 1993. doi:10.1016/0920-5632(93)90023-Y.

[107] B. Foster et al. The Design and construction of the ZEUS central tracking detector. *Nucl. Instrum. Meth.*, A338:254–283, 1994.

[108] R. Hall-Wilton, N. McCubbin, P. Nylander, M. Sutton, and M. Wing. The CTD Tracking Resolution. ZEUS-99-024, 1999.

[109] A. Polini et al. The design and performance of the ZEUS Micro Vertex detector. *Nucl. Instrum. Meth.*, A581:656–686, 2007. doi:10.1016/j.nima.2007.08.167.

[110] J. Kruger. The uranium scintillator calorimeter for the ZEUS detector at the electron - proton collider HERA: the heart of ZEUS. DESY-F35-92-02.

[111] M. Derrick et al. Design and construction of the ZEUS barrel calorimeter. *Nucl. Instrum. Meth.*, A309:77–100, 1991.

[112] A. Andresen et al. Construction and beam test of the ZEUS forward and rear calorimeter. *Nucl. Instrum. Meth.*, A309:101–142, 1991.

[113] A. Caldwell et al. Design and implementation of a high precision readout system for the ZEUS calorimeter. *Nucl. Instrum. Meth.*, A321:356–364, 1992.

[114] A. Bernstein et al. Beam tests of the ZEUS barrel calorimeter. *Nucl. Instrum. Meth.*, A336:23–52, 1993.

[115] H. Bethe and W. Heitler. On the Stopping of fast particles and on the creation of positive electrons. *Proc. Roy. Soc. Lond.*, A146:83–112, 1934.

[116] J. Andruszkow et al. First measurement of HERA luminosity by ZEUS lumi monitor. DESY-92-066.

[117] M. Derrick et al. Measurement of total and partial photon proton cross-sections at 180-GeV center-of-mass energy. *Z. Phys.*, C63:391–408, 1994. doi:10.1007/BF01580320.

[118] J. Andruszkow et al. Luminosity measurement in the ZEUS experiment. *Acta Phys. Polon.*, B32:2025–2058, 2001.

[119] M. Helbich et al. The spectrometer system for measuring ZEUS luminosity at HERA. *Nucl. Instrum. Meth.*, A565:572–588, 2006. doi:10.1016/j.nima.2006.06.049.

[120] J. Chwastowski, J. Figiel, A. Kotarba, K. Olkiewicz, and L. Suszycki. Aerogel Cherenkov detectors for the luminosity measurement at HERA. *Nucl. Instrum. Meth.*, A504:222–227, 2003. doi:10.1016/S0168-9002(03)00794-0.

[121] W. H. Smith, K. Tokushuku, and L. W. Wiggers. The ZEUS trigger system. Contributed to 10th International Conference on Computing in High Energy Physics (CHEP 92), Annecy, France, 21-25 Sept 1992.

[122] R. Carlin, W. H. Smith, K. Tokushuku, and L. Wiggers. Experience with the ZEUS trigger system. *Nucl. Phys. Proc. Suppl.*, 44:430–434, 1995. doi:10.1016/0920-5632(95)00565-X.

[123] R. Carlin, W. H. Smith, K. Tokushuku, and L. W. Wiggers. The trigger of ZEUS, a flexible system for a high bunch crossing rate collider. *Nucl. Instrum. Meth.*, A379:542–544, 1996. doi:10.1016/0168-9002(96)00559-1.

[124] W. H. Smith et al. The ZEUS calorimeter first level trigger. *Nucl. Instrum. Meth.*, A355:278–294, 1995. doi:10.1016/0168-9002(94)01163-X.

[125] G. P. Heath et al. The ZEUS first level tracking trigger. *Nucl. Instrum. Meth.*, A315:431–435, 1992. doi:10.1016/0168-9002(92)90741-L.

[126] Philip Daniel Allfrey et al. The design and performance of the ZEUS global tracking trigger. *Nucl. Instrum. Meth.*, A580:1257–1282, 2007. doi:10.1016/j.nima.2007.06.106.

[127] Hendrikus Alphonsus Jozef Richard Uijterwaal. The Global second level trigger for ZEUS. RX-1392 (AMSTERDAM).

[128] Ulf Behrens, Lars Hagge, and Wolfgang O. Vogel. The Eventbuilder of the ZEUS experiment. *Nucl. Instrum. Meth.*, A332:253–262, 1993. doi:10.1016/0168-9002(93)90767-C.

[129] J. C. Hart. Experience with ADAMO in ZEUS. In *Erice 1990, Proceedings, Data structures for particle physics experiments* 51-57.

[130] David C. Bailey et al. The ZEUS third level trigger hardware architecture. Presented at International Conference on Open Bus Systems 92, Zurich, Switzerland, 13-15 Oct 1992.

[131] S. Bhadra, M. Crombie, David P. Kirkby, and R. S. Orr. The ZEUS third level trigger system. *Comput. Phys. Commun.*, 57:321–324, 1989. doi:10.1016/0010-4655(89)90236-1.

[132] A. Kwiatkowski, H. Spiesberger, and H. J. Mohring. HERACLES: AN EVENT GENERATOR FOR *ep* INTERACTIONS AT HERA ENERGIES INCLUDING RADIATIVE PROCESSES: VERSION 1.0. *Comp. Phys. Commun.*, 69:155–172, 1992. doi:10.1016/0010-4655(92)90136-M.

[133] K. Charchuła, G. A. Schuler, and H. Spiesberger. Combined QED and QCD radiative effects in deep inelastic lepton - proton scattering: The Monte Carlo generator DJANGO6. *Comput. Phys. Commun.*, 81:381–402, 1994. doi:10.1016/0010-4655(94)90086-8.

[134] H. L. Lai et al. Global QCD analysis of parton structure of the nucleon: CTEQ5 parton distributions. *Eur. Phys. J.*, C12:375–392, 2000. doi:10.1007/s100529900196.

[135] H. Plothow-Besch. PDFLIB: A Library of all available parton density functions of the nucleon, the pion and the photon and the corresponding α_s calculations. *Comput. Phys. Commun.*, 75:396–416, 1993. doi:10.1016/0010-4655(93)90051-D.

[136] G. Ingelman, A. Edin, and J. Rathsman. LEPTO 6.5 - A Monte Carlo Generator for Deep Inelastic Lepton-Nucleon Scattering. *Comput. Phys. Commun.*, 101: 108–134, 1997. doi:10.1016/S0010-4655(96)00157-9.

[137] M. Bengtsson, G. Ingelman, and T. Sjöstrand. Parton cascade evolution and event structure at HERA. Hamburg 1987, Proceedings, HERA Workshop, vol. I 149.

[138] T. Sjöstrand. A Model for Initial State Parton Showers. *Phys. Lett.*, B157:321, 1985. doi:10.1016/0370-2693(85)90674-4.

[139] Leif Lonnblad. ARIADNE version 4: A Program for simulation of QCD cascades implementing the color dipole model. *Comput. Phys. Commun.*, 71:15–31, 1992. doi:10.1016/0010-4655(92)90068-A.

[140] Leif Lonnblad. Rapidity gaps and other final state properties in the color dipole model for deep inelastic scattering. *Z. Phys.*, C65:285–292, 1995. doi:10.1007/BF01571885.

[141] G. Gustafson and U. Pettersson. Dipole Formulation of QCD Cascades. *Nucl. Phys.*, B306:746, 1988. doi:10.1016/0550-3213(88)90441-5.

[142] B. Andersson, P. Dahlkvist, and G. Gustafson. AN INFRARED STABLE MULTIPLICITY MEASURE ON QCD PARTON STATES. *Phys. Lett.*, B214: 604–608, 1988. doi:10.1016/0370-2693(88)90128-1.

[143] B. Andersson, G. Gustafson, A. Nilsson, and C. Sjogren. FLUCTUATIONS AND ANOMALOUS DIMENSIONS IN QCD CASCADES. *Z. Phys.*, C49:79–90, 1991. doi:10.1007/BF01570799.

[144] G. Gustafson. Multiplicity distributions in QCD cascades. *Nucl. Phys.*, B392: 251–280, 1993. doi:10.1016/0550-3213(93)90203-2.

[145] B. Andersson, G. Gustafson, L. Lonnblad, and U. Pettersson. Coherence Effects in Deep Inelastic Scattering. *Z. Phys.*, C43:625, 1989. doi:10.1007/BF01550942.

[146] G. Gustafson. Dual Description of a Confined Color Field. *Phys. Lett.*, B175: 453, 1986. doi:10.1016/0370-2693(86)90622-2.

[147] T. Sjöstrand. High-energy physics event generation with PYTHIA 5.7 and JETSET 7.4. *Comput. Phys. Commun.*, 82:74–90, 1994. doi:10.1016/0010-4655(94)90132-5.

[148] T. Sjöstrand. The Lund Monte Carlo for Jet Fragmentation and e^+e^- Physics: Jetset Version 6.2. *Comput. Phys. Commun.*, 39:347–407, 1986. doi:10.1016/0010-4655(86)90096-2.

[149] T. Sjöstrand and M. Bengtsson. The Lund Monte Carlo for Jet Fragmentation and e+ e- Physics. Jetset Version 6.3: An Update. *Comput. Phys. Commun.*, 43:367, 1987. doi:10.1016/0010-4655(87)90054-3.

[150] Bo Andersson, G. Gustafson, G. Ingelman, and T. Sjöstrand. Parton Fragmentation and String Dynamics. *Phys. Rept.*, 97:31–145, 1983. doi:10.1016/0370-1573(83)90080-7.

[151] B. R. Webber. A QCD Model for Jet Fragmentation Including Soft Gluon Interference. *Nucl. Phys.*, B238:492, 1984. doi:10.1016/0550-3213(84)90333-X.

[152] Richard D. Field and Stephen Wolfram. A QCD Model for e^+e^- Annihilation. *Nucl. Phys.*, B213:65, 1983. doi:10.1016/0550-3213(83)90175-X.

[153] R. Brun, F. Bruyant, M. Maire, A. C. McPherson, and P. Zanarini. GEANT3. CERN-DD-EE-84-1.

[154] R. K. Ellis, D. A. Ross, and A. E. Terrano. The Perturbative Calculation of Jet Structure in e^+e^- Annihilation. *Nucl. Phys.*, B178:421, 1981. doi:10.1016/0550-3213(81)90165-6.

[155] Z. Kunszt and D. E. Soper. Calculation of jet cross-sections in hadron collisions at order α_s^3. *Phys. Rev.*, D46:192–221, 1992. doi:10.1103/PhysRevD.46.192.

[156] W. T. Giele and E. W. Nigel Glover. Higher order corrections to jet cross-sections in e^+e^- annihilation. *Phys. Rev.*, D46:1980–2010, 1992. doi:10.1103/PhysRevD.46.1980.

[157] S. Catani and M. H. Seymour. A general algorithm for calculating jet cross sections in NLO QCD. *Nucl. Phys.*, B485:291–419, 1997. doi:10.1016/S0550-3213(96)00589-5.

[158] S. Catani and M. H. Seymour. NLO QCD calculations in DIS at HERA based on the dipole formalism. 1996.

[159] Z. Nagy and Z. Trocsanyi. Multi-jet cross sections in deep inelastic scattering at next-to-leading order. *Phys. Rev. Lett.*, 87:082001, 2001. doi:10.1103/PhysRevLett.87.082001.

[160] Stefano Frixione and Giovanni Ridolfi. Jet photoproduction at HERA. *Nucl. Phys.*, B507:315–333, 1997. doi:10.1016/S0550-3213(97)00575-0.

[161] Andrea Banfi and Mrinal Dasgupta. Dijet rates with symmetric E(t) cuts. *JHEP*, 01:027, 2004.

[162] M. Klasen and G. Kramer. Dijet cross-sections at $O(\alpha\alpha_s^2)$ in photon - proton collisions. *Phys. Lett.*, B366:385–393, 1996. doi:10.1016/0370-2693(95)01352-0.

[163] S. Catani and B. R. Webber. Infrared safe but infinite: Soft gluon divergences inside the physical region. *JHEP*, 10:005, 1997.

[164] G. M. Briskin. *Diffractive dissociation in ep deep inelastic scattering.* PhD thesis, U. Tel Aviv, 1998.

[165] N. Tuning. *Proton Structure Functions at HERA*. PhD thesis, Amsterdam University, 2001.

[166] T. Theedt. *Measurement of Dijet Cross Sections in Deep Inelastic ep Scattering at HERA*. PhD thesis, Universität Hamburg, 2009. DESY-THESIS-2009-046.

[167] J. Grosse-Knetter. Corrections for the Hadronic Final State. Internal ZEUS Note, ZEUS-98-031, 1998.

[168] Halina Abramowicz, Allen Caldwell, and Ralph Sinkus. Neural network based electron identification in the ZEUS calorimeter. *Nucl. Instrum. Meth.*, A365: 508–517, 1995.

[169] J. Breitweg et al. Measurement of high-Q^2 neutral-current e^+p deep inelastic scattering cross-sections at HERA. *Eur. Phys. J.*, C11:427–445, 1999.

[170] B. Straub. The EM Electron Finder. unpublished. URL http://www-zeus.desy.de/~straub/ZEUS_ONLY/doc/em.ps.

[171] Stanislaus Cornelius Maria Bentvelsen, J Engelen, and P M Kooijman. Reconstruction of (x,Q^2) and extraction of structure functions in neutral current scattering at HERA. In W. Buchmüller, G. Ingelman, editor, *Proc. of the Workshop on Physics at HERA*, Amsterdam, Jan 1992. NIKHEF-H-92-02.

[172] G Bernardi and W Hildesheim. A detailed simulation of F_2 measurability at HERA. Technical Report LPNHE-92-01, Paris 6. Lab. Phys. Nucl. Théor. Hautes Enérg., Paris, May 1992.

[173] A Blondel and B Jaquet. Proceedings of the study of an ep facility for Europe. 1979. page 391. DESY 79/48.

[174] O. Kind et al. A ROOT-based client-server event display for the ZEUS experiment. In *In the Proceedings of 2003 Conference for Computing in High-Energy and Nuclear Physics (CHEP 03)*, 2003.

[175] M. Moritz. *Measurement of the High Q^2 Neutral Current DIS Cross Section at HERA*. PhD thesis, University Hamburg, 2001. DESY-THESIS-2002-009.

[176] José Ricardo Morais Silvia Gonçalo. *Measurement of the high-Q^2 neutral current deep inelastic scattering cross sections with the ZEUS detector at HERA*. PhD thesis, Imperial College - London, 2003. DESY-THESIS-2003-022.

[177] A. Arbuzov, Dmitri Yu. Bardin, J. Blümlein, L. Kalinovskaya, and T. Riemann. HECTOR 1.00 - A program for the calculation of QED, QCD and electroweak corrections to ep and lN deep inelastic neutral and charged current scattering. *Comput. Phys. Commun.*, 94:128–184, 1996. doi:10.1016/0010-4655(96)00005-7.

[178] M. Wing. Setting the jet energy scale for the ZEUS calorimeter. In R. Zhu, editor, *Proc. of the 10th International Conference on Calorimetry in High Energy Physics*, page 767, Pasadena, USA, 2002.

[179] S. Chekanov et al. High-mass dijet cross sections in photoproduction at HERA. *Phys. Lett.*, B531:9–27, 2002.

[180] D. S. Bailey et al. The design and performance of the ZEUS central tracking detector z-by-timing system. *Nucl. Instrum. Meth.*, A396:320–349, 1997. doi:10.1016/S0168-9002(97)00790-0.

[181] ZEUS Collab. The CTD FLT event classification. unpublished. URL http://www-zeus.desy.de/components/gflt/yycontents/trkv.html.

[182] James Ferrando. CTD Gas Gain. internal talk. unpublished, 2009. URL https://www-zeus.desy.de/zems/ZEUS_ONLY/display_from_link.php?fid=11166.

[183] Achim Geiser. Trigger and Rate Studies. internal talk. unpublished, 2009. URL https://www-zeus.desy.de/zems/ZEUS_ONLY/display_from_link.php?fid=11165.

[184] Michał Własenko. *Measurement of neutral current deep inelastic e^+p scattering cross sections with longitudinally polarized positrons with ZEUS at HERA*. PhD thesis, Universität Bonn - Physikalisches Institut, 2009.

[185] G. D'Agostini. A Multidimensional unfolding method based on Bayes' theorem. *Nucl. Instrum. Meth.*, A362:487–498, 1995. doi:10.1016/0168-9002(95)00274-X.

[186] G. Cowan. A survey of unfolding methods for particle physics. Prepared for Conference on Advanced Statistical Techniques in Particle Physics, Durham, England, 18-22 Mar 2002.

[187] Claudia Glasman. private communication.

[188] S. Chekanov et al. Measurement of the neutral current cross section and F_2 structure function for deep inelastic e^+p scattering at HERA. *Eur. Phys. J.*, C21:443–471, 2001. doi:10.1007/s100520100749.

[189] S. Chekanov et al. Measurement of high-Q^2 neutral current deep inelastic e^-p scattering cross sections with a longitudinally polarised electron beam at HERA. *Eur. Phys. J.*, C62:625–658, 2009. doi:10.1140/epjc/s10052-009-1055-6.

[190] G. Marchesini et al. HERWIG: A Monte Carlo event generator for simulating hadron emission reactions with interfering gluons. Version 5.1 - April 1991. *Comput. Phys. Commun.*, 67:465–508, 1992. doi:10.1016/0010-4655(92)90055-4.

[191] Yongdok Ri. *Measurement of e^-p Neutral-Current Deep Inelastic Scattering Cross Sections with Longitudinally Polarized Electron Beams at $\sqrt{s} = 318$ GeV.* PhD thesis, Department of Physics, Tokyo Metropolitan University, 2009.

[192] S. Chekanov et al. A ZEUS next-to-leading-order QCD analysis of data on deep inelastic scattering. *Phys. Rev.*, D67:012007, 2003. doi:10.1103/PhysRevD.67.012007.

[193] Marco Battaglia. Physics case and challenges for the vertex tracker at future high-energy e^+e^- linear colliders. *Nucl. Instrum. Meth.*, A473:75–78, 2001. doi:10.1016/S0168-9002(01)01123-8.

[194] Gerald Aarons et al. International Linear Collider Reference Design Report Volume 2: PHYSICS AT THE ILC. 2007.

[195] Ties Behnke, (Ed.) et al. ILC Reference Design Report Volume 4 - Detectors. 2007.

[196] T. Behnke, (ed.), S. Bertolucci, (ed.), R. D. Heuer, (ed.), and R. Settles, (ed.). TESLA: The superconducting electron positron linear collider with an integrated X-ray laser laboratory. Technical design report. Pt. 4: A detector for TESLA. 2001. DESY-01-011.

[197] K. D. Stefanov. CCD vertex detector for the future linear collider. *Nucl. Instrum. Meth.*, A501:245–250, 2003. doi:10.1016/S0168-9002(02)02042-9.

[198] R. Turchetta et al. A monolithic active pixel sensor for charged particle tracking and imaging using standard VLSI CMOS technology. *Nucl. Instrum. Meth.*, A458:677–689, 2001. doi:10.1016/S0168-9002(00)00893-7.

[199] Yu. Gornushkin et al. Tracking performance and radiation tolerance of monolithic active pixel sensors. *Nuclear Instruments and Methods in Physics Research Section A*, 513(1-2):291 – 295, 2003. ISSN 0168-9002. doi:10.1016/j.nima.2003.08.050. Proceedings of the 6th International Conference on Position-Sensitive Detectors.

[200] P. Fischer, W. Neeser, M. Trimpl, J. Ulrici, and N. Wermes. Readout concepts for DEPFET pixel arrays. *Nucl. Instrum. Meth.*, A512:318–325, 2003. doi:10.1016/S0168-9002(03)01909-0.

[201] I. Gregor and C. Muhl. JRA1 - Status of Machanics, Cooling and Infrastructure. EUDET-Memo-2007-26, 2007.

[202] I. Peric, Ch. Takacs, J. Behr, and P. Fischer. The first beam test of a monolithic particle pixel detector in high-voltage CMOSTechnology. In *12th Vienna Conference for Instrumentation VCI2010*. proceedings submitted to Elsevier, 2010.

[203] C. Takacs. TEST SYSTEM SETUP AND EVALUATION OF TESTBEAM MEASUREMENTS OF A NOVEL MONOLITHIC PIXEL PARTICLE DETECTOR IMPLEMENTED IN HIGH VOLTAGE TECHNOLOGY. Diploma thesis, Ruprecht-Karls-Universität Heidelberg, 2009.

[204] The EUDET JRA1 Group. JRA1 Delivery: Test Report on EUDET High Resolution Pixel Telescope. EUDET-Report-2008-04, 2008.

[205] Bart Dierickx, Guy Meynants, and Danny Scheffer. Near-100 % fill factor standard CMOS active pixel. In *IEEE Workshop on Charge-Coupled Devices & Advanced Image Sensors*, 1997.

[206] L. Rossi, P. Fischer, T. Rohe, and N. Wermes. *Pixel detectors: From fundamentals to applications*. Springer, 2006. Berlin, Germany.

[207] M. Deveaux et al. Radiation Tolerance of CMOS Monolithic Active Pixel Sensors with Self-Biased Pixels. *ArXiv e-prints*, August 2009. URL http://adsabs.harvard.edu/abs/2009arXiv0908.4202D.

[208] A. Dorokhov. Optimization of amplifiers for Monolithic Active Pixel Sensors. In S. Claude, editor, *Proc. of the Topical Workshop on Electronics for Particle Physics (TWEPP 07)*, page 423, Prague, Czech Republic, 2007.

[209] W. Dulinski. Status of pixel sensors for the demonstrator phase of the EUDET beam telescope. EUDET-Memo-2007-45, 2007.

[210] P. Niezurawski A.F. Zarnecki. EUDET Telescope Geometry and Resolution Studies. EUDET-Report-2007-01, 2007.

[211] A. Bulgheroni. Results from the EUDET telescope with high resolution planes. EUDET-Report-2009-02, 2009.

[212] M. Gelin et al. Test Results of the Zero Suppressed Digital Chip sensor for EUDET-JRA1 beam telescope. EUDET-Memo-2009-26, 2009.

[213] J. Baudot et al. JRA-1 Milestone: Validation of the Final Sensor Equipping the EUDET Beam Telescope. EUDET-Memo-2009-25, 2009.

[214] G. Claus et al. JRA1 Milestone IDC Prototype ready. EUDET-Memo-2008-03, 2008.

[215] A Himmi, A Doziere, O Torheim, C Hu-Guo, and A Winter. A Zero Suppression Micro-Circuit for Binary Readout CMOS Monolithic Sensors. *TWEPP-09: Topical Workshop on Electronics for Particle Physics, Paris, France*, pages 426–430, 2009.

[216] J. Baudot. First Test Results of MIMOSA-26, a Fast CMOS Sensor With Integrated Zero Suppression and Digitized Output. IEEE Nuclear Science Symposium, 2009.

[217] A. Cotta Ramusino. The EUDET Data Reduction Board (EUDRB). EUDET-Memo-2007-36, 2007.

[218] A. Cotta Ramusino. The EUDET Data Reduction Board (EUDRB). EUDET-Memo-2008-38, 2008.

[219] Ingrid-Maria Gregor. private communication.

[220] D Cussans. A Trigger/Timing Logic Unit for ILC Test-beams. *Topical Workshop on Electronics for Particle Physics, Prague, Czech Republic*, pages 420–422, 2007.

[221] D. Cussans. Description of the JRA1 Trigger Logic Unit (TLU). EUDET-Memo-2007-02, 2007.

[222] D. Cussans. Progress on the JRA1 Trigger Logic Unit (TLU). EUDET-Memo-2007-46, 2007.

[223] D. Cussans. Description of the JRA1 Trigger Logic Unit (TLU), v0.2c. EUDET-Memo-2009-04, 2009.

[224] D. Cussans. Status of the TLU v0.2. EUDET-Memo-2009-29, 2009.

[225] M. Pohl D. Haas, E. Corrin. JRA1 - Data acquisition system. EUDET-Memo-2006-07, 2006.

[226] D. Haas. The DAQ for the EUDET pixel telescope. 2007. In the Proceedings of 2007 International Linear Collider Workshop (LCWS07 and ILC07), Hamburg, Germany.

[227] E. Corrin. EUDAQ Software User Manual. EUDET-Memo-2010-01, 2010.

[228] R. Brun and F. Rademakers. ROOT: An object oriented data analysis framework. *Nucl. Instrum. Meth.*, A389:81–86, 1997. doi:10.1016/S0168-9002(97)00048-X.

[229] Daniel Haas. The EUDET High Resolution Pixel Telescope – Towards the Final Telescope. EUDET-Report-2008-02, 2008.

[230] L. Reuen J. Furletova. JRA1 - The DEPFET sensor as the first fully integrated DUT in the EUDET pixel telescope: The SPS test beam 2008. EUDET-Memo-2008-34, 2008.

[231] A. Bulgheroni et al. Eutelescope: tracking software. EUDET-Memo-2007-20, 2007.

[232] A. Bulgheroni et al. EuTelescope, the JRA1 tracking and reconstruction software: a status report (Milestone). EUDET-Memo-2008-48, 2008.

[233] F. Gaede. Marlin and LCCD: Software tools for the ILC. *Nucl. Instrum. Meth.*, A559:177–180, 2006. doi:10.1016/j.nima.2005.11.138.

[234] Marlin. URL `http://ilcsoft.desy.de/portal/software_packages/marlin/`.

[235] J. Engels F. Gaende. Marlin et al - A Software Framework for ILC detector R&D. EUDET-Report-2007-11, 2007.

[236] Frank Gaede, Ties Behnke, Norman Graf, and Tony Johnson. LCIO: A persistency framework for linear collider simulation studies. 2003.

[237] LCIO. URL http://lcio.desy.de/.

[238] Gear – A geometry description toolkit for ILC reconstruction software. URL http://ilcsoft.desy.de/portal/software_packages/gear.

[239] Volker Blobel and C Kleinwort. A New Method for the High-Precision Alignment of Track Detectors. *DESY-02-077.*, page 10 p, Aug 2002.

[240] Volker Blobel. Millepede. URL http://www.desy.de/~blobel.

[241] Gerald R. Lynch and Orin I. Dahl. Approximations to multiple Coulomb scattering. *Nucl. Instrum. Meth.*, B58:6–10, 1991. doi:10.1016/0168-583X(91)95671-Y.

[242] A. Bulgheroni. First test beam results from the EUDET pixel telescope. In *Nuclear Science Symposium Conference Record, 2007. NSS '07. IEEE*, volume 3, pages 1878 –1884, oct. 2007. doi:10.1109/NSSMIC.2007.4436523.

[243] Bronstein, Semendjajew, Musiol, and Mühlig. *Taschenbuch der Mathematik*, page 785. Verlag Harri Deutsch, 6. edition, 2005.

[244] Emlyn Corrin. private communication.

Danksagung

Ich möchte allen Menschen danken, die mich im Laufe meines Studiums, während meiner Diplomarbeit und während meiner Dissertation unterstützt haben.

Zuerst möchte ich Herrn Prof. Klanner und Herrn Prof. Schleper dafür danken, dass sie mir die Möglichkeit gaben in ihrer Arbeitsgruppe meine Dissertation über ein sehr spannendes Thema anfertigen zu können. Herrn Prof. Klanner und Herrn JProf. Haller danke ich besonders dafür, dass sie sich als Gutachter dieser Arbeit zur Verfügung gestellt haben.

Besonderem Dank bin ich Dr. Thomas Schörner-Sadenius für seine wirklich hervorragende und intensive Betreuung verpflichtet. Ich möchte mich auch bei Monica Turcato, Claudia Glasman, Enrico Tassi bedanken für die Hilfe, die sie mir bei der Analyse gegeben haben. Oleg Kuprash danke ich für die Anfertigung der Zweitanalyse.

Ich danke auch Herrn Klanner, Thomas Schörner-Sadenius und Ingrid Gregor für das Lesen verschiedener Entwürfe meiner Arbeit und für das Vorschlagen von Verbesserungen.

Ich danke auch den Mitgliedern der ZEUS/CMS Gruppe der Univertät Hamburg, den Mitgliedern der ZEUS Kollaboration und dem EUDET JRA1 Team für die gute Arbeitsatmosphäre und Zusammenarbeit.

Danken möchte ich auch meinen Eltern und Freunden für ihre Unterstützung, wenn die Dinge mal nicht so liefen, wie ich es mir vorgestellt habe.